

# N-TYPE ORGANIC SEMICONDUCTORS AND CONDUCTORS FOR PLASTIC ELECTRONICS

Lewis Matthew Cowen

UCL

September 2020

Submitted in partial fulfilment of the requirements for the  
degree of: Doctor of Philosophy

I, Lewis Matthew Cowen, confirm that the work presented in this thesis is my own. Where information has been derived from other sources, I confirm that this has been indicated in the thesis.

Work was carried out under the supervision of Dr Bob C Schroeder.

# Abstract

Organic semiconductors have begun to find a place as viable active materials for a new generation of devices. Throughout the development of this relatively new class of materials, it has been apparent that optimising the performance of n-type semiconductors and dopants has been a challenge compared to their p-type counterparts. Many applications in photovoltaics, thermoelectrics, light-emitting diodes and more, require or can benefit from n-type components. To really benefit from the processability and scalability of organic semiconductors in industry it is therefore necessary to develop stable and high-performing n-type materials.

This thesis aims to advance the understanding of promising n-type semiconductor and dopant pairs through structural characterisation. A new “self-doping” naphthalene diimide conductor, NDI-OH, was designed and synthesised based on previously made structures which exhibited surprisingly stable radical anions. A full spectroscopic characterisation of the self-dopant revealed that it is the product of hydrolysis after ion-exchange in basic conditions. This was found to have a profound effect on the mechanism of charge transfer between dopant and semiconducting moieties and on the lifetime of charge carriers. It was postulated that the mixture of compounds present in doped films is likely to contribute to charge transport pathways and the electronic conductivity.

The interactions between n-type semiconductors and fluoride anions was also explored. Reactions between solvent and fluoride salt were found to have an impact on the efficiency and nature of the subsequent charge transfer on to BDOPV semiconductors. The mechanism of doping relied on factors including the acidity of solvent and the presence of water. Spectroscopic characterisation was carried out in order to determine the active compounds involved in charge transfer between tetrabutylammonium fluoride and BDOPV.

Finally, two new n-type polymers, PbTzTT and PbTz3, were designed with the aim of exhibiting a high degree of long-range order in the solid-state. The reactivity of thiazoles and fused thiazolo[5,4-*d*]thiazole heterocycles was explored at length. The ring-opening of these compounds on metalation and the possibilities of electrophilic substitution were especially of interest. The eventual successful synthesis of the polymer PbTzTT is described via a Stille

cross-coupling polymerisation. The PbTz3 macromonomer was also obtained through a double ring-closing condensation. A comparison of the optoelectronic properties of PbTzTT with the structurally analogous p-type polymer PbTTT was also made.

# Statement of Impact

The work detailed in this thesis was carried out with the intention of expanding the library of usable n-type organic conducting materials. The field of organic semiconductors has grown exponentially over the past 50 years; moving from a purely academic topic to industrial manufacture of devices. Throughout this time the development of stable and high-performing n-type materials has been sluggish. The structural and mechanistic characterisation of n-type semiconductors and dopants outlined here has advanced the understanding of two promising candidates for future air stable n-type systems.

Self-doping organic semiconductors have been identified as an efficient way of avoiding problems in processability that come with introducing external molecular dopants. The structure and mechanisms behind molecular semiconductors bearing quaternary ammonium salts used as self-doping materials was previously unknown. This work has confirmed the structure is not as presumed which will reshape the nature of future discussions about their mechanisms and applications. Outside of academia the development of materials similar to these is of interest due to their processability from aqueous solutions, moving away from the use of chlorinated and other toxic solvents.

Within academia and the field of organic semiconductors the identification of active species in fluoride doping has been discussed for many years and the work carried out here has contributed to that discussion. The detection of fluoride anions through interactions with aromatic compounds has been the topic of recent scientific literature published outside of the field of organic electronics. Methods for qualitatively and quantitatively detecting fluoride have also been widely sought-after for detection in health care, the environment and in industrial processes.

Finally, the use of thiazolo[5,4-*d*]thiazole heterocycles as electron deficient components in donor-acceptor and n-type materials has been hampered by their synthetic underactivity. The synthetic work carried out in this thesis explores possible ways of utilising these previously inaccessible heterocycles. The synthesis of the new polymer PbTzTT will hopefully add to a category of polymers which are both n-type and exhibit long-range order in the solid state.

# Acknowledgements

Parts of the synthetic work and analysis discussed in this thesis was undertaken by individuals across various institutions who are acknowledged at the end of each chapter. I am very thankful to everyone who has taken time to carry out any work or given any advice contributing to this thesis.

I would especially like to thank my supervisor Bob Schroeder for taking a chance on me and for his seemingly unending patience and enthusiasm. It has been a privilege to receive so much advice, both scientifically and personally, and I could not have asked for a better supervisor. I am also very grateful for all of the contributions from Christian Nielsen to various aspects of this work.

Many of the members of the Schroeder and Nielsen groups, both past and present, have become close friends throughout the course of this PhD. Charlie, Christina, Pete, Sam, Saumya, Will, Yasmin, Zach, Zach, Zilu and all of the people who made the labs and offices of UCL and QMUL places worth going to. I am lucky to have been surrounded by people who are both great friends and scientists. (Special thanks to Charlie who gave me the bike that got me in to work every day).

I am lucky to say I have a big family who have offered a lot of love. Mum and Dad, I cannot thank you enough for all of the support throughout my life, I know I was not always easy.

Eve, the past six months have been very strange, and it has not helped with me writing this. None of it would have been possible without you holding me together.

# Publications

Cowen, L. M.; Atoyo, J.; Carnie, M. J.; Baran, D.; Schroeder, B. C., Review—Organic Materials for Thermoelectric Energy Generation. *ECS Journal of Solid State Science and Technology* **2017**, *6* (3), N3080-N3088

Milita, S.; Liscio, F.; Cowen, L.; Cavallini, M.; Drain, B. A.; Degousée, T.; Luong, S.; Fenwick, O.; Guagliardi, A.; Schroeder, B. C.; Masciocchi, N., Polymorphism in N,N'-dialkyl-naphthalene diimides. *Journal of Materials Chemistry C* **2020**, *8* (9), 3097-3112.

Zhang, S.; Cheng, Y.-H.; Galuska, L.; Roy, A.; Lorenz, M.; Chen, B.; Luo, S.; Li, Y.-T.; Hung, C.-C.; Qian, Z.; St. Onge, P. B. J.; Mason, G. T.; Cowen, L.; Zhou, D.; Nazarenko, S. I.; Storey, R. F.; Schroeder, B. C.; Rondeau-Gagné, S.; Chiu, Y.-C.; Gu, X., Tacky Elastomers to Enable Tear-Resistant and Autonomous Self-Healing Semiconductor Composites. *Advanced Functional Materials* **2020**, *30* (27), 2000663.

## Table of Contents

Abstract.....	iii
Statement of Impact.....	v
Acknowledgements.....	vi
Publications.....	vii
List of Abbreviations .....	1
Chapter 1. Introduction .....	4
1.1 Organic materials as semiconductors .....	5
1.1.1 Conjugated systems .....	5
1.1.2 Generation of charges .....	7
1.1.3 Band transport and charge transport by hopping in organic semiconductors .....	10
1.2 Organic semiconductor doping.....	13
1.2.1 The Fermi-level in semiconductors.....	14
1.2.2 Doping to control the Fermi-level.....	15
1.2.3 Doping of organics .....	16
1.2.4 Integer charge transfer .....	17
1.2.5 Hybrid charge transfer .....	20
1.2.6 Morphological considerations when doping.....	21
1.2.7 Review of organic p-doped systems .....	22
1.2.8 Review of organic n-doped systems .....	27
1.3 Molecular design and synthesis of organic semiconductors .....	32
1.3.1 Introduction .....	32
1.3.2 Manipulating frontier molecular orbitals through molecular design.....	33
1.3.3 Improving charge transport through molecular design .....	36
1.3.4 Intramolecular conformational control .....	37



1.3.5	Supramolecular structure .....	40
1.3.6	Sidechain engineering.....	42
1.4	Scope of the thesis .....	44
Chapter 2.	Structure and Mechanisms of Quaternary Amine Self-Dopants .....	46
2.1	Introduction.....	46
2.2	Results and Discussion .....	50
2.2.1	Synthesis .....	50
2.2.2	Optoelectronic properties of NDI-OH.....	60
2.2.3	Absorption Spectra of NDI-OH Solution and Thin-films .....	61
2.2.4	Structure of Dehydrated NDI-OH.....	66
2.2.5	Electronic and Morphological Characterisation of NDI-OH Thin-films.....	76
2.3	Conclusions and Outlook.....	79
2.4	Acknowledgements.....	81
Chapter 3.	Exploring the chemical mechanism behind n-type fluoride doping of BDOPV semiconductors.....	82
3.1	Introduction.....	82
3.2	Results and Discussion .....	86
3.2.1	Optoelectronic Properties of BDOPV and 2F-BDOPV .....	86
3.2.2	Absorption Spectra of Fluoride Doped BDOPV and 2F-BDOPV.....	87
3.2.3	Characterisation of TBAF·3H <sub>2</sub> O solutions .....	89
3.2.4	Structures of Fluoride Doped BDOPV and 2F-BDOPV .....	93
3.2.5	Electron Paramagnetic Spectroscopy .....	97
3.3	Conclusions and Outlook.....	100
3.4	Acknowledgements.....	101
Chapter 4.	Synthesis of thiazole containing highly ordered polymers.....	102

4.1	Introduction.....	102
4.2	Results and Discussion .....	105
4.2.1	Synthesis and Characterisation of PbTTT and PbTzTT .....	105
4.2.2	Synthesis of PbTz3 and the Reactivity of Thiazoles .....	108
4.3	Conclusions and Outlook.....	123
Chapter 5.	Conclusions .....	126
Chapter 6.	Experimental Section .....	132
6.1	Experimental Chapter 2 - Structure and Mechanisms of Quaternary Amine Self-Dopants.....	132
6.2	Experimental Chapter 3 - Exploring the Chemical Mechanism Behind n-type Fluoride Doping of BDOPV Semiconductors .....	137
6.3	Experimental Chapter 4 - Synthesis of Thiazole Containing Highly Ordered Polymers 139	
	References .....	150

# List of Abbreviations

4T	Quarterthiophene
AFM	Atomic force microscopy
BDOPV	Benzodifurandione oligo( <i>p</i> -phenylene vinylene)
CB	Conduction band
COSY	2D <sup>1</sup> H- <sup>1</sup> H correlation spectroscopy
CPX	Charge transfer complex
CV	Cyclic voltammetry
Đ	Dispersity
DFT	Density functional theory
DMBI-H	2,3-dihydro-1 <i>H</i> -benzimidazoles
DMF	Dimethyl formamide
DOS	Density of states
DPP	Diketopyrrolopyrrole
DSC	Differential scanning calorimetry
EA	Electron affinity
E <sub>F</sub>	Fermi level
E <sub>fund</sub>	Fundamental band gap
E <sub>g</sub>	Band Gap
E <sub>opt</sub>	Optical band gap
E <sub>ox</sub>	Oxidation potential
EPR	Electron paramagnetic resonance
E <sub>red</sub>	Reduction potential
ESI	Electrospray ionisation
F <sub>4</sub> -TCNQ	2,3,5,6-Tetrafluoro-7,7,8,8-tetracyanoquinodimethane
FMO	Frontier molecular orbital
FTIR	Fourier transform infrared
GIXD	Grazing-incidence X-ray diffraction
GPC	Gel permeation chromatography
HMBC	Heteronuclear multi bond correlation
HOMO	Highest occupied molecular orbital
HRMS	High resolution mass spectrometry

HSQC	Heteronuclear single quantum coherence
ICT	Integer charge transfer
IP	Ionisation potential
IPF	Ion pair formation
LDA	Lithium diisopropylamide
LUMO	Lowest unoccupied molecular orbital
$M_n$	Number average molecular weight
$M_w$	Weight average molecular weight
NBS	N-bromosuccinimide
<i>n</i> -BuLi	<i>n</i> -butyllithium
NDA	Naphthalenetetracarboxylic dianhydride
NDI	Naphthalenetetracarboxylic dianhydride
NIS	N-iodosuccinimide
NMR	Nuclear magnetic resonance
OFET	Organic field effect transistor
OLED	Organic light emitting diode
OPV	Organic photovoltaics
OSC	Organic solar cell
P3HT	Poly(3-hexylthiophene)
PANI	Polyaniline
PbTTT	Poly(2,5-bis(3-hexadecylthiophen-2-yl)thieno[3,2-b]thiophene)
PCBM	Phenyl-C <sub>61</sub> -butyric acid methyl ester
PCE	Power conversion efficiency
PDI	Perylene diimide
PEDOT	Poly(3,4-ethylenedioxythiophene)
PSS	Polystyrenesulfonate
r.t.	Room temperature
$S_EAr$	Electrophilic aromatic substitution
$S_NAr$	Nucleophilic aromatic substitution
SOMO	Singularly occupied molecular orbital
TBAF	Tetrabutylammonium fluoride
TBAF.3H <sub>2</sub> O	Tetrabutylammonium fluoride trihydrate
<i>t</i> -BuLi	<i>t</i> -butyllithium
TIPS	Triisopropylsilyl

TMS	Trimethylsilyl
UPS	Ultraviolet photoemission spectroscopy
UV-vis	Ultraviolet-visible
UV-vis-NIR	Ultraviolet-visible-near-infrared
VB	Valence band
XPS	X-ray photoelectron spectroscopy
XRD	X-ray diffraction
XRF	X-ray fluorescence spectroscopy
$\Delta G$	Gibbs free energy
$\mu$	Mobility
$\sigma$	Electrical conductivity
$\lambda_{\max}$	Absorption maxima
$\lambda_{\text{onset}}$	Onset of absorption

# Chapter 1. Introduction

Since the discovery of electrical conductivity in *trans*-polyacetylene,<sup>1</sup> organic electronics has grown into a field which has drawn interest from countless researchers including engineers, biologists, chemists and physicists. Compared to their inorganic counterparts carbon-based materials are often not ideal charge transporters. Low-cost, large-area solution processability, inherent flexibility and synthetic versatility however means that organic materials can be engineered to go where rigid and expensive metals, semi-metals and alloys cannot. Mass manufacture through printing of these materials means that they are now being found beyond the world of academic research. A future can now be imagined in which lightweight and portable devices for clean energy generation, displays and medical sensing may be mass produced.

For organic materials, the scope of synthetic capability is so broad that it is possible to tune the molecular structure to be applicable to an ever-growing list of functions. A recent boom in organic photovoltaics (OPV) saw a rise in power conversion efficiency (PCE) to over 17% in an all-organic tandem cell.<sup>2</sup> Lightweight, flexibility and possibly even transparency means that organic solar cells (OSCs) can be mounted on almost any surface allowing for power generation anywhere there is sunlight.<sup>3-7</sup> Organic light emitting diodes (OLEDs) can emit in the full visible light spectrum with better contrast ratios and less bulky back panels than liquid crystal displays which has led to them becoming a commercial success.<sup>8-10</sup> Thermoelectrics involves the use of semiconductors to generate a potential difference from a temperature gradient and organics are emerging as a viable candidate for harvesting low energy waste heat.<sup>11-17</sup> The list of possible applications extends to organic field-effect transistors (OFETs),<sup>18-20</sup> biosensors,<sup>21, 22</sup> photoacoustic sensors,<sup>23</sup> anolytes and catholytes in redox flow batteries<sup>24-26</sup> and beyond. The synthetic diversity, processability, low-cost, availability and biocompatibility of organic semiconductors means that the list of possible applications is only expanding.

Semiconductors are not intrinsically conducting and for many applications introducing or removing electrons using external atomic or molecular dopants is necessary. N-type dopants

are always at risk of oxidation from atmospheric oxygen and their development has been slow. In recent years new dopants and stable precursors to n-doping have emerged; however, the fundamental mechanisms underlying the transfer of charge on to organic semiconductors are not well understood. This chapter will introduce the concept of organic materials as semiconductors and compare their doping to the traditional doping of crystalline inorganics. The role of molecular design and the part a synthetic chemist can play in tailoring organic semiconductor functionality is described in the last section of this chapter.

Chapter 2 of this work introduces a new molecular conductor in which dopant and semiconductor are covalently bound. The mechanism of this intrinsic doping and the structure of the doped species is also investigated. Chapter 3 describes the interaction of a popular n-dopant with a recently developed n-type semiconductor and uses techniques common to molecular analysis to determine the structure of the doped species and the intermediates active in charge transfer. Chapter 4 then describes the use of organic synthetic techniques to develop a new n-type polymeric semiconductor structurally analogous to a high-performance p-type.

## 1.1 Organic materials as semiconductors

### 1.1.1 *Conjugated systems*

Conduction of charges through organic materials relies on conjugation, or a continuous alternation of carbon-carbon  $\sigma$ -bonds and  $\pi$ -bonds. The  $sp^2$  hybridisation of carbon orbitals in these systems allows for three  $\sigma$ -bonds and, perpendicular to these bonds, for the overlap of  $p_z$ -orbitals. Each carbon atom donates an electron from its  $p_z$ -orbital in to  $\pi$ -bonds and it is these electrons which can delocalise across the conjugated section. The extent of  $\pi$ -conjugation in organic semiconductors can vary massively. Small molecular semiconductors<sup>27</sup> can contain only a few  $\pi$ -bonds per molecule whereas polymers<sup>28</sup> and covalent organic frameworks<sup>29-31</sup> can have extended sections of alternate  $\pi$ -bonds well beyond thousands of bonds.

In the simplest example of ethylene there are two  $sp^2$  hybridised carbon atoms which contain one electron each in the  $p_z$  orbitals. According to molecular orbital theory these two atomic orbitals combine to form two molecular orbitals. Figure 1.1 shows how the linear combination of two  $p_z$  orbitals in  $sp^2$  hybridised atoms can combine to form overlapping  $\pi$ -bonding molecular orbitals and  $\pi^*$  anti-bonding orbitals. The lower energy  $\pi$  orbital contains the electrons from both  $p_z$  atomic orbitals whereas the higher energy  $\pi^*$  contains none. It should be noted that the  $sp^2$  orbitals involved in  $\sigma$ -bonding and  $\sigma^*$ -antibonding orbitals are omitted from the diagram but sit below and above the  $\pi$ -bonding and  $\pi^*$ -antibonding orbitals, respectively.

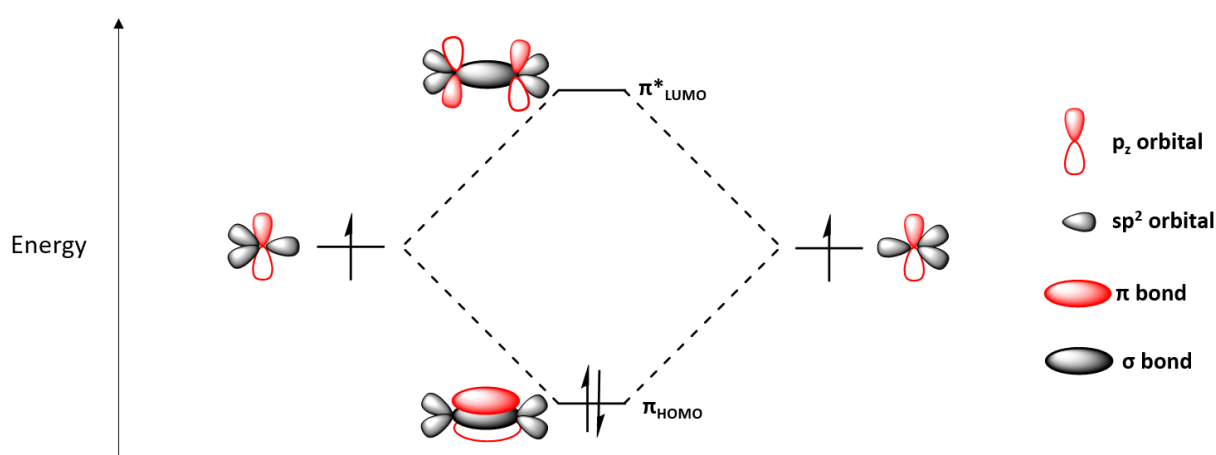


**Figure 1.1** Linear combination of two  $p_z$  atomic orbitals to give  $\pi$ -bonding and  $\pi^*$ -antibonding molecular orbitals.

In the case of a simple molecule containing two  $sp^2$  hybridised carbons, such as ethylene, a molecular orbital diagram like the one in Figure 1.1 can be applied. Extending the conjugation by adding two more carbon atoms gives butadiene and the introduction of two more electrons in  $p_z$  orbitals gives one more bonding and antibonding orbital and a total of four  $\pi$  molecular orbitals. Figure 1.2 shows the molecular orbitals of simple molecules containing low numbers of  $\pi$ -bonds (ethylene and butadiene) up to the theoretically infinite amount present in polyacetylene.

Molecular orbital theory ascribes each of these orbitals a discrete energy level. The Highest Occupied Molecular Orbital (HOMO) and the Lowest Unoccupied Molecular Orbital (LUMO) are known as the Frontier Molecular Orbitals (FMOs) and are separated by the band gap ( $E_g$ ). In ethylene, this band gap is 7.6 eV and much greater than the energy which can be supplied by visible light.<sup>28</sup> Adding occupied bonding orbitals destabilises the HOMO (increase in



energy) and adding antibonding orbitals stabilises the LUMO (decrease in energy). As is shown in Figure 1.2 adding bonding and anti-bonding orbitals in butadiene brings the FMOs closer together and  $E_g$  is lowered to 5.4 eV.<sup>28</sup> In reaching the theoretically infinite amount of molecular orbitals present in polyacetylene, the  $\pi$ -bonding orbitals form a valence band (VB) and the  $\pi^*$ -antibonding orbitals form a conduction band (CB). This model is analogous to band theory, which is classically used to describe conduction in inorganic semiconductors. The HOMO can be considered the top of the VB and the LUMO the bottom of the CB. Band gaps are now much smaller, in the range of 1 eV to 4 eV, meaning excitation from visible and UV light is possible and semiconducting behaviour is observed.

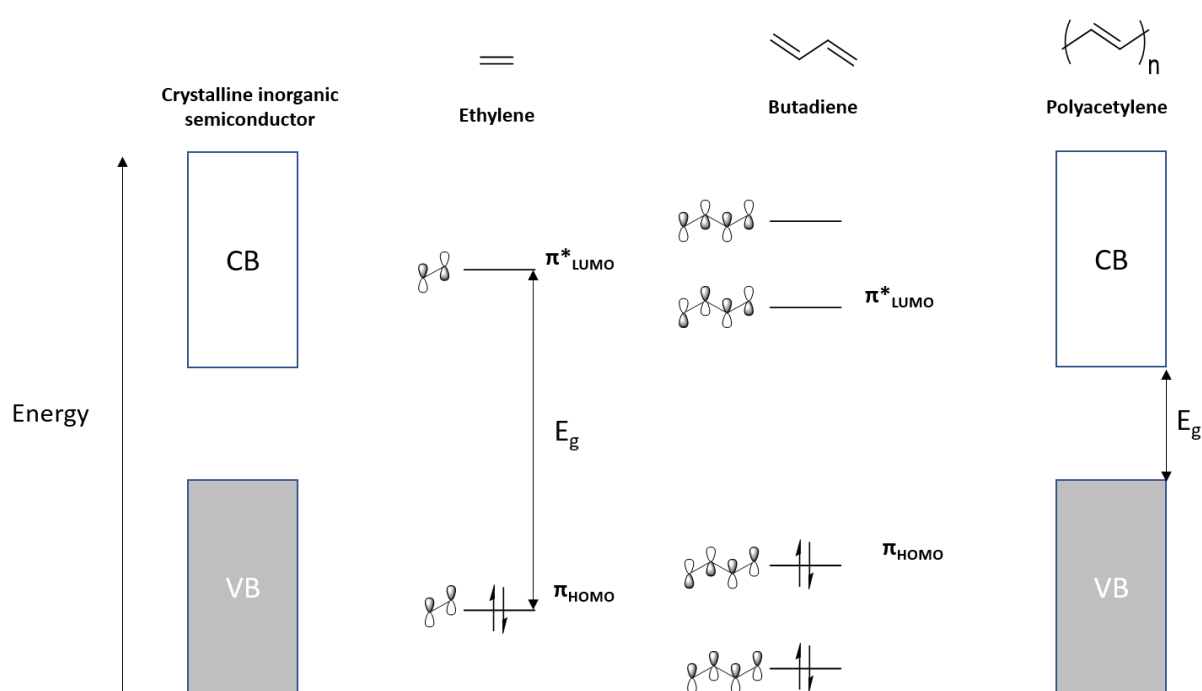


**Figure 1.2** Gas phase molecular orbital diagrams for simple small pi-conjugated systems building up to an infinite chain length in polyacetylene and analogous band structure in inorganic semiconductors. Overlapping  $p_z$  atomic orbitals are shown for the smaller ethylene and butadiene.

### 1.1.2 Generation of charges

In the ground state semiconductors are insulating materials. Charges must therefore be introduced for most applications. The injection of an electron into a  $\pi^*$  antibonding molecular orbital (conduction band) leads to negative (n-type) carriers. Extracting an electron from a  $\pi$  bonding orbital (valence band) leaves behind an electron hole and these are positive (p-type)

carriers. This can be done in a variety of ways and often the injection/extraction method is dependent on the application.

Metal electrodes can be used to extract or inject charges at the interface with the semiconductor. This injection method, through an applied electric field, is utilised in both OFETs and OLEDs. The excitation of an electron from the HOMO to the LUMO creates a bound electron-hole pair which are electrostatically attracted, this overall charge neutral state is called an exciton. Exothermically separating the bound electron-hole pair by electron transfer to an adjacent molecule is relied upon in the operation of OSCs.<sup>32</sup> A third method of charge generation is through a process known as doping which involves the introduction of an external chemical species to transfer an electron. For organics doping normally involves the use of external molecular dopants with high electron affinities (p-type doping) or low ionisation potentials (n-type doping) to oxidise or reduce the semiconductor respectively. This process will be explored in greater detail in later sections of this chapter and in subsequent chapters of this thesis.

The introduction of charges through the addition or removal of an electron requires an energetic stabilisation in the molecule which is achieved through a spatial reorientation of the electrons in the molecular orbitals. The coupling of a hole or electron with this distortion in the molecular structure is the charge carrier which moves through the semiconductor and is a quasiparticle known as a polaron.<sup>33</sup> The quinoidal stabilisation of polythiophene doped by boron trifluoride is shown in Figure 1.3. The new energy level associated with a polaron is found within the band gap and is observable as a new lower energy (higher wavelength) band in absorption spectra. An n-type polaronic state lies just beneath the LUMO whereas a p-type polaron lies just above the HOMO.

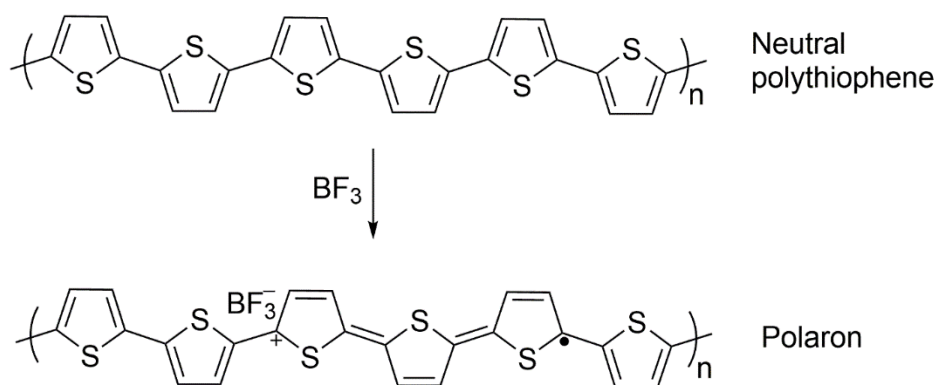


**Figure 1.3** Polythiophene p-doped by boron trifluoride and the resultant quinoidal polaron structure.

It should be noted that polarons are different from excitons in which an electron-hole pair is generated. The hole and electron of an exciton will lie further from the HOMO and LUMO than in polarons due to the attractive Coulombic forces they feel from each other.<sup>34</sup> Similarly to a polaron, the generation of the exciton also comes with its own stabilising structural distortion. The relative positions of positive and negative polarons and excitons within the band gap are shown in Figure 1.4.

Two different band gaps exist. The optical band gap,  $E_{opt}$  is defined as the “energy of the lowest electronic transition accessible via absorption of a single photon.”<sup>35</sup> This is the difference between the ground singlet state,  $S_0$ , and the first available excited singlet state,  $S_1$ , and generally leads to the formation of a bound exciton in organics. This differs from the fundamental band gap,  $E_{fund}$ , which is the difference between the ionisation potential (IP) and the electron affinity (EA), equation 1.1.

$$E_{fund} = IP - EA \quad 1.1$$

IP being the energy required to remove an electron from the HOMO to the vacuum level and EA the energy required to add an electron from the vacuum level to the LUMO. The vacuum level is the energy of a stationary electron free from a material. HOMO and LUMO energies can therefore be estimated from the IP and EA. The difference between  $E_{fund}$  and  $E_{opt}$  is the binding energy of the bound exciton,  $E_b$ , equation 1.2.

$$E_b = E_{fund} - E_{opt} \quad 1.2$$

In real life solid-state examples the actual band gap,  $E_g$ , is found to be much smaller than  $E_{fund}$  because  $\pi$ -systems adjacent to the generated charge will polarise, stabilising the charged

state.<sup>35</sup> Figure 1.4 shows the relationship between the different gaps described above in relation to the HOMO and LUMO.

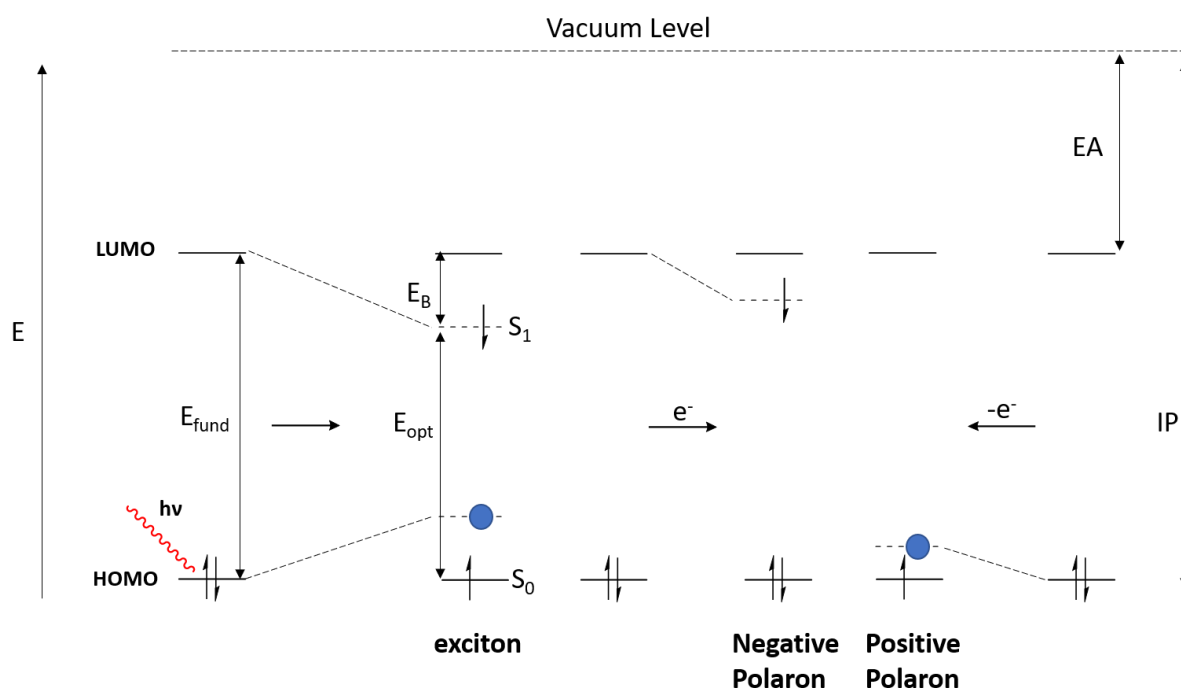


**Figure 1.4** Relative positions of excitons, negative and positive polarons with respect to the energies of the frontier molecular orbitals. Also shown is the difference between optical and fundamental band gaps and electron affinity and ionisation potential.

### 1.1.3 Band transport and charge transport by hopping in organic semiconductors

Once generated, charge carriers will move through a material in the direction of an applied electric field. The ease with which electrons and holes move through a material is given by the charge mobility,  $\mu$ .<sup>36</sup> Mobility is the measure of charge velocity,  $v$ , in a given electric field,  $F$ , and is shown in equation 1.3.

$$\mu = \frac{v}{F} \quad 1.3$$

Band theory can be used to describe the transport of charges through the two different bands. If an electron is excited or introduced into the CB, then it is delocalised across the whole band. Similarly, if an electron is removed from the VB it leaves behind a positive hole freely moving across the overlapping wavefunctions of the band. In the solid state these charge carriers are then only scattered by collisions with other particles or interactions with vibrations in the

crystal structure, called phonons, brought about by increased temperature. Equation 1.4 shows the inverse relationship of band-like mobility with increasing temperature.

$$\mu = \frac{De}{K_b T} \quad 1.4$$

$D$  is the diffusion coefficient of the carrier,  $e$  is the elementary charge of an electron and  $k_b$  the Boltzmann constant. This gives rise to the characteristic linear decrease in mobility with increasing temperature observed in band transport.

Band transport is a reliable model when describing large atomic crystals with a relatively small amount of charge carriers. It is very rare however to find organic semiconductors as highly ordered as metals and semimetals. Instead of atomic crystals organic semiconductors mostly exhibit amorphous morphologies or at best molecular crystals with less long-range order than bound atomic crystals. Increased disorder means the overlap of wavefunctions is poor and this causes the width of both valence and conduction bands to narrow. The bandwidth can narrow to a point where the charges are not considered to be delocalised across overlapping wavefunctions. Instead the charges can be considered as localised to a particular site and will then “hop” or tunnel between sites in a process known as hopping.<sup>37</sup> The distribution of possible sites, or density of states (DOS), in amorphous systems can be represented by a Gaussian curve and is shown in comparison to band-like structures in Figure 1.5.

The ease with which charge carriers can hop between sites can be described by Marcus theory.<sup>38</sup> The rate of electron transfer between two given sites,  $k$ , is given in equation 1.5.

$$k = \frac{2\pi}{\hbar} \frac{J^2}{\sqrt{4\pi\lambda K_b T}} e^{-\frac{\lambda}{4K_b T}} \quad 1.5$$

$J$  is the transfer integral which gives the degree of overlap between wavefunctions at each site. Each charge carrier comes with a molecular distortion which is given by the reorganization energy,  $\lambda$ .

Lower charge mobilities compared to band transport are characteristic of hopping. This is because there is an activation energy associated and mobilities increase with temperature. This is the opposite of the inverse relationship seen between temperature and mobility in band transport. It can be seen from equation 1.5 that an increase in temperature will lead to an increase in charge transfer between sites and therefore, an increase in the overall mobility.

It is likely that the transport behaviour observed in organic semiconductors is a hybrid between band and hopping with more ordered molecular crystals exhibiting more band like behaviour and amorphous solids, such as polymers, exhibiting more hopping characteristics between certain sites.

The overall electrical conductivity,  $\sigma$ , of a material is given as a product of the mobility of each type of charge, the number of each type of charge generated and the elementary charge of an electron,  $e$ . This relationship is shown in equation 1.6.

$$\sigma = e(n\mu_p + n\mu_e) \quad 1.6$$

One further consideration when describing transport is in the relative energies of the localised sites. Impurities or structural defects can lead to energetic sites which lie above the valence band or below the conduction band in band transport type systems, or above and below the HOMO and LUMO respectively in hopping type mechanisms. These sites, in which a carrier can occupy and no longer take part in transport, are known as traps. Given more energy a trapped charge may be released and move to a neighbouring transport site. Carriers in deeper traps which lie further from the band edge, at an energy known as the release energy,  $E_t$ ,<sup>39</sup> may become permanently trapped or become targets for recombination if the opposite charge is present.<sup>40</sup> Possible trap-sites are shown in Figure 1.5 as above the HOMO or below the LUMO. Deep traps are located within the band gap and between the two lines marked  $E_t$ .

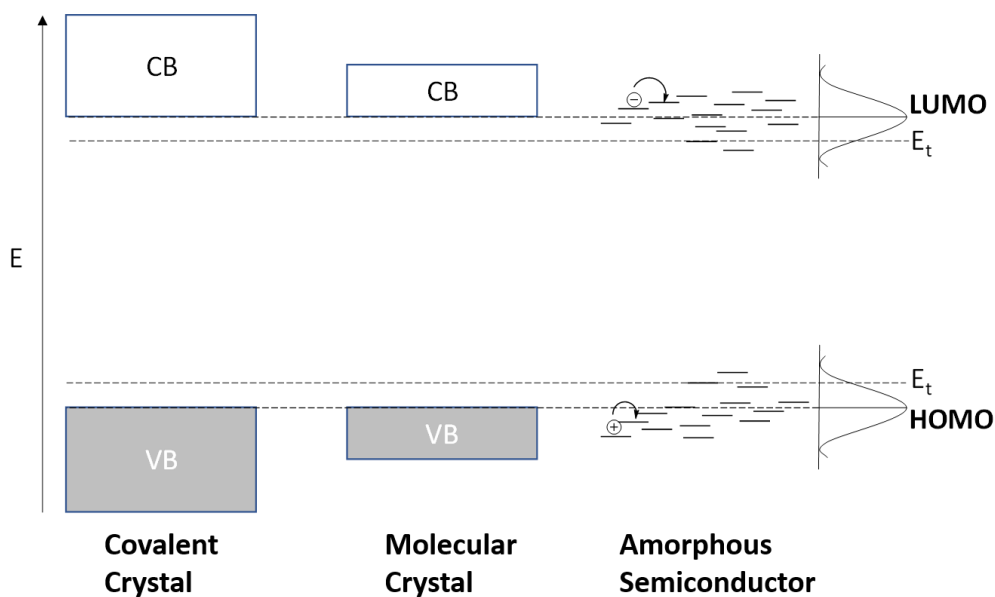


**Figure 1.5.** Bandwidths in ordered covalent crystals, less ordered molecular crystals and localised sites for charges to “hop” between in amorphous semiconductors. Deep traps are shown as sites located above/below the energy  $E_t$ .

## 1.2 Organic semiconductor doping

By their nature semiconductors are not intrinsically conducting and as described above they must be manipulated in order for free charges to be generated. This manipulation could be through the absorption of energy to generate an excitonic electron-hole pair or through the doping of the host semiconductor with external oxidising or reducing species. The concept of doping, as related to the Fermi level, is briefly introduced in this section and described in terms of traditional techniques of atomic doping of crystalline inorganic semiconductors. Similarities to the use of molecular dopants in organic semiconductors are then explored. The limitations of such comparisons are then highlighted by descriptions of the prevailing theories of organic molecular doping and through a review of the most prominent doping systems in organic semiconductor research and the mechanisms underlining them.

### 1.2.1 The Fermi-level in semiconductors

For an undoped pure semiconducting material at a temperature of absolute zero ( $T = 0$  K) VB will be completely filled with electrons and CB will remain empty. These are referred to as intrinsic semiconductors. In these materials the probability that a hole exists in the VB or an electron exists in the CB are exactly the same, this probability can be represented by an energy which will lie exactly in the middle of the band gap and is known as the Fermi-level,  $E_F$ . For intrinsic semiconductors, the fermi-level is given by equation 1.7.

$$E_F = \frac{E_c + E_v}{2} \quad 1.7$$

$E_v$  and  $E_c$  are the energies of the edges of the valence and conduction bands respectively but could be interchanged with HOMO and LUMO. The probability that any given energetic state,  $f(E)$ , will be filled by an electron is given by the Fermi Function (equation 1.8).

$$f(E) = \frac{1}{1 + e^{\frac{(E-E_F)}{k_b T}}} \quad 1.8$$

Increasing the temperature means there is a chance that some electrons can be thermally excited to higher energy states and may cross  $E_F$ .<sup>41</sup> Charges generated in this way are called the intrinsic charge carriers. The relationship between charge carrier concentration and temperature in silicon and gallium arsenide (GaAs) is shown in Figure 1.6. This model works when describing atomically crystalline materials, in which there is a higher density of states near  $E_F$  and a negligible band gap. In semiconductors any sites with a probability of being filled located in the band gap will be traps.



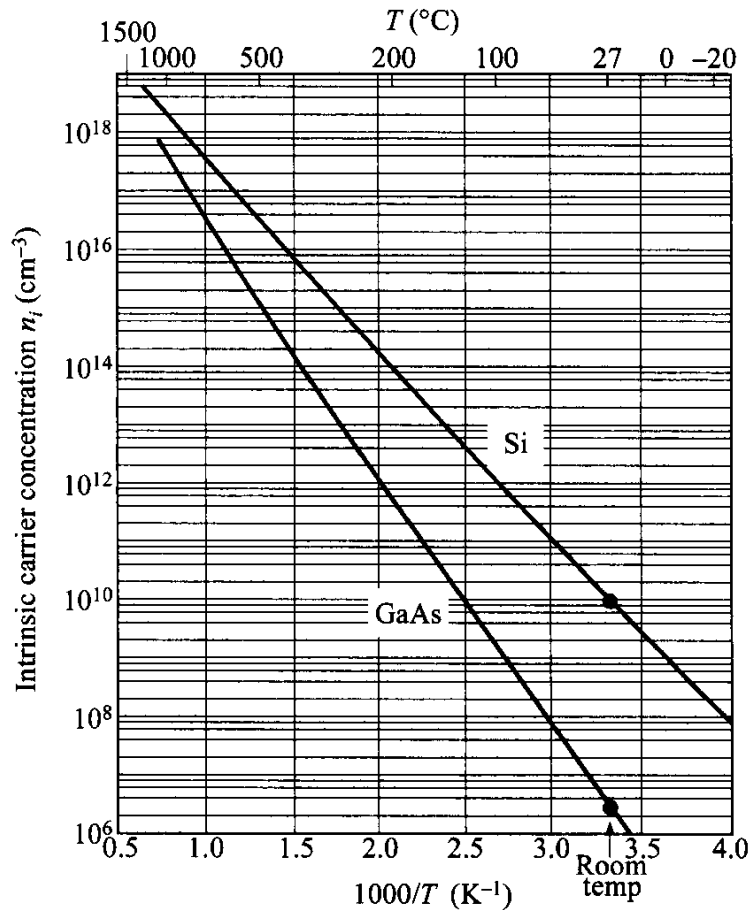


**Figure 1.6.** Relationship between temperature and the intrinsic charge carrier concentration for the two inorganic semiconductors silicon and gallium arsenide. (Originally published in reference 41 using data from references 42 and 43)

### 1.2.2 Doping to control the Fermi-level

If electrons are added to the conduction band then there is now more chance of finding available energetic sites filled by electrons in the conduction band than there is of finding holes in the valence band. The point at which there is a 50 % probability of finding a state filled by a hole or electron has now shifted towards the conduction band. This means for n-type semiconductors the Fermi level shifts towards the populated conduction band. Similarly, if electrons are removed from the valence band forming holes in a p-type semiconductor, then the Fermi level will shift towards the valence band.

Doping therefore involves introducing energy levels close to the band edges and controlling the Fermi level. In inorganic atomic crystals doping is achieved by the introduction of an

impurity atom into the crystal lattice. A dopant atom containing more valence electrons than the host atoms of the crystal matrix will populate energy levels close to the conduction band with its extra electron and shift the Fermi level towards the conduction band. Dopant atoms with less valence electrons than the host semiconductor will accept electrons from the valence band leaving behind holes populating energy levels just above the valence band. The shifting of the Fermi level due to the introduction of dopants is shown in Figure 1.7.

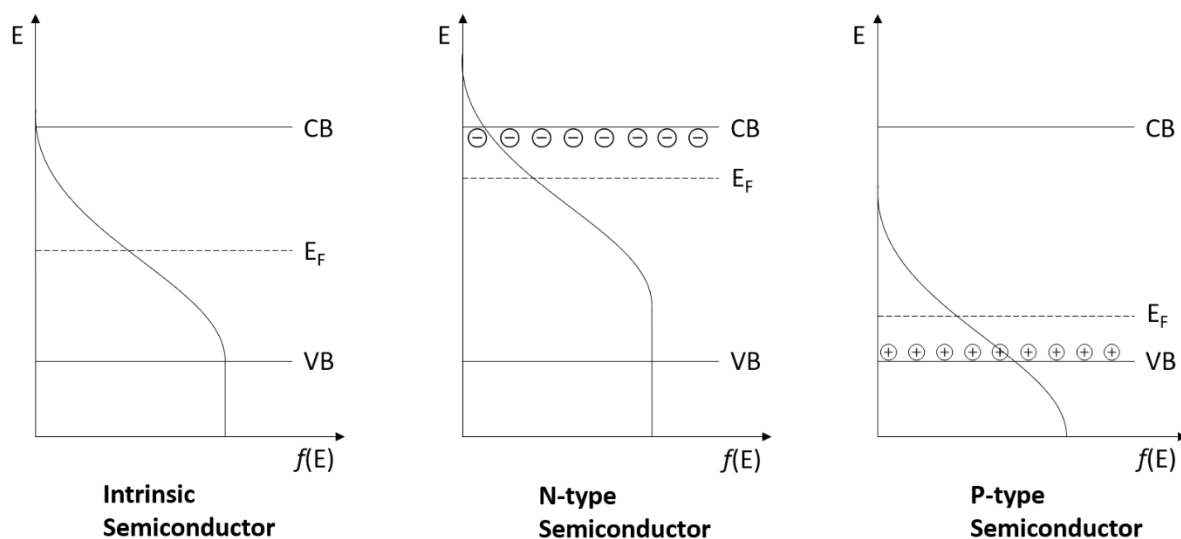


**Figure 1.7.** Shift in the Fermi-level from intrinsic semiconductor to n-type, when levels just beneath the conduction band are filled, and p-type, when levels just above the valence band are filled.

It is common therefore to see crystalline silicon in group IV to be n-doped by group V atoms, such as arsenic and phosphorous, or to be p-doped by group III elements such as boron or aluminium.<sup>44</sup> Once the Fermi-level shifts to above or below the band edges the semiconductor can be said to be “degenerately doped” and treated as metallic.<sup>45</sup>

### 1.2.3 Doping of organics

Like previously explained concepts, the doping of organic semiconductors is analogous to the doping of inorganics with some fundamental differences. In each case charge carriers are generated in a semiconducting matrix by the addition, or removal, of an electron by another chemical species. Much like inorganics we see a shift in the Fermi level towards the band edges.<sup>46, 47</sup> The molecular nature of organic solids and higher degrees of disorder compared

to inorganics, means that it is difficult to control the population of bands by adding impurity atoms. Instead external molecular species (or in some rare cases covalently bound moieties) are introduced which undergo charge transfer type processes.

One unifying theory cannot be used to describe the nature by which holes or electrons are actually introduced. The myriad of possible semiconductor and dopant combinations means that factors such as FMO alignment,<sup>48</sup> chemical mechanism<sup>49</sup> and the miscibility of host and dopant<sup>50</sup> can determine how successful doping actually is and the mechanisms by which it occurs.

The rest of this chapter will attempt to give a picture of the models already in place to describe doping in organics followed by relevant examples. Two sections of this work are concerned with the interactions of ionic dopants with conjugated organics. It is difficult to assign either of these systems to one of the models below and in fact most systems will exhibit behaviours somewhere in between the two major theories.

#### *1.2.4 Integer charge transfer*

This model of doping involves the transfer of an electron from one species to another, analogous to reduction for n-type or oxidation for p-type. This is known as the Integer Charge Transfer (ICT) model. A pair of ions is formed which are Coulombically bound, reminiscent of an ionic bond, this gives rise to the other name for this model of Ion Pair Formation (IPF). For p-type doping, the semiconductor HOMO must be aligned with the dopant LUMO. In contrast for n-type doping the dopant HOMO must lie high enough to align with the semiconductor LUMO, this relationship is shown in Figure 1.8.

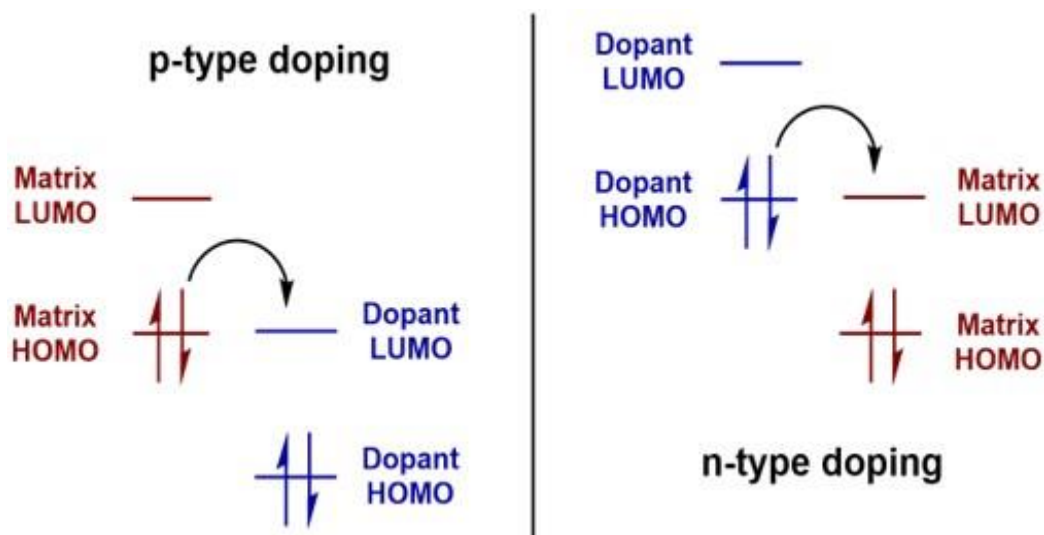


**Figure 1.8.** Schematic representation of p and n-type doping through the Integer Charge Transfer model, with full electron transfer between aligned HOMO and LUMOs.

A commonly quoted example used to illustrate IPF is the widely studied system of poly-3-hexylthiophene (P3HT) p-doped by 2,3,5,6-tetrafluoro-7,7,8,8-tetracyanoquinodimethane (F<sub>4</sub>-TCNQ); structures are shown in Figure 1.9. Panel a of Figure 1.9 shows ultraviolet-visible-near-infrared (UV-vis-NIR) absorption spectra which have been used to identify IPF between dopant and semiconductor.<sup>51</sup> Spectra of neutral F<sub>4</sub>-TCNQ and its reduced anion are shown for reference. Upon doping P3HT with F<sub>4</sub>-TCNQ a growth in the dopant anion absorption is observed at a lower energy than the P3HT optical absorption, and is labelled ICT, suggesting an electron transfer between the two. The anionic state of F<sub>4</sub>-TCNQ was also observed in Fourier transform infrared spectroscopy (FTIR).<sup>51, 52</sup> The resultant polaron states within the bandgap were observed as absorptions labelled P1 and P2.

Reducing the content of electron withdrawing fluorine atoms on the dopant quinoidal ring leads to weaker p-dopants F<sub>2</sub>-TCNQ, F-TCNQ and TCNQ. Panel c of Figure 1.9 shows that IPF is still observed when reducing the fluorine content from F<sub>4</sub>-TCNQ to F-TCNQ, however the EA of TCNQ is too low compared to the IP of P3HT and no charge transfer occurs. Increasing the EA of the polythiophene backbone by inserting sulphur atoms between thiophene units and alkyl side chains has led to high conductivities of 350 S cm<sup>-1</sup> when doping with the inorganic salt nitrosonium tetrafluoroborate (NOBF<sub>4</sub>).<sup>53</sup> It is therefore reasonable to assume that for p-type IPF to occur dopant EA must be greater than semiconductor IP and for n-types the dopant IP must be greater than the semiconductor EA. This rather simplistic explanation however does not account for the stabilisation of attractive Coulombic forces felt between

the two generated ions in the solid state.<sup>54</sup> IP and EA are measured from the vacuum level and consider the insertion of an electron from free space. Even in cases where IPF can be used to describe the doping, we therefore still cannot predict the solid-state doping based on alignment of FMOs or the relative sizes of EA and IP alone.

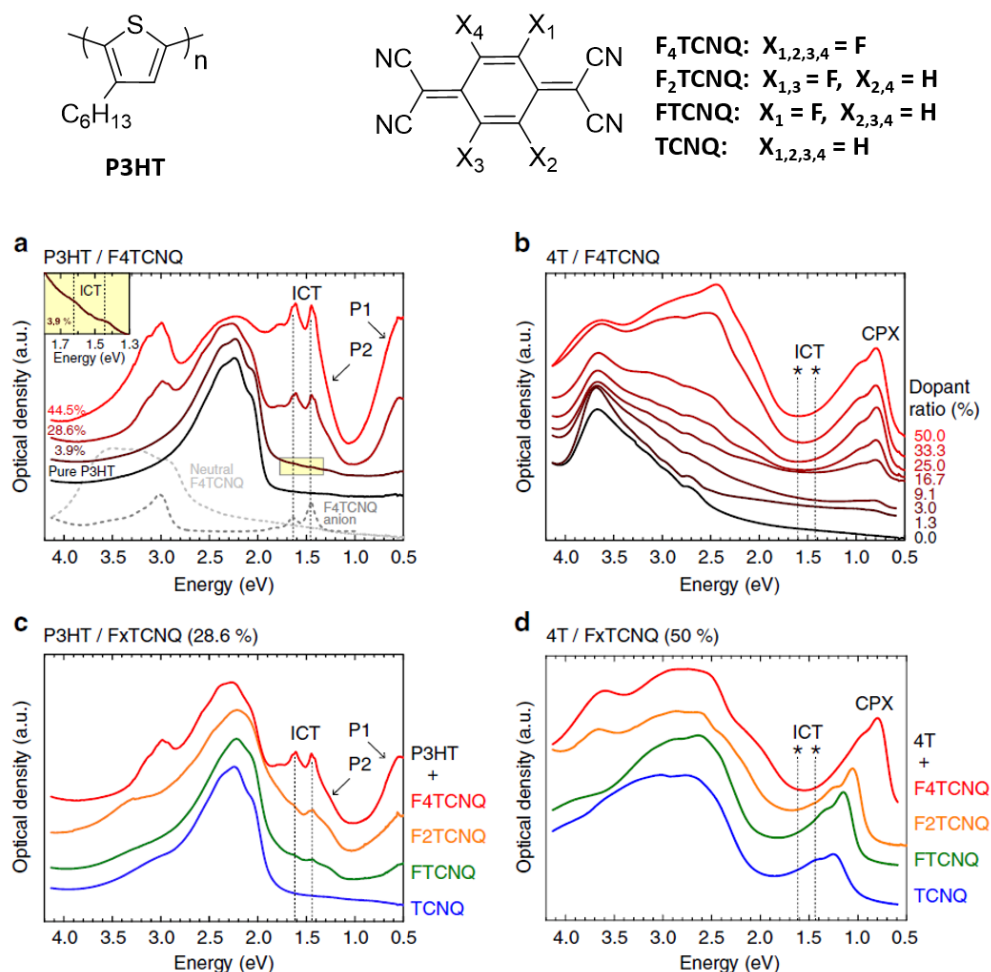


**Figure 1.9. Top:** Structures of P3HT and the four fluorinated TCNQ derivatives used as dopants; **Bottom:** Panel a: UV-vis/NIR absorption spectroscopy of F<sub>4</sub>-TCNQ and its anion (dashed lines) and P3HT doped with increasing concentrations of F<sub>4</sub>-TCNQ; Panel b: UV-vis/NIR spectroscopy of 4T oligomer doped with increasing concentrations of F<sub>4</sub>-TCNQ; Panel c: UV-vis/NIR spectroscopy of P3HT doped with 28.6 mol% of four different fluorinated TCNQ derivatives; Panel d: UV-vis/NIR spectroscopy of 4T doped with 50 mol% of four different fluorinated TCNQ derivatives. Panels a, b, c and d reprinted from reference 51.

It cannot be assumed that all charges generated in this way are free to conduct through the semiconductor matrix. Although the transfer of charges between F<sub>4</sub>-TCNQ and P3HT has been shown as very efficient, it has been suggested that the amount of charges which actually dissociate from the bound ion pair is as low as 5%.<sup>55</sup> Even though the Fermi-level is shown to shift towards the HOMO, the large amount of Coulombically trapped ion pairs can become traps for dissociated free charge carriers and have a negative impact on the mobility.<sup>56, 57</sup>

### 1.2.5 Hybrid charge transfer

Over time it has become clear that doping cannot always be described by the formation of ion pairs through the transfer of one electron, and as explained above doping cannot always be predicted from the alignment of FMOs. Even when both of these conditions are true it is only a fraction of ions generated which become free charge carriers.<sup>58</sup> It is therefore necessary to consider another model for doping.

Analogous to the linear combination of atomic orbitals in a covalent bond, new bonding and anti-bonding molecular orbitals can be formed between a dopant and host. This is shown in Figure 1.10. For p-types both of the electrons from the semiconductor HOMO are stabilised while the dopant LUMO is destabilised in the new charge transfer complex (CPX). For n-types the dopant HOMO is stabilised while the semiconductor LUMO is destabilised. A full charge is not transferred between the two and this model is therefore termed hybrid charge transfer.

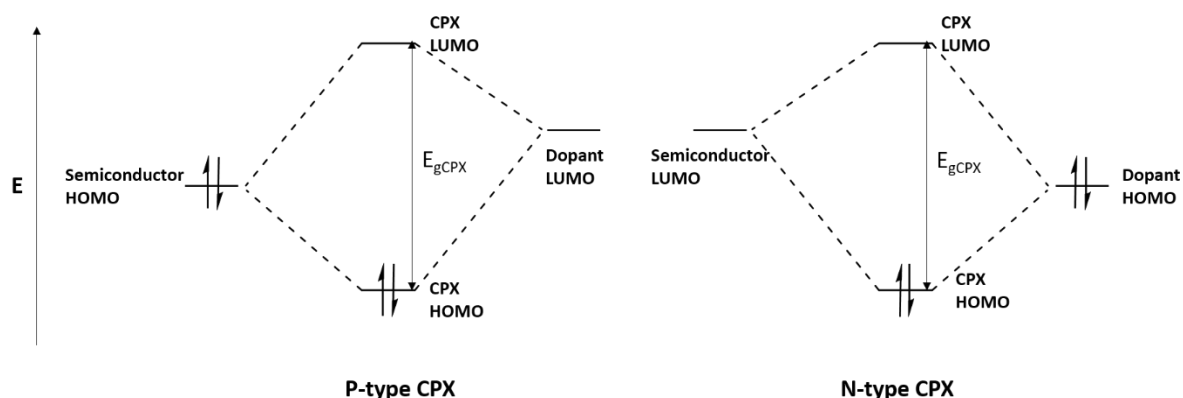


**Figure 1.10.** Relative energy levels of charge transfer complexes formed from the splitting of frontier molecular orbitals in the hybrid charge transfer model.

Panel b of Figure 1.9 shows the UV-vis-NIR absorbance spectra of the oligomer quarterthiophene (4T) doped with  $F_4$ -TCNQ. The dopant anion absorptions at approximately 1.6 and 1.4 eV are no longer observed unlike in the case of P3HT. Instead one broad peak is observed at 0.7 eV which is the band gap of the CPX, labelled  $E_{gCPX}$  in Figure 1.10. The two electrons from the 4T HOMO have formed part of the CPX bonding HOMO and the  $F_4$ -TCNQ LUMO has formed the anti-bonding CPX LUMO. A fractional charge has been shared between the two.

Figure 1.9 panel d shows absorption spectra for 4T doped by TCNQ derivatives with decreasing fluorine substitution and therefore decreasing EA. Again, in contrast to P3HT, only one additional absorption is observed for a charge transfer complex. The peak maxima for the CPX also red shifted with increasing dopant EA which suggests that the anti-bonding orbital of the CPX is stabilised when the dopant EA is increased. Other factors however effect the energy level splitting, which causes the CPX band gap, including the favourable overlap of FMOs in space.<sup>48</sup> There is no strict requirement for energy levels to align for a CPX to form. This is illustrated by 4T with an IP of 5.30 eV,<sup>51</sup> being higher than the EA of F<sub>4</sub>-TCNQ (EA = 5.23 eV).<sup>59</sup> The formation of a CPX is still observed between 4T and TCNQ which has a considerably lower EA of 4.23 eV.<sup>60</sup>

There is a clear difference between the number of free charges generated in IPF and CPX models. The neutral CPX state is firstly not a full charge carrier and is localized to a site. To generate a full charge in the case of a p-type CPX a neutral semiconductor electron from the HOMO must then be thermally excited into the higher energy LUMO of the CPX. For an n-type an electron is accepted into the semiconductor LUMO from the CPX HOMO. Neither of these transitions are energetically favoured making CPX doping inefficient.<sup>51, 61</sup>

### *1.2.6 Morphological considerations when doping*

When considering the efficiency and mechanisms of doping there are factors to consider in addition to the mostly energetic descriptions above. The relative geometry of dopant and semiconductor in the solid state has been shown to be of significant importance. The processing techniques used to introduce the dopant can be employed to optimise this geometry.<sup>62, 63</sup> The polymer poly(2,5-bis(3-hexadecylthiophen-2-yl)thieno[3,2-*b*]thiophene) (PbTTT) doped with F<sub>4</sub>-TCNQ illustrates this point. A blend of PbTTT and F<sub>4</sub>-TCNQ was dissolved in solvent and cast as thin-film leading to the dopant sitting between the chains in a face to face  $\pi$ -stack with PbTTT. A maximum conductivity of 2 S cm<sup>-1</sup> was achieved.<sup>62</sup> Introducing the F<sub>4</sub>-TCNQ by evaporating it into a film of PbTTT lead to the dopant occupying space between the interdigitating side chains in the lamellar stack.<sup>63</sup> Figure 1.11 panel a shows a schematic representation of this. Panel b shows grazing incidence wide angle X-ray

scattering (GIWAXS) in which the peak at  $q_z = 0.27 \text{ \AA}^{-1}$  for the undoped PbTTT corresponds to a Lamellar distance of  $22.9 \text{ \AA}$ . For the doped PbTTT this peak shifts to  $q_z = 0.25 \text{ \AA}^{-1}$  and a larger Lamellar spacing of  $24.7 \text{ \AA}$ , indicating the  $F_4$ -TCNQ is present between the sidechains. This relative position of dopant causes less distortion of the linear polymer chain and a higher mobility. Less Coulombic interaction between the generated ion pair was also observed, leading to more mobile free charges. Conductivity was therefore seen to increase by a factor of more than 100 using the same semiconductor and dopant pair but different processing technique.

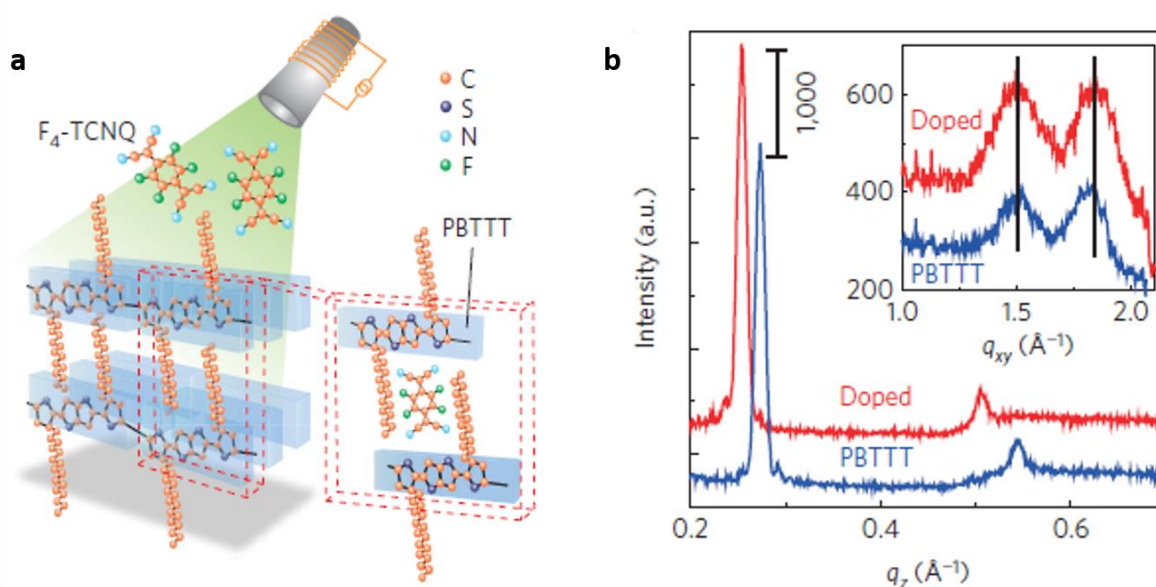


**Figure 1.11.** **a:** Schematic representation of  $F_4$ -TCNQ vapor deposited on to films of PbTTT with the  $F_4$ -TCNQ sitting between side-chains within the Lamellar stack. **b:** Grazing incidence wide angle X-ray scattering measurements for the out-of-plane profile shown as  $q_z$  for doped and undoped PbTTT. Inset shows the in-plane  $q_{xy}$  from 2D grazing incidence wide angle X-ray scattering. Both panels reprinted from reference 63.

### 1.2.7 Review of organic p-doped systems

The very earliest examples of dopants are molecular halogens. As early as 1977 it was found that exposing *trans*-polyacetylene to vapours of halides increased the conductivity by up to seven orders of magnitude.<sup>64, 65</sup> The volatile nature of the halogens ( $Cl_2$ ,  $Br_2$ ,  $I_2$ ) meant that diffusion into the solid semiconductor matrix was easy. The use of halogens in p-doping other organics with high IP (approx. 5 eV) has been widely studied. These include pentacene,<sup>66-70</sup> poly-3-alkylthiophenes<sup>71-73</sup> and polypyrroles.<sup>74</sup> The practical applications of these small



dopants were limited due to their tendency to diffuse.<sup>47, 70</sup> When attempting to fabricate multilayer devices, halogen diffusion through the different layers rendered the devices useless. It was however shown that high conductivities in organics are possible through doping.

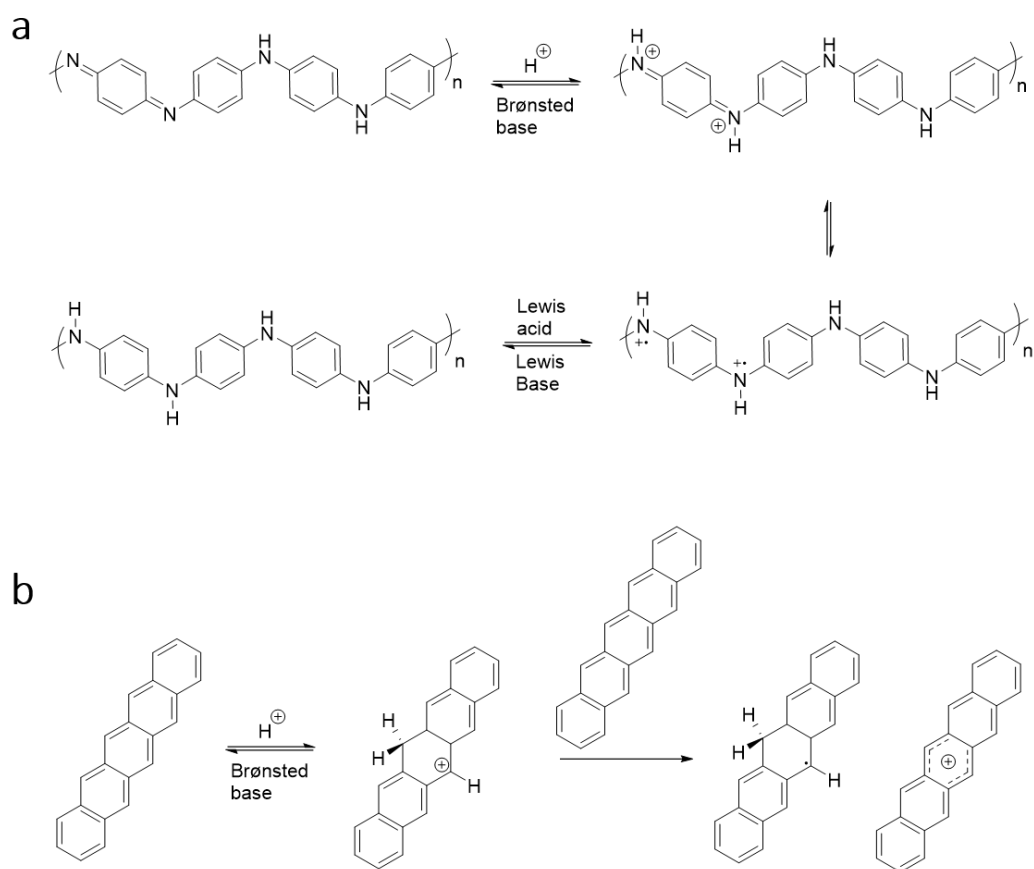
The successful synthesis of conducting polypyrrole was achieved in the 1980s.<sup>75-77</sup> The pyrrole monomer was oxidatively polymerised in the presence of excess oxidant which also served as p-dopant. At this point the dopants most commonly used were Lewis acidic metal halides. Metal centres including Fe(III), Cu(II), Sn(IV) and Sb(V) have all found success in doping polypyrroles.<sup>75, 76</sup> Although EA values for these compounds seem relatively modest (FeCl<sub>3</sub>, EA  $\approx$  4.3 to 4.7 eV),<sup>78, 79</sup> conductivities of up to 19 S cm<sup>-1</sup> were observed when FeCl<sub>3</sub> was used to dope a polymer with an IP of 5.0 eV.<sup>79</sup>

Tuning the Lewis acidity of the metal complexes proved to be an effective strategy for the design of many new p-dopants. A series of Cu(I) and Bi(III) benzoates have been used to dope hole transporting materials in OLEDs; fluorinating the benzene ring lead to increased doping due to an increase in the Lewis acidity.<sup>80, 81</sup> The complex molybdenum tris[1,2-bis(trifluoromethyl) ethane-1,2-dithiolene] (Mo(tfd)<sub>3</sub>),<sup>82</sup> shown in Figure 1.13, contains thiolene and CF<sub>3</sub> groups on the ligand which stabilises an additional electron around the whole ligand leading to a very high EA of 5.6 eV.<sup>83, 84</sup>

Polymerising aniline in the presence of Brønsted acid was shown to give conductive forms of polyaniline (PANI) as early as the 1960s.<sup>85-90</sup> It was shown that the emeraldine form of PANI, in which some amine bonds are replaced by imines, becomes protonated and forms polaron like sections along the polymer chain.<sup>88, 91-94</sup> This process is shown in Scheme 1.1 along with de-doping by a Brønsted base. A wide range of organic and inorganic Brønsted acids in combination with PANI have been studied since the 1980s.

Protonic doping has been applied to semiconductors other than PANI. In semiconductors which do not contain a basic nitrogen as part of the conjugation, proton doping occurs via a slightly different mechanism. This is illustrated using pentacene in Scheme 1.1. Using an organic sulfonic acid as dopant, pentacene is protonated on the central benzene ring. The generated positive charge then hops between pentacene molecules as a hole.<sup>95</sup> It has recently been proposed that a strong Lewis acid dopant can form a complex with trace amounts of

water. The resultant complex is Brønsted acidic leading to the proton doping of the donor-acceptor polymer PCPDTB.<sup>96</sup>



**Scheme 1.1. a:** The Brønsted acid doping of emeraldine PANI to give the cationic then polaronic forms in the forward direction. In the backwards direction the Lewis acid doping of PANI to give the polaronic form of PANI. **b:** The Brønsted acid doping of pentacene then following hole transfer to a neutral pentacene molecule.

Likely the most commonly applied p-type organic system is the combination of poly(3,4-ethylenedioxythiophene) (PEDOT) and polystyrene sulfonate (PSS), a mixture known as PEDOT:PSS. Commercially available as an aqueous dispersion PEDOT:PSS has now been the subject of numerous reviews over the course of many years.<sup>97-102</sup> The most commonly quoted doped structure is shown in Scheme 1.1 with deprotonated styrene units on the PSS acting as counterion to the hole transporting PEDOT.

The synthesis of PEDOT from the monomer 3,4-ethylenedioxythiophene (EDOT) is generally carried out in the presence of an oxidant such as  $\text{FeCl}_3$  or  $\text{Na}_2\text{S}_2\text{O}_8$ . The doping occurs at this point with the oxidant removing an electron. Brønsted acids are then often used as a stabilising counterion. Using deprotonated PSS as counterion gives the water dispersible PEDOT:PSS which forms a coiled shell with conducting PEDOT on the inside and solubilising

PSS on the outside.<sup>103</sup> The residual H<sup>+</sup> is removed in purification however an excess of oxidising agent and dopant likely remain.<sup>104</sup> Small molecule counterions can be used but PSS remains by far the most widely studied and developed.<sup>102</sup>

Upon drying PEDOT:PSS forms opaque homogeneous films. Either through treatment of the aqueous dispersion or through post-film formation treatments PEDOT:PSS has exhibited extremely high electrical conductivities greater than 1000 S cm<sup>-1</sup>.<sup>105, 106</sup> These treatments are often called “secondary doping” although there is no evidence that they actually increase the number of charge carriers. Often secondary doping involves the introduction of additive solvents which lead to an uncoiled morphology more favourable for charge transport upon film formation.<sup>107, 108</sup> Washing with acids designed to remove an excess of non-conducting PSS, also uncoiling the polymer chain, often leads to higher mobility and conductivity.<sup>109</sup>

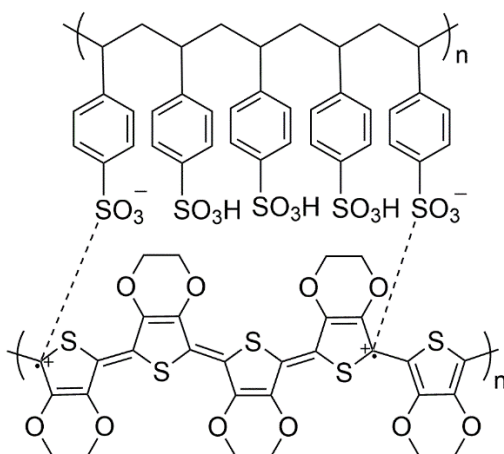


**Figure 1.12.** Chemical structures of the semiconducting polymer PEDOT (bottom) and deprotonated PSS counterion (top).

Currently, the most commonly used p-dopants are high EA organic molecules. The most widely used is F<sub>4</sub>-TCNQ and various examples of its use are described in sections 1.2.4, 1.2.5 and 1.2.6. In addition to these examples, a recent report has shown that it is possible for F<sub>4</sub>-TCNQ to accept two electrons from low ionisation energy polymers.<sup>110</sup> The F<sub>4</sub>-TCNQ<sup>-</sup> anion had an EA greater than the IP of the polymer, a PbTTT derivative with glycolated side chains, allowing it to accept an electron from another neutral PbTTT chain. This doubles the theoretical maximum yield when doping lower IP semiconductors.

A soluble derivative of F<sub>4</sub>-TCNQ, called F<sub>3</sub>-TCNQ-Ad1 and shown in Figure 1.13, has been designed with one of the fluorine atoms substituted with an adamantyl group.<sup>111</sup> No considerable difference in electronic properties compared to F<sub>4</sub>-TCNQ were observed when

films were processed from solution; using the idealised vapour deposition of F<sub>4</sub>-TCNQ was not possible since F<sub>3</sub>-TCNQ-Ad1 was not stable to sublimation. A derivative of F<sub>4</sub>-TCNQ, with two nitrile groups in place of fluorine atoms, called F<sub>2</sub>-HCNQ has been reported.<sup>112</sup> A LUMO of -5.59 eV was observed, which is approximately 0.3 eV lower lying than that for F<sub>4</sub>-TCNQ.

Some very high EA molecular dopants have been designed in order to oxidise materials with higher IP than F<sub>4</sub>-TCNQ is capable of. The extremely electron deficient 2,2'-(perfluoronaphthalene-2,6-diylidene)dimalononitrile (F6-TCNNQ) is shown in Figure 1.13. From initial electrochemical measurements a LUMO of -5.37 eV was reported,<sup>113</sup> however an EA of 5.60 eV has since been measured by photoelectron spectroscopy.<sup>114</sup> A similar nitrile functionalised cyclic molecule which has recently found use as a molecular p-dopant is hexacyano-trimethylene-cyclopropane (CN6-CP). Originally synthesised by Fukunaga in the 1970s,<sup>115, 116</sup> its extremely low lying LUMO of -5.87 eV<sup>117</sup> has led to its employment as a useful p-dopant in recent years.<sup>118, 119</sup> Replacing three CN6-CP nitrile groups with methoxycarbonyls gave trimethyl 2,2',2''-(cyclopropane-1,2,3-triylidene)-tris(cyanoacetate) (TMCN3-CP), a solution processable dopant with a higher lying LUMO of -5.50 eV.<sup>120</sup>

The use of high EA fullerenes as p-dopants has been explored. The fluorinated derivative C<sub>60</sub>F<sub>36</sub><sup>121</sup> was shown to have an EA of 5.38 eV.<sup>122</sup> The fluorinated fullerene C<sub>60</sub>F<sub>48</sub> has been used to dope graphene.<sup>123</sup> Fullerene's large sizes mean they are much less likely to diffuse than smaller molecular dopants, although they also tend to disrupt the molecular packing of the host.

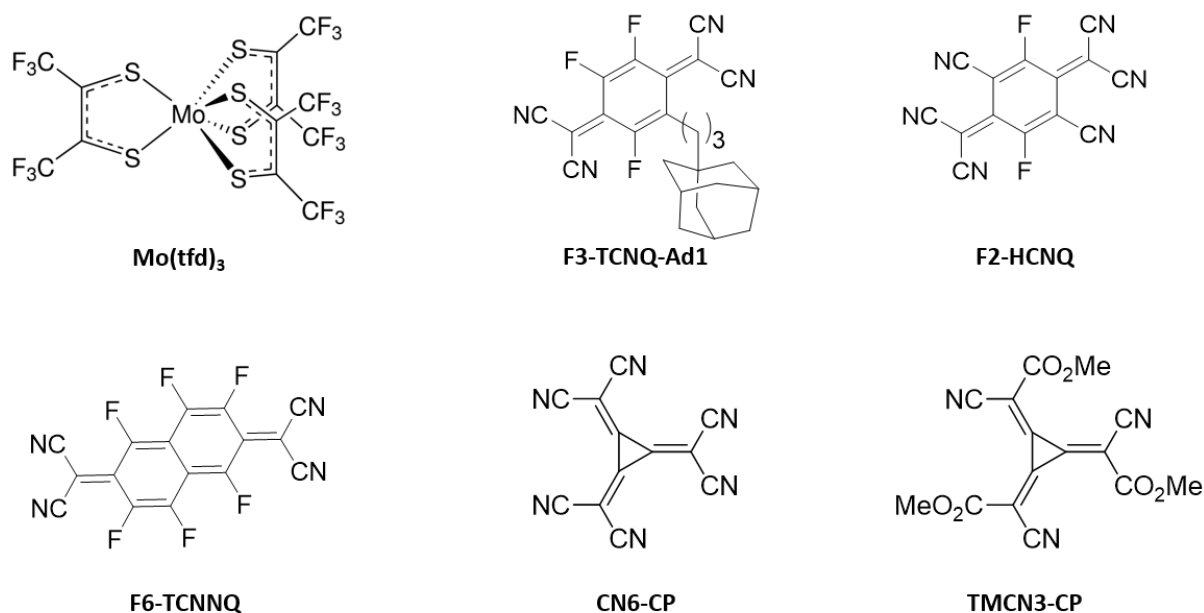


**Figure 1.13.** Chemical structures of molecular p-dopants.

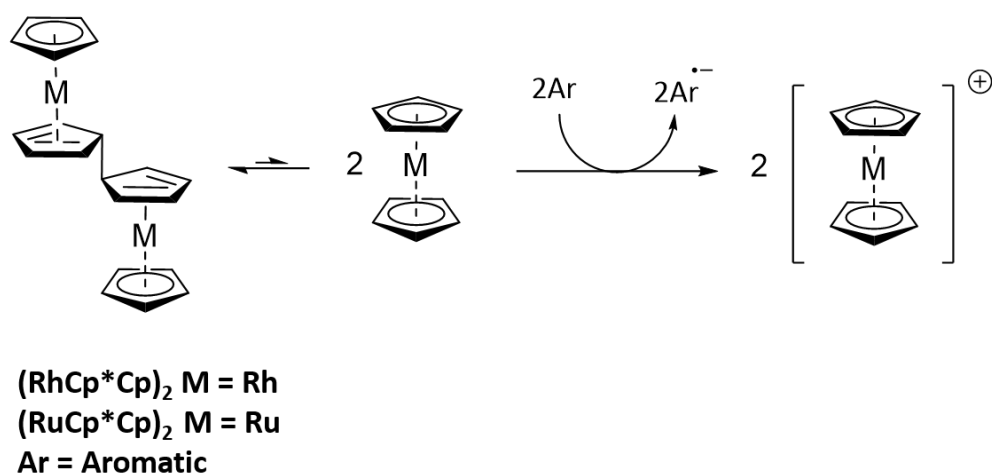
### 1.2.8 Review of organic n-doped systems

The development of n-dopants has been somewhat stagnant compared to p-types. The necessity for very low IP (or high lying HOMO) in dopants makes the synthesis of new structures stable to oxidation in air very difficult. Atmospheric oxygen also causes problems through the oxidation, or “de-doping,” of the n-doped semiconductor. Until very recently the efficiency of free charge generation in systems using the benchmark semiconductor and dopant had been limited by a lack of miscibility between the two.<sup>124, 125</sup> Using examples this section will outline some of the strategies used to overcome the factors limiting n-type performance and highlight some of the emerging new materials.

Successful n-doping of polyacetylene was first achieved by vapour deposition of alkali metals such as lithium, sodium and potassium.<sup>47, 126, 127</sup> As with the p-type halogen dopants, diffusion was an issue and their use in devices was severely limited.<sup>47</sup> In addition to this, their instability under ambient conditions and hazardous properties make atomic alkali metals impractical for use in most applications.

Cobaltocene, and its derivatives, have been used to dope a range of molecular,<sup>128-131</sup> polymeric<sup>132</sup> and fullerene<sup>133</sup> semiconductors. An IP of 4.07 eV for cobaltocene<sup>129</sup> and 3.30 eV

for decamethylcobaltocene<sup>131</sup> were measured by ultraviolet photoemission spectroscopy (UPS). Both are unstable to air due to their low IP. A promising route to solution processable and air stable dopants has been to use the dimers of metallocenes. Some structures are shown in Scheme 1.2 along with a schematic representation of cleavage and electron transfer. Cyclopentadienyl sandwich complexes of ruthenium<sup>134</sup> and rhodium<sup>135-137</sup> are most often used as dimers. The 18-electron configuration of the dimer means it has a much longer shelf-life and is easier to handle. Upon vapour deposition or casting from solution the dimers cleave to form the corresponding 19-electron monomer, which readily donates an electron to form the more stable 18-electron cation.



**Scheme 1.2.** Cleavage of 18 electron sandwich complex dimers to form two 19 electron complexes capable of n-doping aromatics.

In addition to the low IP metallocenes other metal complexes have shown promise as electron donors. Ru(terpy)<sub>2</sub> has been found to have a low IP and has been used to n-dope the organometallic complex ZnPC<sup>138, 139</sup> as well as pentacene.<sup>140</sup> The metal complexes Cr<sub>2</sub>(hpp)<sub>4</sub> and W<sub>2</sub>(hpp)<sub>4</sub> were used to dope fullerenes with both dopants achieving high n-type conductivities over 4 S cm<sup>-1</sup>.<sup>141</sup> W<sub>2</sub>(hpp)<sub>4</sub> has also been used to alter the majority charge carrier from p-type to n-type in OFETs using pentacene.<sup>142</sup> Fully organic low IP molecules have also been employed. Tetrathiofulvalene (TTF) was first used as a donor in charge transfer salts.<sup>143</sup> TTF and its derivative bis(ethylenedithio)-tetrathiafulvalene (BEDT-TTF) have since been used as n-type dopants for molecular semiconductors such as naphthalenetetracarboxylic dianhydride (NDA).<sup>144</sup> The donor tetrathianaphthacene (TTN) has been shown to have an IP 4.3 eV<sup>145</sup> and has since been used to n-dope a fluorinated derivative of ZnPC with increased EA.<sup>146</sup>

Some of the most widely used dopants in recent years are those derived from 2,3-dihydro-1*H*-benzimidazoles (DMBI-H). A lot of their success can be attributed to their air stability. The first example of their use came in a 2010 report<sup>147</sup> in which N-DMBI, structure shown in Figure 1.14, was used to dope phenyl-C<sub>61</sub>-butyric acid methyl ester (PCBM). The charge transfer between these two cannot be as simple as a direct electron transfer, PCBM has a LUMO of -3.80 eV<sup>148</sup> while N-DMBI HOMO is -4.67 eV.<sup>149</sup> It was originally proposed that the C2 hydrogen was abstracted leaving behind a Singularity Occupied Molecular Orbital (SOMO) on a N-DMBI radical, with an energy of -2.36 eV, capable of donating an electron to PCBM (Scheme 1.3, Mechanism I). The nature in which hydrogen actually leaves DMBI-H derivatives is complex, however the homolysis required to form the N-DMBI radical is likely unfavoured compared to hydride abstraction leaving behind a N-DMBI cation.<sup>149</sup> While the use of DMBI-H dopants has grown rapidly in the past decade the mechanism of their doping is still under debate and it is likely that the mechanism is substrate dependant<sup>150, 151</sup> and is affected by dopant-semiconductor miscibility.<sup>124</sup> The mechanism through hydride transfer on to PCBM and a subsequent electron transfer from hydride reduced PCBM to neutral PCBM is widely accepted for the case of PCBM as acceptor (Scheme 1.3, Mechanism II).<sup>152</sup>

Various dimers of benzimidazoles (DMBI)<sub>2</sub> have been synthesized and tested as n-dopants. A high n-type conductivity of 12 S cm<sup>-1</sup> was reported when doping C<sub>60</sub> fullerene.<sup>153</sup> In the same study it was found that conductivities on the order of 10<sup>-2</sup> S cm<sup>-1</sup> were possible when doping PCBM, comparable to DMBI-H, and on the order of 10<sup>-3</sup> S cm<sup>-1</sup> when doping poly(n,n'-bis(2-octyldodecyl)-1,4,5,8-naphthalenediimide-2,6-diyl)-*alt*-5,5'-(2,2'-bithiophene) P(NDI2OD-T<sub>2</sub>) which is higher than possible with DMBI-H dopants at the time. It was also found that dimers could dope TIPS-pentacene with an approximate EA of 3.4 eV,<sup>154</sup> this could not be done with DMBI-H dopants. Unlike DMBI-H the mechanism of doping is not through the abstraction of hydrogen or hydride. Instead one of two mechanisms are followed dependant on the nature of the substituent, labelled Y in Figure 1.14, and the acceptor. The dimer either homolytically dissociates into the neutral radical monomer units which undergo electron transfer with two acceptor units, similar to the metallocene dimers, (Scheme 1.3, Mechanism III) or electron transfer occurs before dimer dissociation (Scheme 1.3, Mechanism IV).<sup>155, 156</sup> High conductivities and thermoelectric performance have been reported using these dopants and

electron transfer likely occurs via a cleaner mechanism than the hydride transferring monomers.<sup>156, 157</sup>

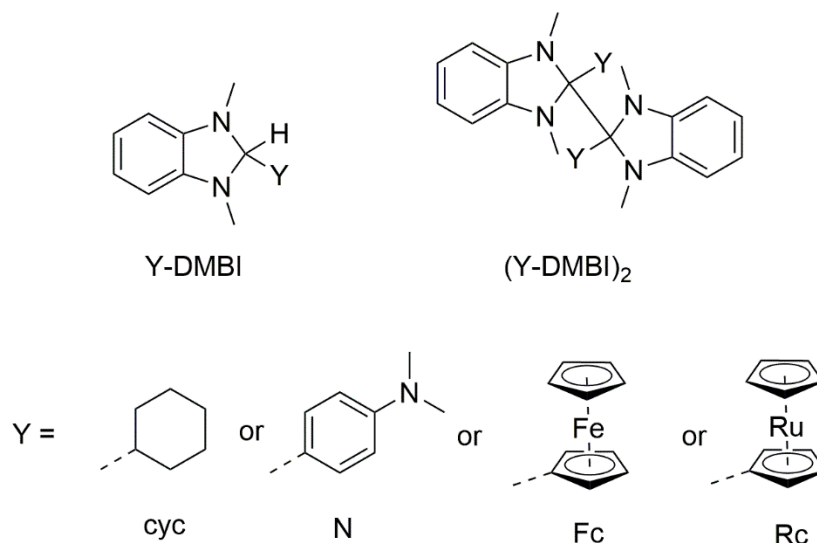
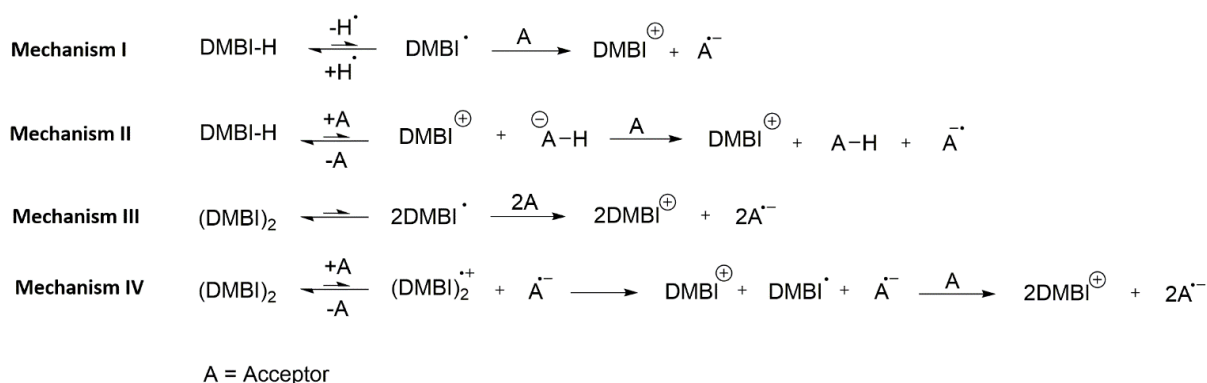


**Figure 1.14.** Structures of some DMBI-H and (DMBI)<sub>2</sub> dimers.



**Scheme 1.3.** Mechanism I shows DMBI-H doping via hydrogen abstraction and electron transfer from DMBI neutral radical. Mechanism II shows the later proposed mechanism of DMBI-H doping via hydride transfer and a subsequent electron transfer between acceptors. Mechanism III shows (DMBI)<sub>2</sub> homolytic cleavage then electron transfer to acceptors. Mechanism IV shows electron transfer from (DMBI)<sub>2</sub> to acceptor prior to cleavage and a subsequent electron transfer. Scheme is adapted from references 147, 152, 155.

Some recent reports of high-performance n-type materials have employed fluoride anions as n-dopants.<sup>49, 158</sup> The interaction of fluoride anions and aromatic systems has been studied over the past decade, often in the context of ion sensing applications as well as for semiconductor doping. In the majority of studies, a salt of fluoride anion and quaternary alkylamine cation are used as a source of fluoride; the organic soluble tetrabutylammonium fluoride (TBAF) being the most commonly applied. The possibility of  $\pi$ -anion complexation



between fluorides and planar electron-deficient aromatic systems has been used to explain the initial interaction between semiconductor and fluoride dopant.<sup>159-164</sup> This is then often quoted as leading to a direct electron transfer from fluoride to semiconductor and it is this step which has recently been called in to question.<sup>165-167</sup> The enthalpy of a direct electron transfer between fluoride and an NDI based small molecule has been computationally calculated as  $\Delta H = 76 \text{ kcal mol}^{-1}$  and therefore endothermic.<sup>168</sup> With fluorine being the most electronegative element and its atomic anion having a completely filled valence shell it seems likely there is a large barrier to fluoride donating an electron. It now appears that fluorides are precursors to the actual doping species and the mechanism is more complicated.<sup>169, 170</sup> The reaction between benzodifurandione oligo(p-phenylene vinylene) (BDOPV) molecular semiconductors and crystals of TBAF in solution is investigated in Chapter 3.

A technique known as n-type self-doping or intrinsic doping was first introduced by Gregg in 2001.<sup>171</sup> The aim was to create a doping system resembling the generally more efficient inorganics in which the dopant is not so chemically and structurally different from the host as to distort the crystal lattice or create deep electronic traps. A quaternary alkylamine with counterion was covalently bound to a perylenediimide (PDI) aromatic core and is considered the dopant precursor, the structure is labelled as PPEEB-NCl in Figure 1.15. The covalently bound nature of a doping moiety means that diffusion is brought under control. By reducing PPEEB-NCl with Na it was postulated a zwitterionic doping species, labelled PBEEB-N<sup>+</sup> in Figure 1.15, was formed. Films from a mixture of this solution and neutral PBEEB gave a ten-fold increase in conductivity at 1 mol% of the doping zwitterion. In a later study by Gregg *et al.* it was suggested the mechanism of self-doping in PDI-X compounds (Figure 1.15) upon drying also goes through a similar zwitterion.<sup>172</sup> After removing solvent molecules during film formation the stabilising solvation energy on an X<sup>-</sup> anion is removed. Spatially the X<sup>-</sup> is brought closer to the PDI core in the solid state and the negative charge is transferred to the PDI unit where it can be stabilised by delocalisation across aromatic rings. The n-doped forms were found to be surprisingly stable in dry air for months, although increasing humidity lead to a reversal of doping. The PDI-OH compounds from this series were later revisited by Segalman *et al.* in which the mechanism of doping was again studied.<sup>173, 174</sup> Based on X-ray photoelectron spectroscopy (XPS) data, it is proposed that the mechanism proceeds via nucleophilic attack of nitrogen-methyl group by hydroxyl anion to generate a bound tertiary

amine. This is followed by an electron transfer from tertiary amine to aromatic core. The possibility of a Hoffmann style elimination to generate an alkene and release an amine species from the semiconductor is also mentioned but not studied. The mechanism of doping using a quaternary ammonium group bound to a naphthalene diimide (NDI) core is discussed in Chapter 2.

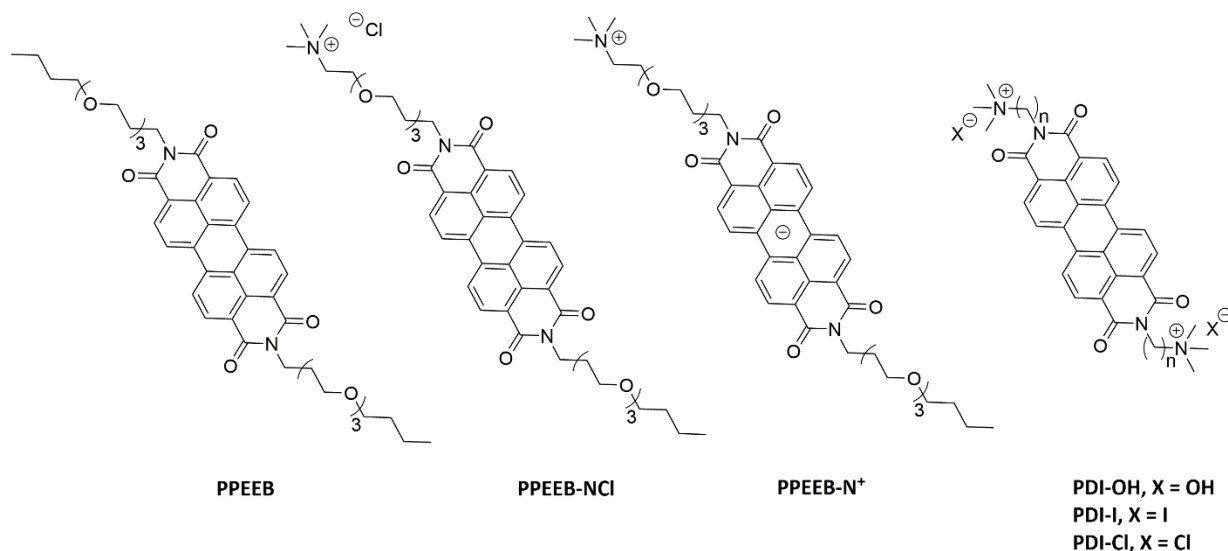


**Figure 1.15.** Structures of n-type PDI molecular semiconductors. PPEEB-NCl and PDI-X series of compounds are covalently bound to quaternary amine moieties which act as precursors to doping. PPEEB-N<sup>+</sup> shows a “doped” zwitterionic form.

## 1.3 Molecular design and synthesis of organic semiconductors

### 1.3.1 Introduction

Using the well-established and versatile techniques available through synthetic chemistry a large and ever-growing pool of organic semiconductors are available for use. The two main classes of material are the well-defined molecular semiconductors and polymers consisting of conjugated repeating units. The only necessity is to keep the band gap low enough for the material to still be considered semiconducting. For this reason, a wide range of olefin and aromatic components are used as building-blocks, and to a lesser extent alkyne bonds have been incorporated. Incorporation of heteroatoms into these conjugated cores and decoration with electron withdrawing and donating groups can help tune the energetic properties. Long solubilising alkyl and alkoxy chains have been used to alter the processability. For polymers

dramatic changes in performance are also observed with varying chain-lengths and regio-regularities.<sup>175</sup> Other material classes such as carbon-nanotubes and fullerenes find extensive use in the field of organic electronics, but molecular design plays less of a role in their functionality.

### *1.3.2 Manipulating frontier molecular orbitals through molecular design*

Changing the position of HOMO and LUMO energy levels is important for controlling various electronic properties. Charge injection and extraction at material interfaces, as well as electron transfer in doping, relies on the alignment of the respective materials energy levels. In addition to this, a materials band gap has been shown to be important for various light absorption and emission processes.

Decreasing the  $\pi$ -electron density will stabilise the LUMO and increase a materials EA. Heterocycles which incorporate imine bonds are often found in low LUMO materials; the nitrogen of the imine bond inductively withdraws electrons away from the aromatic ring while not mesomerically contributing a lone pair. Thiazole and thiadiazoles are therefore often incorporated as “electron-deficient” components or acceptors in semiconductors.<sup>176-179</sup> Inductively electron withdrawing groups such as halogens and mesomerically withdrawing groups such as carbonitriles, amides and imides, remove electron density from  $\pi$ -systems and lower both HOMO and LUMO.<sup>180</sup>

Both the HOMO and LUMO levels can be manipulated through the electron density. Increasing electron density will destabilise the HOMO and in turn lower the solid-state IP. In synthesis this can be achieved through incorporating heteroatoms with lone pairs into semiconductor back-bones. The five-membered rings: furan, thiophene and pyrrole are commonly used as the donor units in donor-acceptor polymers.<sup>181, 182</sup> Homopolymers of these materials are also majority p-type charge carriers.<sup>76, 183</sup> The mesomeric contribution of the lone pair on these heteroatoms leads to them being considered “electron-rich” ring systems. It should be noted however that the same heteroatoms can act to inductively withdraw electrons from the ring; the dipole moment of thiophene and furan reported as approximately 0.5 D and 0.7 D respectively in the direction of the heteroatom.<sup>184, 185</sup> Alternatively, pendant

groups which inductively push electrons to the conjugated core, such as alkyls, can be used to raise both the HOMO and the LUMO.

An example of the effect of ring atom substitution on position of FMOs can be seen in Figure 1.16 by comparing polymers derived from the well-studied P3HT.<sup>186</sup> Adding an imine nitrogen to one third of all thiophene units and converting them to thiazoles gives the polymer PTTTz and using half thiazole units gives PTTz. The addition of an increasing amount of electron-withdrawing thiazole rings into the polymer backbone leads to a stabilisation of both HOMO and LUMO. A consistent decrease in both FMOs is observed from empirical analysis (UV-Vis, CV and photoelectron spectroscopy) as well as density functional theory (DFT) and time-dependent density functional theory (TD-DFT) calculations.

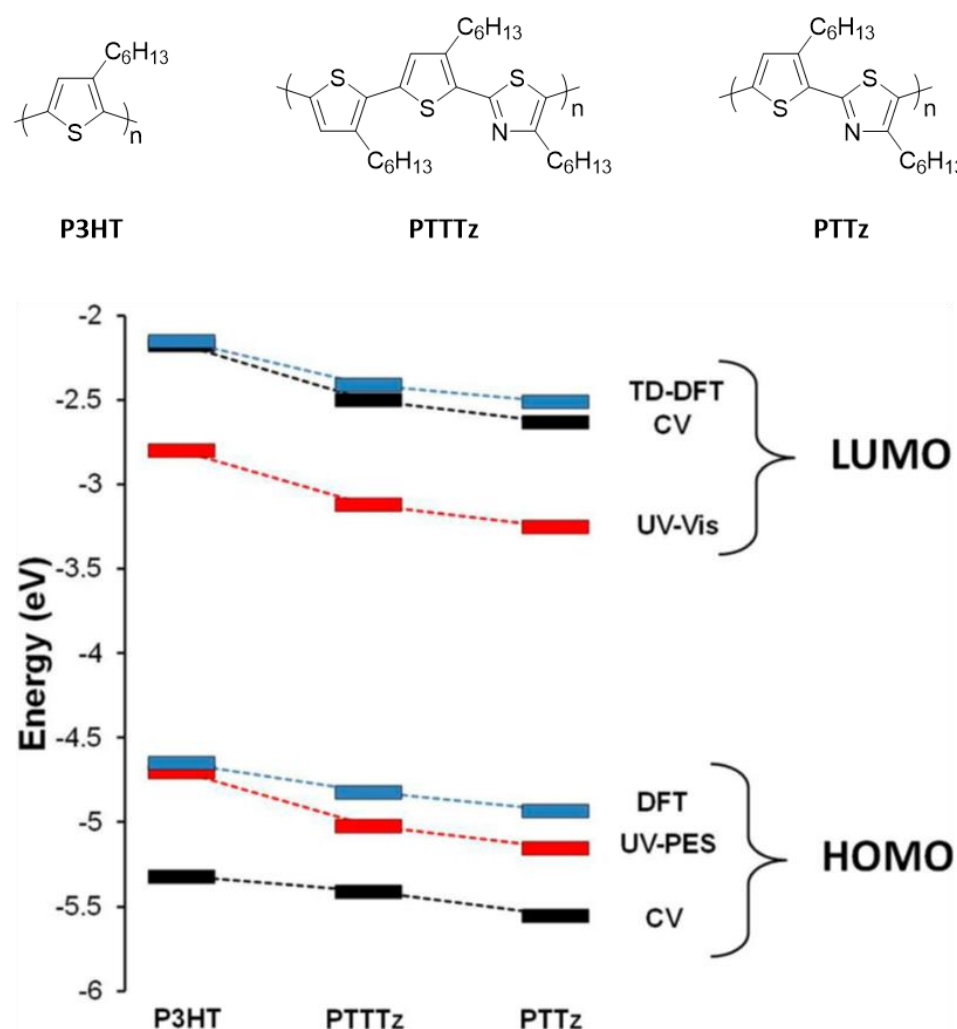


**Figure 1.16. Top:** Chemical structures of the polymer P3HT, PTTTz and PTTz. **Bottom:** Graphical representation of the frontier molecular orbital energies of the three polymers when measured empirically by Cyclic Voltammetry (CV), Ultraviolet Photoelectron Spectroscopy (UPS) and Ultraviolet-Visible Absorption Spectroscopy (UV-Vis). Energy levels Calculated by Density Functional Theory (DFT) are also shown. Reprinted from reference 186.

In the design of new active materials for OSCs it became necessary to reduce the bandgap in order to maximise the number of photons absorbed. An effective way of reducing, and tuning, the bandgap was to design molecular and polymeric semiconductors consisting of alternating electron rich (donor) and electron deficient (acceptor) units, i.e. donor-acceptor semiconductors.<sup>187-189</sup> The combination of extremely electron rich and electron deficient components bonded by a single  $\sigma$ -bond means that the generation of an exciton is more energetically favourable. The electron deficient acceptor stabilising a negative charge and electron rich donor stabilising a positive charge in the excited state. In terms of FMOs, hybridisation of the high donor HOMO and low acceptor LUMO leads to a reduced gap between the two, this hybridisation is shown in Figure 1.17.<sup>190, 191</sup> Extending this isolated donor-acceptor unit over many more repeat units increases the amount of hybridisation even further leading to some oligomeric and polymeric semiconductors with extremely low band gaps.

The first donor-acceptor polymers used nitrogen containing moieties as donor units. Stable acceptor units were hard to come by but derivatives of squaric acid and croconic acid proved to be effective.<sup>192, 193</sup> Condensation polymerisation of donor with acceptor gave polymers with a large amount of quinoidal characteristics, as shown in Figure 1.17. Band gaps as low as 0.5 eV were measured in polymers of this kind.<sup>194, 195</sup> Materials which absorb low energy visible and near infrared light are very useful for photoacoustic imaging purposes. With relatively low bio-toxicities and extremely low band gaps, allowing for absorption in the NIR region and subsequent non-radiative decay, donor-acceptor polymer nanoparticles have been applied as active materials.<sup>23</sup> Diketopyrrolopyrrole (DPP) and benzothiadiazole are often employed as acceptors with thiophene derivatives used as donors. Polymers and oligomers such as PDPP-3T<sup>196</sup> and BBT-2FT<sup>197</sup> have been used to absorb radiation of wavelengths above 800 nm, corresponding to energies of less than 1.5 eV, for photoacoustic imaging.

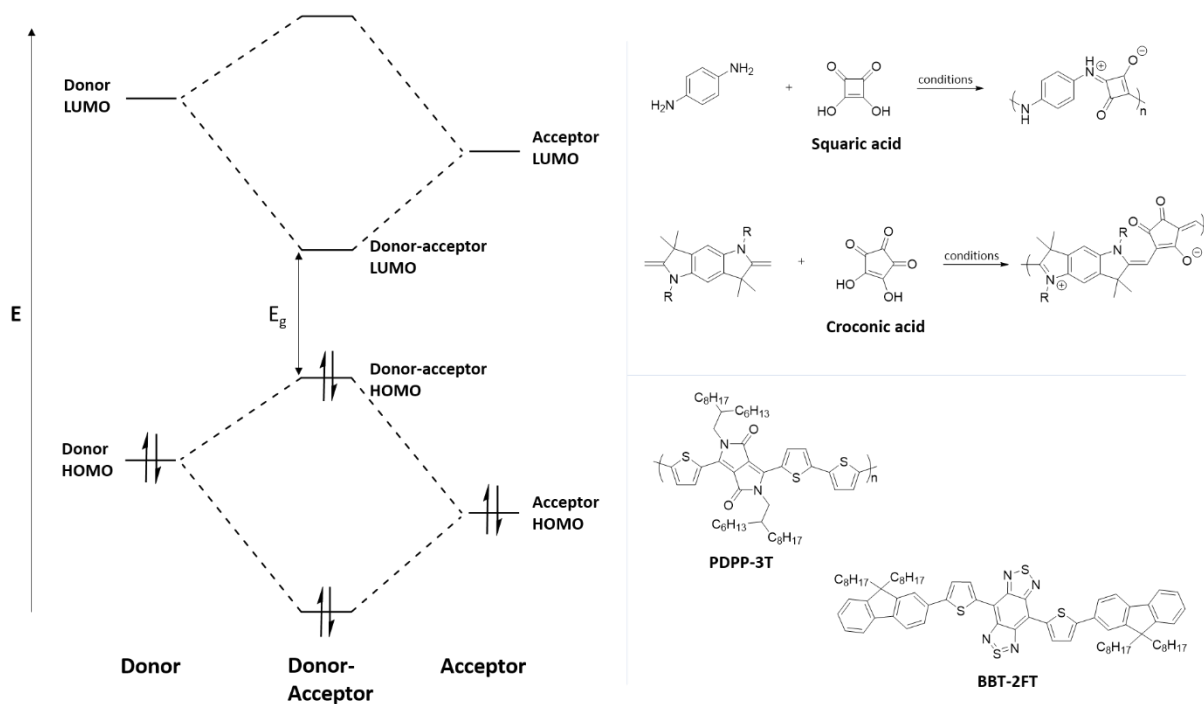


**Figure 1.17. Left:** Hybridised molecular orbitals of donor and acceptor leading to a reduced band gap donor-acceptor. **Top right:** Condensation polymerisations of squaric acid and croconic acid with donor units to give early donor-acceptor polymers. Conditions: reflux in alcohol in the presence of inorganic acid (HCl,  $\text{H}_2\text{SO}_4$ ) or strong base (quinoline).<sup>195</sup> **Bottom right:** Structures of donor-acceptor polymer PDPP-3T and oligomer BBT-2FT, used as contrast agent in photoacoustic imaging.

The use of donor-acceptor materials in certain applications has proven to be problematic. Many polymers will exhibit a degree of torsional twisting between the donor and acceptor units which leads to poor intramolecular overlap of  $p_z$  orbitals and decreased intramolecular charge transport. Some applications also simply do not require extremely low band gaps; even in the case of active materials for bulk heterojunction solar cells if the donor will absorb over a wide wavelength range it is not strictly necessary for the acceptor to do the same.

### 1.3.3 Improving charge transport through molecular design

Charge transport across a material is chiefly determined by the intramolecular conformation of the conjugated section and the supramolecular solid-state packing. Polaron and exciton delocalisation across a polymer chain is important to increase intramolecular mobilities. Structurally this is achieved by reducing torsional angles between sections of the polymer chain and using synthetic design to promote planarity and good overlap of  $p_z$  orbitals.

Intermolecular charge transport is dominant in molecular semiconductors and is occasionally necessary for interchain charge transfer in polymers. Due to the increased distances between molecules it is necessary for charge carriers to tunnel, in a hopping mechanism, for most intermolecular charge transport to be successful. This hopping can be improved upon by promoting structural regularity by utilising noncovalent interactions.

#### 1.3.4 Intramolecular conformational control

Decreasing free rotation around single bonds has been shown to be an effective way of increasing overlap between  $p_z$  orbitals and increasing the total  $\pi$ -conjugation length.<sup>198</sup> In cases where hopping transport models can be applied it can be seen from equation 1.5 that an increase in transfer integral,  $J$ , from better orbital overlap will lead to higher rates of transfer between localised sites.

One commonly encountered interaction between single bonded ring systems is intramolecular hydrogen-bonding. An example of full intramolecular hydrogen bonding can be seen in Figure 1.18 in which a sulfonamide -NH acts as hydrogen donor to a quinoidal carbonyl.<sup>199</sup> Increasing the amount of these hydrogen bonds planarises the central anthraquinone (AQ) conjugated unit and increases charge distribution ultimately stabilising the LUMO. Commonly hydrogen bonds are found when lactam and cyclic imide moieties are incorporated into the conjugated section of semiconductors.<sup>200-202</sup> These ring systems contain carbonyl oxygen atoms with partial negative charges able to act as hydrogen bond acceptors. The effect of hydrogen-bonding type interactions between carbonyl and aromatic -CH hydrogens has been widely reported and iso-indigo is shown in Figure 1.18 with the partial hydrogen bond highlighted.<sup>203-205</sup> It has been claimed that this interaction is favoured over other non-covalent interactions between heteroatoms and is the dominant electrostatic interaction between thiophene and lactam containing heterocycles.<sup>206</sup>

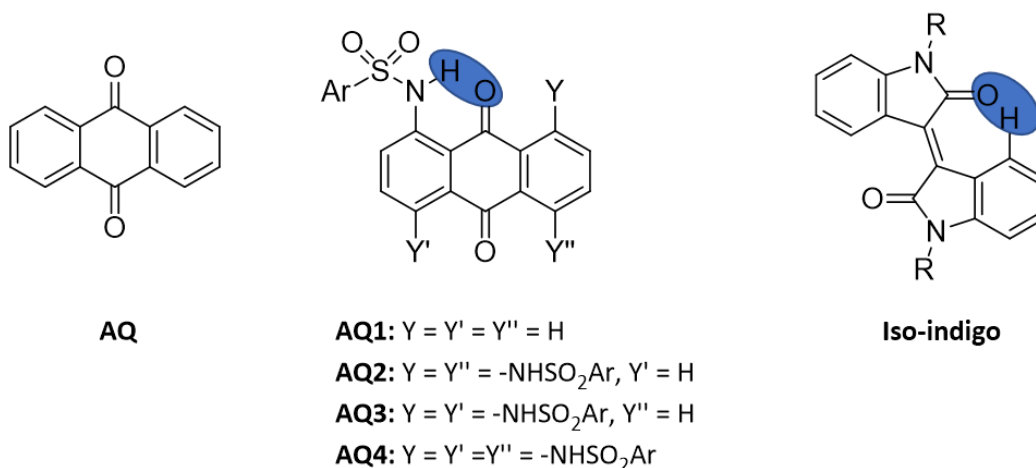


**Figure 1.18. left:** Structures of derivatives of anthraquinone (AQ, AQ1, AQ2, AQ3 and AQ4) decorated with sulfonamide groups capable of intramolecularly hydrogen bonding with anthraquinone carbonyl oxygen. **Right:** Structure of iso-indigo with intramolecular hydrogen bond between lactam carbonyl and phenyl hydrogen highlighted.

One tactic used to minimise torsional angles and promote better orbital overlap between ring systems is to utilise attractive non-covalent intramolecular interactions between heteroatoms. Calculations have suggested that the lone pair of nitrogen can donate into the anti-bonding orbital of carbon to sulphur bonds. Subsequently this interaction increases planarity in copolymers of thiophene and thiazole.<sup>186, 207</sup> Similar interactions between oxygen and sulphur have been reported to planarise oligomers of EDOT<sup>207</sup> and the oxygen of alkoxy solubilising chains has been reported to planarise thiophene containing polymers.<sup>208-210</sup> The fluorination of semiconductors is not only a useful tool for lowering FMOs but can also be used to increase molecular order. An attractive interaction between fluorine atoms on benzothiadiazole and sulphur in adjacent thiophene rings has been reported to decrease torsional angles between the two heterocycles.<sup>210-212</sup> The calculated optimal ground state of a thiophene based oligomer, BTTT, showed a torsional angle between thiophene units of 12.7° which decreased to 0.1° when fluorine was substituted onto the ring, FBTTT (Figure 1.19).<sup>213</sup> The same study also found that the polymer PbTTT exhibited a nearly four times increase in hole mobility as well as a small increase in EA.



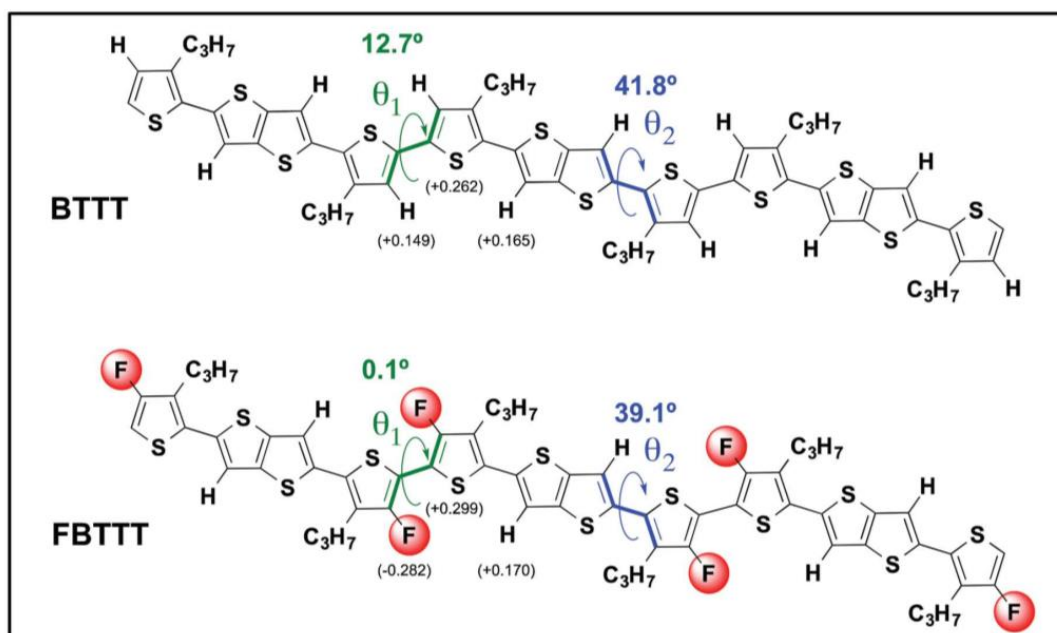


**Figure 1.19.** Calculated optimised structures of BTTT and FBTTT with dihedral angles between thiophene units marked as  $\theta_1$  and thienothiophene to thiophene units marked as  $\theta_2$ . Some atomic charges are shown in parenthesis calculated through Mulliken population analysis. Adapted from reference 213.

Whether these sulphur to heteroatom interactions are strong enough to promote increased planarity has been called into question. It has been claimed that because sulphur, nitrogen, oxygen and fluorine are all electronegative they undergo electrostatic repulsion with each other, destabilising any attractive interaction. In the case of oxygen and nitrogen substituents in proximity to a thiophene ring the heteroatom to thiophene hydrogen interaction was calculated to be more attractive, leading to more stable conformations with dihedral angles of  $180^\circ$  between the thiophene sulphur and the heteroatom.<sup>206</sup> Further studies have indicated however that interactions other than electrostatics need to be considered.<sup>207, 210</sup> Other attractive interactions can be realised through the alignment of dipoles and induced dipoles and through donation of correctly aligned lone pairs into antibonding orbitals. It is clear that multiple competing factors must be considered when attempting to describe the impact of heteroatom non-covalent interactions on conformation and no one stabilising or destabilising effect can be treated in isolation. In addition, factors on a larger scale must be considered such as the increased stabilisation from greater conjugation lengths and the overall supramolecular structure.

### 1.3.5 Supramolecular structure

The efficiency of charge transfer intermolecularly is reliant on good overlap between molecular  $\pi$ -orbitals and this can be controlled through careful synthetic design.<sup>214</sup> Intermolecular charge transport is often considered a barrier to high mobilities since charges will be required to tunnel the distance between small molecules or polymer chains. Typically, intermolecular cofacial  $\pi$ - $\pi$  stacking distances in the solid state are approximately 3.4 Å and any increase on this will negatively affect transfer rates between sites. A portion of the popularity of lactam, lactone and imide containing units can be owed to the polarisation of their carbonyl bonds, causing an attractive interaction between adjacent units.<sup>215</sup> DPP, NDI and iso-indigo are therefore commonly utilised. Removing the normal solubilising N-substituted groups in these units leaves an N-H bond free for hydrogen bonding with an adjacent molecule. Decreasing the cofacial  $\pi$ - $\pi$  stacking distance further through H-bonding in this way has been shown to give higher charge mobilities, albeit by sacrificing a solubilising group.<sup>216-218</sup>

It is not only  $\pi$ - $\pi$  stacking distances which can affect the intermolecular charge transfer but also the relative positions of molecules in the solid-state packing structure. A mixture of theoretical and experimental techniques have been used to demonstrate the drastic effect subtle changes in molecular design can have on supramolecular structure and charge transfer properties.<sup>219</sup> Five fluorinated derivatives of benzodifurandione-based oligo (*p*-phenylenevinylene) (BDOPV) were synthesised and are shown in Figure 1.20. Significant differences in morphology between the derivatives can be attributed to the subtle differences in charge distribution caused by fluorine substitution. Electrostatic potential calculations, Figure 1.20, showed that for *p*-F<sub>2</sub>-BDOPV and F<sub>4</sub>-BDOPV the overall molecular dipole allowed for favourable Coulombic interactions between one molecule and an adjacent flipped molecule within the  $\pi$ -stack. These attractive electrostatic interactions gave rise to the antiparallel cofacial arrangement between adjacent molecules with minimised longitudinal and transverse offsets. Both of these derivatives therefore showed good intermolecular orbital overlap with high calculated transfer integrals and electron mobilities of 6.6 and 12.6 cm<sup>2</sup>V<sup>-1</sup>s<sup>-1</sup> for *p*-F<sub>2</sub>-BDOPV and F<sub>4</sub>-BDOPV respectively, measured from bottom-gate top-contact single crystal transistor devices. The most substituted derivative, F<sub>6</sub>-BDOPV, had the

lowest lying LUMO level of -4.10 eV and would therefore be expected to best stabilise an electron. The charge distribution shown from ESP calculations suggests there is electrostatic repulsion felt between the longitudinal edges of each molecule and large offsets in both dimensions between  $\pi$ - $\pi$  stacked neighbours. A slip-stacked 1D morphology consisting of  $\pi$  columns was calculated which did not give ideal intermolecular orbital overlap. This is reflected in a lower electron mobility of  $4.6 \text{ cm}^2 \text{ V}^{-1} \text{ s}^{-1}$ . Unsubstituted BDOPV, also with a slip-stacked 1D morphology, and *o*-F<sub>2</sub>-BDOPV, with large offsets between molecules and a herringbone 2D morphology, had even lower electron mobilities. This example highlights that small changes on the molecular level, intended to manipulate the FMOs, may have a large impact on the morphology and device performance.

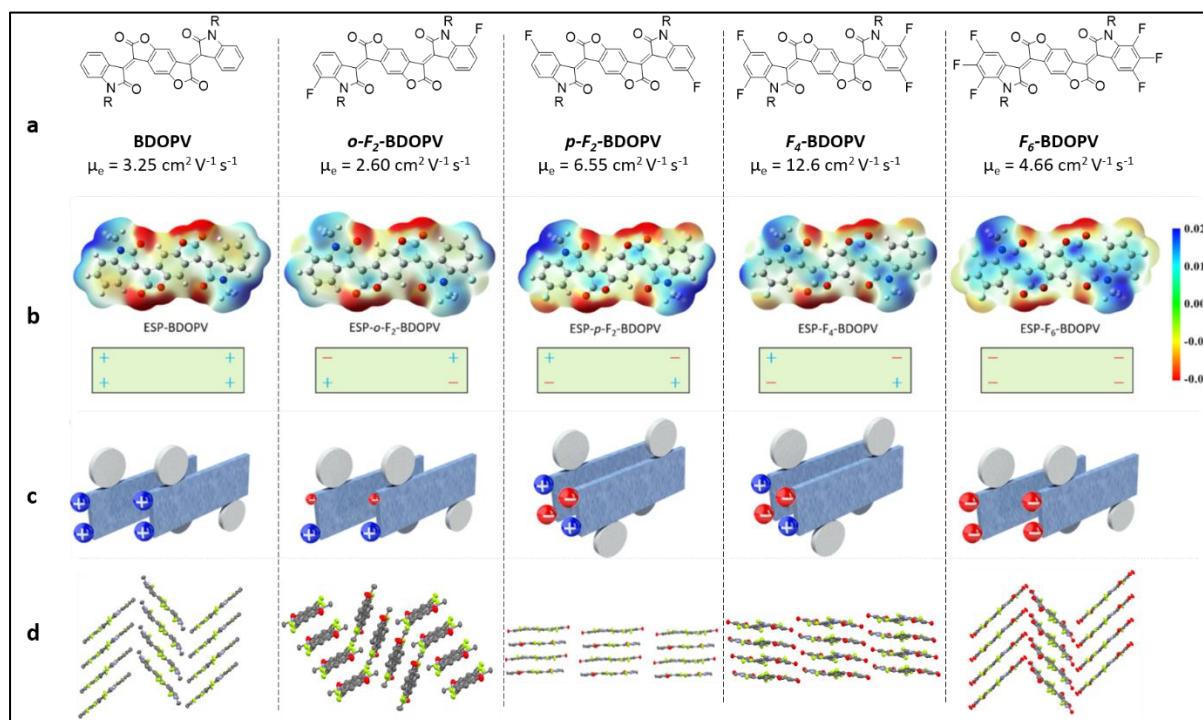


**Figure 1.20. a:** Structures of BDOPV and fluorinated derivatives with electron mobilities,  $\mu_e$ , obtained from bottom-gate top-contact single crystal transistors. Alkyl sidechain, R, is 2-ethylhexyl. **b:** Calculated electrostatic maps of BDOPV and five fluorinated derivatives with schematic representation of overall charge distribution in the corners of the molecule. Ethylhexyl sidechains have been replaced with methyl groups for calculations. **c:** Schematic representation of the  $\pi$ - $\pi$  molecular packing conformation with the rectangles as the conjugated BDOPV core and circles as the solubilising alkyl sidechains. **d:** Molecular packing arrangements for BDOPV and the five fluorinated derivatives. Figure adapted from reference 219.

### 1.3.6 Sidechain engineering

The understanding of the role of the pendant sidechain on functionality has evolved in recent years. Originally deployed to increase the solubility of the rigid semiconducting components,<sup>73</sup> it is now clear that their modification can have a profound effect on optoelectronic properties and device performance. Section 1.2.8 of this chapter explored some examples in which the sidechain could be modified to introduce doping moieties, circumnavigating the need for external molecular dopants. Sidechains for intrinsic doping will not be described any further here. Instead their use as tools for imparting intramolecular and supramolecular control is the focus of this section.

Chapter 4 of this work is concerned with the design and synthesis of a n-type polymer structurally analogous to the p-type polymer PbTTT.<sup>220</sup> PbTTT exhibits a high degree of order in solid state thin films both perpendicular and parallel to the substrate, as shown by grazing-incidence X-ray diffraction (GIXD) patterns in Figure 1.21.<sup>221</sup> Good charge transport properties are therefore observed along the polymer chain and between chains.<sup>63, 222, 223</sup> The regular spacing of linear alkyl chains orthogonal to the polymer backbone leads to their interdigitation in the lamellar direction, also known as molecular docking. This interdigitation locks the polymer chain in a more rigid and planar conformation promoting long conjugation lengths and good charge transport along the polymer chain.<sup>224</sup> High planarity within the chain also means strong  $\pi$ - $\pi$  interactions between adjacent chains and PbTTT also exhibits ordered cofacial  $\pi$ -stacking.<sup>221, 223, 225, 226</sup> The increased order makes it possible to use crystallographic techniques to observe the morphology of mixtures containing dopants. See Figure 1.11 for a visualisation of dopant F<sub>4</sub>-TCNQ favourably aligning between the interdigitated sidechains of PbTTT.<sup>63</sup> Similarly, the fullerene derivative PC<sub>71</sub>BM has been shown to sit between the PbTTT sidechains in blends for bulk heterojunction (BHJ) solar cells, this does however lead to more conformational distortion of the polymer backbone.<sup>221</sup>

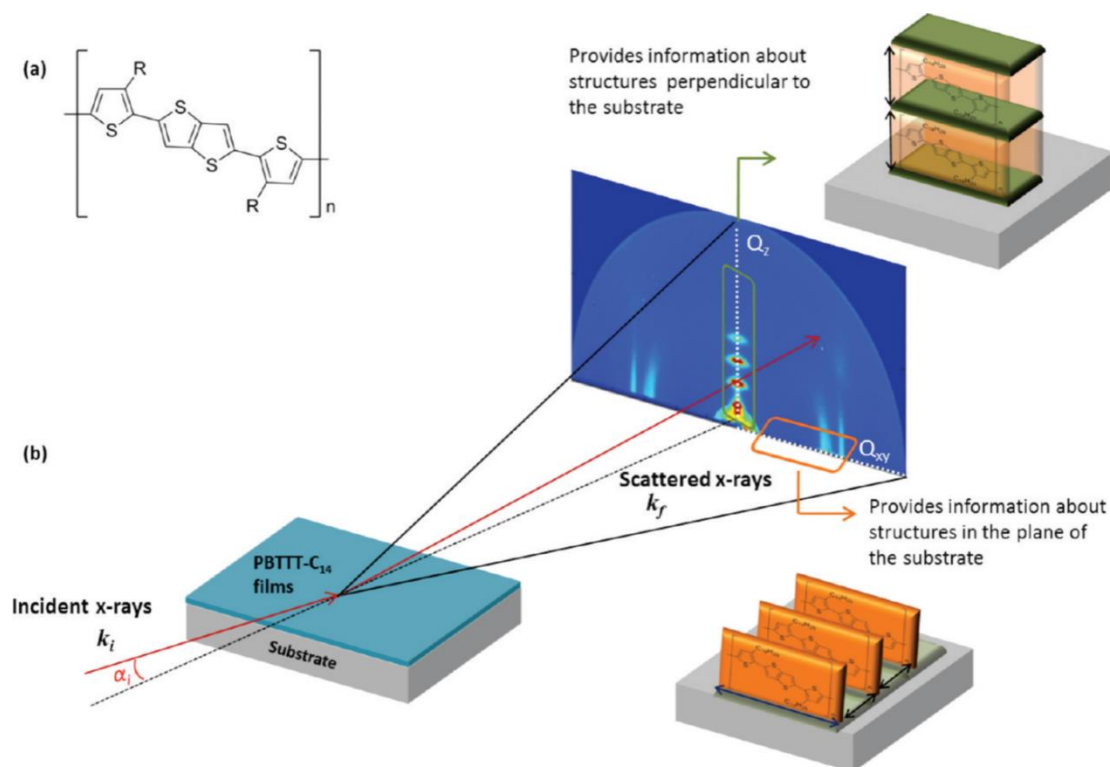


**Figure 1.21. a:** Chemical structure of the polymer PbTTT. **b:** Schematic representation of grazing-incidence X-ray diffraction patterns of thin-films of PbTTT. Peaks in the  $Q_{xy}$  direction are for repeating units parallel to the plane of substrate, in this case the  $\pi$ - $\pi$  structure. Peaks in the  $Q_z$  direction represent repeating units perpendicular to the plane of the substrate, in this case the Lamellar structure. Figure reprinted from reference 221.

Favourable alignment of neighbouring polymer sidechains has also been explored on multiple donor-acceptor polymers.<sup>227</sup> Figure 1.22 shows a cartoon representation of polymers with axisymmetric donor and acceptor units, which exhibit curved conjugated backbones. It was determined that polymers with the axisymmetric conformation experience a lot of steric hindrance between alkyl sidechains leading to more disorder intramolecularly, poor cofacial  $\pi$ - $\pi$  stacking between polymer chains and increased Lamellar distances. All of these factors lead to decreased charge mobilities, presumably within and between polymer chains, compared to centrosymmetric polymers which exhibit rigid straight backbones. In centrosymmetric polymers the sidechains are correctly aligned to form “molecular docks” and do not sterically repel each other leading to more ordered and crystalline thin films. This increased order is then reflected in increased charge mobilities.

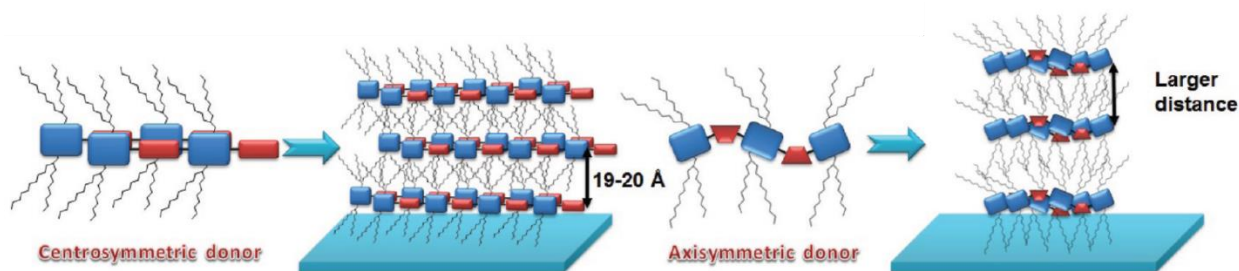


**Figure 1.22.** Schematic representation of centrosymmetric donor-acceptor polymers and the long-range order they exhibit due to preferable sidechain docking. Representation axisymmetric donor-acceptor polymers in which the sidechains are sterically clash due to the curved conformation of the polymer backbone. Figure reprinted from reference 227.

## 1.4 Scope of the thesis

This thesis focusses on two of the major themes outlined above. First, two different n-type dopants and the mechanisms by which they insert negative charges on to organic semiconductors are studied. Then the synthesis of two novel polymers with the aim of making n-type materials morphologically analogous to highly ordered p-type polymers. The chapters are presented as follows:

### *Chapter 2 – Structure and mechanisms of quaternary amine self-dopants*

This chapter focusses on probing the structure of previously studied self-doping n-type molecular semiconductors. A naphthalene diimide core was decorated with an ionic quaternary ammonium moiety and the aqueous solution of its hydroxide salt was subjected to spectroscopic analysis. The mechanism by which the quaternary ammonium hydroxide moiety undergoes “self-doping” was also explored in the context of the new insights gained from the structural characterisation.

### *Chapter 3 – Exploring the chemical mechanism behind n-type fluoride doping of BDOPV semiconductors*

Chapter 3 explores the various pathways by which fluoride anions may act as n-type dopants to high EA semiconductors. The molecular semiconductor BDOPV and its *para*-difluorinated derivative 2F-BDOPV were used as acceptors. Various spectroscopic techniques were used to

probe the interaction of fluoride anions with two different solvents and the subsequent interactions between fluoride, solvent and acceptors.

#### *Chapter 4 – Synthesis of thiazole containing highly-ordered polymers*

This chapter outlines the design and synthesis of two polymers analogous to the p-type polymer PbTTT but including electron withdrawing imine bonds incorporated into the polymer chain. The polymer PbTzTT was successfully synthesised and initial electrochemical characterisation revealed a stabilised LUMO compared to PbTTT. The synthetic attempts at reaching the PbTz3 polymer, with higher concentration of imine bonds, are also described.

# Chapter 2. Structure and Mechanisms of Quaternary Amine Self-Dopants.

## 2.1 Introduction

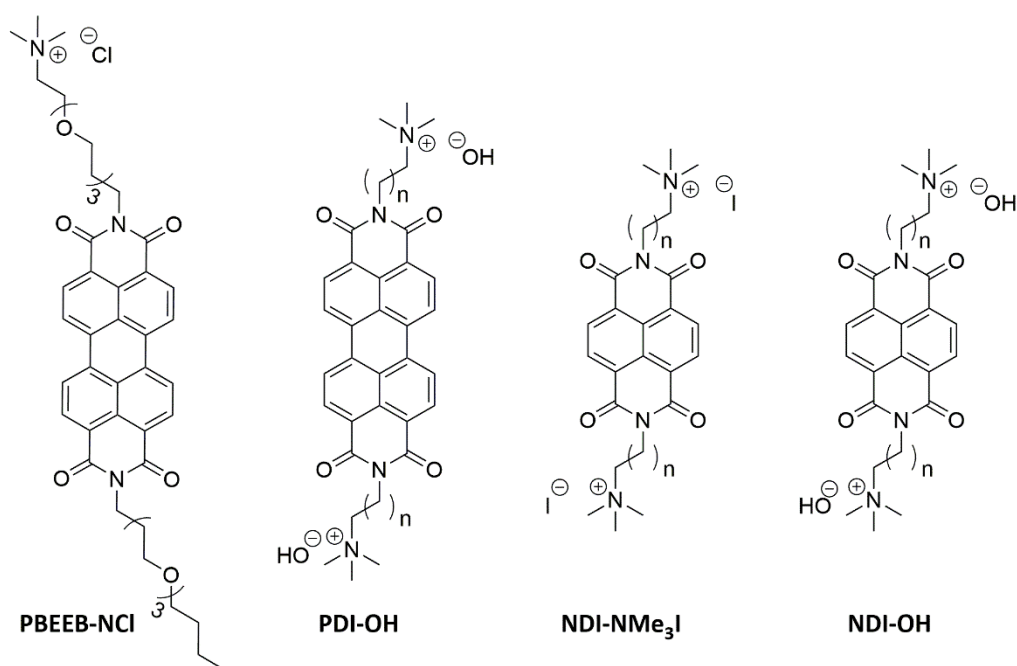
Chapter 1 introduced the fundamental concept of n-type doping and outlined various examples of n-type dopants which undergo single electron transfer with organic semiconductors due to their low IPs. Dopants with low solid state IP values are capable of reducing  $O_2$  to  $O_2^-$  and  $H_2O$  to  $OH^-$  under atmospheric conditions.<sup>228</sup> Problems are therefore encountered in their handling and the experimental study of their applications is mostly limited to glove-box work. In addition to this, and much like molecular p-dopants, the introduction of molecular n-dopants can lead to significant disruption in the morphology of the semiconducting matrix, leading to non-ideal charge transport and the formation of traps. Poor miscibility between the doped semiconductor and oxidised dopant can also lead to the dopant crystallising out of the thin film disrupting charge transport even further.

In an effort to produce n-type organic semiconductors which experience minimal morphological disruption upon doping, Gregg et al.<sup>171, 229</sup> designed a dopant precursor covalently bound to a perylene diimide aromatic acceptor. The structure of the precursor is labelled PBEEB-NCl in Figure 2.1 and contains a quaternary amine moiety with a halide counterion. Reducing PBEEB-NCl with sodium lead to the zwitterionic “doped” semiconductor PBEEB-N<sup>+</sup> which exhibited conductivities of  $0.01 \text{ S cm}^{-1}$  when blended with a neutral PDI derivative. This study paved the way to air stable n-type dopant precursors which could be processed from water.

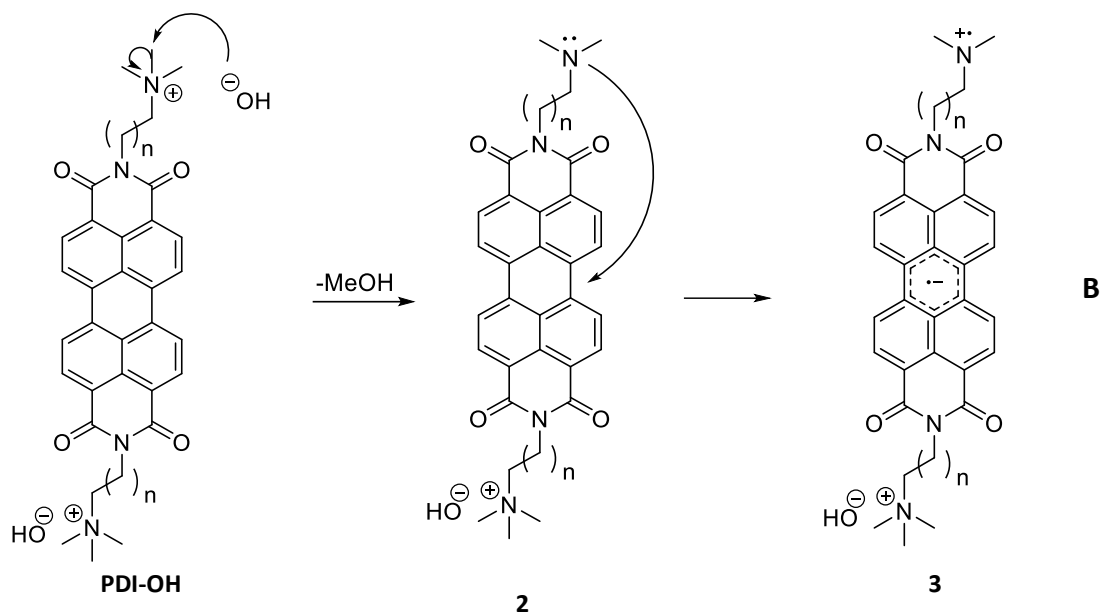
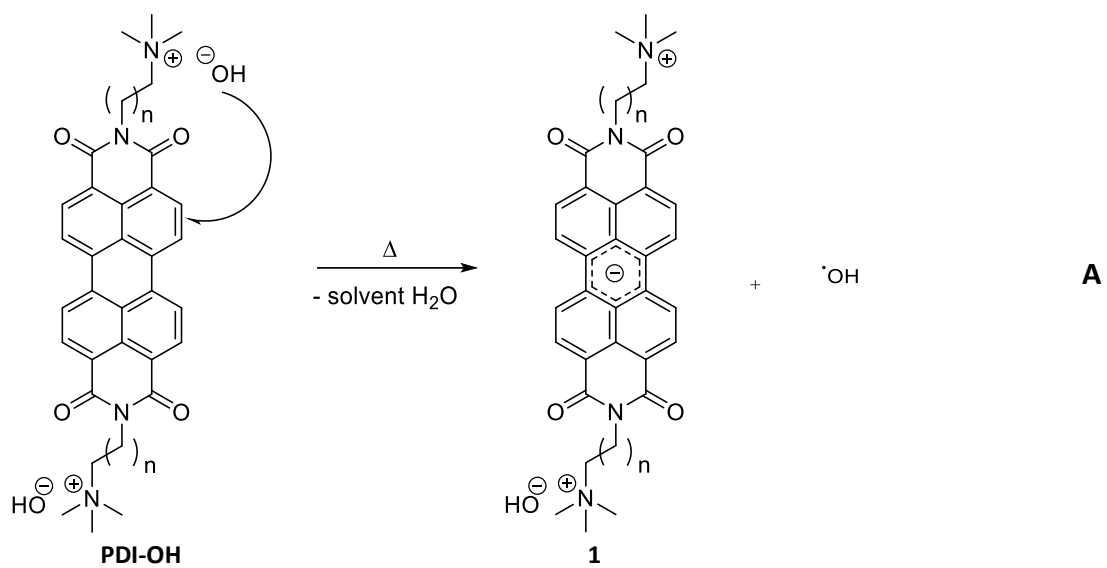
Quaternary amines as covalently bound dopants for PDI have since been studied further. It was found that using ion exchange resin to exchange the halide of PBEEB-NCl gave PDI-OH, a quaternary amine terminated derivative with hydroxyl counterions. PDI-OH (Figure 2.1) was found to be stable in aqueous solutions and forms homogeneous thin films which upon drying

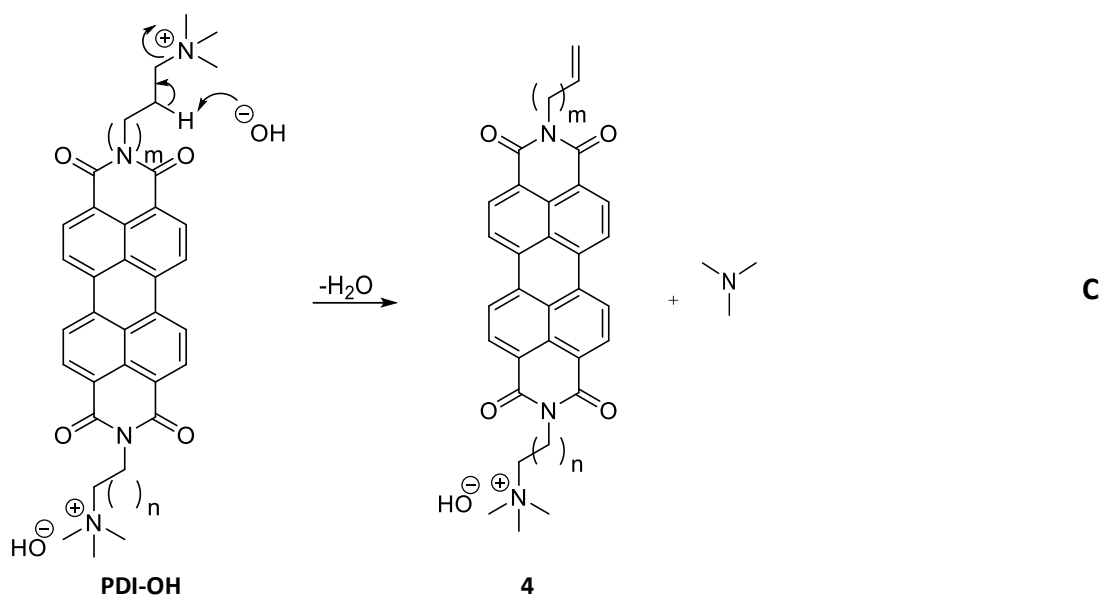


show evidence of charge carriers. A summary of suggested mechanisms of charge transfer are shown in Scheme 2.1. Reilly et al.<sup>172</sup> suggest that the driving force behind doping is the loss of solvation energy around the anion upon film formation, leading to a destabilisation of the anion. The negative charge is therefore transferred to the PDI aromatic core, the large PDI unit being more polarisable and more capable of stabilising the charge. Russ et al.<sup>174</sup> reported that the hydroxyl anion acts as a nucleophile to attack a methyl group generating methanol and leaving a dimethylamine group bound to the PDI sidechain. It was then the dimethylamine moiety which underwent electron transfer with the aromatic core, this was evidenced by a growth in XPS signal for NMe<sub>2</sub> nitrogen upon film annealing while the NMe<sub>3</sub><sup>+</sup> signal diminished. Electron transfers, of the type shown in Scheme 2.1, between tertiary amines and naphthalene diimide semiconductors have previously been observed.<sup>230-232</sup> Assigning the decomposition of the quaternary ammonium hydroxide to nucleophilic attack however ignores the preference for an E2 Hoffmann elimination when  $\beta$ -hydrogens are present and sterically available for abstraction.<sup>233-235</sup>



**Figure 2.1.** Structure of previously studied PBEEB-NCl and PDI-OH as well as compounds studied in this chapter including NDI-Me<sub>3</sub>I and NDI-OH. For PDI-OH  $n = 1$  or  $5$ , for NDI-NMe<sub>3</sub>I and NDI-OH  $n = 7$ .





**Scheme 2.1.** Mechanisms previously used to describe the solid-state doping of PDI-OH. **A:** Mechanism suggested by Reilly et al.<sup>172</sup> including single electron transfer from hydroxyl to PDI. ( $n = 1$ ). **b:** Mechanism suggested by Russ et al.<sup>174</sup> in which hydroxyl acts as nucleophile and electron transfer occurs between amine nitrogen and PDI. ( $n = 5$ ). **c:** Possible degradation of quaternary ammonium headgroup via Hoffmann elimination ( $n = 7$ ,  $m = 6$ ).

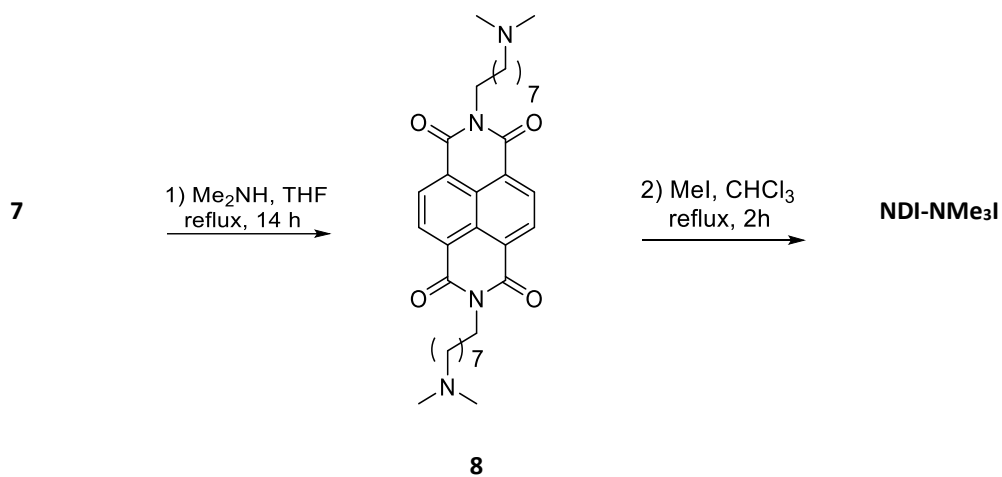
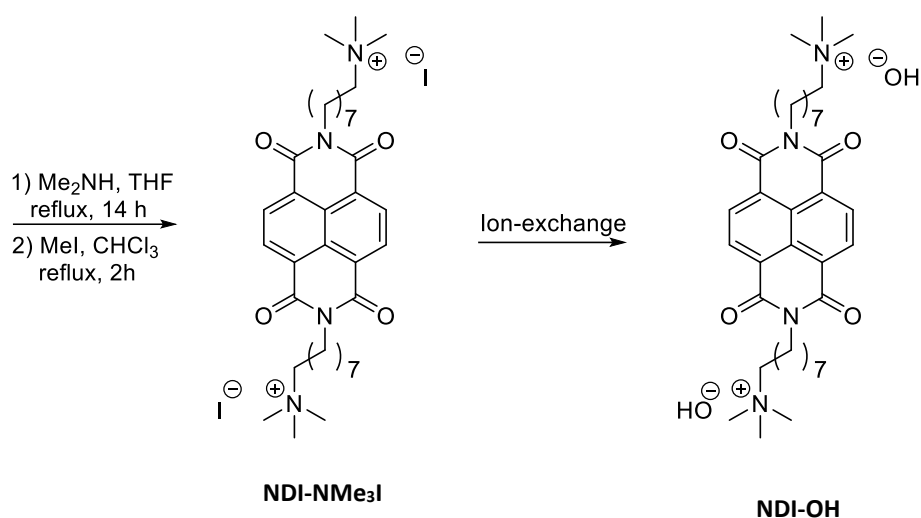
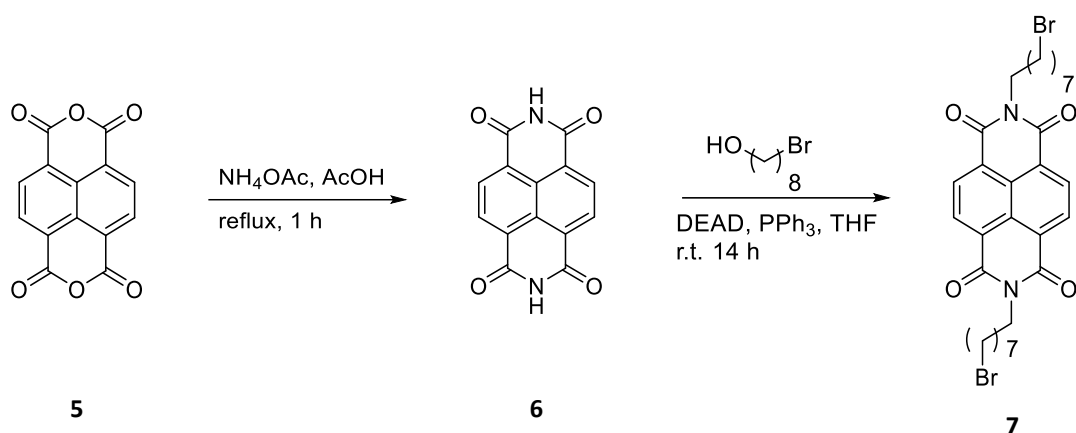
In all studies concerning self-doping n-type semiconductors of this nature few possible mechanisms of doping have actually been studied in detail. Further to this there is a lack of structural characterisation of the aqueous dopant precursors. In order to further elucidate the chemical pathways through which quaternary amines act as n-type dopants to bound rylene diimides, we synthesised a naphthalene diimide (NDI) derivative with sidechains terminated with quaternary amine groups. The dopant precursor with iodide counterion N,N'-bis(8-(trimethylammoniumiodide)octylene)-1,4,5,8-naphthalenetetracarboxylic diimide (NDI-NMe<sub>3</sub>I) and the aqueous stable N,N'-bis(8-(trimethylammoniumhydroxide)octylene)-1,4,5,8-naphthalenetetracarboxylic diimide (NDI-OH) are shown in Figure 2.1. Using an NDI aromatic core reduces the conjugation length when compared to PDI, with the intent that solubility would be increased and making solution spectroscopic characterisation less complicated to analyse.

A combination of NMR and infra-red spectroscopies, as well as mass-spectrometry, have been used to confirm the structure of the dopant precursor for the first time as well as analyse the product of doping upon drying. In combination with this UV-vis spectroscopy, cyclic voltammetry (CV), Van der Pauw conductivity measurements, atomic force microscopy (AFM) and X-ray fluorescence spectroscopy (XRF) have been used to help probe both the mechanism and efficiency of intramolecular charge transfer.

## 2.2 Results and Discussion

### 2.2.1 Synthesis

The synthetic route to NDI-OH is shown in Scheme 2.2. Naphthalenetetracarboxylic dianhydride (5) was reacted with ammonium acetate to give naphthalenetetracarboxylic diimide (6). A Mitsunobu type reaction with 8-bromo-1-octanol was then used to obtain compound 7. A  $S_N2$  substitution of bromide using dimethylamine and subsequent methylation with iodomethane to give NDI-NMe<sub>3</sub>I was carried out in one-pot because of the instability of 8. NDI-NMe<sub>3</sub>I was then dissolved in de-ionised water and eluted slowly through a column of ion-exchange resin (DOWEX Monosphere 550a) to give aqueous solutions of NDI-OH. Several NDI-OH solutions were made of concentrations between 1 and 5 mg/mL. The overall multistep reaction yield in going from 5 to NDI-Me<sub>3</sub>I was 7 %.

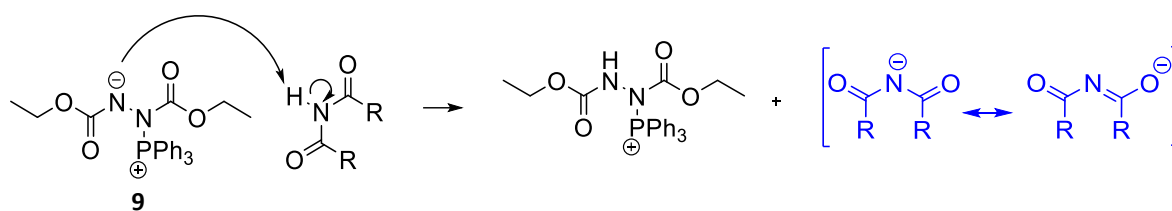


**Scheme 2.2. Top:** Synthetic route used to obtain NDI-OH. **Bottom:** One-pot procedure for the synthesis of NDI-NMe<sub>3</sub>I including the tertiary amine intermediate.

The Mitsunobu reaction of 6 to give compound 7 gave the lowest yield of 21%. Normally N-alkylated NDI cores are obtained through a condensation reaction of 5 with primary alkylamine, however the (dimethylamino)alkylamines previously used in the synthesis of PDI-OH are no longer widely commercially available.<sup>173, 174</sup> Mitsunobu reactions between fused

thiophene derivatives of NDIs and alcohols have previously been successful as a way of avoiding the use of expensive amines and was applied here.<sup>236</sup> Previously NDI derivatives used as Mitsunobu reagents were functionalised on the aromatic core with alkyl-silane groups, which were reported to increase solubility and yield of the di-alkylated product. The low yield of Mitsunobu reaction to obtain 7 may be explained by the poor solubility of 6. At the conclusion of the reaction there was a significant amount of undissolved starting material and the insolubility of 6 has previously been claimed to hamper Mitsunobu macrocyclizations.<sup>237</sup>

The  $pK_a$  of substrates in Mitsunobu reactions has previously been said to be important. Scheme 2.3 shows the betaine intermediate, 9, generated from mixtures of diethylazodicarboxylate (DEAD) and triphenylphosphine (PPh<sub>3</sub>) in Mitsunobu reactions. The use of nucleophiles which are too basic ( $pK_a > 11$ ) often leads to no reaction or low yields due to the need for the nucleophile to be deprotonated by 9 ( $pK_a = 13$ ).<sup>238</sup> The  $pK_a$  of phthalimide is quoted as 8.7 and therefore the deprotonation of 6 should not be a problem. Alternately poor yields may be caused by side reactions. The resonance of deprotonated 6 is highlighted in blue in Scheme 2.3; the oxygen anion contribution to this resonance may be capable of acting as an unintended nucleophile later in the reaction to give 11. There is however no conclusive evidence for this in analysis of separated impurities. <sup>1</sup>H NMR analysis of crude material and side products separated by chromatography showed two doublets at 8.65 and 8.17 ppm, an example of which is shown in Figure 2.2. A possible explanation for this is mono substitution on to the naphthalene ring to give 12 although this seems unlikely. Halogenated derivatives of 6 are well known to be targets for nucleophilic attack in  $S_NAr$  reactions,<sup>162, 239, 240</sup> however no such halogens are present here to act as a leaving group. It seems more likely that these signals arise due to a mixture of di-alkylated product 7 (singlet  $\delta = 8.75$  ppm) and mono alkylated impurity 10 (doublets,  $\delta = 8.65$  and 8.17 ppm).



**Scheme 2.3.** Part of the mechanism of Mitsunobu reactions using imides showing deprotonation of imide nitrogen by betaine intermediate and the resulting resonance stabilised anion capable of undergoing alkylation on nitrogen or oxygen.

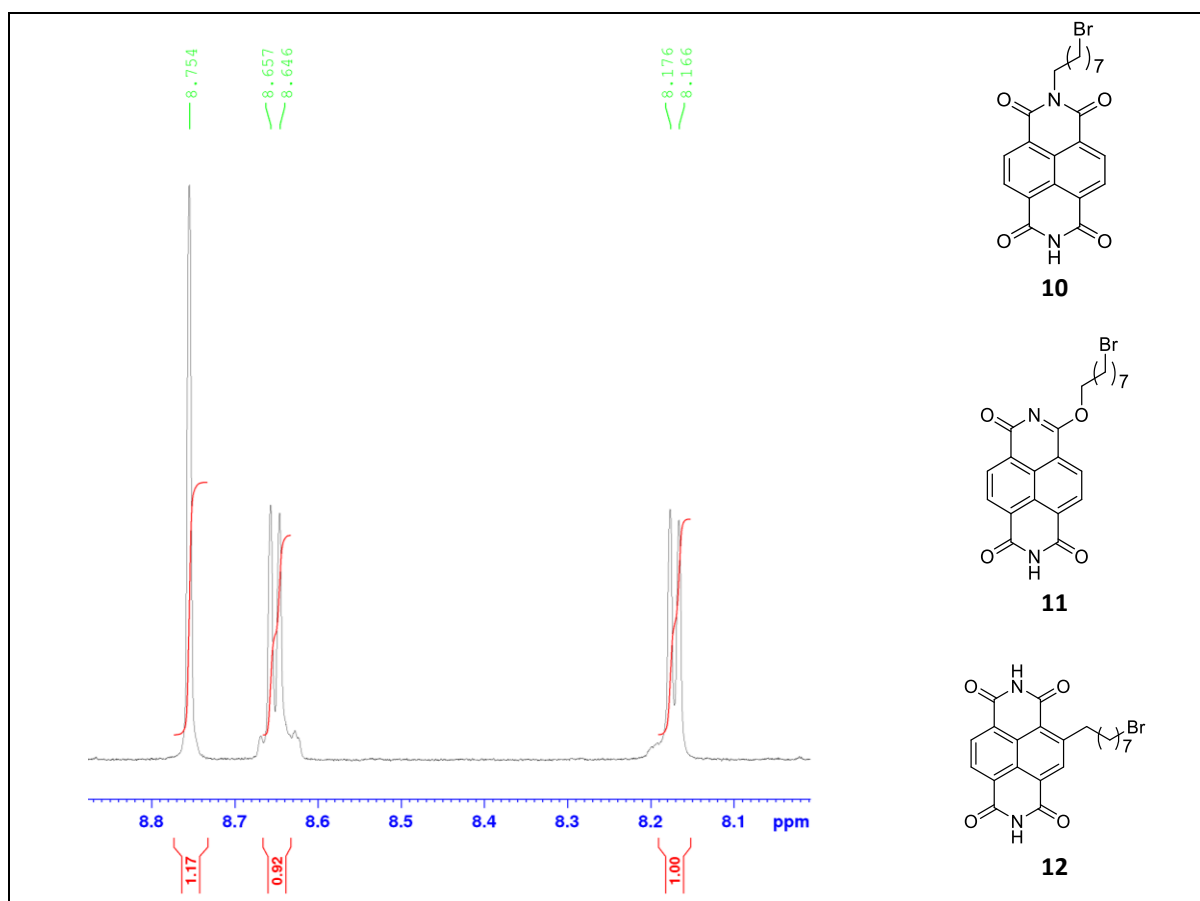


**Figure 2.2.** Left: Section of  $^1\text{H}$  NMR of impurity from the separation of crude reaction mixture from to form 7. Right: Structures of possible impurities and side products from reaction.

An unknown in previous studies was the chemical structure of the product of counter ion exchange. In order to confirm the structure of the self-doping NDI-OH we thought it necessary to perform NMR spectroscopy and mass spectrometry of the ion exchanged product in solution. Solution NMR analysis would need to be performed in deuterated solvent and a procedure for running the ion-exchange column in deuterium oxide is described in the experimental section for NDI-OH. It should be noted that NDI-NMe<sub>3</sub>I was not fully soluble in water or deuterium oxide alone and mixtures of polar organic solvent and water were required to solubilise for the ion-exchange procedure. Organic solvents were later removed

from the NDI-OH solution in vacuo. Subsequent structural analysis of NDI-OH in this solution suggests that the ion-exchange procedure is not 100% efficient.

Figure 2.3 shows sections of the  $^1\text{H}$  NMR spectra of NDI-NMe<sub>3</sub>I and NDI-OH. A singlet, corresponding to the four equivalent aromatic protons normally observed in symmetrical NDI compounds, was seen in NDI-NMe<sub>3</sub>I but not for NDI-OH. Instead doublets are observed at 8.59, 8.57, 7.95 and 7.92 ppm. These four peaks could be treated as two doublets of doublets, however this assignment was ruled out due the requirement for each proton on the aromatic core to be spin-coupled to two inequivalent protons. Other than the proton on the adjacent carbon the nearest proton to H<sub>a</sub> and H<sub>b</sub> are five bonds away and coupling is not observed in 2D  $^1\text{H}$ - $^1\text{H}$  correlation spectroscopy (COSY) between aromatic protons and any other proton (appendix 1.8). The splitting of these peaks into doublets therefore suggests that the chemical environments of the protons on the naphthalene unit are no longer equivalent and symmetry has been lost in the molecule.

As well as the aromatic protons, the protons of the two alkyl chains in NDI-OH seem to exhibit an inequivalence. Signals in the spectrum for NDI-NMe<sub>3</sub>I at 4.04 ppm and 3.27 ppm correspond to hydrogens one and two carbons away from imide nitrogen, respectively. The same signals are observed in NDI-OH, however two more signals are observed at 3.40 ppm and 3.30 ppm with the same integration values and splitting patterns. Again, this indicates a lack of symmetry in the two alkyl chains. Two separate singlets with integrations of 9 each at 3.09 ppm and 3.08 ppm are also observed for the methyl protons of the quaternary ammonium groups.

Initially it was assumed that the ion-exchange process was only 50% efficient, leaving one -NMe<sub>3</sub>I headgroup and one -NMe<sub>3</sub>OH headgroup. It seemed unlikely however that a change in counterion on quaternary amine groups 8 carbons away from the aromatic core would lead to such a pronounced loss in the equivalency of the aromatic proton signals. This also did not explain the small cluster of impurity signals between 7.77 and 7.72 ppm outlined in the inset of Figure 2.3. In addition to this the two singlets at 3.10 and 3.09 ppm, for quaternary ammonium methyl hydrogens, in the NDI-OH spectrum are down-shifted compared to NDI-NMe<sub>3</sub>I. This was expected due to the increased electronegativity of the hydroxide counterion compared to iodide. Upon film formation in section 2.2.3 a yellowing of the films was observed which was also attributed to left over iodine in the films. This prompted us to run



X-ray fluorescence (XRF) spectroscopy on films, the results of which are summarised in Table 2.1. Iodine was not detected at levels above 1 ppm and it was concluded that all iodide had been exchanged in the column.

**Table 2.1.** XRF analysis for elemental contents, in weight %, of thin-films of NDI-OH drop-cast from aqueous solutions of NDI-OH. Measurement also includes the composition of glass substrate.

Drop-cast 45 °C		Drop-cast 75 °C		Drop-cast 85 °C		Drop-cast 125 °C	
Element	Weight %	Element	Weight %	Element	Weight %	Element	Weight %
Na	0.69%	Na	0.86%	Na	0.45%	Na	0.98%
Mg	1.03%	Mg	1.09%	Mg	0.81%	Mg	1.29%
Al	0.0 ppm	Al	0.0 ppm	Al	0.51%	Al	0.0 ppm
Si	54.60%	Si	55.44%	Si	48.92%	Si	46.24%
P	2.17%	P	1.89%	P	1.39%	P	1.40%
S	0.39%	S	0.39%	S	0.42%	S	0.44%
Cl	0.35%	Cl	0.39%	Cl	6.73%	Cl	0.47%
K	4.68%	K	4.64%	K	4.72%	K	5.47%
Ca	33.86%	Ca	33.14%	Ca	33.56%	Ca	40.55%
Ti	0.13%	Ti	0.12%	Ti	0.12%	Ti	0.14%
Cr	40.5 ppm	Cr	39.1 ppm	Cr	16.5 ppm	Cr	22.2 ppm
Mn	228.0 ppm	Mn	222.5 ppm	Mn	628.0 ppm	Mn	596.1 ppm
Fe	0.18%	Fe	0.17%	Fe	0.17%	Fe	0.22%
Ni	203.5 ppm	Ni	228.4 ppm	Co	104.1 ppm	Co	24.3 ppm
Zn	0.0 ppm	Zn	0.0 ppm	Ni	0.19%	Ni	0.22%
As	1.37%	As	1.34%	Zn	0.0 ppm	Zn	0.0 ppm
Rb	389.4 ppm	Rb	379.8 ppm	As	1.38%	As	1.80%
Sr	396.0 ppm	Sr	388.7 ppm	Rb	392.5 ppm	Rb	520.9 ppm
Y	22.1 ppm	Y	19.5 ppm	Sr	400.6 ppm	Sr	530.4 ppm
Zr	0.19%	Zr	0.19%	Y	21.1 ppm	Y	26.5 ppm
Rh	0.0 ppm	Rh	0.0 ppm	Zr	0.19%	Zr	0.26%
Sn	544.2 ppm	Sn	527.6 ppm	Sn	533.8 ppm	Sn	687.0 ppm
Sb	156.9 ppm	Sb	161.1 ppm	Sb	139.3 ppm	Sb	185.4 ppm
Te	453.1 ppm	Te	435.5 ppm	Te	448.3 ppm	Te	562.5 ppm
Ba	935.5 ppm	Ba	912.9 ppm	Ba	915.5 ppm	Ba	0.12%
Ce	224.1 ppm	Ce	177.7 ppm	Ce	288.0 ppm	Ce	52.9 ppm
Eu	0.0 ppm	Eu	0.0 ppm	Eu	0.0 ppm	Eu	16.4 ppm
Yb	1.1 ppm	Yb	0.0 ppm	Er	490.5 ppm	Er	610.4 ppm
Re	112.8 ppm	Re	96.7 ppm	Re	98.2 ppm	Re	129.8 ppm

It has been reported that the imide groups of the rylene diimide ring systems are susceptible to ring-opening through hydrolysis in the presence of aqueous base.<sup>241, 242</sup> The ion-exchange procedure which NDI-NMe<sub>3</sub>I was subjected to involved a high concentration of hydroxyl anions, from the ion-exchange resin, and took place in an aqueous solution. It was therefore hypothesised that NDI-OH in an aqueous solution was not actually a ring-closed naphthalene

diimide species but a mixture of ring-opened products of base catalysed hydrolysis. This ring-opening is outlined in Figure 2.3.

The NMR spectrum of NDI-OH in Figure 2.3 strongly resembles that of spectra from previous literature in which naphthalene diimide derivatives were exposed to pH 9 buffer solution.<sup>241</sup> The four doublets at 8.59, 8.57, 7.95 and 7.92 ppm were assigned as the mono-hydrolysed product 13. The signals between 7.77 and 7.72 ppm were assigned as the two di-hydrolysed products 14 and 15. The *anti*-product, 14, gives rise to an AB quartet and then two singlets at 7.76 and 7.72 ppm are assigned to the *syn*-product, 15. In comparison to the ring-closed diimide NDI-NMe<sub>3</sub>I all three of the hydrolysed products exhibit upshifted aromatic signals due to the decrease in aromatic conjugation length and subsequent electron shielding.

Mass spectrometry, shown in Figure 2.4, was then used to confirm the hydrolysis of the imide moieties. The peak at 623 *m/z* corresponds to the mono-hydrolysed ring-opened NDI-OH. The major peak at 312 *m/z* is for the doubly charged ion of the same structure. We assume that the carboxylate anions in structures 13, 14 and 15 remain deprotonated as the conjugate acids are likely to have a lower *pK<sub>a</sub>* than water (*pK<sub>a</sub>* = 15.7).

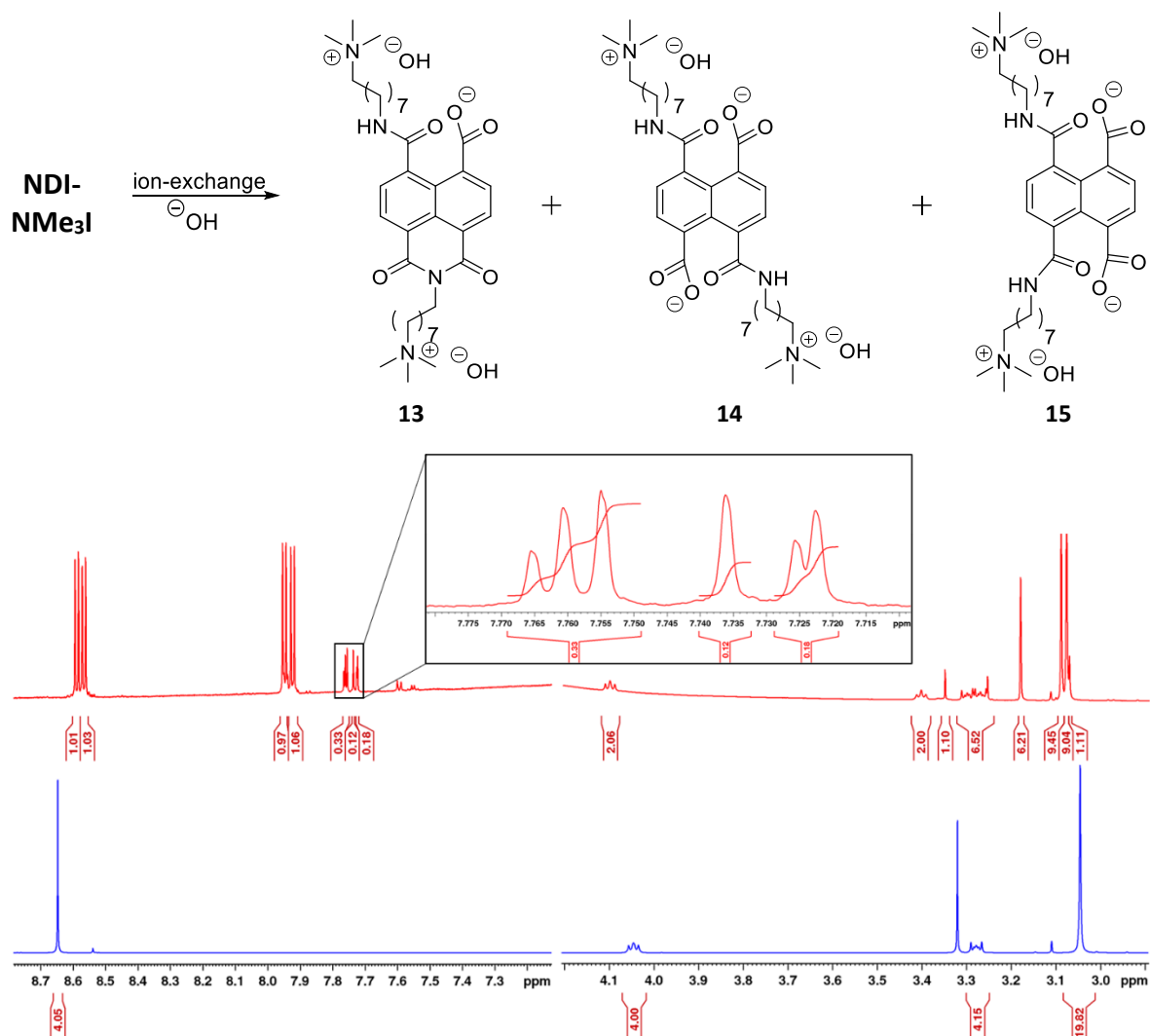


**Figure 2.3.** Scheme showing the mixture of products from hydrolysis of NDI-NMe<sub>3</sub>l under the basic conditions of the ion-exchange column. Bottom shows the <sup>1</sup>H NMR spectra of NDI-NMe<sub>3</sub>l (bottom) and the mixture of products from ion-exchange under aqueous basic conditions.

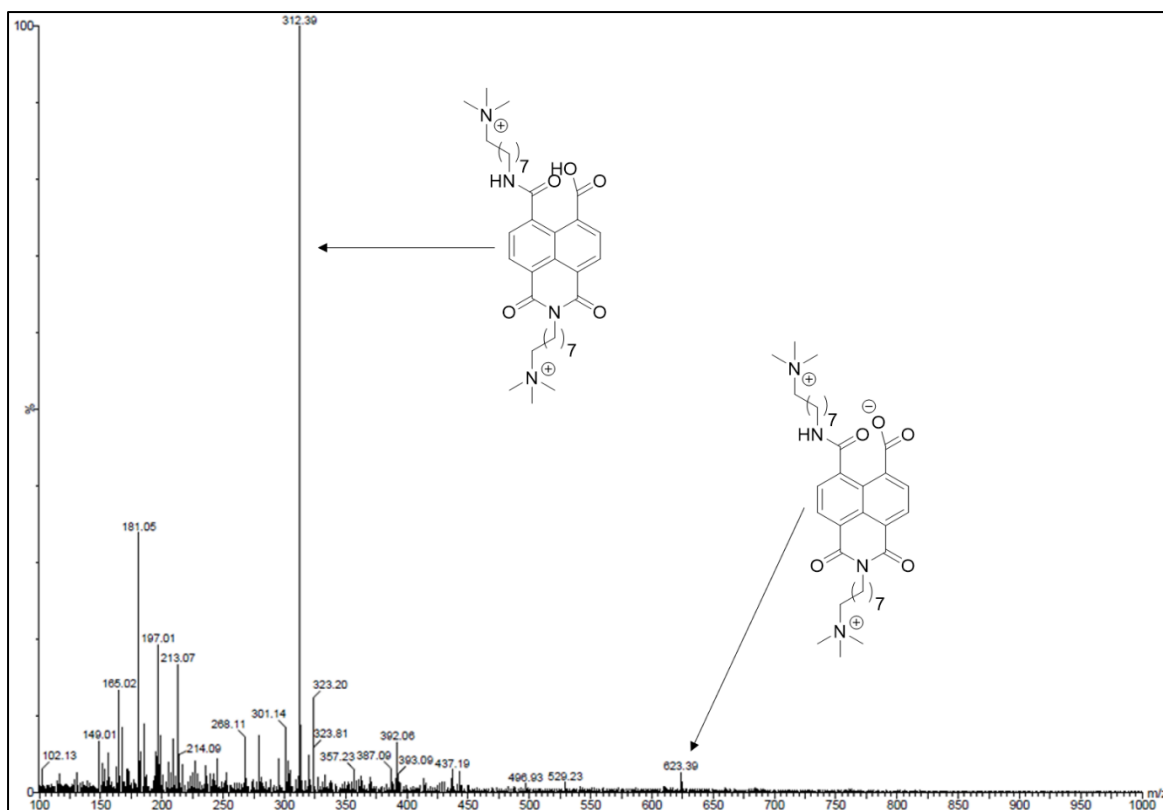


**Figure 2.4.** Mass spectrum of hydrolysed NDI-OH.

In addition, the base catalysed hydrolysis can be tracked through the UV-vis absorption spectra. Figure 2.5 shows a comparison between the solution absorption spectra of NDI-NMe<sub>3</sub>I and NDI-OH. The spectrum of NDI-NMe<sub>3</sub>I closely matches previous naphthalene diimide derivatives with two absorption maxima at 361 and 381 nm.<sup>241, 243</sup> For NDI-OH a single absorption band with a small shoulder is observed with maxima at 350 nm. Similar absorption spectra have been observed for 1,8-naphthalamides<sup>244</sup> and have previously been assigned as mono-hydrolysed products when naphthalenediimides are treated with aqueous base.<sup>241</sup> A possible explanation for the blue-shifted absorption is the decreased conjugation length in the ring-opened hydrolysed compounds which destabilises the LUMO and increases the band-gap.

Solution absorption spectra of NDI-OH at elevated temperatures up to 99 °C are also shown in Figure 2.5. The single broad absorption band at 350 nm shows a growth in two maxima at 362 and 382 nm as the temperature of solution is increased. The red-shifting in this absorption maxima indicates the presence of NDI type ring systems, similar to those observed in NDI-NMe<sub>3</sub>I. A less intense absorption band (278 – 315 nm) is also seen to appear at higher temperatures; this could be attributed to H-aggregation or a band in a similar range has

previously been attributed to di-hydrolysed products like 14 and 15.<sup>241</sup> A return to absorption features similar to NDI-NMe<sub>3</sub>I indicates that the hydrolysis is reversible. The consequences of this reversal on the mechanism of doping are discussed later in this chapter.

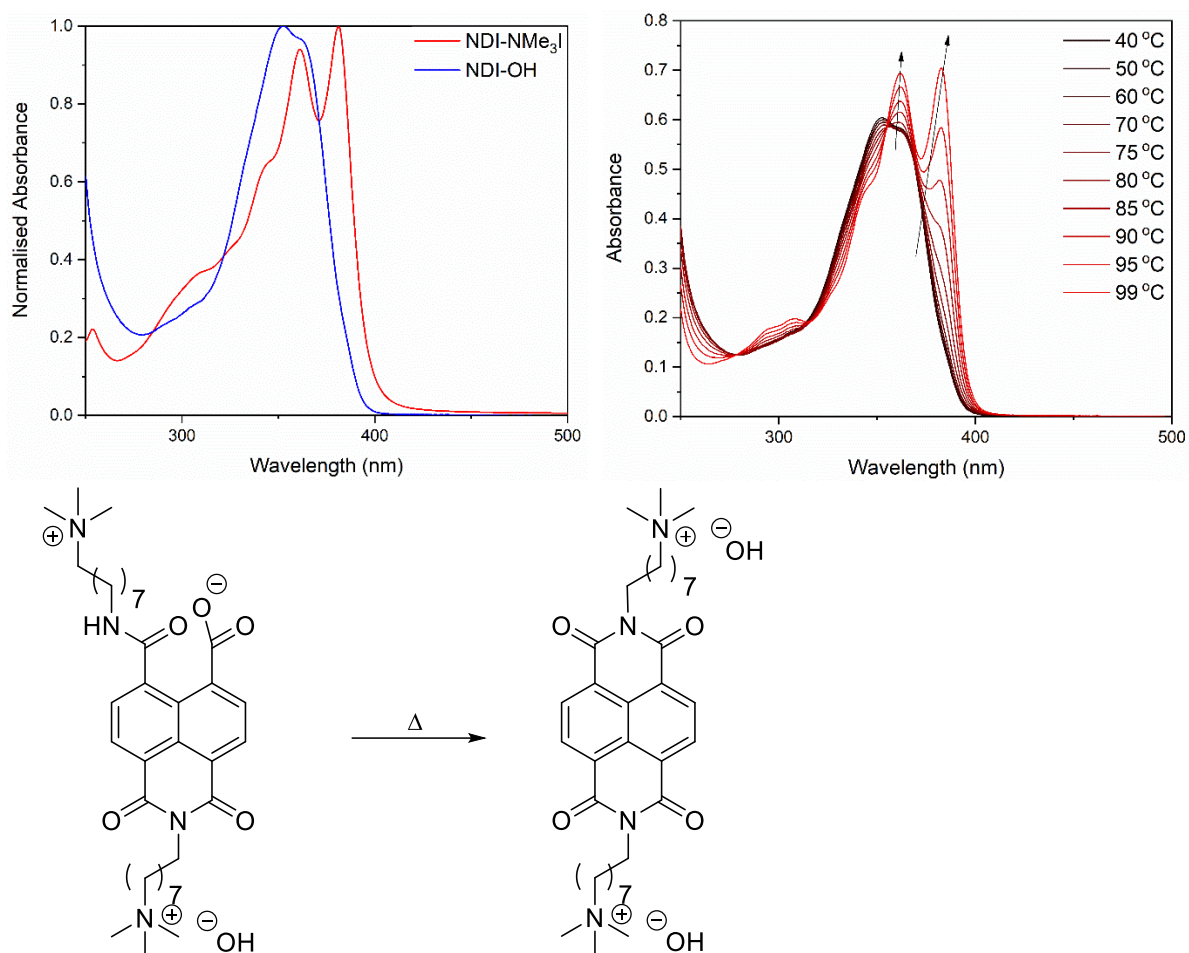


**Figure 2.5.** **Top left:** Solution UV-vis absorption spectra of NDI-NMe<sub>3</sub>I in DMSO and NDI-OH in water after ion-exchange. **Top right:** Solution UV-vis absorption spectra of NDI-OH in water after ion-exchange recorded at temperatures between 40 and 99 °C. **Bottom:** Scheme showing the possible reversibility of NDI-OH hydrolysis upon heating.

As a result of the above analysis of an aqueous solution of NDI-OH, it was determined that the major product of ion-exchange was the mono-hydrolysed naphthalene imide, 13. Two minor di-hydrolysed products, 14 and 15, were also seen by NMR. The likely cause of this mixture of materials was a large excess of hydroxyl anions in aqueous media during anion exchange. These basic conditions are known to cause ring-opening hydrolysis of naphthalene diimides. Any reference to NDI-OH from here on refers to the mixture of compounds 13, 14 and 15.

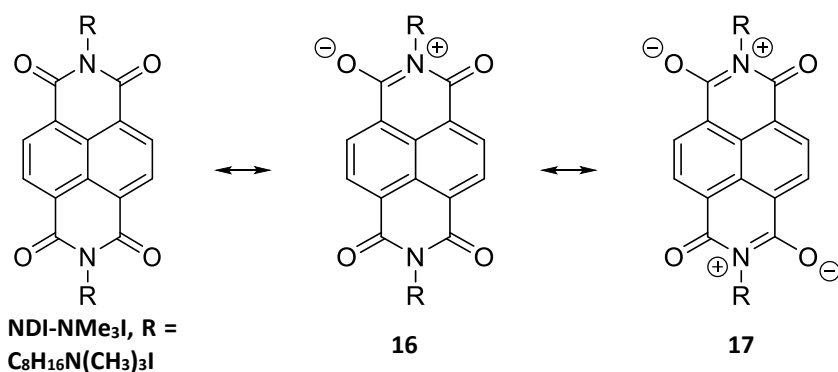
Previous examples of self-doping PDI species which were subjected to hydroxy form ion-exchange or highly basic conditions were never structurally characterised.<sup>171-174</sup> Solution UV-

vis absorption spectra of these compounds did exhibit a similar featureless and blue-shifted absorption band when compared to PDI precursors.<sup>174</sup> It is possible therefore that the actual structures of these compounds were the products of hydrolysis analogous to 13, 14, and 15.

### 2.2.2 Optoelectronic properties of NDI-OH

Having determined the structure of NDI-OH, its optoelectronic properties were measured and compared to those of NDI-NMe<sub>3</sub>I. The mixture of products obtained from hydrolysis, outlined above, may have complicated these measurements. The results, however, provide some context for the studying of their intrinsic doping.

First the LUMO energy levels of NDI-NMe<sub>3</sub>I and NDI-OH in solution were established electrochemically. Figure 2.6 shows the cyclic voltammograms of NDI-NMe<sub>3</sub>I in acetonitrile and NDI-OH in an aqueous solution referenced to the potential of an Ag/Ag<sup>+</sup> electrode. NDI-NMe<sub>3</sub>I shows a fully reversible reduction with anodic peak potential ( $E_{pa}$ ) = -0.95 V. A reduction peak for NDI-OH is observed which exhibits quasi-reversibility and  $E_{pa}$  = -1.03 V. From the onsets of reduction ( $E_{onset}$ ) LUMO values for NDI-NMe<sub>3</sub>I and NDI-OH of -3.97 eV and -3.89 eV were estimated respectively, according to the equations outlined in the experimental section 6.1. This reduction in electron affinity by 0.08 eV is likely due to the loss of a conjugated imide ring in 13 when compared to NDI-NMe<sub>3</sub>I. The resonance structures 16 and 17 in Scheme 2.4 likely contribute to the first excited state in full NDI ring-systems and the loss of one imide ring group in 13 decreases the stabilisation this gives to an occupied LUMO.<sup>243</sup>



**Scheme 2.4.** Contributing resonance structures to NDI derivatives.

The UV-Vis absorption spectrum for NDI-OH in aqueous solution can be seen in Figure 2.6. From an onset of absorption ( $\lambda_{\text{onset}}$ ) estimated to be 385 nm a corresponding optical bandgap of 3.22 eV was calculated for NDI-OH. A  $\lambda_{\text{onset}}$  of 400 nm leads to an estimated optical band gap of 3.11 eV for NDI-NMe<sub>3</sub>I. Taking the bandgap away from the electrochemically calculated LUMO gives an estimated HOMO of -7.02 eV for NDI-OH and -6.99 eV for NDI-NMe<sub>3</sub>I. All of these results are summarised in Table 2.2. It was assumed that energy level values for NDI-OH were actually a measurement of the majority product 13.

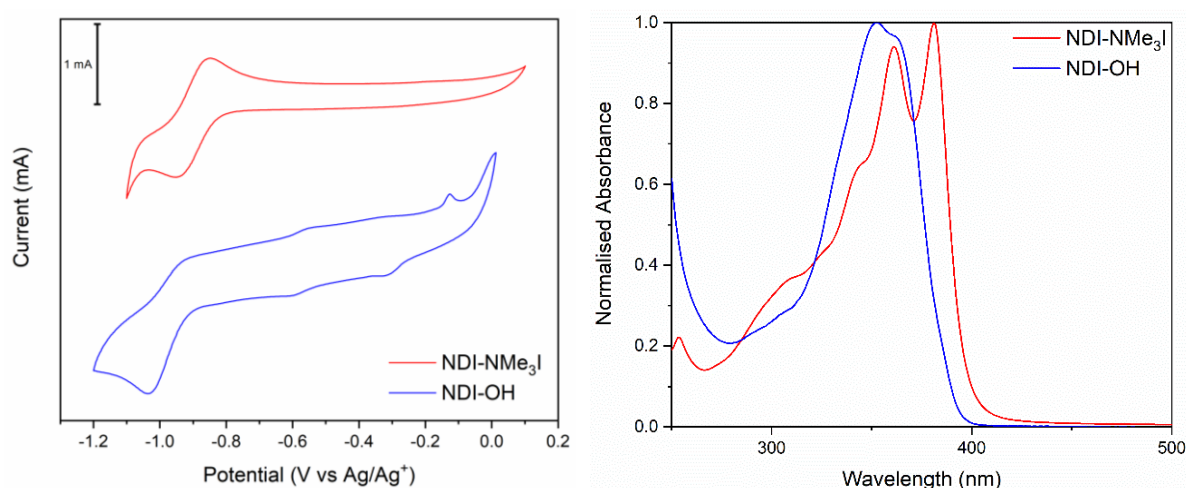


**Figure 2.6.** Left: Cyclic voltammograms of NDI-NMe<sub>3</sub>I and NDI-OH run in solutions of acetonitrile and water, respectively. Referenced to Ag/Ag<sup>+</sup> electrode with platinum wire as counter electrode and glassy carbon working electrode. Right: UV-vis absorption spectrum of NDI-OH in aqueous solution.

Table 2.2. Electrochemical and optical properties of NDI-NMe <sub>3</sub> I and NDI-OH							
Compound	$E_{\text{pa}}$ [a] (V)	$E_{\text{onset}}$ [a] (V)	$\lambda_{\text{max}}$ (nm)	$\lambda_{\text{onset}}$ (nm)	Optical band gap [d] (eV)	LUMO [e] (eV)	HOMO [f] (eV)
NDI-NMe <sub>3</sub> I	-0.95	-0.83	381 and 361 [b]	400 [b]	3.11	-3.88	-6.99
NDI-OH	-1.03	-0.91	350 [c]	385 [c]	3.22	-3.80	-7.02

[a] From solution cyclic voltammetry using glassy carbon working electrode, platinum wire counter electrode and Ag/Ag<sup>+</sup> reference electrode. Values are reported from the 4<sup>th</sup> cycle and measured at 100 mV.s<sup>-1</sup>. [b] From solution UV-vis absorption spectroscopy in DMSO. [c] From solution UV-vis absorption spectroscopy in water. [d] Estimated from  $\lambda_{\text{onset}}$ . [e] Estimated from electrochemical onset of reduction ( $E_{\text{onset}}$ ). [f] Estimated using equation HOMO = LUMO – Optical band gap.

### 2.2.3 Absorption Spectra of NDI-OH Solution and Thin-films

In previous studies of quaternary amine dopants bound to diimide species, films have been formed by both spin-coating<sup>172</sup> and drop-casting.<sup>173, 174</sup> In either case annealing at high

temperatures of 120 °C was carried out and it was claimed that it was this process which triggered doping and the formation of charge carriers. Further to this it was possible that the process of heating caused the reverse hydrolysis reaction observed in the absorption spectra of Figure 2.5.

Absorption spectroscopy was used to confirm the presence of radical type charge carriers occupying sub-band-gap energy levels caused by doping. Initially the aqueous solution of NDI-OH was drop-cast on to glass slides at 85 °C and annealed at this temperature for 30 min. The absorption spectrum for the annealed thin film, in Figure 2.7, shows one absorption feature at 359 nm as well as an additional band with maxima at 458 nm. The band with  $\lambda_{\text{max}} = 458$  nm is consistent with NDI radical anions previously generated both electrochemically and by chemical doping.<sup>165, 170</sup>

In an effort to observe doping in solid-state NDI-OH without heightened temperatures, the aqueous solution was freeze dried. The freeze-dried solid was then re-dissolved in water and UV-vis absorption was measured. It can be seen in Figure 2.7 that the absorption band at 458 nm is still observed in freeze dried NDI-OH suggesting the presence of radical anions; it is much less intense, however, than in the annealed thin film. The solution absorption spectrum of NDI-OH is also shown in Figure 2.7 for reference.



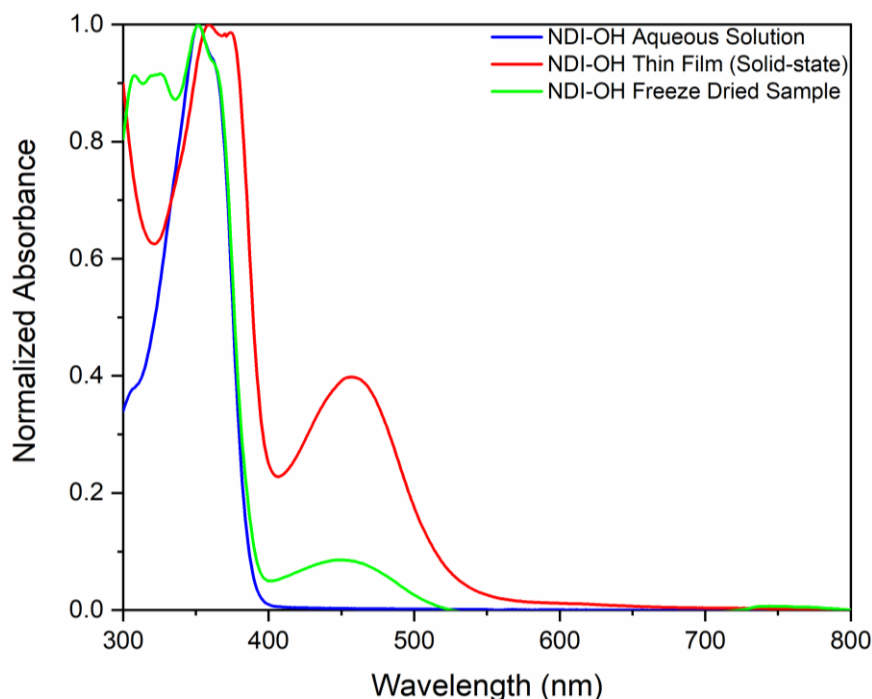


**Figure 2.7.** UV-vis absorption spectra of NDI-OH aqueous solution (blue), drop cast thin film (red) and an aqueous solution of a freeze-dried sample (green).

Having observed evidence of doping in absorption spectra of drop-cast and annealed films but less so in freeze-dried NDI-OH, we formed films of NDI-OH by drop-casting at different temperatures. Glass slides were heated to temperatures between 45 °C and 125 °C and 5 mg/mL solutions of NDI-OH were drop-cast on to each and annealed at the given temperature for 30 minutes in air. Figure 2.8 shows the UV-vis absorption spectra of the films obtained at each temperature. At the lower temperatures only the NDI  $\pi$ - $\pi^*$  absorption band at 350 nm is observed. At drop-casting temperatures of 75 °C the higher wavelength absorption at 458 nm is observed. On increasing the temperature further, the absorbance maxima of the radical anion band increases and the  $\pi$ - $\pi^*$  transition decreases. At 125 °C only the radical anion band remains.

The pictures of the slides on the bottom of Figure 2.8 show a drastic change in colour. The undoped NDI-OH aqueous solution is colourless whereas films are yellow. A deepening of the yellow colour is observed at higher drop-casting temperatures consistent with an absorbance of 458 nm light. There is evidence of the coffee-ring effect for each drop-cast film. A darkening of colour is observed on the edges of the substrate where the rate of evaporation is highest

and dissolved solid from the interior has flowed to the edge to replace it, this leaves a higher concentration of material on the edge of the drop-cast film.<sup>245</sup>

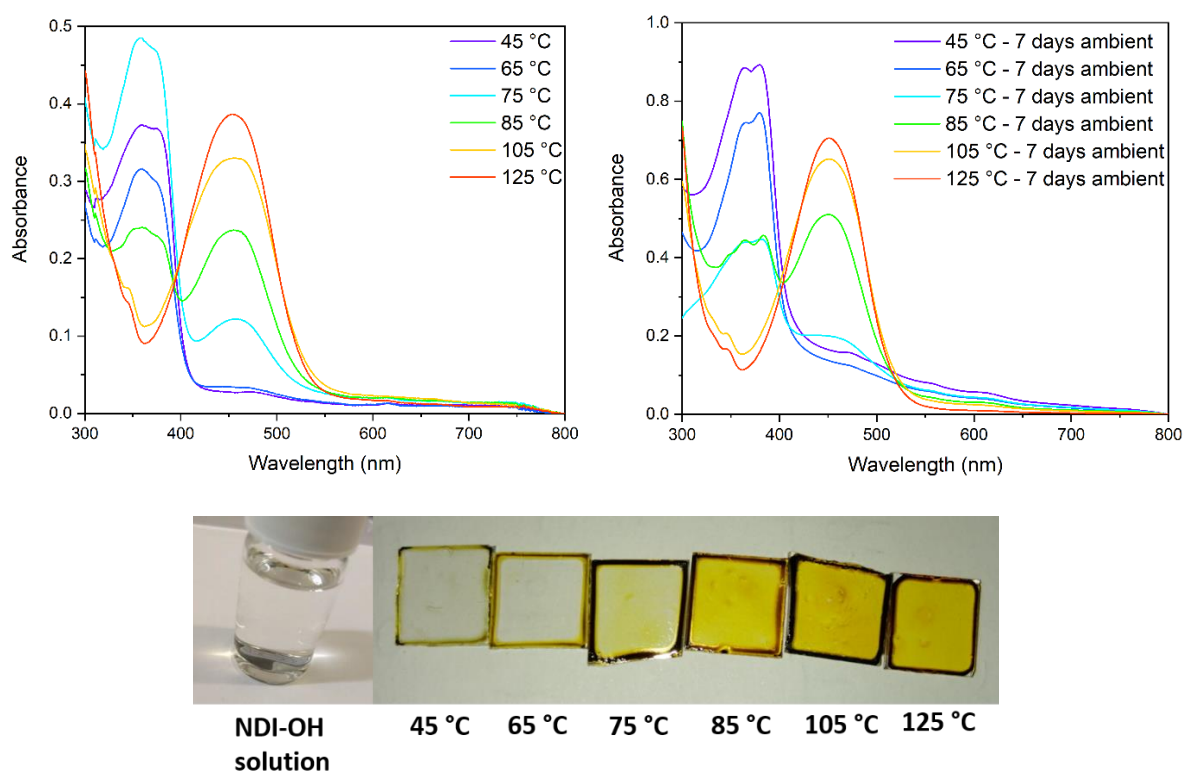


**Figure 2.8.** **Top Left:** UV-vis absorption spectra of NDI-OH thin films formed by drop-casting and annealing at temperatures between 45 °C and 125 °C. **Top Right:** UV-vis absorption spectra of NDI-OH thin films after 7 days left under ambient conditions. **Bottom:** Pictures of films drop-cast at different temperatures with colourless NDI-OH aqueous solution for comparison.

It is widely believed that semiconductors carrying a negative charge require a LUMO level of less than  $-4.0$  eV in order to avoid oxidation by ambient oxygen.<sup>246, 247</sup> This has been shown to be the case in NDI radical anions, which are notoriously difficult to stabilise. In fact, stabilisation has only effectively been achieved by substitution of highly electron withdrawing groups directly on to the aromatic core.<sup>232, 247-249</sup> Figure 2.8 also shows the UV-vis of NDI-OH films drop-cast and annealed at various temperatures after 7 days left in ambient conditions. The stability of the NDI radical anion band at 458 nm was surprising given the LUMO level of  $-3.80$  eV from electrochemical characterisation of NDI-OH.

Previous experiments on PDI-OH type self-dopants involved film-formation at lower temperatures, either by spin-coating or mild temperature drop-casting, and subsequent annealing of the film at 120 °C.<sup>172-174</sup> It is claimed that the high temperature annealing step initiates the formation of charge carriers. In order to confirm that our NDI-OH system is

comparable to PDI-OH, films formed at 45 °C were annealed at 85 °C and 125 °C for 30 minutes. As a control, a film formed at 125 °C was also annealed for a further 30 minutes at 125 °C. UV-vis absorption spectra of both films subjected to 125 °C annealing are compared in Figure 2.9.

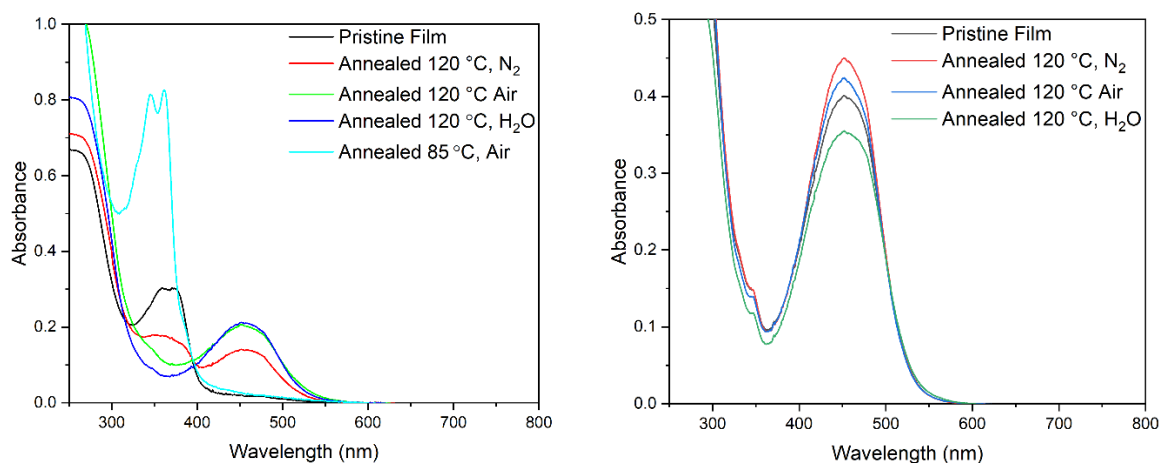


**Figure 2.9. Left:** UV-vis absorption spectra of the thin film formed by drop-casting at 45 °C then annealed at 85 °C in air for 30 minutes and annealed at 125 °C for 30 minutes under various atmospheric conditions. **Right:** UV-vis absorption spectra of the thin film formed by drop-casting at 125 °C then annealed at 125 °C for 30 minutes under various atmospheric conditions.

Annealing of the 45 °C film at 125 °C in air does lead to a full quenching of the  $\pi$ - $\pi^*$  absorption at 358 nm and a rise in the radical anion like absorption at 458 nm. No real change is observed between the unannealed and annealed samples when the annealing temperature was 85 °C. This first indicates that a similar activation energy to doping in the solid-state is required in NDI-OH when compared to PDI-OH. By comparing these results to the film formed by drop-casting at 85 °C in Figure 2.8, it can also be seen the barrier to doping is much lower in solution. By heating the solution to 85 °C and forming a film in this way, radical anion absorptions are observed. When annealing a film formed at low temperatures at 85 °C no radical anion is observed by absorption.

Previously films of PDI-OH exposed to high humidity atmospheres have exhibited a slow reduction in higher wavelength absorptions.<sup>172</sup> It was claimed that the presence of water was detrimental to doping and that doped films were stable in dry air. It has already been shown in Figure 2.8 that films of NDI-OH were stable to atmospheric water for 7 days. To confirm atmospheric conditions were not having a detrimental effect on the initial doping of NDI-OH however, annealing of films drop-cast at 45 °C was also carried out under nitrogen and under high humidity at 120 °C for 30 minutes. Absorption spectra for these annealed films

is also shown in Figure 2.9. High humidity was achieved by placing a vial of water in the same closed container as the annealing films. Under an inert atmosphere of nitrogen, the absorption band at 458 nm is seen to be less intense than when annealed in air. This suggests that the extent of radical anion formation was less than when annealed in air and that the doping mechanism is reliant on either water or oxygen. The presence of additional atmospheric water under high humidity atmospheres made no significant change in the absorption features when compared to annealing in air. By comparison, the film formed at 120 °C showed no significant changes in absorption features when heating under any atmosphere. Both this, and the stability of films observed in Figure 2.8, contradict previous PDI-OH absorption measurements.<sup>172</sup> Similarly to PDI-OH, doping can occur in both solution and in the solid-state, however the barrier to electron transfer is higher in the solid state.

#### *2.2.4 Structure of Dehydrated NDI-OH*

Although absorption spectra seem to indicate the presence of NDI radical anions when films are formed at high temperatures, it seems unlikely that they are capable of remaining inert to oxygen for extended periods of time without if they are NDI type radical species. In addition to this the role of the terminal quaternary ammonium groups in the mechanism of doping is still not fully understood.<sup>174, 233-235</sup> There are still further unknowns such as how the products of trimethylammonium hydroxide group breakdown will interact with the products of NDI-OH hydrolysis and if the hydrolysed products undergo the reverse reaction back to the imide. Finally, the active doping species needs to be identified.

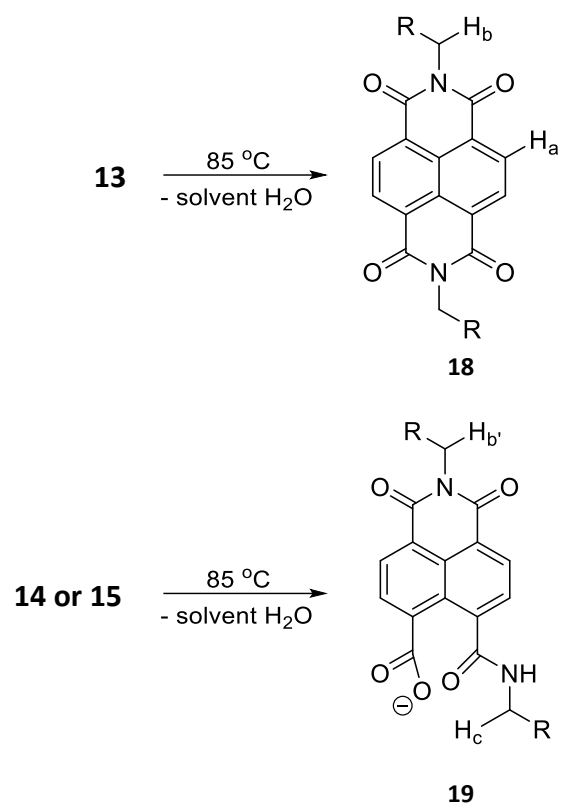
In order to investigate the nature of the chemical transformations NDI-OH undergoes upon heating and dehydration we performed solution <sup>1</sup>H, <sup>13</sup>C and COSY NMR experiments on a film formed at 85 °C and the freeze-dried sample. 2D <sup>1</sup>H – <sup>13</sup>C heteronuclear NMR experiments were also performed. Two types of correlation experiment have been used. Heteronuclear Single Quantum Coherence (HSQC) shows coupling between protons and carbons a single bond away from each other and Heteronuclear Multi Bond Correlation (HMBC) shows correlations between protons and carbons separated by multiple bonds. The HSQC experiments were also multiplicity edited. Much like in DEPT-135 experiments this means signals for protons in CH or CH<sub>3</sub> environments are shown as positive (blue correlation in

spectrum) and those in methylene CH<sub>2</sub> environments are negative (red correlation in spectrum).

The <sup>1</sup>H NMR region between 8.80 and 6.20 ppm of NDI-OH drop-cast, freeze dried and in solution are compared to NDI-NMe<sub>3</sub>I in Figure 2.10. No significant change is observed between NDI-OH solution and the freeze-dried sample, in agreement with the UV-vis absorption shown in Figure 2.7. This indicates that the freeze-dried sample is a solid made up of mostly compound 13 and the two minority di-hydrolysed compounds 14 and 15.

In the spectrum of the drop-cast thin film the four doublets, characteristic of mono-hydrolysed 13, were still present. A cluster of broadened signals were observed between 7.80 and 7.70 ppm; the region in which aromatic signals of compounds 14 and 15 were observed. A previously unseen singlet is also observed at 8.26 ppm. The singlet at 8.26 ppm is assigned as H<sub>a</sub> in structure 18 and has an integration value of 4. HSQC experiments reveal a short-range correlation with a <sup>13</sup>C signal at 131.1 ppm and multiplicity editing identifies the proton as CH or CH<sub>3</sub> (highlighted blue correlation in Figure 2.11). HMBC reveals long range correlation with <sup>13</sup>C signals at 164.2 ppm and 125.9 ppm (Figure 2.11).

Figure 2.10 also shows the presence of a broadened multiplet at 4.01 ppm, not observed in NDI-OH solution or freeze-dried sample. This signal had an integration value of 6 and is assigned the labels H<sub>b</sub> and H<sub>b'</sub> in structures 18 and 19. COSY experiments revealed a correlation with alkyl <sup>1</sup>H signals at 1.73 ppm and 1.64 ppm, these are shown in appendix 1.17 and 1.18. HSQC experiments identified a correlation with a <sup>13</sup>C signal at 41.2 ppm and confirmed the proton as being in a CH<sub>2</sub> environment (highlighted red correlation in Figure 2.11). HMBC revealed long-range correlation with <sup>13</sup>C signals at 165.9 ppm, 164.0 ppm and 26.9 ppm. This broadened multiplet is likely caused by two different overlapping protons.



**Scheme 2.5.** Ring-closing reactions undergone by the compounds 13, 14 and 15 upon heating to 85 °C and dehydration to form thin-films. Key identifying protons H<sub>a</sub>, H<sub>b</sub> and H<sub>c</sub> are labelled and shown on the <sup>1</sup>H NMR spectra in Figure 2.10.

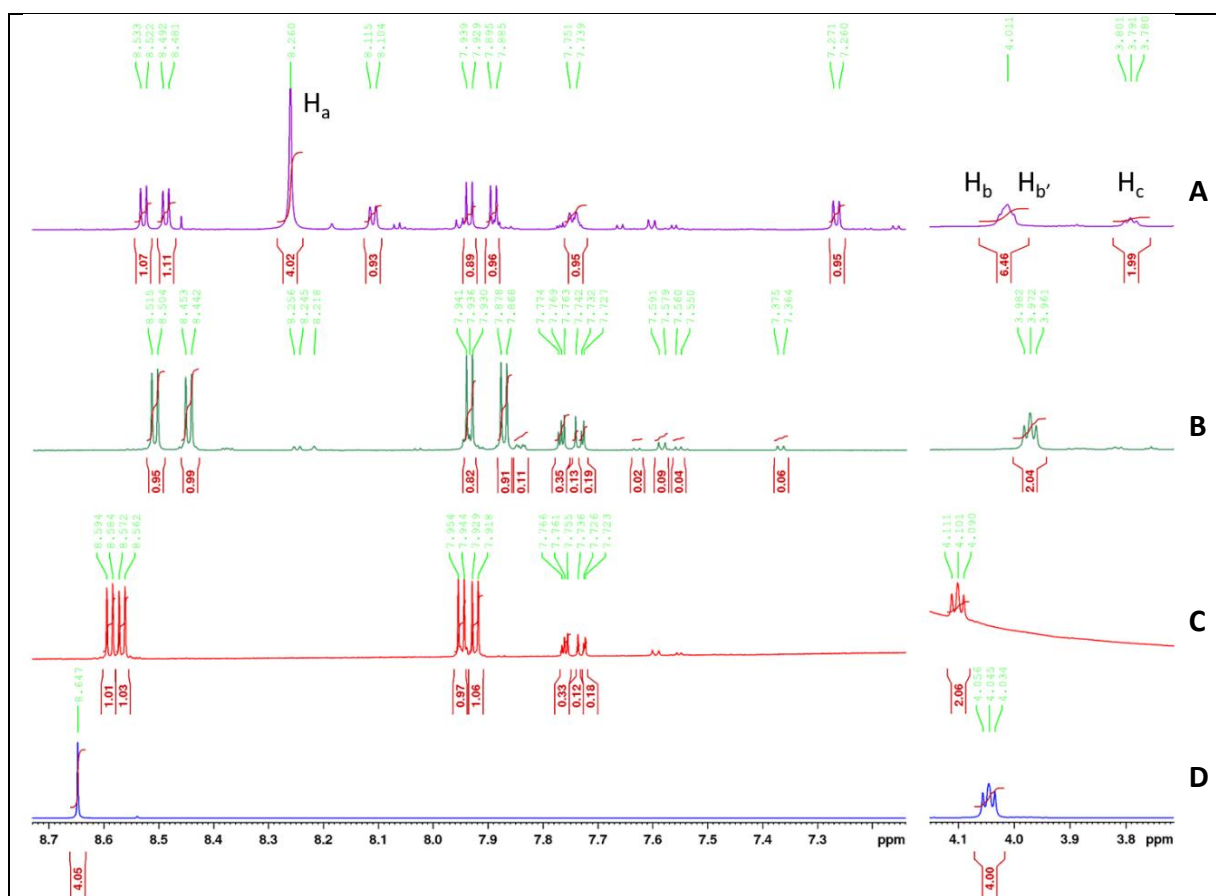


**Figure 2.10.** Overlays of  $^1\text{H}$  NMR spectra in the regions 8.70 – 7.20 ppm and 4.15 – 3.70 ppm. **A:** NDI-OH drop-cast thin-film at 85 °C and re-dissolved in  $\text{D}_2\text{O}$ . Key proton signals for identifying the structures 18 and 19 are labelled  $\text{H}_a$ ,  $\text{H}_b$  and  $\text{H}_c$ . **B:** Freeze-dried NDI-OH in  $\text{D}_2\text{O}$  solution. **C:** NDI-OH in  $\text{D}_2\text{O}$  solution untreated. **D:** NDI-NMe $_3$ l in  $d_6$ -DMSO solution.

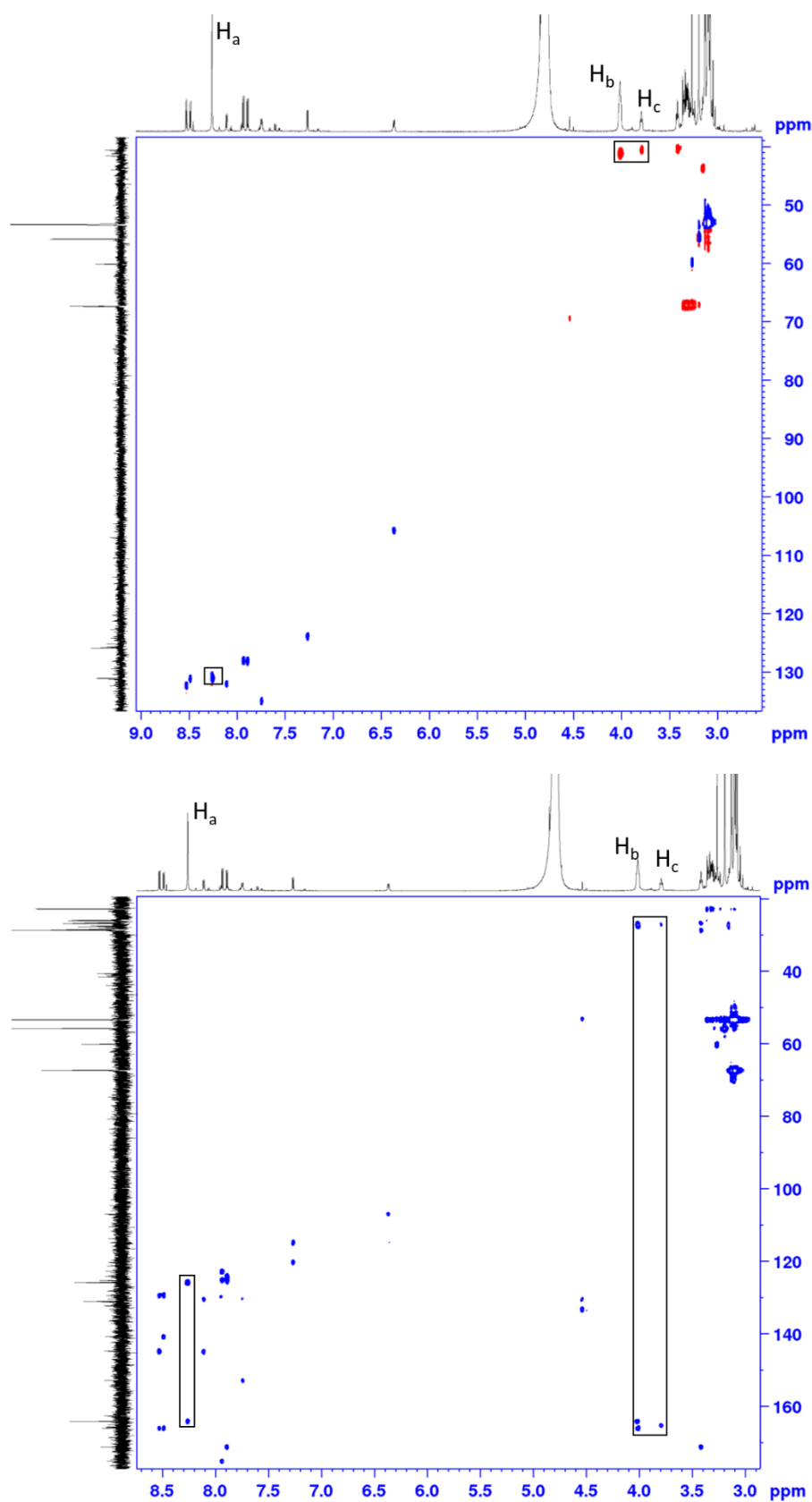


**Figure 2.11. Top:** HSQC spectrum of NDI-OH thin film with short-range correlation between key identifying protons, outlined in Scheme 2.5, highlighted. **Bottom:** HMBC spectrum of NDI-OH thin film with long-range correlation between key identifying protons, outlined in Scheme 2.5, highlighted.



The spectroscopic characterisation, shown in Figure 2.10 and Figure 2.11, suggest that a ring-closing reverse hydrolysis of the structures 13, 14 and 15 has occurred as outlined in Scheme 2.5. The singlet at 8.26 ppm is similar to those seen for the four equivalent naphthalene protons of symmetrical NDIs. Short-range correlation, seen in HSQC, with an aromatic naphthalene carbon ( $^{13}\text{C}$ ,  $\delta = 131.1$  ppm) suggests the protons in this environment are bound to a naphthalene ring and multiplicity editing identifies it as CH or  $\text{CH}_3$ . The long-range correlation, seen in HMBC, with a carbonyl carbon ( $^{13}\text{C}$ ,  $\delta = 164.2$  ppm) of very close chemical shift value to the imide carbon of NDI-NMe<sub>3</sub>I ( $^{13}\text{C}$ ,  $\delta = 162.6$  ppm) suggests the reformation of an imide. The  $^{13}\text{C}$  signal at 164.2 ppm could be assigned as an amide, like in the products 13, 14 and 15. The presence of amides can be ruled out however due to a lack of multiplicity in the  $^1\text{H}$  signal at 8.26 ppm. The lack of splitting suggests the hydrogen is in the presence of equivalent protons meaning a return to symmetry on the naphthalene ring. A lack of  $^1\text{H} - ^1\text{H}$  correlation between the signal at 8.62 ppm and any other proton was also confirmed by COSY experiment shown in the appendix 1.13 and 1.14. This structural characterisation supports the previously observed return to NDI like absorption features in heated solutions of NDI-OH seen in Figure 2.5.

The presence of the four doublets seen for mono-hydrolysed compound 13 in  $^1\text{H}$  NMR of drop-cast thin films, suggests that not all hydrolysed products underwent the ring-closing reaction to reform imide groups. The broadened multiplet at 4.01 ppm and another triplet at 3.79 ppm further confirm that there is still a mixture of amide and imide products which make up the drop-cast film. HSQC experiments reveal that each of these proton environments is  $\text{CH}_2$ , suggesting that each is on an alkyl chain. Each show short-range correlation with alkyl carbons adjacent to an imide or amide group ( $^{13}\text{C}$ ,  $\delta \approx 41.5 - 40.0$  ppm) indicating that there are new amide or imide groups present when compared to NDI-OH solution and freeze-dried sample. This is further confirmed by each of these protons exhibiting long-range correlation in HMBC experiments with carbonyl carbons ( $^{13}\text{C}$ ,  $\delta \approx 172.0 - 164.0$  ppm). From the complicated NMR spectra obtained from the NDI-OH film, drop-cast at 85 °C, we concluded that ring-closing reversal of the hydrolysed products 13, 14 and 15 had occurred giving rise to naphthalene diimides analogous to structure 18. At these temperatures however ring-closure on 14 and 15 had only occurred on one side of the naphthalene ring in some cases, leading to some products analogous to the structure 19. The reason R groups are used to identify the

pendant alkyl chains in 18 and 19, is that the complex NMR spectra of the thin-film suggests that reactions other than the reverse hydrolysis ring-closure have occurred and the exact structure of the pendant chains is unknown.

The role that the quaternary ammonium group plays in the mechanism of doping rylene diimides has previously been investigated. According to the mechanism proposed by Russ et al.,<sup>174</sup> and shown in Scheme 2.1, hydroxyl anions demethylate the ammonium group to form methanol. The resultant bound tertiary amine acts as n-type dopant, which there is previous precedent for.<sup>230, 232</sup> No signal for methanol at 3.34 ppm<sup>250</sup> was seen in either the spectrum for the drop-cast NDI-OH film or for the freeze-dried sample, although the low boiling point of methanol (64.7 °C) means it likely evaporated during film formation at 85 °C or under the low pressures of freeze drying. It has previously been shown that an E2 Hoffmann elimination, as shown in Scheme 2.1, is favoured over the S<sub>N</sub>2 decomposition when β-hydrogens are available for abstraction.<sup>233-235</sup> The resultant trimethyl amine could then possibly act as tertiary amine dopant.

Overlays in the region of 3.45 – 3.00 ppm of the two dehydrated NDI-OH samples with solutions of NDI-NMe<sub>3</sub>I and NDI-OH are compared in Figure 2.12. The <sup>1</sup>H NMR spectrum for the freeze-dried sample again shows no significant change from the aqueous solution of NDI-OH. The freeze dried sample and NDI-OH solution show two major signals at approximately 3.10 and 3.09 ppm which correspond to the two different quaternary ammonium methyl hydrogen environments in 13. It is assumed that smaller peaks in the same area correspond to the quaternary ammonium proton environments of the two minor products 14 and 15. In the same region of the spectrum for the drop-cast thin film, at least five singlets can be observed indicating a change in the quaternary ammonium chemical environment. Peak broadening is also observed across most of the <sup>1</sup>H NMR spectrum for the thin-film of NDI-OH, which would be expected in the presence of paramagnetic compounds.<sup>251</sup>

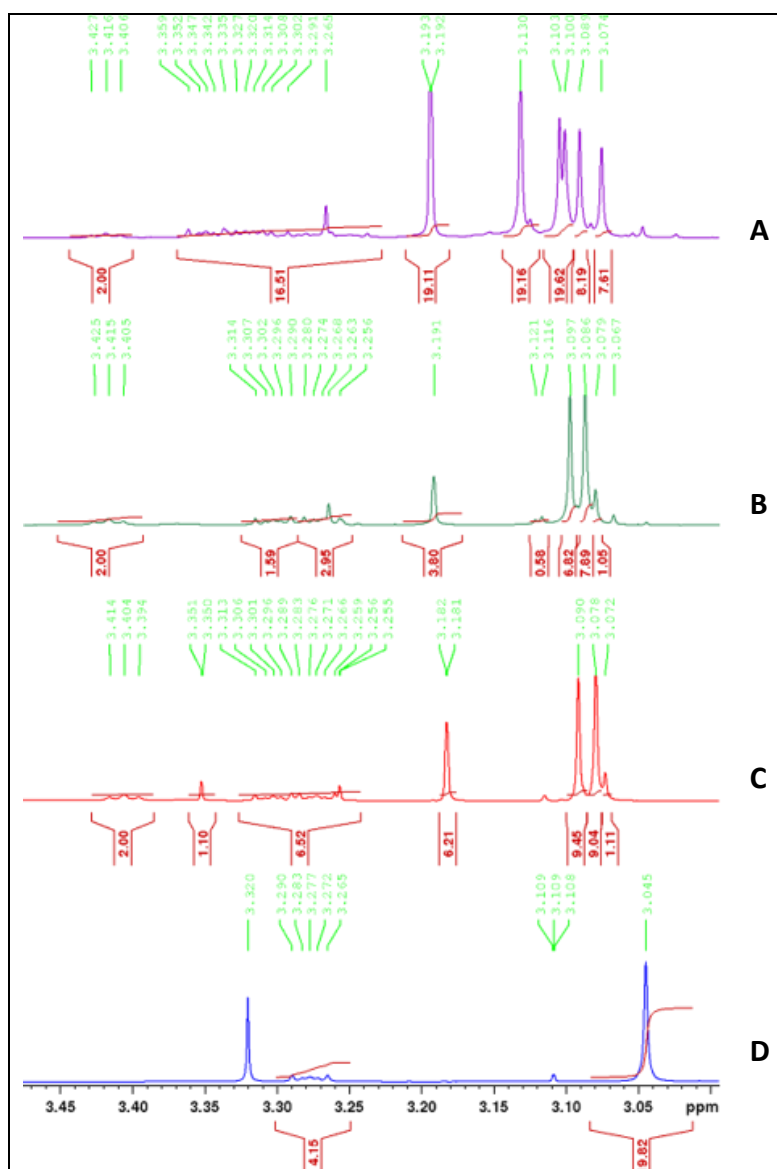


**Figure 2.12.** Overlays of  $^1\text{H}$  NMR spectra in the region of 3.45 – 3.00 ppm. **A:** NDI-OH drop-cast thin-film at 85 °C and re-dissolved in  $\text{D}_2\text{O}$ . **B:** Freeze-dried NDI-OH in  $\text{D}_2\text{O}$  solution. **C:** NDI-OH in  $\text{D}_2\text{O}$  solution untreated. **D:** NDI-NMe $_3$  in  $\text{d}_6$ -DMSO solution.

The HSQC spectrum of the drop-cast thin film in Figure 2.13 shows that all of the signals in the region between 3.15 -3.05 ppm observed single bond coupling with the  $-\text{N}^+(\text{CH}_3)_3$  carbon at 53.33 ppm. Each correlation is also shown as positive which confirms that each of the four signals in this area corresponds to a methyl proton on an ammonium moiety. The singlet at 3.19 ppm in the  $^1\text{H}$  spectrum shows single bond coupling with a  $^{13}\text{C}$  signal at 55.87 ppm and is positive so is either a CH or  $\text{CH}_3$  proton.

HMBC shows long-range coupling between the protons with chemical shifts at 3.15 and 3.05 ppm and the  $-\text{CH}_2\text{N}^+(\text{CH}_3)_3$  methylene carbon at 67.34 ppm. This suggests that the quaternary ammonium groups have undergone a chemical transformation but have remained bound to

the NDI alkyl sidechain, offering support to the mechanism of  $S_N2$  substitution and generation of methanol outlined by Russ.<sup>174</sup> The  $^1H$  signal at 3.19 ppm however only shows a strong long-range coupling with the  $^{13}C$  signal at 55.87 ppm. The lack of definitive long-range coupling with any carbons assigned to the alkyl sidechain suggests that at least a portion of the quaternary ammonium groups have been eliminated from NDI-OH. This would support the alternative mechanism of an E2 Hoffmann elimination, outlined in Scheme 2.1.

There are problems with assigning these spectra to the products of either the  $S_N2$  or Hoffmann elimination reactions. The product of  $S_N2$  reaction would be expected to leave a terminal tertiary amine similar to 2 or 3. Previously the methyl protons on products like this have been assigned chemical shift values between 2.2 and 2.4 ppm.<sup>173, 174, 230</sup> No major peaks in this area were observed. Similarly one of the products of Hoffmann elimination would be trimethylamine with an expected methyl proton chemical shift of 2.20 ppm.<sup>252</sup> The resultant terminal alkene (compound 4) from Hoffmann elimination would be expected to give rise to doublets of doublets in the regions described in Figure 2.10 and Figure 2.12., these could also not be positively identified. This does not mean that the  $S_N2$  degradation or Hoffmann elimination are the actual pathways by which the active doping species are formed. NMR just may not be the most suitable method to identify them. The doped species will likely contain paramagnetic free radicals making nuclei close to the free electrons unobservable. In addition, the doping species may also only be needed on very small scales to give an observable amount of radical anion in the absorption spectra of previous sections (< 10 mol %). Confirming the presence of these species on this scale by NMR, in already complicated spectra, is likely to be difficult.

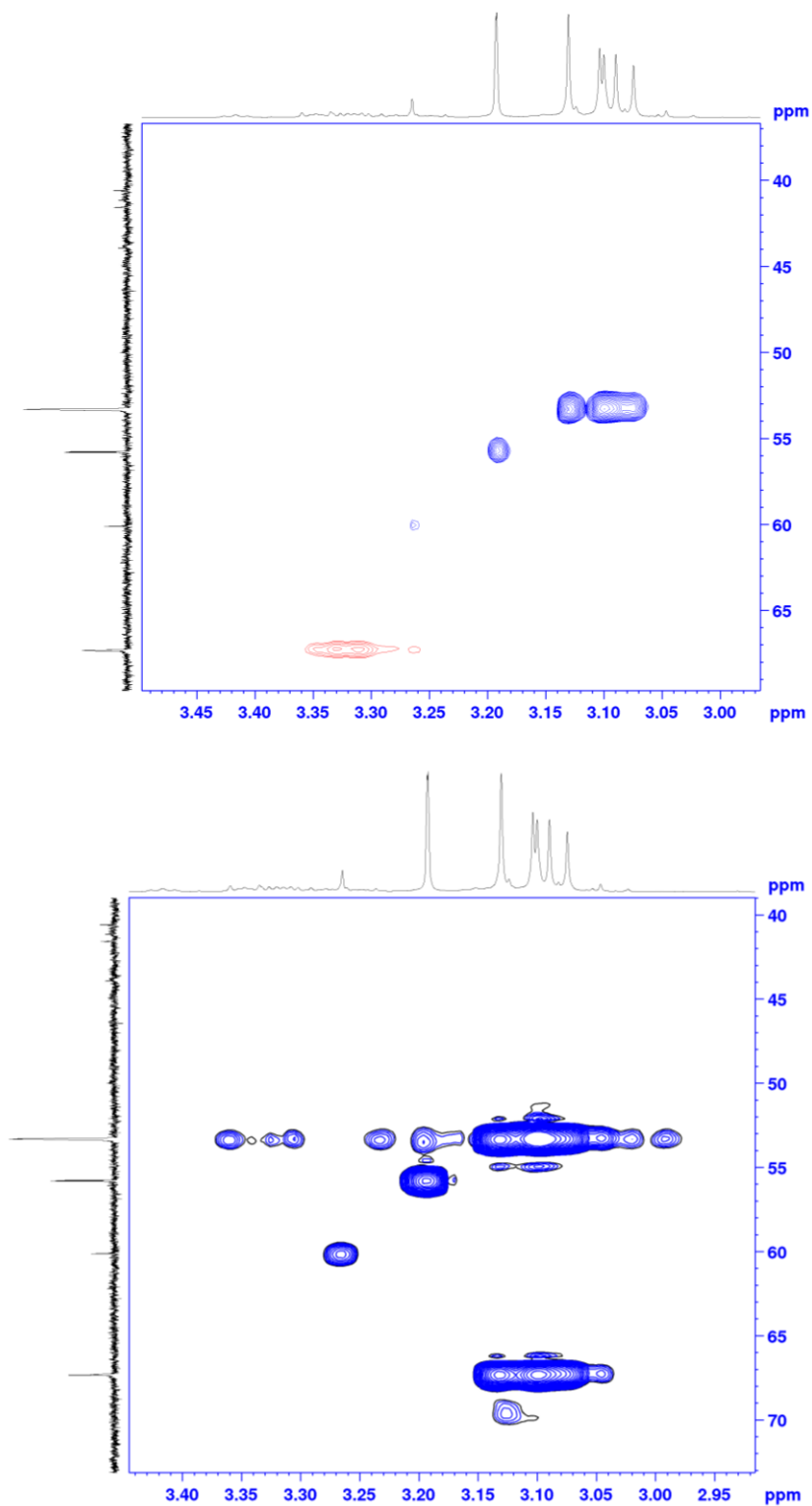


**Figure 2.13: Top:** Zoom of HSQC spectrum of NDI-OH thin film in the  $^1\text{H}$  range between approx. 3.50 and 3.00 ppm. **Bottom:** Zoom of HMBC spectrum of NDI-OH thin film in the  $^1\text{H}$  range between approx. 3.50 and 3.00 ppm.

No definitive characterisation of the quaternary ammonium groups involvement in the doping mechanism can be identified from the above analysis and further experiments on how to confirm this are discussed in the outlook. The spectroscopic characterisation of a thin-film

drop-cast at 85 °C has confirmed that the doped thin film is a mixture of ring-opened and ring-closed products. Further structural characterisation of films formed at higher temperature is needed to quantify the degree of ring-closing at different temperatures. The contribution of the ring-closing reaction to the doping mechanism also still needs to be confirmed.

### *2.2.5 Electronic and Morphological Characterisation of NDI-OH Thin-films*

The above spectroscopic data gives an indication that charge carrying species were generated upon the dehydration of NDI-OH solutions. Measurement of electronic conductivity,  $\sigma$ , can be a useful way of judging the practical performance of doped semiconductors. As shown in equation 1.6,  $\sigma$  is a product of the carrier concentration and the mobility. This means that the conductivity can be used as an assessment of the number of charges generated and the ease with which these charges move through the doped material. The optimisation of both these factors will be affected by the structure of the compound which makes up the thin films. It is unknown whether the NDI-OH hydrolysed products will be advantageous or detrimental to overall doping efficiency and charge transport through the film. Electrical conductivities of the NDI-OH films formed by drop-casting at temperatures between 45 °C and 125 °C were measured using a Van der Pauw setup and the results are summarised in the plot of conductivity versus drop-casting temperature in Figure 2.14.

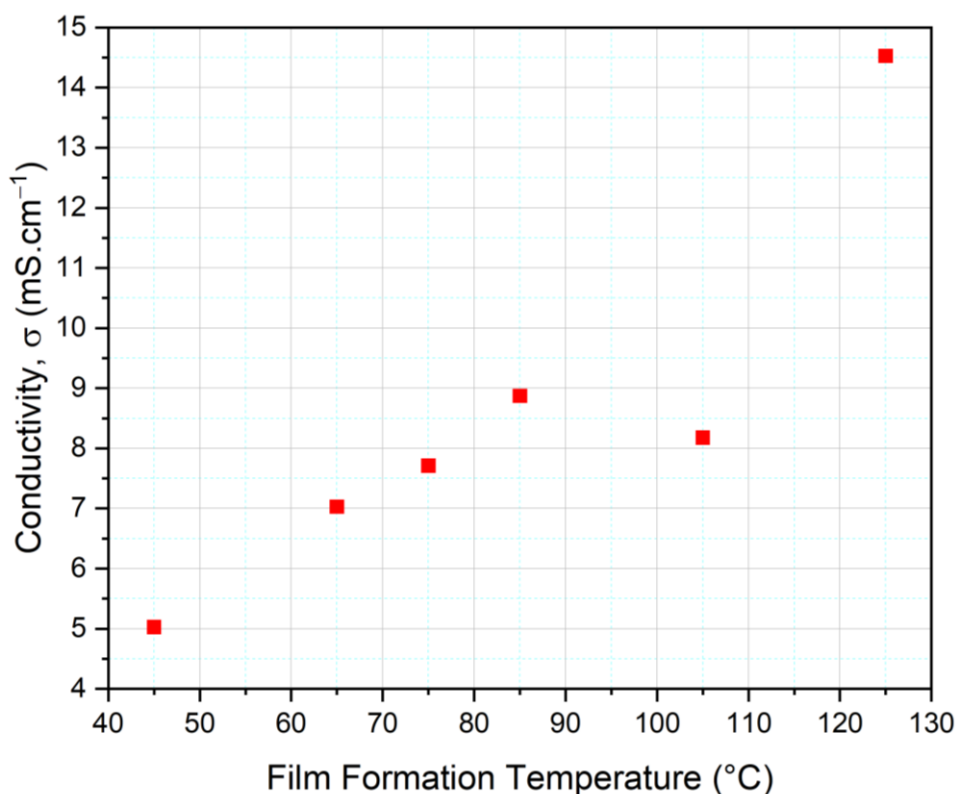


**Figure 2.14.** Plot of electronic conductivity versus the temperature NDI-OH thin-films were drop-cast at.

The highest  $\sigma$  of  $14.5 \text{ mS cm}^{-1}$  was seen in the film formed at the highest temperature of  $125 \text{ }^\circ\text{C}$ . The lowest  $\sigma$  of  $5.0 \text{ mS cm}^{-1}$  was observed at a film formation temperature of  $65 \text{ }^\circ\text{C}$ . A linear trend of increasing  $\sigma$  with increased film formation temperature was observed. This agrees with the UV-vis absorption data which shows a greater absorption for the NDI radical anion at higher film forming temperatures.

Based on cyclic voltammetry measurements in Figure 2.6 the full naphthalene diimide ring of NDI-NMe<sub>3</sub> has a lower lying LUMO than the ring-opened products of NDI-OH hydrolysis. The lower lying LUMO of the closed NDI ring-system is more suited to accepting and stabilising n-type charge carriers. Higher conductivities at higher temperatures of film formation therefore supports the theory that cyclisation of the NDI-OH amides back to imides has occurred upon heating. Films at  $125 \text{ }^\circ\text{C}$  contain more NDI rings and have a higher solid-state EA, this leads to more efficient n-type doping and higher electrical conductivities. Films at  $45 \text{ }^\circ\text{C}$  contain a large amount of 13, 14 and 15, lowering the EA and leading to lower electrical conductivities.

In addition to the electronic and chemical difference, morphological differences between the films may lead to preferential charge transport and hence increased conductivity. To investigate this atomic force microscopy (AFM) was used to map the surface morphology of

each film Images of films formed at temperatures between 45 °C and 75 °C, shown in Figure 2.15, exhibited defined needle like crystals with lengths up to approximately 5 μm. Increasing the film formation temperatures lead to a more homogenous morphology at 105 °C and 125 °C. The complete disappearance of larger crystals was observed in favour of a much flatter surface. The lack of crystalline domains at higher temperatures suggests that the path for charge transport will contain fewer grain boundaries. It has been proposed that grain boundaries, and especially grain boundaries of complex orientations relative to each other, are high energy barriers which are difficult to cross.<sup>253</sup>

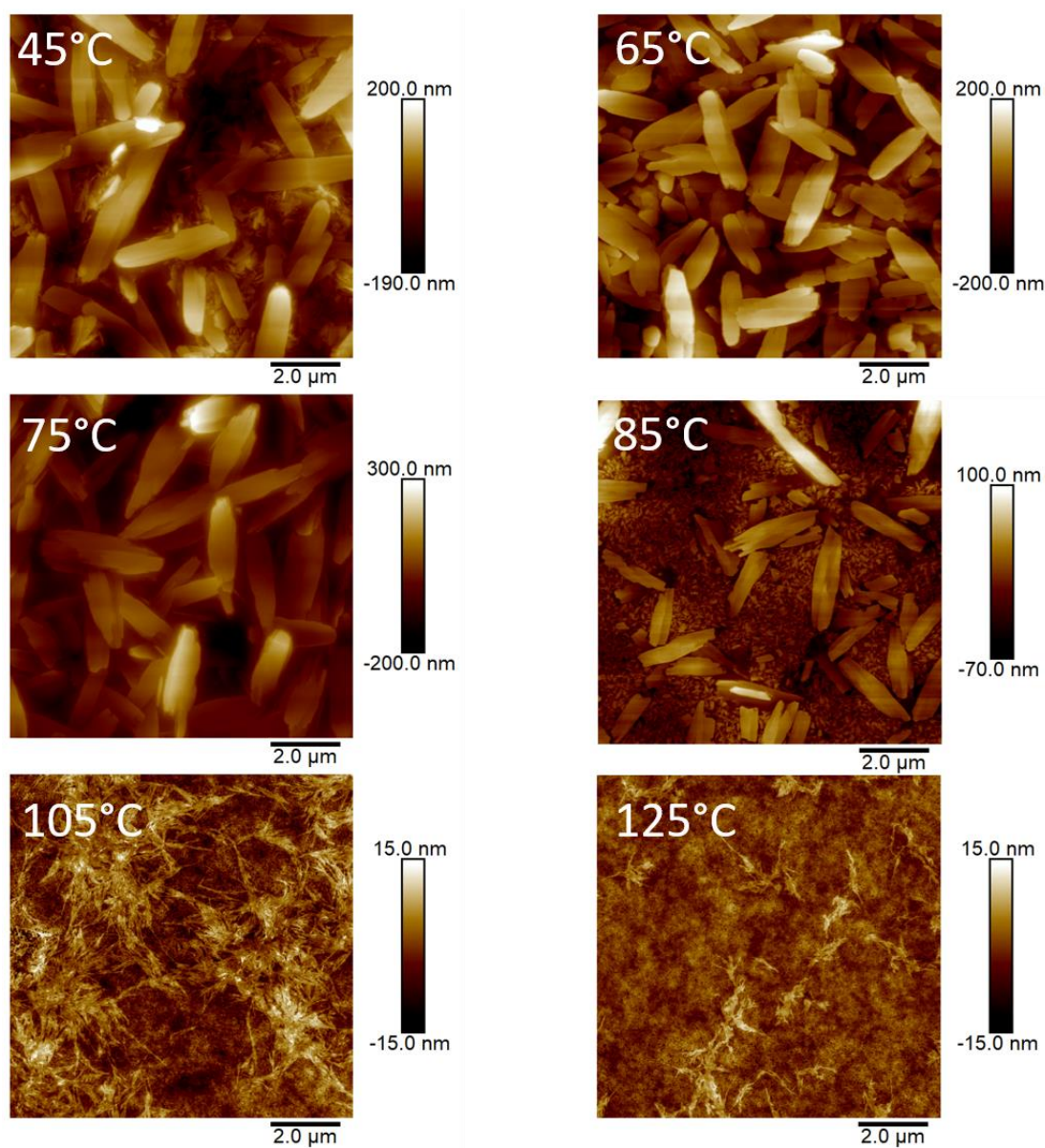


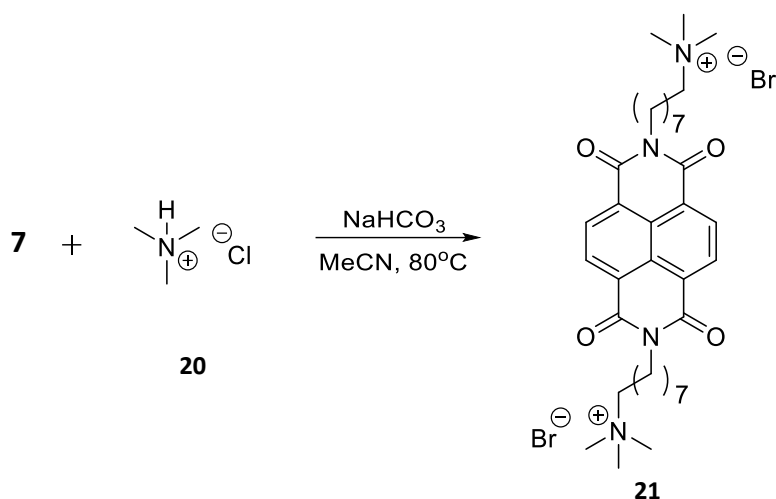
**Figure 2.15.** Atomic force microscopy topological images of the surface of NDI-OH dehydrated films formed at different temperatures.



The lower electronic conductivities in the lower temperature films are therefore not surprising due to combination of lower EAs and larger amounts of grain boundaries. In a previous collaboration we explored polymorphism in straight chain alkyl NDI derivatives.<sup>254</sup> Differential scanning calorimetry (DSC) along with a 2D map of XRD patterns with temperature of an NDI with linear hexyl chain is discussed briefly in the appendix section 1.3. The data from this study shows that, upon heightened temperatures, numerous NDI derivatives exhibit polymorphism. It is possible that a similar phenomenon is being observed in the AFM images in Figure 2.15. In addition, it is clear that the films are mixtures of NDI rings with the hydrolysed naphthalene products, which could complicate thin film morphology further. It is possible therefore that the film formed at 105 °C does not exhibit an anomalously low electrical conductivity (Figure 2.14) but actually suffers from unfavourable film morphology for charge transport. The amount of NDI reformed from reverse hydrolysis reactions coupled with the crystalline phase the mixture exhibits at that temperature, may have led to a thin film with extremely poor pathways for charge transport. The chemical and morphological compositions of each film must be determined to help elucidate the ideal film forming temperature for maximum NDI regeneration coupled with ideal charge transport morphologies.

## 2.3 Conclusions and Outlook

A modified synthetic route to NDI-NMe<sub>3</sub>I with overall yield of 7% was reported. Future attempts at reaching NDIs with pendant quaternary ammonium halides will likely employ a reaction similar to the one outlined in Scheme 2.6.<sup>255</sup> The trimethylamine hydrochloride salt, 20, being easier to handle than the large excesses of dimethylamine used to form 8. In addition to this trimethylamine acts as nucleophile to generate the bromide salt, 21, which could be used in subsequent ion exchanges to form NDI-OH. This is also advantageous since this route avoids the alkylation step with methyl iodide to form NDI-NMe<sub>3</sub>I.



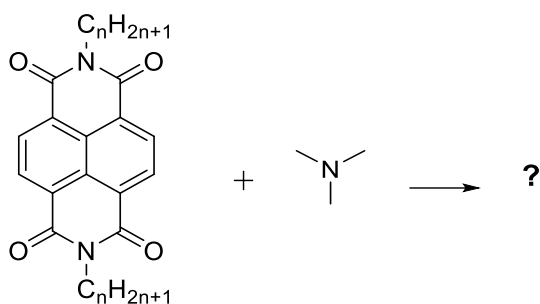
**Scheme 2.6.** Possible reaction between NDI alkyl bromide, 7, and trimethylamine hydrochloride in the presence of base to the NDI quaternary ammonium bromide salt 21.

It was also determined that the structure of self-doping quaternary ammonium hydroxides on rylene diimide semiconductors are not as previously reported. The basic conditions provided by ion-exchange resin led to hydrolysis of the imide functionality and a mixture of ring-opened compounds were therefore seen in the NDI-OH aqueous solution. The ring-opened products had a detrimental effect on the ability of NDI-OH to accept and stabilise a negative charge which was observed through a rise in the LUMO level. Upon heating a reversal of this hydrolysis was observed in both UV-vis absorption and NMR spectroscopies. The contribution of the ring-opened products of hydrolysis to the overall thin-film morphology as well as their effect on the solid-state EA still needs to be determined. Initial studies into the electrical conductivity and surface morphology however, revealed that the reverse reaction at higher film-forming temperatures lead to higher electrical conductivities.

The outlook for this project will mostly focus on determining the actual doped and doping species. Absorption spectroscopy suggests that NDI radical anions are present however this still needs to be confirmed. In addition, the surprising lifetimes of these radicals still needs to be investigated. Investigation into possible causes of stabilisation of the radicals is likely to be achieved by a combination of EPR spectroscopy and further structural characterisation through mass spectrometry and IR.

The role of the quaternary ammonium groups, and their possible degradation products upon heating, could not be determined by the structural characterisation carried out on doped films in this study. Past literature suggests that tertiary amines are capable of doping NDIs,<sup>230-</sup>

<sup>232</sup> however two possible reaction pathways lead to tertiary amine products. The previously suggested decomposition of the quaternary ammonium via  $S_N2$  substitution of hydroxide leads to dimethyl amines. Previous studies into the degradation of these moieties suggests that a Hoffmann elimination is favoured over the  $S_N2$  pathway and this would lead to trimethylamine.<sup>233-235</sup> A simple experiment to help determine the applicability of this is outlined in. Trimethylamine is mixed with neutral NDI molecules and subsequent generation of n-doped NDI could be tracked by absorption spectroscopy, electron paramagnetic resonance (EPR) spectroscopy and conductivity measurements.



**Scheme 2.7.** Doping of neutral NDI small molecules with trimethylamine to demonstrate the applicability of Hoffmann elimination product trimethylamine as n-type dopant.

## 2.4 Acknowledgements

The work presented in this chapter was obtained in collaboration with several researchers. We would like to thank the following people for their contributions.

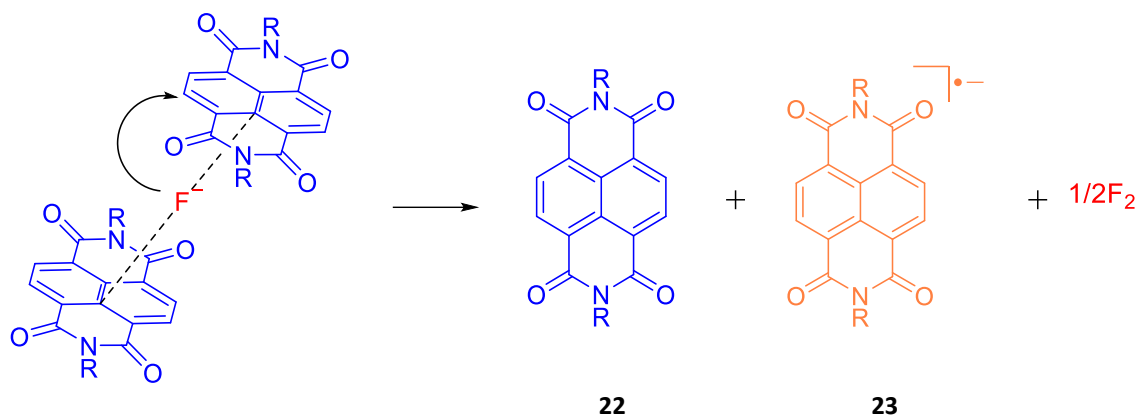
- Peter Finn for spectroscopic and electronic measurements, as well as extensive intellectual contributions regarding optical spectra and electronic characterisation.
- William Neal for obtaining AFM images.
- Dr Christian Nielsen for intellectual contributions regarding optical spectra and electronic characterisation.
- Zilu Liu for XRF measurements.
- Dr Silvia Milita and Dr Fabiola Liscio for crystallographic work performed on neutral NDI materials.

# Chapter 3. Exploring the chemical mechanism behind n-type fluoride doping of BDOPV semiconductors

## 3.1 Introduction

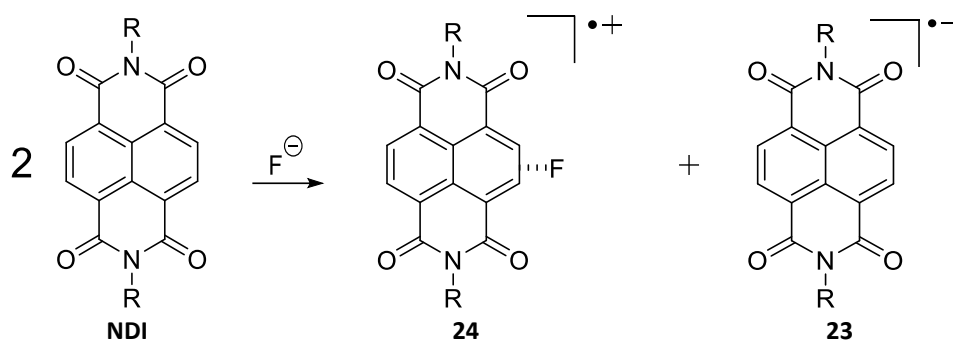
The use of fluoride anions as n-type dopants for organic semiconductors was briefly introduced in Chapter 1. The nature of interactions between fluoride anions and conjugated organics have mostly been studied with applications of fluoride anion sensing in mind. Commonly naphthalene diimides (NDI) are used as the fluoride sensing component in which there is precedent for a non-covalent  $\pi$ -anion interaction with fluoride anions.<sup>165, 166</sup> Numerous claims of a direct electron transfer between fluoride anions and the electron deficient NDI unit have been reported.<sup>165-167, 256</sup>

Scheme 3.1 shows a schematic representation of a previously suggested mechanism of electron transfer between NDI and fluoride anions. Included is a  $\pi$ -anion complexation with fluoride followed by a full electron transfer to generate the radical anion 23. There is strong evidence for  $\pi$ -anion interactions between fluoride and electron deficient aromatics.<sup>159-161, 163, 164, 257</sup> When using fluoride anions as n-type dopants for polymeric semiconductors an increase in electrical conductivity and thermoelectric performance was also observed.<sup>49</sup> Radical anions have also been observed in spectroscopic data of organic semiconductors doped with fluoride containing salts.<sup>167, 256</sup>



**Scheme 3.1.** Schematic representation of direct electron transfer from fluoride anions to  $\pi$ -system to form radical anion, preceded by a  $\pi$ -anion intermolecular interaction.

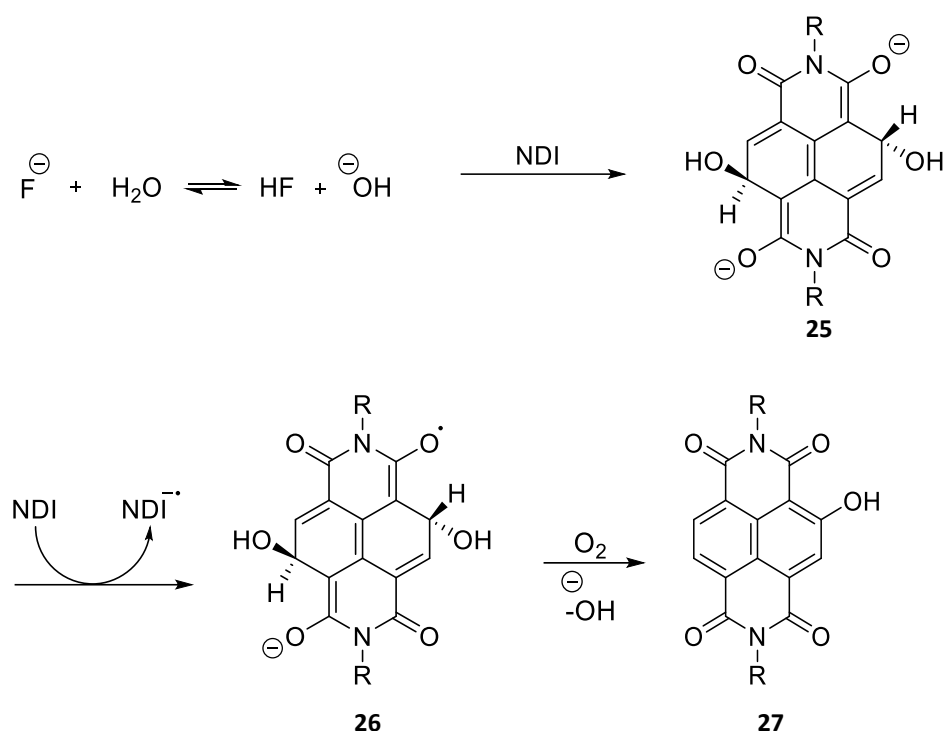
Previously however doubts have been cast on fluoride anions abilities to act as an electron donor to electron deficient aromatics.<sup>258</sup> A recent communication from Gabbai *et al.* claimed that a full electron transfer is thermodynamically unfavourable, calculating an endothermic change in enthalpy of  $76 \text{ kcal mol}^{-1}$  when two fluoride anions are oxidised to fluorine by NDIs.<sup>259</sup> With eight valence electrons and very high electronegativity it does seem unlikely that fluoride anions would easily give up an electron. An alternative route to NDI type radicals is shown in Scheme 3.2 and is taken from a 2014 study.<sup>170</sup> The authors were concerned with the relatively long stability of NDI and PDI radicals in air, generated from fluoride doping. They concluded that the air stable UV-vis absorption and electron paramagnetic resonance (EPR) signals must be due to an NDI radical cation complexed to fluoride (24), the electronegative fluoride stabilising the radical cation. The other product is an NDI radical anion (23), which undergoes oxidation back to neutral NDI upon exposure to air.



**Scheme 3.2.** The generation of an air stable NDI fluoride radical cation complex and an unstable radical anion complex from the addition of fluoride anions to NDI. Scheme adapted from reference 170.

A different mechanism has recently been proposed in which hydroxyl anions are generated from the deprotonation of water by fluoride. It is then an aromatic-hydroxyl complex which

undergoes electron transfer with a neutral aromatic as is outlined in Scheme 3.3.<sup>169</sup> Based on calculated Gibbs free energy ( $\Delta G$ ), and basis set superposition error (BSSE) corrected interaction energies ( $\Delta E$ ), it was determined that a  $\pi$ -anion interaction between NDI and hydroxyl anions was more favourable than with fluoride anions. Based on the same calculations it was predicted that the structures 25 and 26 exhibited actual C-OH bonds and were not merely complexes exhibiting  $\pi$ -anion interactions. It was then claimed that oxidation of 26 lead to the phenol type product 27, isolated in yields of 5 to 10 %.



**Scheme 3.3.** Schematic representation of acid-base reaction between fluoride and water and subsequent doping of NDI by hydroxyl anions. Isolation of the hydroxy substituted NDI, produced by oxidation of the radical anion, is then shown. Scheme adapted from reference 169.

The most common source of fluoride anions used as dopants throughout the literature is from tetraalkylammonium fluoride salts. Heeney *et al.* have reported more idealised transistor behaviour when doping a well-known NDI polymer with tetrabutylammonium fluoride (TBAF) as the source of  $F^-$ . Successful doping was also achieved using salts of other halogens in this study.<sup>158</sup> Katz *et al.* used TBAF dopants to achieve a high thermoelectric power factor with benzodifurandione-based polymers. They suggested a mechanism which includes nucleophilic aromatic substitution of a fluoride anion on to the conjugated polymer and a subsequent electron transfer on to a neutral polymer chain.<sup>49</sup> The same mechanism has been used to explain the interactions between fluoride and fullerene derivatives.<sup>260</sup>

Benzodifurandione-based oligo (p-phenylenevinylene) (BDOPV) has recently shown promise as an electron deficient building block in the synthesis of molecular and polymeric organic semiconductors.<sup>205, 215, 261</sup> Small molecule BDOPVs have been shown to possess low band gaps and conformationally rigid structures due to vinyl bonds and intramolecular hydrogen bonding. Polymers containing BDOPV units have exhibited some of the highest electron mobilities of all organic semiconductors and have low lying LUMO levels, often reported between  $-4.00$  and  $-4.30$  eV, allowing for efficient n-type doping.<sup>49, 262, 263</sup>

This chapter aims to extend the fundamental work previously carried out on fluoride doped NDI systems to BDOPV derivatives. This study employs a soluble BDOPV small molecule and a difluorinated derivative (2F-BDOPV) with increased electron affinity, as electron deficient acceptors. The two BDOPV molecular derivatives are decorated with polar oligoethylene sidechains to increase polar solvent solubility and dopant acceptor miscibility in the solid-state.<sup>50, 264-268</sup> Tetrabutylammonium fluoride trihydrate (TBAF·3H<sub>2</sub>O) is used as the source of fluoride anion. The structures of BDOPV acceptors and dopant salt TBAF·3H<sub>2</sub>O are shown in Figure 3.1.

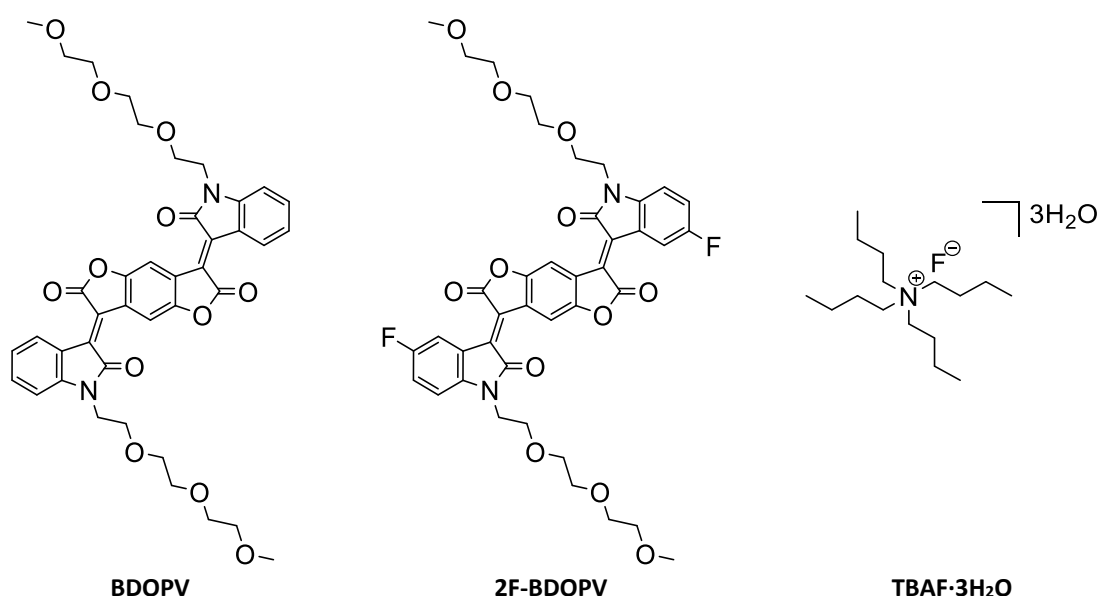


**Figure 3.1.** Structures of BDOPV, 2F-BDOPV and TBAF·3H<sub>2</sub>O.

Of interest in this study was the solvent dependencies on the system and how switching from protic to aprotic solvents affects interactions between ions and  $\pi$ -systems. The protic solvent, chloroform, and a polar aprotic solvent, dimethylformamide (DMF) were compared. The composition of solutions of TBAF·3H<sub>2</sub>O in these two solvents were strikingly different. The

consequences this has on the ability of TBAF·3H<sub>2</sub>O to act as an n-type dopant were then explored. Finally, characterisation of the products of doping was carried out in order to determine if fluoride anions act to donate electrons, in a similar fashion to Scheme 3.1, or if hydroxyl anions are the active dopant, as outlined in Scheme 3.3.

## 3.2 Results and Discussion

### 3.2.1 Optoelectronic Properties of BDOPV and 2F-BDOPV

In order to confirm the FMO values, and their applicability as electron acceptors from n-type dopants, solution CV was performed on BDOPV and 2F-BDOPV. In Figure 3.2 it can be seen that both exhibit two fully reversible electrochemical reductions at potentials up to -1.00 V. The LUMO was estimated from the onset of the first reduction peak for each. LUMO levels of -4.15 eV and -4.25 eV were calculated for BDOPV and 2F-BDOPV, respectively. This agrees with previous literature on molecular BDOPV<sup>215, 261</sup> and *p*-difluorinated derivatives.<sup>219</sup> A stabilisation in the LUMO of 0.10 eV should allow for more accessible n-type doping on to 2F-BDOPV compared to BDOPV.

Figure 3.2 also shows the solution UV-vis absorption spectra of both BDOPV and 2F-BDOPV. Both observe a broad absorption band between approximately 800 nm and 300 nm with two maxima at approximately 550 nm and 440 nm. The optical band gap was calculated from the onset of absorption and was 1.79 eV and 1.76 eV for BDOPV and 2F-BDOPV, respectively. All of these features again agree with previous literature on similar compounds with alkyl side chains.<sup>219, 261</sup> The HOMO was then estimated by subtracting the optical band gap from the LUMO. The energy levels are summarised in Table 2.2. As discussed in Chapter 1, the optical band gap used here is likely lower than the fundamental band gap.<sup>35</sup> Since the rest of this study relies mostly on solution measurements, and the HOMO of BDOPV derivatives is not essential for understanding their roles as acceptors, it was decided that the optical band gap measured from solution absorption spectra was sufficient for the estimation of the HOMO.



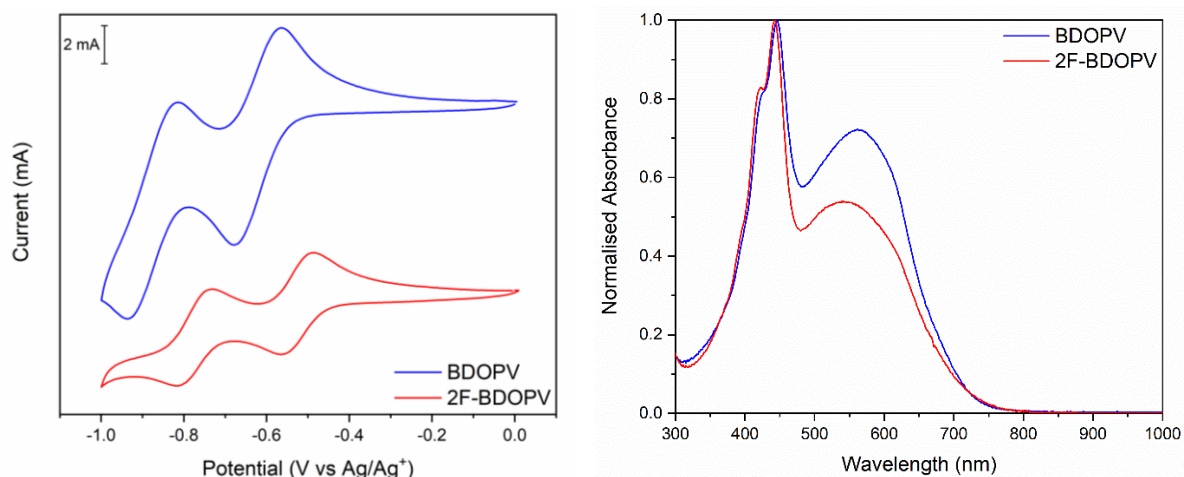


**Figure 3.2.** Left: Cyclic voltammograms of 0.001 M BDOPV and 2F-BDOPV run in solutions of dichloromethane. Referenced to Ag/Ag<sup>+</sup> electrode with platinum wire as counter electrode and glassy carbon working electrode. Right: UV-vis absorption spectra of BDOPV and 2F-BDOPV in chloroform solutions.

Table 3.1. Electrochemical and optical properties of BDOPV and 2F-BDOPV							
Compound	$E_{pa}$ [a] (V)	$E_{onset}$ [a] (V)	$\lambda_{max}$ [b] (nm)	$\lambda_{onset}$ [b] (nm)	Optical band gap [c] (eV)	LUMO [d] (eV)	HOMO [e] (eV)
BDOPV	-0.68 and -0.94	-0.56 and -0.82	562 and 446	694	1.79	-4.15	-5.94
2F-BDOPV	-0.56 and -0.82	-0.46 and -0.72	542 and 443	705	1.76	-4.25	-6.01

[a] From solution cyclic voltammetry using glassy carbon working electrode, platinum wire counter electrode and Ag/Ag<sup>+</sup> reference electrode. Values are reported from the 4<sup>th</sup> cycle and measured at 50 mV.s<sup>-1</sup>. [b] From solution UV-vis absorption spectroscopy in chloroform. [c] Estimated from  $\lambda_{onset}$ . [d] Estimated from electrochemical onset of first reduction ( $E_{onset}$ ). [e] Estimated using equation HOMO = LUMO – Optical band gap.

### 3.2.2 Absorption Spectra of Fluoride Doped BDOPV and 2F-BDOPV

It has previously been reported that no electron transfer takes place between NDI and TBAF in solutions of chloroform, dichloromethane and toluene. In DMF solutions, however, UV-Vis absorption features matching those of NDI radical anions have been seen.<sup>170</sup> UV-Vis-NIR spectrophotometry was used to investigate the presence of BDOPV radical species when doped with TBAF·3H<sub>2</sub>O in solutions of DMF, and spectra are shown in panels **a** and **b** of Figure 3.3. Absorption characteristics for undoped BDOPV and 2F-BDOPV in chloroform are shown in Figure 3.2.

Compared to chloroform (Figure 3.2) the spectra for neat BDOPV and 2F-BDOPV in DMF showed similar absorption characteristics with two maxima at approximately 560 nm and 440

nm. An additional, less intense, band was also observed with a maximum at 750 nm which increases in intensity upon the addition of TBAF·3H<sub>2</sub>O. Due to the increase in intensity upon increased dopant concentration, it was assumed that this absorption band was indicative of an additional energy level introduced between the HOMO and LUMO of BDOPV upon doping. The observation of this absorbance at 0 equivalents of TBAF·3H<sub>2</sub>O contradicted this explanation, however. One possibility was that BDOPV was being doped unintentionally through a solvent impurity such as the DMF breakdown product dimethylamine.<sup>269</sup> Previously amines have been used for n-doping of electron deficient aromatics.<sup>174, 230-232</sup> Alternatively the absorbance at 750 nm may not be associated with any electron transfer and was actually a red-shifting commonly observed with J-type aggregations.<sup>270</sup> J-aggregation is often promoted when head-to-tail orientations are favoured<sup>271</sup> and 2F-BDOPV has previously been seen to exhibit head-to-tail  $\pi$ - $\pi$  cofacial stacks in the solid state.<sup>219</sup> The likelihood of both doping via DMF breakdown and formation of aggregates in DMF is considered again later in this chapter.

Panels **c** and **d** of Figure 3.3 show the absorption spectra of BDOPV and 2F-BDOPV titrated with TBAF·3H<sub>2</sub>O in a chloroform solution. The absorption band at 750 nm was only observed at concentrations of TBAF·3H<sub>2</sub>O above 1 molar equivalent. These were much higher dopant concentrations than were seen in DMF. If chloroform acts as a better solvent for BDOPV than DMF then this may suggest that absorbance at 750 nm was due to J-aggregates which were broken up more in solutions of chloroform. An alternate explanation may come from a possible acid base reaction between fluoride and solvents. The fluoride anions may act as a Brønsted base to deprotonate the acidic chloroform rendering them useless as dopants or dopant precursors to BDOPV. Literature does provide an example of TBAF being used to deprotonate chloroform to form trichloromethanide anions in trichloromethylation reactions of aromatic aldehydes.<sup>272</sup>

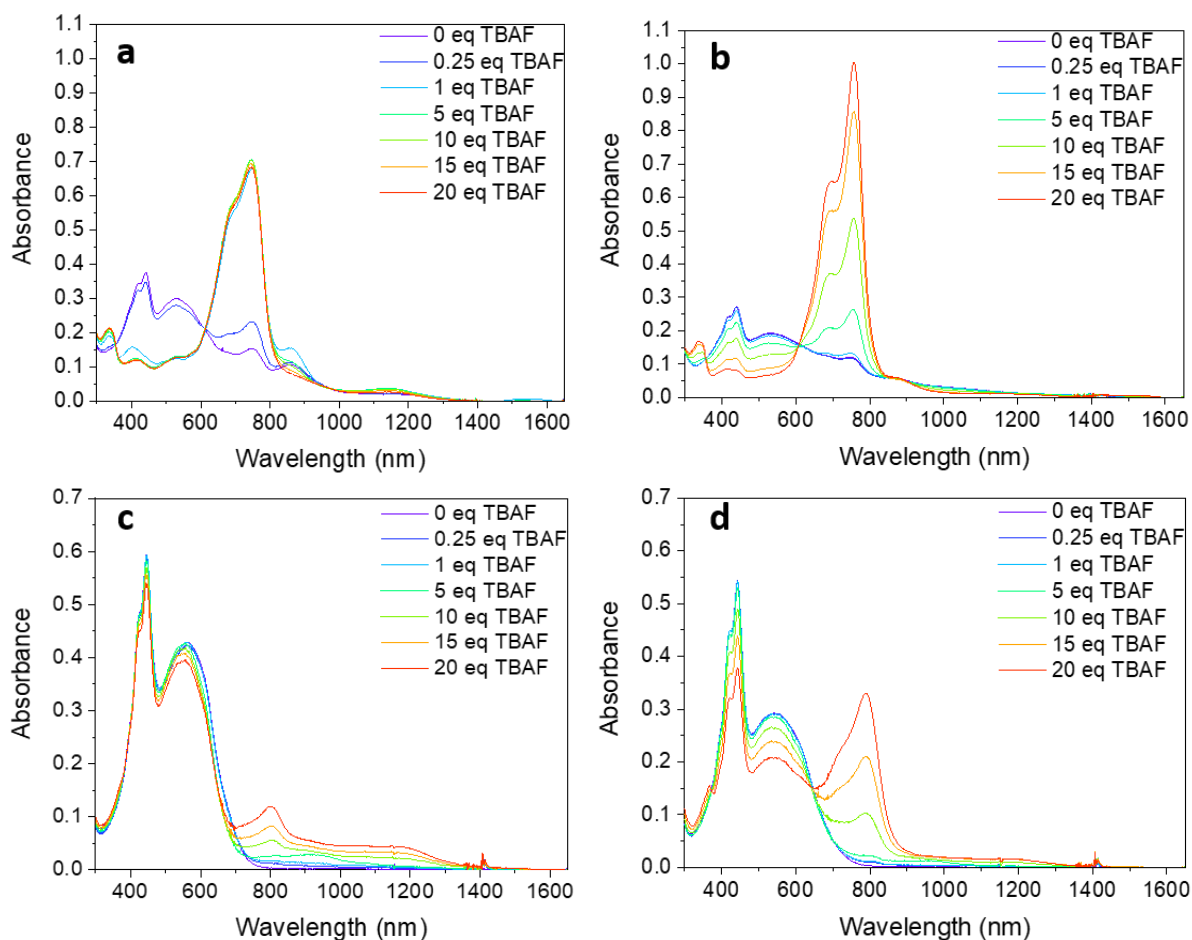


**Figure 3.3.** Solution UV-Vis-NIR absorbance spectra of **a:** BDOPV in DMF, **b:** 2F-BDOPV in DMF, **c:** BDOPV in chloroform and **d:** 2F-BDOPV in chloroform. BDOPV and 2F-BDOPV at concentrations of  $2 \times 10^{-5}$  M and amount of TBAF is given in molar equivalents with respect to BDOPV or 2F-BDOPV.

### 3.2.3 Characterisation of TBAF·3H<sub>2</sub>O solutions

In order to confirm the deprotonation of chloroform upon introduction of TBAF·3H<sub>2</sub>O: <sup>1</sup>H, <sup>13</sup>C and <sup>19</sup>F NMR spectroscopy experiments were performed in a solution of deuterated chloroform (CDCl<sub>3</sub>). A possible acid-base reaction between TBAF and solvating CDCl<sub>3</sub> is shown in Scheme 3.4 and the corresponding NMR spectra are shown in Figure 3.4. <sup>13</sup>C NMR in CDCl<sub>3</sub> gave rise to four peaks indicative of tetrabutylammonium alkyl carbons between 58.36 ppm and 13.47 ppm. An additional signal was observed at 77.36 ppm overlapping with the residual <sup>13</sup>C chemical shift for CDCl<sub>3</sub>. This suggests that there was an additional carbon environment present, possibly due to fluoride deprotonation of solvent to form trichloromethanide anions. In the presence of water from TBAF·3H<sub>2</sub>O trichloromethanide likely acts as a base and is protonated giving chloroform (CHCl<sub>3</sub>). The signal at 77.36 ppm matches that of impurity CHCl<sub>3</sub>

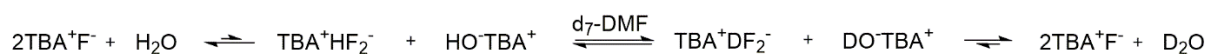
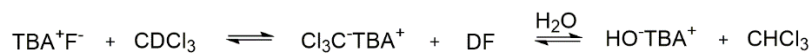
in solutions of  $\text{CDCl}_3$ .<sup>250</sup> The formation of  $\text{CHCl}_3$  is further supported by the presence of a positive signal (CH) at 77.56 ppm in DEPT 135 NMR experiments (appendix 2.2).

The  $^1\text{H}$  NMR spectrum of  $\text{TBAF}\cdot 3\text{H}_2\text{O}$  in  $\text{CDCl}_3$  shows only the four alkyl signals of a tetrabutylammonium species as the major peaks between 3.84 ppm and 0.84 ppm. The deprotonation of water by trichloromethanide ions to form  $\text{CHCl}_3$  is further supported by the absence of a water signal at 1.56 ppm<sup>250</sup> in the  $^1\text{H}$  spectrum in  $\text{CDCl}_3$ . The proton decoupled  $^{19}\text{F}$  NMR spectrum of neat  $\text{TBAF}\cdot 3\text{H}_2\text{O}$  in  $\text{CDCl}_3$  is slightly more complex. A major broad shift is observed at  $-123.8$  ppm. Five more minor peaks can then be seen between  $-70.9$  ppm and  $-81.2$  ppm which could not be assigned. The major broad peak, with a shift of  $-123.8$  ppm, corresponds to the deuterium fluoride (DF) fluorine atom, which likely undergoes a slow deuterium-hydrogen exchange with  $\text{H}_2\text{O}$ . The  $^{19}\text{F}$  chemical shift for HF and DF fluorine atoms has been reported over a wide range and can be dependent on solvent and concentration.<sup>273</sup>

In order to confirm that the same chemical reactions are not taking place in DMF as in chloroform, solution NMR of  $\text{TBAF}\cdot 3\text{H}_2\text{O}$  in deuterated DMF ( $d_7$ -DMF) was performed. The  $^{13}\text{C}$  NMR spectrum of  $\text{TBAF}\cdot 3\text{H}_2\text{O}$  in  $d_7$ -DMF in Figure 3.4 shows only the alkyl carbons from the tetrabutylammonium cation.  $^{19}\text{F}$  NMR of  $\text{TBAF}\cdot 3\text{H}_2\text{O}$  in  $d_7$ -DMF shows two sharp peaks at  $-113.5$  ppm and  $-148.5$  ppm consistent with  $\text{F}^-$  and hydrogen difluoride ( $\text{HF}_2^-$ ) respectively.<sup>165, 166, 274, 275</sup> In DMF a  $\text{F}^-$  to  $\text{HF}_2^-$  integrated area ratio of 82:18 is observed which is similar to values obtained when  $d_6$ -DMSO is used as solvent.<sup>259</sup> The ratio of integrated areas for each of these peaks has been seen to vary for different solvents, one possible explanation is the ease of conversion of  $\text{F}^-$  to  $\text{HF}_2^-$  by deprotonation of solvent depending on the relative acidity of the solvent.<sup>259</sup> Alternatively, it has been shown that the formamide deuterium atom of  $d_7$ -DMF will undergo a deuterium-hydrogen exchange with water in the presence of *t*-BuOK.<sup>276, 277</sup> A mechanism for a slow deuterium/hydrogen exchange has also been proposed for anhydrous TBAF in solutions of  $d_6$ -DMSO when doped with  $\text{H}_2\text{O}$ . Based on the observation of both  $\text{F}^-$  and  $\text{HF}_2^-$  in  $^{19}\text{F}$  NMR we believe it is reasonable to apply the same mechanism of "hydroxide catalysed deuterium exchange"<sup>274</sup> to the system of  $\text{TBAF}\cdot 3\text{H}_2\text{O}$  in  $d_7$ -DMF, which is shown at the bottom of Scheme 3.4.

$^1\text{H}$  NMR of  $\text{TBAF}\cdot 3\text{H}_2\text{O}$  in  $d_7$ -DMF solution shows an unexpected broad singlet at 4.3 ppm. The shift for  $\text{HF}_2^-$  has previously been reported as much further downfield than this.<sup>275</sup> Another possibility is that water is hydrogen bonding with the  $\text{HO}^-\text{TBA}^+$  and  $\text{DO}^-\text{TBA}^+$  shown in Scheme

3.4. The hydrogen bonding interaction causes deshielding of the water protons and a downfield shift to 4.31 ppm from the expected 3.50 ppm in  $d_7$ -DMF.<sup>278</sup> The lack of a significant signal in this area in  $CDCl_3$  solutions suggests that the same deprotonation cannot happen due to fluoride preferentially acting as a base to  $CDCl_3$ .



**Scheme 3.4.** Reaction of TBAF with deuterated chloroform (top) and deuterium-hydrogen exchange between TBAOH and  $d_7$ -DMF (bottom).

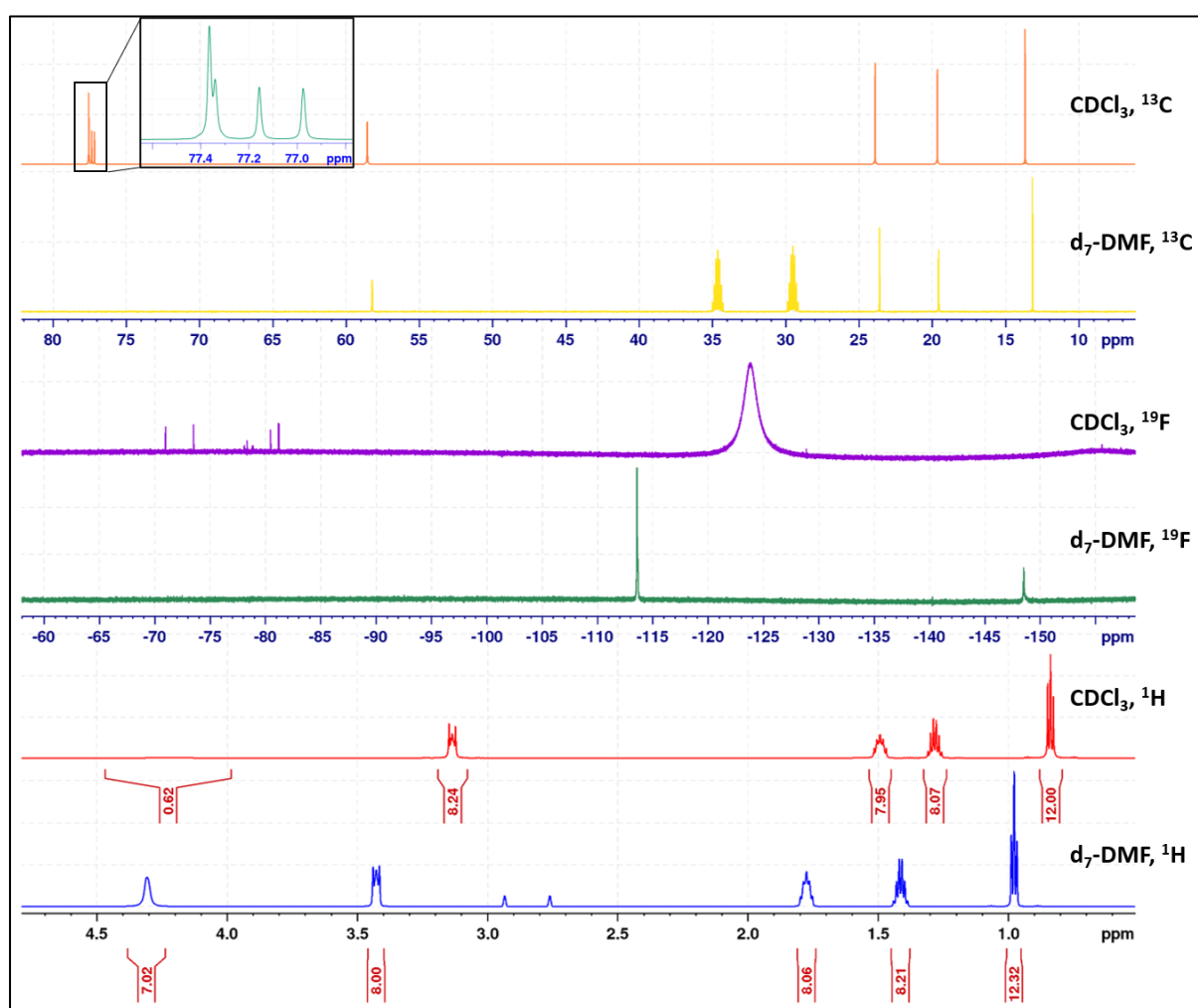


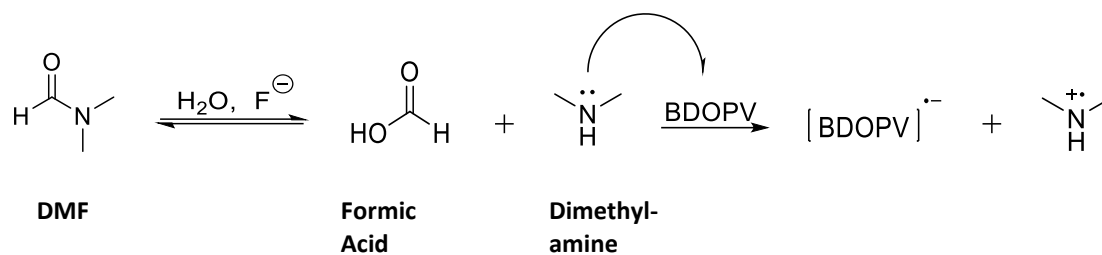
**Figure 3.4.**  $^{13}C$  (top),  $^{19}F$  (middle) and  $^1H$  (bottom) NMR of TBAF·3H<sub>2</sub>O crystals in deuterated chloroform and DMF solutions. Inset shows  $CHCl_3$  carbon at 77.56 ppm which overlaps with  $CDCl_3$  solvent triplet. Shifts at approx. 2.9 and 2.8 ppm in  $^1H$  spectrum and 29.5 and 34.6 ppm in  $^{13}C$  spectrum run in  $d_7$ -DMF are residual  $^1H$  and  $^{13}C$  from solvent.

The products of interactions between TBAF·3H<sub>2</sub>O and the solvents  $d_7$ -DMF and  $CDCl_3$  outlined in Scheme 3.4 are sensible predictions based on previous literature and the spectroscopic

data acquired. At this point it seems likely that fluoride is acting as a base in both solvents. In the case of  $d_7$ -DMF fluoride deprotonates water from the TBAF·3H<sub>2</sub>O crystals to produce hydroxyl anions which can then go on to dope electron deficient aromatics as outlined in Scheme 3.3.<sup>169</sup> In CDCl<sub>3</sub> the fluoride anion acts as base to the solvent to give trichloromethanide anions, these subsequently go on to deprotonate water and generate chloroform.

These predictions do not provide an adequate explanation, however, as to the dramatic differences in absorption spectra in DMF and chloroform solutions outlined in Figure 3.3. If both reactions occur as they are presented in Scheme 3.4 then hydroxyl anions are formed in both solvents. If hydroxyl is the active dopant then why does it appear as if more radical species are present in absorption spectra run in solutions of DMF? In addition to this the  $pK_a$  of fluorides conjugate acid is 3.1, this is much lower than the  $pK_a$  of both water and chloroform (approx. 15.7 for both). This suggests that fluoride should not act as a Brønsted base to either of these compounds.

As an alternative pathway the base catalysed hydrolysis of solvent DMF was suggested in the previous section. The product of solvent breakdown dimethylamine may act as an electron donor to BDOPV, as outlined in Scheme 3.5 mechanism. Since the NMR solvent  $d_7$ -DMF is deuterated it would be expected that the products of hydrolysis, formic acid and dimethylamine, would also be deuterated and therefore invisible in the <sup>1</sup>H NMR spectrum. The <sup>13</sup>C NMR spectrum of TBAF·3H<sub>2</sub>O in solutions of  $d_7$ -DMF revealed no signs of DMF breakdown products, however. Formic acid has previously been reported to exhibit a <sup>13</sup>C shift at 162.86 ppm in the aprotic polar solvent  $d_6$ -DMSO.<sup>279</sup> Dimethylamine was also not seen at the previously reported shift of 38.21 ppm.<sup>280</sup> In addition to this it is likely that HF is formed from the deprotonation of water in the hydrolysis of DMF. HF is likely to act as a Brønsted acid to dimethylamine to give the dimethylammonium cation. The mechanism of doping outlined in Scheme 3.5 with dimethylamine as active dopant was therefore ruled out.



**Scheme 3.5.** Base catalysed hydrolysis of solvent DMF to give formic acid and dimethylamine. Possible subsequent n-type doping of BDOPV by dimethylamine.

### 3.2.4 Structures of Fluoride Doped BDOPV and 2F-BDOPV

The doped structure of BDOPV and 2F-BDOPV may present further insights into the active doping species. <sup>1</sup>H and <sup>19</sup>F NMR titrations were therefore carried out on BDOPV and 2F-BDOPV in solutions of CDCl<sub>3</sub> and d<sub>7</sub>-DMF. TBAF·3H<sub>2</sub>O concentrations between 0 and 1 molar equivalents were used for solutions of d<sub>7</sub>-DMF. In order to track the point of significant change to the UV-Vis-NIR spectra in solutions of chloroform (Figure 3.3), up to 20 molar equivalents were used in NMR titrations in solutions of CDCl<sub>3</sub>. Overlays of the full spectra are shown in appendix section 2.2. Both neat BDOPV and 2F-BDOPV were not soluble in d<sub>7</sub>-DMF at NMR concentrations however after the addition of over 0.5 equivalents of TBAF·3H<sub>2</sub>O the samples completely solubilised by eye. At these concentrations <sup>1</sup>H NMR signals for BDOPV and 2F-BDOPV, as well as <sup>19</sup>F signals in 2F-BDOPV were observable.

<sup>19</sup>F NMR titrations have previously been used to evaluate the reaction between fluoride anions and NDI.<sup>165, 166, 168</sup> As expected, no <sup>19</sup>F signal was observed for the neat spectrum of BDOPV in DMF (appendix 2.13). On increasing concentration of TBAF·3H<sub>2</sub>O up to 1 equivalent no <sup>19</sup>F signal was observed, however. Titrations of 2F-BDOPV with TBAF·3H<sub>2</sub>O up to 0.5 equivalents gave no <sup>19</sup>F signals. Two shifts were observed however at 1 equivalent of TBAF·3H<sub>2</sub>O at -122.8 pm and -125.0 ppm.

It was initially surprising to not observe either of the signals assigned as F<sup>-</sup> and HF<sub>2</sub><sup>-</sup> in the <sup>19</sup>F NMR of neat TBAF·3H<sub>2</sub>O (Figure 3.4). The observation of broadening and disappearance of <sup>19</sup>F signals has previously been suggested to be caused by an oxidation of fluoride anions to the paramagnetic F<sup>·</sup> in solutions of d<sub>6</sub>-DMSO<sup>165, 166</sup> or simply through the interaction of fluoride with radicals of another species.<sup>169, 281</sup> We determined that <sup>19</sup>F NMR in d<sub>7</sub>-DMF solution was

not a reliable technique for analysis of BDOPVs due to poor solubility, however the lack of  $^{19}\text{F}$  signals from  $\text{TBAF}\cdot 3\text{H}_2\text{O}$ , even at high concentrations, suggests the presence of radical BDOPV species.

$^{19}\text{F}$  NMR titrations of both BDOPV derivatives with  $\text{TBAF}\cdot 3\text{H}_2\text{O}$  in  $\text{CDCl}_3$  showed no significant changes at concentrations of  $\text{TBAF}\cdot 3\text{H}_2\text{O}$  below 1 equivalent (appendix 2.9 and 2.10), in agreement with UV-Vis-NIR spectra in Figure 3.3. Continuing to titrate until 20 equivalents of  $\text{TBAF}\cdot 3\text{H}_2\text{O}$  had been added did show changes. In both derivatives of BDOPV 3 equivalents of fluoride or more gave rise to a shift at  $-129.0$  ppm. For 2F-BDOPV a shift at  $-119.7$  ppm was seen to gradually decay upon addition of  $\text{TBAF}\cdot 3\text{H}_2\text{O}$  until it was no longer visible at 10 equivalents of  $\text{TBAF}\cdot 3\text{H}_2\text{O}$ .

Figure 3.5 shows aromatic regions ( $\delta \approx 6.5 - 9.6$  ppm) of  $^1\text{H}$  NMR spectra of BDOPV and 2F-BDOPV in deuterated chloroform ( $\text{CDCl}_3$ ) neat (**a** and **d**) and doped with 1 equivalent TBAF (**b** and **e**). No change in chemical shift can be observed between doped and undoped samples in  $\text{CDCl}_3$  solution although there is some peak broadening. This suggests that doping is severely quenched in chloroform with 1 equivalent of fluoride anions, a relatively high dopant concentration, causing no observable chemical change to BDOPV and 2F-BDOPV.

Both BDOPV derivatives were not soluble in DMF at NMR concentrations and an NMR of neat semiconductors could not be taken, however addition of 1 equivalent of  $\text{TBAF}\cdot 3\text{H}_2\text{O}$  lead to both samples solubilising completely. Figure 3.5 shows solution NMR spectra of BDOPV (**c**) and 2F-BDOPV (**f**) doped with 1 equivalent  $\text{TBAF}\cdot 3\text{H}_2\text{O}$  in  $d_7$ -DMF. Changes in the aromatic region are observed when changing solvent from chloroform to  $d_7$ -DMF. Both changes in solubility and chemical environment suggest that the doping mechanism in  $d_7$ -DMF involves a chemical change to the BDOPV derivatives, although the complexity of the aromatic regions represent a surprisingly large change and suggests the presence of more than one BDOPV species.

Singlets at 9.10 ppm to 9.20 ppm are observed in  $^1\text{H}$  spectra obtained in  $\text{CDCl}_3$  for both BDOPV and 2F-BDOPV (Figure 3.5; **a**, **b**, **d**, **e**). These peaks are not visible in spectra obtained in  $d_7$ -DMF, a possible explanation being a nucleophilic aromatic substitution of fluoride ion at the position marked with \* in Figure 3.5. There are examples of quaternary ammonium fluoride salts being used in nucleophilic aromatic substitution ( $\text{S}_{\text{N}}\text{Ar}$ ).<sup>282-284</sup> These reactions typically



require the in situ generation of an anhydrous form of the quaternary ammonium fluoride salt unlike the addition of TBAF·3H<sub>2</sub>O crystals used here. Another possibility is the opening of the lactone rings via nucleophilic attack by fluoride on the carbonyl carbon leading to an upfield shift in the position of peak \*. A search of the literature provides no examples of ring openings of this kind or fluoride nucleophilic attack on esters or lactones suggesting something other than F<sup>-</sup> is the active dopant.

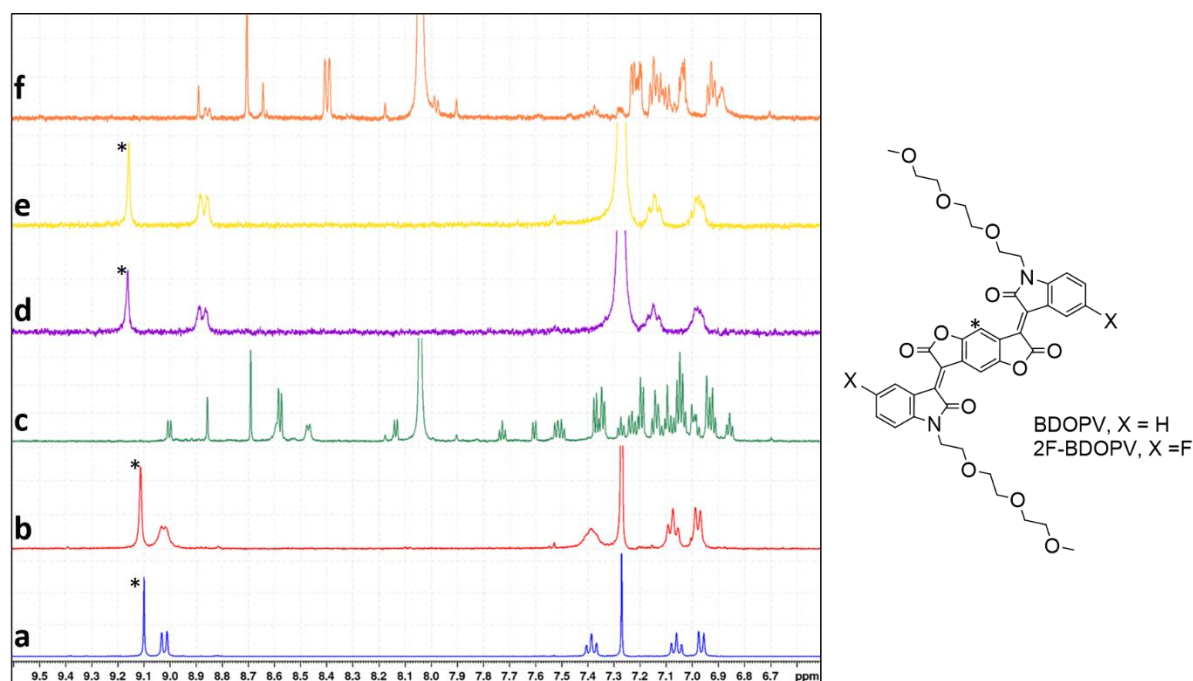


**Figure 3.5.** Overlays of <sup>1</sup>H NMR aromatic regions. BDOPV in deuterated chloroform neat (a), doped with 1 equivalent TBAF (b) and in deuterated DMF doped with 1 equivalent TBAF (c). 2F-BDOPV in deuterated chloroform neat (d), doped with 1 equivalent TBAF (e) and in deuterated DMF doped with 1 equivalent TBAF (f).

The mechanism proposed by Tam et al.<sup>169</sup> and, outlined in Scheme 3.3, points towards deprotonation of H<sub>2</sub>O by fluoride and the subsequent hydroxyl anion as the reactive species. Applying this to BDOPV we would expect to see a [BDOPV-2OH]<sup>2-</sup> type species undergo electron transfer with neutral BDOPV to give a [BDOPV-2OH]<sup>•-</sup> complex and [BDOPV]<sup>•-</sup>. In proton NMRs run in d<sub>7</sub>-DMF we could therefore expect to see hydroxyl proton shifts for both the [BDOPV-OH] dianions and radical anions. Two different proton environments were seen at 13.63 ppm and 13.28 ppm in d<sub>7</sub>-DMF solutions of BDOPV with 1 equivalent TBAF·3H<sub>2</sub>O which were not present in solutions of chloroform either neat or doped (Figure 3.6). In 2F-BDOPV, a shift at 13.29 ppm is also observed (Figure 3.6). It has previously been shown that OH protons on aromatic and quinoidal rings experiencing intramolecular hydrogen bonding show significant deshielding and chemical shifts in the region of 10 to 15 ppm.<sup>285</sup> Any hydroxyl

proton on the benzene or quinoidal carbon \* of [BDOPV] complexes would be expected to experience hydrogen bonding from the carbonyl bond of the neighbouring lactam ring and a reasonable assignment of 13 to 14 ppm can be made for this proton. The use of DMF as solvent, with its ability to act as hydrogen bond acceptor, may also contribute to the deshielding of the OH proton. For possible chemical structures of the aromatic and quinoidal hydroxyl substituted BDOPV derivatives, see Scheme 3.6.

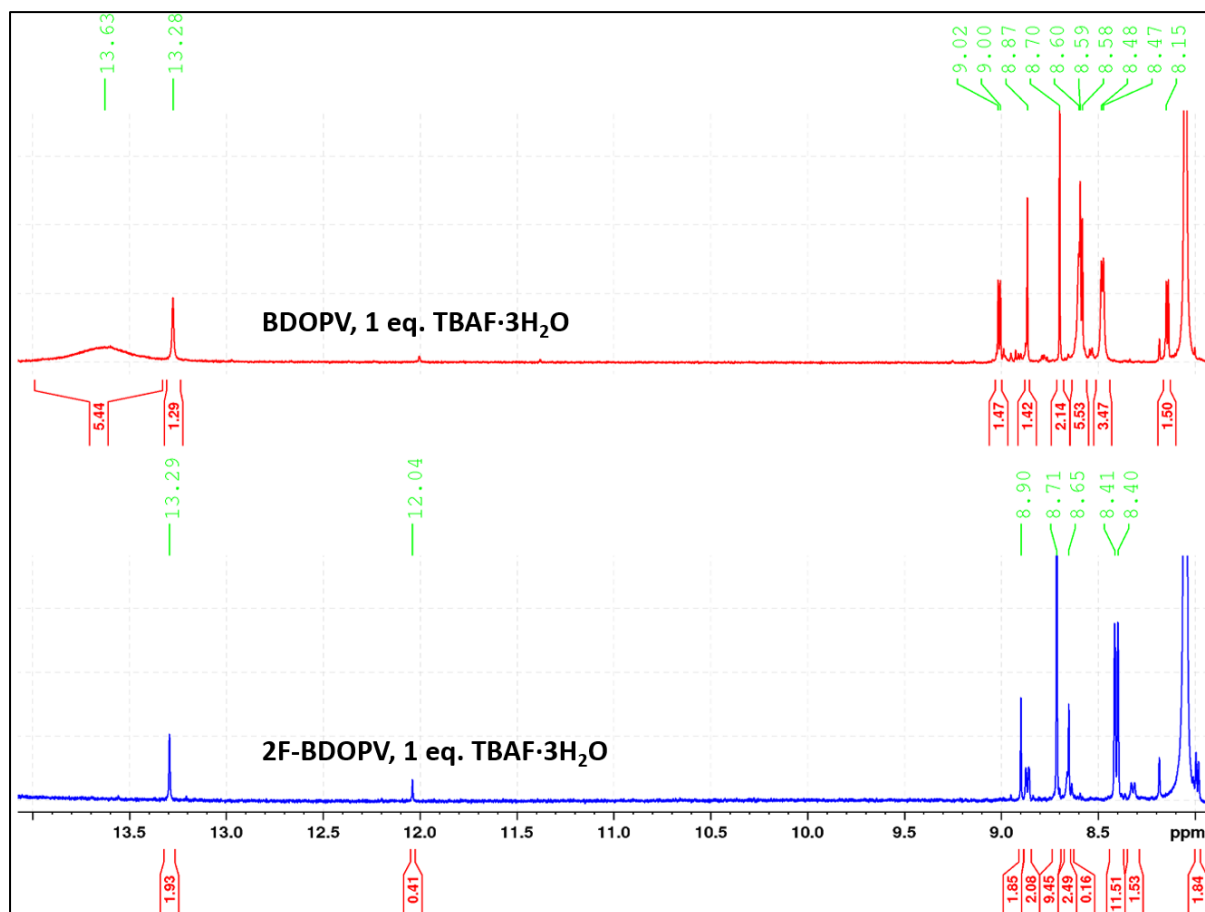
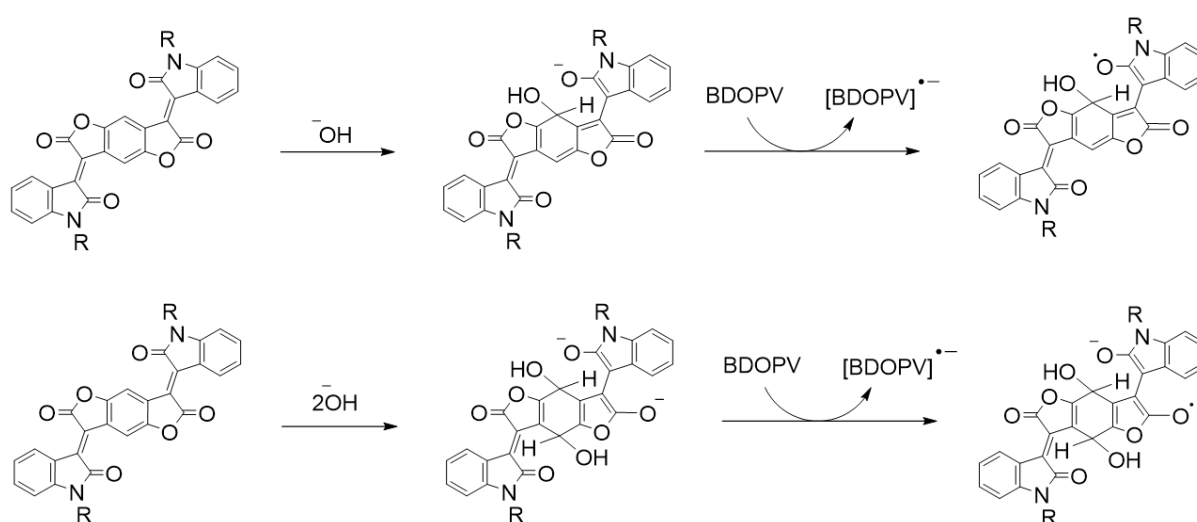


**Figure 3.6.** Downfield area of  $^1\text{H}$  NMR spectra of BDOPV (**top**) and 2F-BDOPV (**bottom**) in solutions of  $d_7$ -DMF doped with one equivalent TBAF·3H<sub>2</sub>O.

Based on the data above two possible mechanisms of doping through hydroxyl anions are presented in Scheme 3.6. In a solution of DMF, water molecules from the water of crystallisation were deprotonated by F<sup>-</sup>, as evidenced by the presence of HF<sub>2</sub><sup>-</sup> anions, and hydroxyl anions are formed. Subsequently hydroxyl anions form a charge transfer complex at the electron deficient central benzene ring of BDOPV generating a [BDOPV-OH]<sup>-</sup> species. This anionic complex then undergoes an electron transfer with a neutral BDOPV to give a BDOPV-OH neutral radical and a BDOPV radical anion. This is similar to the mechanism presented for

3-dimethyl-2-phenyl-2,3-dihydro-1*H*-benzo[*d*]imidazole (DMBI) hydride transfer dopants, using hydroxyl anions rather than hydrides.<sup>152</sup> Alternatively hydroxyl anions in the presence of BDOPV can form a [BDOPV-2OH]<sup>2-</sup> complex. A subsequent electron transfer on to neutral BDOPV molecules leads to BDOPV-OH radical anion and BDOPV radical anion. This is analogous to the mechanism reported by Tam for when TBAF·3H<sub>2</sub>O is used to dope an NDI compound.<sup>169</sup> The presence of an hydroxyl group having added on to the central benzene ring is supported by down-field chemical shifts in <sup>1</sup>H NMRs (approx. 13 – 14 ppm). Increased solubility of BDOPV upon doping also suggests that vinyl bonds have been broken and an increase in rotational freedom is possible between lactam and lactone rings.



**Scheme 3.6.** Possible mechanisms of doping in DMF solutions assuming the formation of hydroxyl anions. Top: Addition of hydroxyl anion to form BDOPV anion and a single electron transfer with neutral BDOPV to form a radical anion and neutral radical. Bottom: Addition of two hydroxyl anions on to BDOPV and a single electron transfer with neutral BDOPV to form two radical anions.

### 3.2.5 Electron Paramagnetic Spectroscopy

In order to confirm the presence of radical BDOPV species, like those shown in Scheme 3.6, electron paramagnetic resonance spectroscopy (EPR) was performed. Previously EPR has been used to identify the types of radical species present in NDI doped with TBAF·3H<sub>2</sub>O in solutions of DMF. The formation of an air stable NDI fluoride radical cation complex and air sensitive radical anion, as outlined in Scheme 3.2, was justified by the presence of a broad EPR signal not representative of the NDI radical anion when performed under ambient

conditions.<sup>170</sup> When air was removed from the system hyperfine splitting matching that of the NDI radical anion was observed.<sup>169, 286</sup>

Delocalised radicals in BDOPV would be expected to give rise to an EPR signal exhibiting hyperfine splitting with nitrogen and hydrogen. Figure 3.8. shows EPR spectra of BDOPV titrated with TBAF·3H<sub>2</sub>O in a solution DMF. Spectra were obtained in an ambient atmosphere. The overlays reveal BDOPV with 0.25 molar equivalents of TBAF·3H<sub>2</sub>O showed no EPR signal. At higher concentrations of TBAF·3H<sub>2</sub>O, up to 4 molar equivalents, no significant signal was still observed. The surprising observation of no EPR signal in BDOPV lead us to test fluoride doping on a known system in DMF. As a comparison to previous literature on fluoride doping with NDI type aromatics, NDI-TEG shown Figure 3.7 was chosen as control sample. The EPR titrations of NDI-TEG are shown in Figure 3.8. In the case of neat NDI-TEG no signal was observed and upon addition of TBAF·3H<sub>2</sub>O a broad signal formed which increased in intensity upon further addition of TBAF·3H<sub>2</sub>O. Previously the broadened signal in NDI has been attributed to a localisation of the radical in a complex similar to 24 shown in Scheme 3.2<sup>170</sup> or 26 shown in Scheme 3.3.<sup>169</sup>

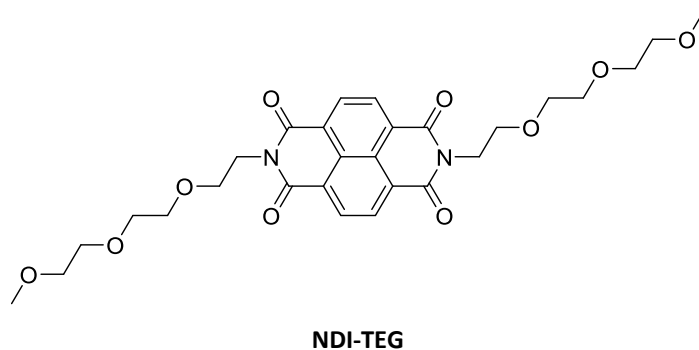


**Figure 3.7.** Structure of NDI-TEG.

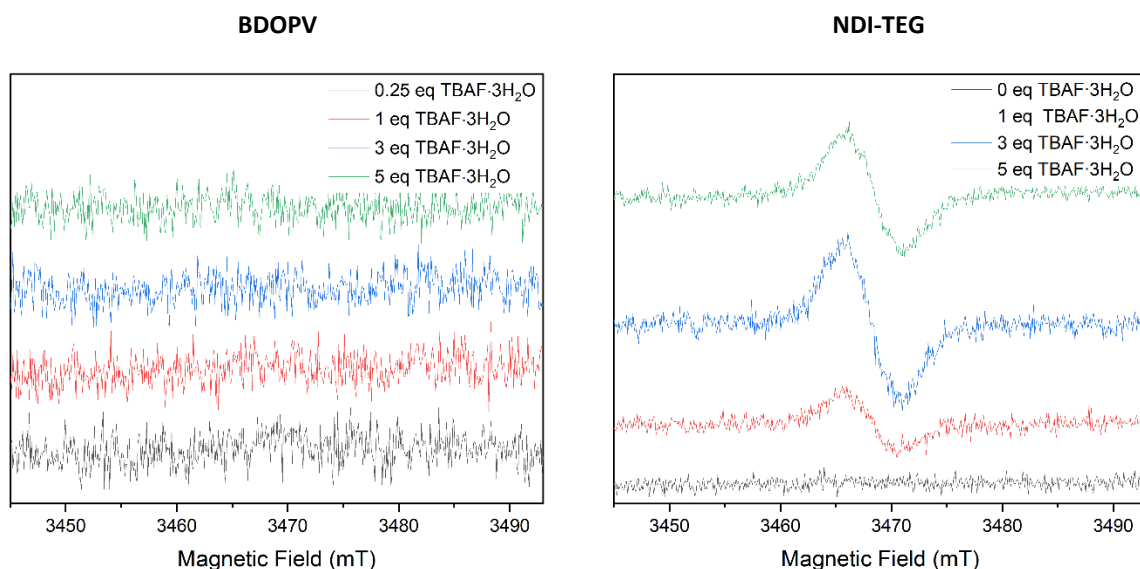


**Figure 3.8. Left:** EPR titrations of BDOPV with TBAF·3H<sub>2</sub>O in a solution of DMF under ambient atmosphere. **Right:** EPR titrations of NDI-TEG with TBAF·3H<sub>2</sub>O in a solution of DMF under ambient atmosphere. Molar equivalents of TBAF·3H<sub>2</sub>O are given in the legend.

The lack of an EPR signal for BDOPV when mixed with even large equivalents of TBAF·3H<sub>2</sub>O suggests that the production of an air stable radical cation fluoride complex, as outlined in Scheme 3.2, does not occur in BDOPV systems. Additionally, the EPR spectra cast doubt on the mechanisms presented in Scheme 3.6. It is possible that the BDOPV radical anion is oxidised under ambient conditions, similar to the NDI radical anions described in previous literature.<sup>170</sup> The lower lying LUMO of BDOPV compared to NDIs previously used however, would be expected to give an air stable radical anion observable by EPR. In addition to this the hydroxyl complexed radicals outlined in Scheme 3.6 would also be expected to produce an EPR signal. It could again be argued that ambient conditions lead to the oxidation of these radicals to neutral compounds, however a previous study observed a broad EPR signal under ambient conditions for when the hydroxyl substituted NDIs were later isolated as outlined in Scheme 3.3.<sup>169</sup>

Another possibility is the presence of bipolaron type charge carriers. The electrochemical measurements in Figure 3.2 indicated that BDOPV was capable of a second reduction at a modest potential of  $-0.82$  eV and it is possible that BDOPV has been doubly reduced to a bipolaron containing two radical species. Bipolarons are spin neutral and therefore invisible to EPR.<sup>287</sup> This does not explain why at low concentrations of TBAF·3H<sub>2</sub>O, i.e. 0.25 and 1 equivalents, no signal was observed as it would be expected that paramagnetic polarons would first be seen.

As an alternative to reactions involving electron transfer between BDOPV derivatives and TBAF·3H<sub>2</sub>O through radical pathways, it is possible that the features observed in absorption spectra in Figure 3.3 are due to the formation of aggregate complexes. The lack of observable radicals by EPR supports this theory. Chloroform acting merely as a better solvent to BDOPV and 2F-BDOPV may have led to the formation of less J-aggregates than in DMF and therefore a less intense red-shifted absorption at 750 nm. The addition of fluoride ions through TBAF·3H<sub>2</sub>O may further induce a change in light absorbing properties through a change in solvent polarity.<sup>288</sup> In order to confirm this more experimentation would be needed involving EPR, absorbance and emission spectra. The formation of aggregates also does not explain the complicated NMR spectra observed in solutions of d<sub>7</sub>-DMF (Figure 3.5).

### 3.3 Conclusions and Outlook

It has been shown that the introduction of TBAF·3H<sub>2</sub>O to BDOPV and 2F-BDOPV in solutions of DMF leads to a dramatic change in the absorptive properties of both BDOPV derivatives. A less dramatic change was observed when chloroform was used as solvent. It is unclear as to whether the differences in absorption spectra are due to differing pathways to electron transfer in each solvent or if red-shifting in absorption has occurred due to supramolecular reorganisation, such as the formation of J-aggregates.

In favour of the case for electron transfer reactions is the clear change in chemical environments observed in NMR spectra of both dopant and acceptors. NMR of TBAF·3H<sub>2</sub>O suggest that in DMF, fluoride anions are acting as a base to generate HF<sub>2</sub><sup>-</sup> anions which have previously been observed in successful examples of electron transfer to generate NDI radicals.<sup>165, 166, 169, 170, 259</sup> In chloroform, in which absorption spectra reveal less of a change upon addition of TBAF·3H<sub>2</sub>O, NMR spectra seem to suggest fluoride anions interact with the solvent. The lack of <sup>19</sup>F NMR signal upon titrations of acceptor with fluoride has previously been used to indicate the presence of radicals spatially close to fluorine atoms and was also observed here.<sup>169, 259</sup>

It is unclear however if electron transfer reactions actually took place. Previous studies have revealed fluoride anion donating an electron would be thermodynamically unfavourable<sup>170, 259</sup> and it has even been suggested that hydroxyl anions may be the active donors.<sup>169</sup> From NMR titrations of BDOPV and 2F-BDOPV in DMF it is clear that a change in chemical environment and solubility occurs upon addition of TBAF·3H<sub>2</sub>O. Although not isolated, these spectra suggest that the most likely products of reaction are hydroxy substituted BDOPV and 2F-BDOPV, similar to those outlined as the final product in Scheme 3.3.

It is unclear however as to why these systems do not exhibit any radical type species by EPR. Signals in EPR spectra of NDI acceptors have previously been observed, although it is still debateable as to why they are stable to air.<sup>170</sup> EPR spectra should be recorded in the future on BDOPV systems under inert conditions free of oxygen, avoiding the possibility of any radicals formed will be oxidised. BDOPV and 2F-BDOPV both contain lower lying LUMO levels than previously studied NDI derivatives however and should therefore be more capable of stabilising radicals. This points towards an explanation of the absorption spectra in Figure 3.3 which does not involve the intermolecular transfer of electrons. A change in the supramolecular interactions in DMF solutions may explain the additional absorption feature red-shifted with respect to molecular BDOPV electronic transitions. Photoluminescence spectroscopy may be able to detect if the absorbance at 750 nm is from vibrational modes in BDOPV aggregates or electronic excitations.

### 3.4 Acknowledgements

The work presented in this chapter was obtained in collaboration with several researchers. We would like to thank the following people for their contributions.

- Zhijie Guo for the synthesis of the electron acceptors BDOPV, 2F-BDOPV and NDI-TEG
- Dr Christian Nielsen for intellectual contributions concerning possible doping mechanisms and EPR measurements.
- Enrico Salvadori for EPR measurements.

# Chapter 4. Synthesis of thiazole containing highly ordered polymers

## 4.1 Introduction

For over a decade poly(2,5-bis-5-(4-tetradecylthiophene)thieno[3,2-*b*]thiophene) (PbTTT) has been a popular high-performance p-type semiconducting polymer.<sup>220</sup> Highlights of previous research on PbTTT are outlined in the introduction and the structure shown in Figure 4.1. To summarise, backbone planarity and a relatively large degree of supramolecular order lead to efficient charge transport both intramolecularly, along polymer chains, and intermolecularly, hopping between chains.<sup>221, 223-226</sup> In addition to this the alignment of interdigitated sidechains allows for dopants to be incorporated into the lamellar structure, minimising disruption to the polymer morphology.<sup>63</sup>

Relatively electron rich thiophene units make up the conjugated section of PbTTT. This leads to high IPs and low EAs and the stabilisation of p-type charges. The possibility of studying n-type charge transport and n-type doping in a system with comparable macromolecular structure to PbTTT is an attractive prospect. In order to go some way to achieving this we designed the two polymers poly(2,5-bis-5-(4-tetradecylthiazole)thieno[3,2-*b*]thiophene) (PbTzTT) and poly(2,5-bis-5-(4-tetradecylthiazole)thiazolo[5,4-*d*]thiazole) (PbTz3) (Figure 4.1). Introducing electron deficient thiazole units as a way of stabilising the LUMO has been shown to be effective in both donor-acceptor<sup>179, 289, 290</sup> and homopolymer<sup>186</sup> type systems. The pattern of alkylated five membered ring single bonded to a fused five membered ring system has been maintained with the intent of inducing the same interdigitation observed in PbTTT. In addition, the introduction of imine nitrogen allows for the possibility of attractive intramolecular interactions between sulphur and nitrogen leading to reduction in torsion between heterocycles.<sup>186, 207</sup> These attractive interactions between heteroatoms are illustrated in Figure 4.2 for previously described copolymers of alkylated thiophenes and thiazoles.<sup>186</sup> Calculations of the electron density in the orbital containing the thiazole nitrogen



lone-pair show that electron-density from this lone-pair is donated into the two C-S anti-bonding orbitals of the adjacent thiophene. This interaction acts to reduce the torsional angle between the two heterocycle units.

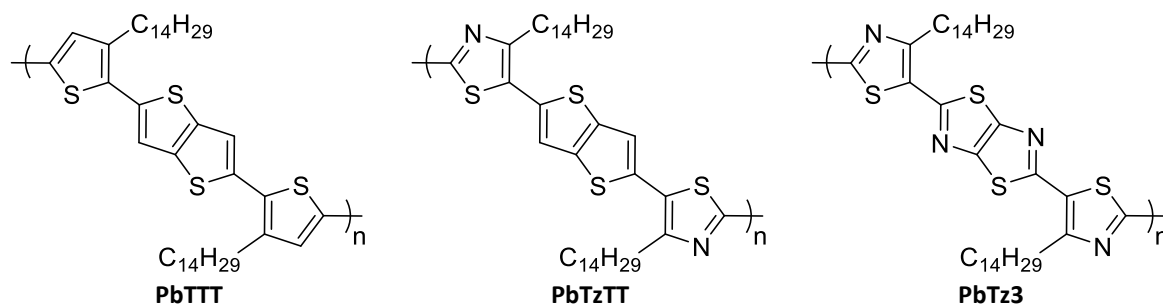


**Figure 4.1.** Structures of the three polymers discussed in this chapter.

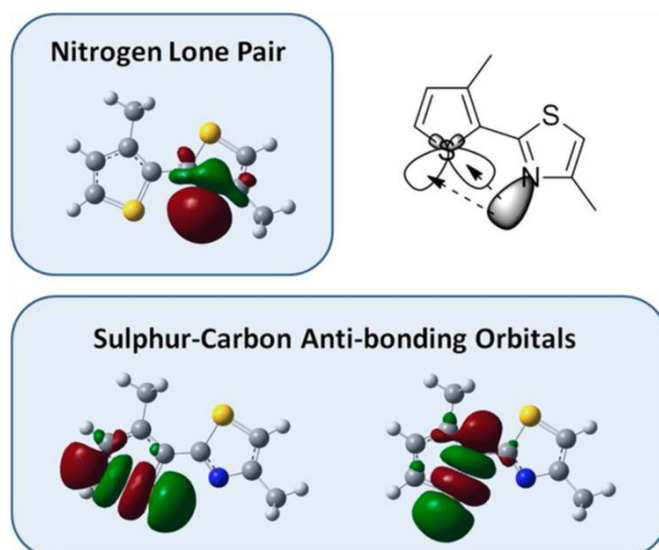
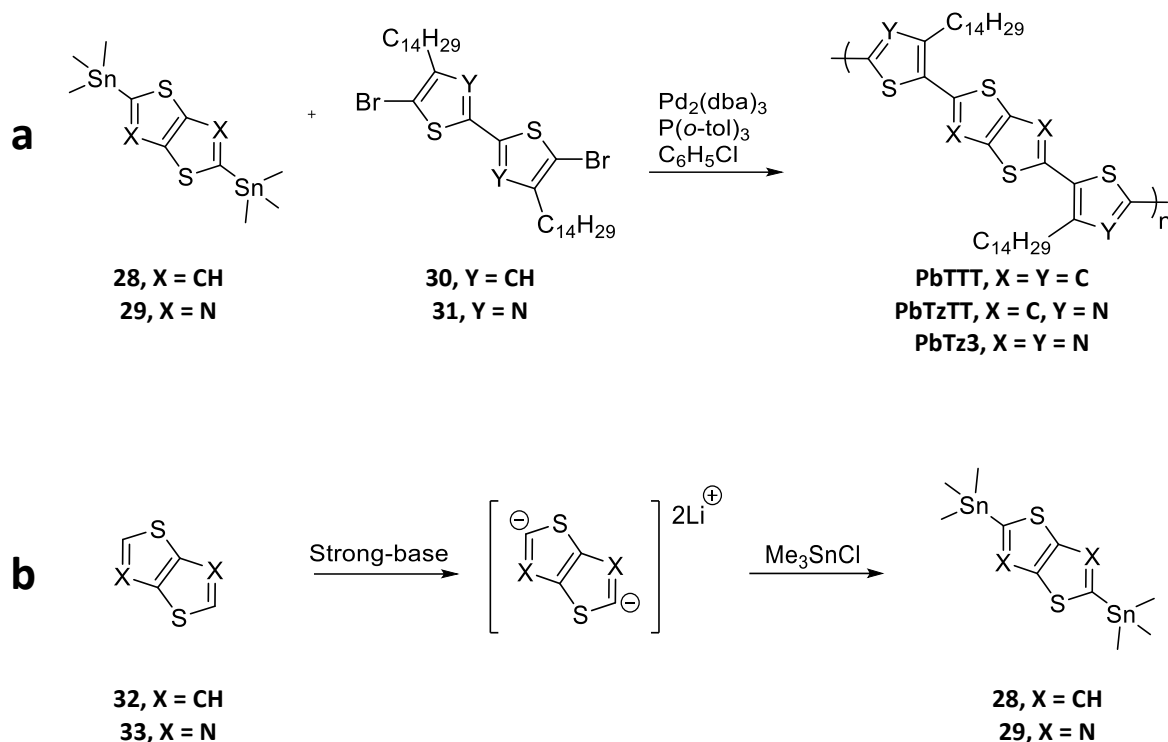


**Figure 4.2.** Natural bond orbital (NBO) calculations of the thiazole nitrogen lone-pair and the two C-S anti-bonding orbitals in thiophene. A schematic representation of the donation of the nitrogen lone-pair electron density into C-S anti-bonding orbitals is shown on the top right. Figure reprinted from reference 186.

PbTTT is routinely obtained through a palladium catalysed Stille cross-coupling polymerisation.<sup>220, 291</sup> This requires the synthesis of the monomer 2,5-bis(trimethylstannyl)thieno[3,2-*b*]thiophene (28) through the deprotonation of thieno[3,2-*b*]thiophene using strong-base and quenching with trimethyltin chloride as electrophile.<sup>220</sup> Both the polymerisation and monomer synthesis are outlined in Scheme 4.1. Described in this work is the successful synthesis of the polymer PbTzTT using the same Stille cross-coupling conditions. Some challenges in the synthesis of PbTz3 can however be foreseen. Preparation

of the stannylated thiazolo[5,4-d]thiazole (29) monomer would require treatment of thiazolo[5,4-d]thiazole (33) with strong-base and a subsequent treatment of the carbanion with trimethyltin chloride. A combination of previous literature and experimental work described in this chapter however suggests that the carbanion of 33 is not stable. A ring-opening similar to oxazoles<sup>292-294</sup> and subsequent decomposition similar to thiazoles with electron withdrawing groups on the 5-position<sup>295, 296</sup> was observed.



**Scheme 4.1.** **a)** Generalised scheme showing the Stille cross-coupling procedure used to make PbTTT<sup>220</sup> and the target polymers described in this chapter PbTzTT and PbTz3. The synthesis of the novel monomers 29 and 31 are also described in this chapter. **b)** Scheme outlining the deprotonation of fused heterocycles with strong-base then electrophilic attack of carbanion with trimethyltin chloride to give the previously made monomer 28<sup>220</sup> and the novel monomer 29.

Previous literature has also highlighted the challenges of direct electrophilic substitution onto 33.<sup>297, 298</sup> The two imine groups make it a very electron-deficient ring system and aromatic electrophilic attack on 33 by conventional means has never been observed. The only reported examples of direct electrophilic substitution on the 2-position of 'naked' 33 are pyridine catalysed bromination using a large excess of bromine, and chlorination using excess trichloroisocyanuric acid (TCICA).<sup>298</sup> Both reactions were not fully selective to mono or di-substituted products, were low yielding and were carried out in refluxing CCl<sub>4</sub>, a solvent which is too expensive to feasibly run reactions on large scales.

The rest of this chapter outlines attempts to reach the required monomers for Stille cross-coupling polymerisation to form PbTzTT and PbTz3. Some of the optoelectronic properties of the successfully synthesised PbTzTT are shown and compared to PbTTT. In attempting to synthesise PbTz3 some light is shed on the reactivity of the electron deficient thiazolothiazole ring-system and on functionalised thiazoles. An alternate route to PbTz3 via a double ring-closing condensation to form the macromonomer is then described.

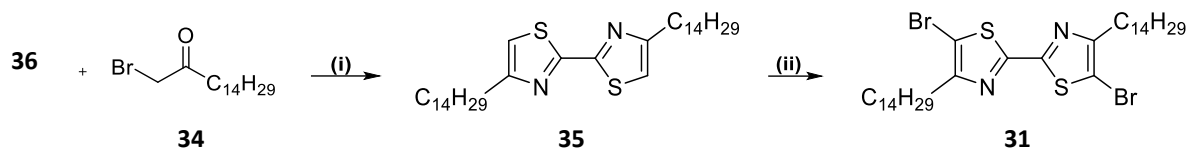
## 4.2 Results and Discussion

### 4.2.1 Synthesis and Characterisation of PbTTT and PbTzTT

The polymer PbTTT was synthesised via the procedure previously reported by McCulloch.<sup>220</sup> Monomers 28 and 30 were polymerised by Stille cross-coupling, as outlined in Scheme 4.1, to give PbTTT in a yield of 62%. The number average molecular weight,  $M_n$ , weight average molecular weight,  $M_w$ , and dispersity,  $\mathcal{D}$ , were determined by gel permeation chromatography (GPC) and are given in Table 2.2.

In addition to the stannylated thieno[3,2-*b*]thiophene monomer 28, the brominated 2,2'-bithiazole monomer 31 was also required for Stille polymerisation to make PbTzTT. The synthesis of 31 is described in Scheme 4.2. Using dithiooxamide (36) a double Hantzsch thiazole synthesis with  $\alpha$ -bromoketone (34) was performed to give the 4,4'-dialkyl-2,2'-bithiazole (35). The moderate yields of 40% were compensated for by the avoidance of functionalising the 2-position of thiazoles and then performing metal-catalysed cross-couplings to make 2,2'-bithiazoles.<sup>296, 299, 300</sup>

Compound 35 was then electrophilically brominated with N-bromosuccinimide (NBS) to give 31, in low yields of 36%. The imine nitrogen of the thiazole aromatic rings deactivates 31 to electrophilic attack. In addition to this the electron withdrawing nature of the 2-substituted thiazole ring deactivated the 5-position even further leading to low yields of bromination.<sup>301</sup> The multi-step yield in reaching 31 was 14% and was achieved in only two steps.



**Scheme 4.2.** Reagents and conditions: **(i)** 1,4-dioxane, r.t., overnight. **(ii)** 1:1  $\text{CHCl}_3$ :AcOH, NBS (3 eq.), 50 °C, overnight.

Stille cross-coupling polymerisation using monomers 28 and 31 to give the polymer PbTzTT is outlined in Scheme 4.1. After purification by Soxhlet extraction the polymer was obtained in 37% yield. The polymer was poorly soluble in most solvents including polar organics such as THF and DMF and the chlorinated solvents dichloromethane, chloroform and room temperature chlorobenzene. Any solutions used for analysis or thin-film formation were first heated at 140 °C under microwave irradiation for 20 mins in chlorobenzene or tetrachloroethane (TCE). The  $^1\text{H}$  NMR spectrum, obtained in a solution of deuterated tetrachloroethane ( $\text{d}_2$ -TCE) at a temperature of 60 °C, featured broad and unresolved peaks characteristic of polymers and is shown in Figure 4.3. A broad signal at 7.41 ppm was assigned as thienothiophene aromatic protons. Broad signals at 3.03 ppm, 1.53 ppm and 1.31 ppm were assigned to methylene protons of the sidechain. A broad signal at 0.92 ppm was assigned as the sidechain terminal methyl protons.

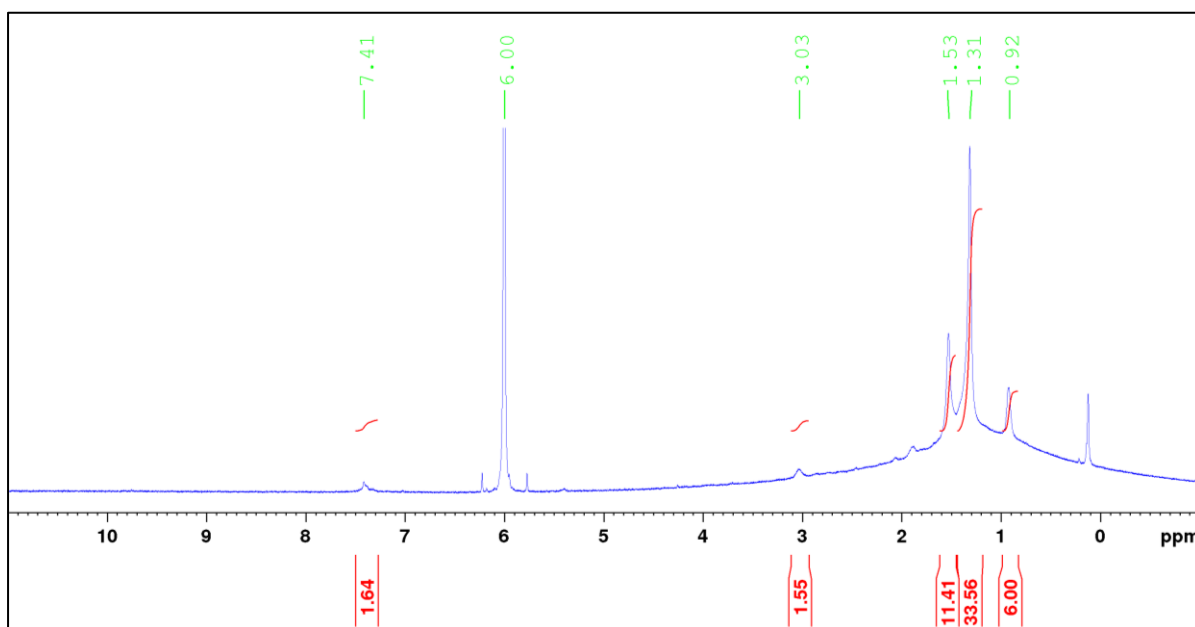


**Figure 4.3.**  $^1\text{H}$  NMR spectrum of PbTzTT in a solution of  $\text{d}_2$ -TCE.

The optoelectronic properties of PbTzTT are also outlined in Table 2.2 and are compared to PbTTT. Solution UV-vis absorption spectra of both polymers is shown in Figure 4.4. A red

shifting in the peak maxima and shoulders were observed in solution spectra of PbTzTT compared to PbTTT, suggesting the presence of J-aggregates through increased  $\pi$ -stacking in solution.<sup>302, 303</sup> The onset of absorption is also red shifted in thin film spectra, this leads to a decrease in the optical band gap of 1.87 eV in PbTzTT compared to 1.93 eV in PbTTT.

The electrochemical oxidation and reduction potentials of both polymers were measured on thin films using cyclic voltammetry. The IP of both polymers was estimated from the onset of oxidation. The PbTTT onset of oxidation of 0.24 V corresponded to an IP of 5.04 eV, which closely matched literature values.<sup>220</sup> In the positive CV of PbTzTT a surprisingly large increase in the oxidation potential was observed. The onset of oxidation was 0.70 V corresponding to a high IP of 5.50 eV. The onsets of reduction for PbTTT and PbTzTT were observed at -1.24 and -1.21 V respectively corresponding to EAs of 3.56 eV and 3.59 eV.

As has previously been observed in thiazole containing polymers, the introduction of imine nitrogen atoms in PbTzTT were seen to stabilise both HOMO and LUMO.<sup>186, 304, 305</sup> The electron withdrawing nature of the imine nitrogen decreases the electron density across the polymer chain and localises the LUMO to the thiazoles in PbTzTT, leading to an increase in the solid-state EA. A dramatic stabilisation of the HOMO was also observed in PbTzTT leading to a large increase in IP of 0.46 eV compared to PbTTT. This seems surprising when compared to previous studies in which both the HOMO and LUMO have been stabilised approximately equally in polymers in which thiazoles have been used to replace thiophenes.<sup>186, 304, 305</sup> Further studies including photoelectron spectroscopy, theoretical calculations and a comparison to PbTz3 are needed to confirm the origin of the extremely high electrochemical IP in PbTzTT.

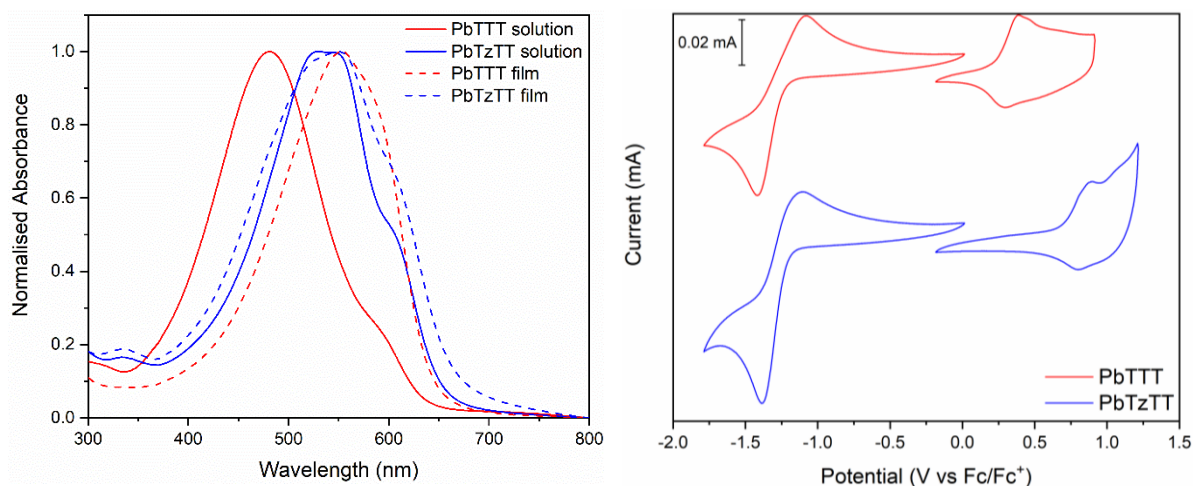


**Figure 4.4.** Left: Solution and thin-film UV-vis spectra of PbTTT and PbTzTT in chlorobenzene. Right: Cyclic voltammograms of thin films of PbTTT and PbTzTT. Referenced to Fc/Fc<sup>+</sup> standard with Ag/Ag<sup>+</sup> pseudo-reference electrode, platinum wire as counter electrode and glassy carbon working electrode.

**Table 4.1.** Molecular weight, optical and electrochemical Properties of PbTTT and PTzTT.

Polymer	$M_w^{[a]}$ (g.mol <sup>-1</sup> )	$M_n^{[a]}$ (g.mol <sup>-1</sup> )	Oxidation $E_{onset}^{[b]}$ (V)	Reduction $E_{onset}^{[b]}$ (V)	$\lambda_{max}^{[c]}$ (nm)	$\lambda_{onset}^{[c]}$ (nm)	Optical band gap <sup>[d]</sup> (eV)	IP <sup>[e]</sup> (eV)	EA <sup>[f]</sup> (eV)
PbTTT	69,903	34,099	0.24	-1.24	553	643	1.93	5.04	3.56
PbTzTT			0.70	-1.21	551	664	1.87	5.50	3.59

[a] Taken from gel permeation chromatography in chlorobenzene using calibration curve from polystyrene standards. [b] From thin film cyclic voltammetry using glassy carbon working electrode, platinum wire counter electrode and Ag/Ag<sup>+</sup> pseudo-reference electrode. Fc/Fc<sup>+</sup> half potential used as an external standard. Values are reported from the 4<sup>th</sup> cycle and measured at 100 mV.s<sup>-1</sup>. [c] From thin film UV-vis absorption spectroscopy. [d] Estimated from  $\lambda_{onset}$ . [e] Estimated from electrochemical onset of oxidation ( $E_{onset}$ ). [f] Estimated from electrochemical onset of reduction ( $E_{onset}$ ).

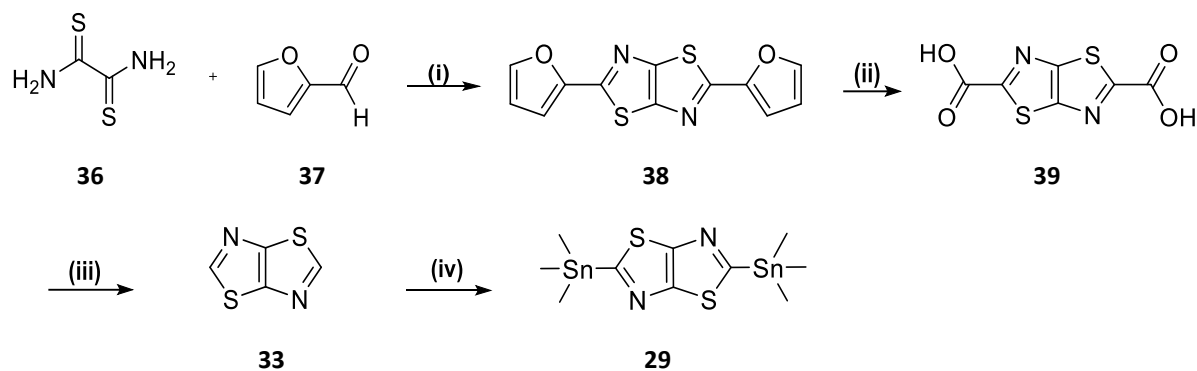
#### 4.2.2 Synthesis of PbTz3 and the Reactivity of Thiazoles

To synthesise PbTz3 by Stille cross-coupling polymerisation it was necessary to synthesise thiazolo[5,4-*d*]thiazole, 33. The first reported synthesis and identification of thiazolothiazole ring systems was reported by Ketcham<sup>297, 306</sup> and a slightly modified procedure reported by Benin<sup>298</sup> was used here and is shown in Scheme 4.3. Two steps in the route to 33 contain considerable practical problems. The ring-closing condensation to give the bis-furyl product (38) is inefficient, after recrystallisation the overall yield is 22 %. The nature of the double ring-closing condensation to form one molecule from three means the reaction is not

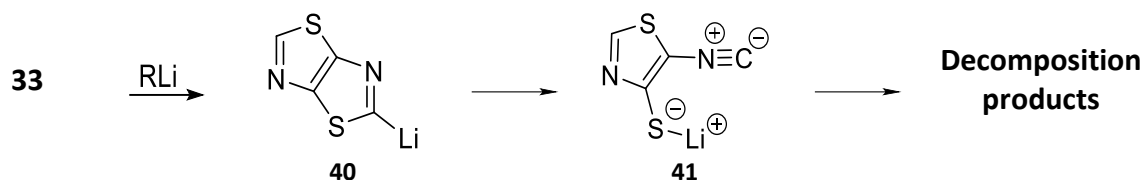
favoured entropically. In addition to this the high temperatures required produce a large amount of difficult to separate by-products.

The oxidation of 38 to give the di-acid 39 is also low-yielding, requiring over ten equivalents of potassium permanganate as oxidising agent. When scaling up, the large amounts of oxidising agent bring the risk of exothermic runaway and careful monitoring of the reaction is required. Separation of the product from black tarry side-products and excess manganese dioxide, from reduced potassium permanganate, was labour intensive and reduced the yield to 39%. Other routes to 2,5-substituted thiazolo[5,4-*d*]thiazole derivatives have been reported,<sup>307</sup> however this is the only route to unsubstituted thiazolo[5,4-*d*]thiazole currently available.

The monomer 29 was obtained in a yield of 17% by deprotonation of 33 using lithium diisopropylamide (LDA) and subsequent quenching of the carbanion with the electrophile trimethyltin chloride. The highest yields were obtained by deprotonating 33 with one equivalent of LDA and quenching with one equivalent trimethyltin chloride. This was followed by a subsequent deprotonation and electrophilic attack on the remaining unsubstituted carbon. Lower yields, of less than 5%, were obtained when adding 2 equivalents of *n*-butyllithium (*n*-BuLi) or LDA at once. A large amount of insoluble black material was found in the completed reaction mixture. Yields of 2-stannyl products less than 20% and the observation of decomposed side-products has also been reported for the deprotonation of thiazoles with electron withdrawing groups on the 5-position.<sup>295, 296, 298</sup> This was attributed to a stabilisation of the ring-opened isocyanate intermediate (41), shown in Scheme 4.4 for when 33 is metalated, which goes on to decompose. Computational studies have previously identified cleavage at the S-C2 bond in thiazole anions.<sup>308</sup>



**Scheme 4.3.** Reagents and conditions: **(i)** phenol (4.0 eq.), 190 °C, 1 h. **(ii)** *t*-BuOH, 90 °C, 2 h, then cooled to 60 °C, H<sub>2</sub>O, aliquat 336, then cooled to 10 °C, KMnO<sub>4</sub> (10.6 eq.), 14 h, H<sub>2</sub>O, NaHSO<sub>3</sub>. **(iii)** EtOH, reflux, 14 h. **(iv)** THF, -78 °C, LDA (1.2 eq.), 1 h, Me<sub>3</sub>SnCl (1.2 eq.), 1 h to r.t., -78 °C, LDA (1.2 eq.), 1 h, Me<sub>3</sub>SnCl (1.2 eq.), 1 h to r.t.



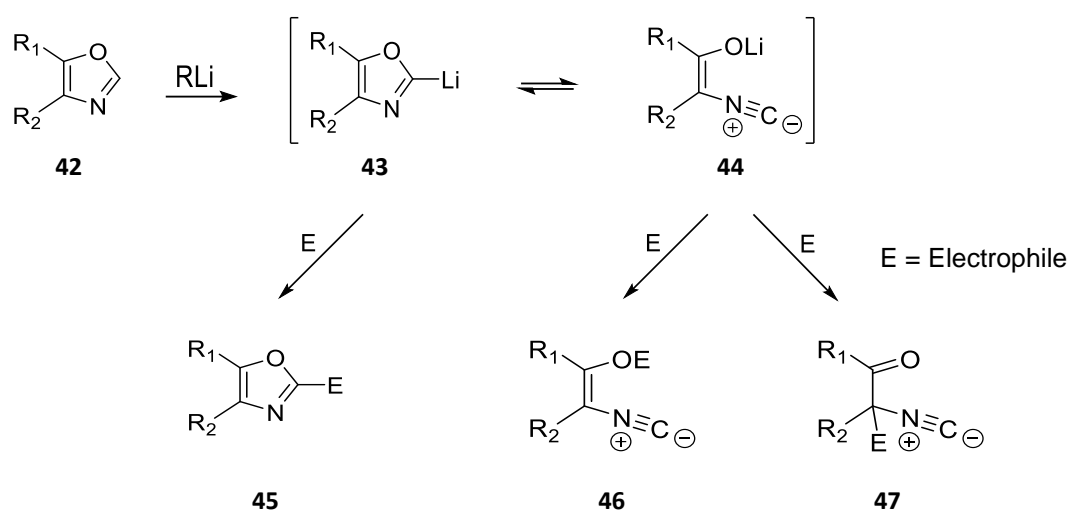
**Scheme 4.4.** Metalation of thiazolo[5,4-*d*]thiazole with alkyllithium and subsequent ring-opening to give isocyanate and decomposition.

The ring-opening described in Scheme 4.4 has also been extensively studied as a result of oxazole metalation on the most acidic 2-position. In oxazoles however it has been possible to selectively isolate ring-closed and ring-opened products in yields above 20% by selecting the correct electrophile. Scheme 4.5 summarises the products of oxazole metalation and quenching with different electrophiles. It has previously been reported that treatment of the metalated oxazoles with acyl chlorides<sup>292, 293, 309</sup> and silyl chlorides<sup>310</sup> leads to products similar to 46. The *O*-silyl isocyanate (46) product has however been known to ring-close into the 2-silyloxazole (45).<sup>292, 309</sup> Electrophilic substitution on to C4, to give 47, has only been observed when iodine is used as electrophile.<sup>311</sup> If R<sub>2</sub> = H ring-closure occurs to give 4-iodo-oxazole.

Since the product of metalation and substitution, 29, was isolable it was worthwhile to investigate the reaction of 40 with other electrophiles. 33 was first treated with one equivalent of *n*-BuLi and subsequently quenched with acetyl chloride. A large amount of insoluble black material was found in the completed reaction mixture which was filtered. The <sup>1</sup>H NMR of a separated compound, with lower *R<sub>f</sub>* than 33 and obtained in 13% yield, is shown in Figure 4.5. Either singlet at 2.57 ppm or 2.89 ppm could be attributed to the acetyl CH<sub>3</sub> protons. In addition, two singlets at 25.8 ppm and 21.9 ppm are observed in the <sup>13</sup>C NMR



spectrum, which could be attributed to CH<sub>3</sub> carbon of the acetyl group. <sup>13</sup>C signals at 173.0 ppm and 168.7 ppm could be attributed to the isocyanate or possibly to the C2 carbon of the ring-closed acetyl thiazolo[5,4-*d*]thiazole. It is impossible to conclude if the majority product from this brief study is the ring-closed 2-substituted thiazole 48 or one of the two possible ring-opened isocyanates 49 or 50. These results, coupled with the reaction to make 29, do suggest however that it is possible to isolate a substituted product from metalation and electrophilic substitution of thiazolo[5,4-*d*]thiazoles.



**Scheme 4.5.** Summary of the possible products of metalation and electrophilic substitution from previous reports. Scheme is adapted from previous reports by Pirrung<sup>293</sup> and Dondoni.<sup>292</sup>

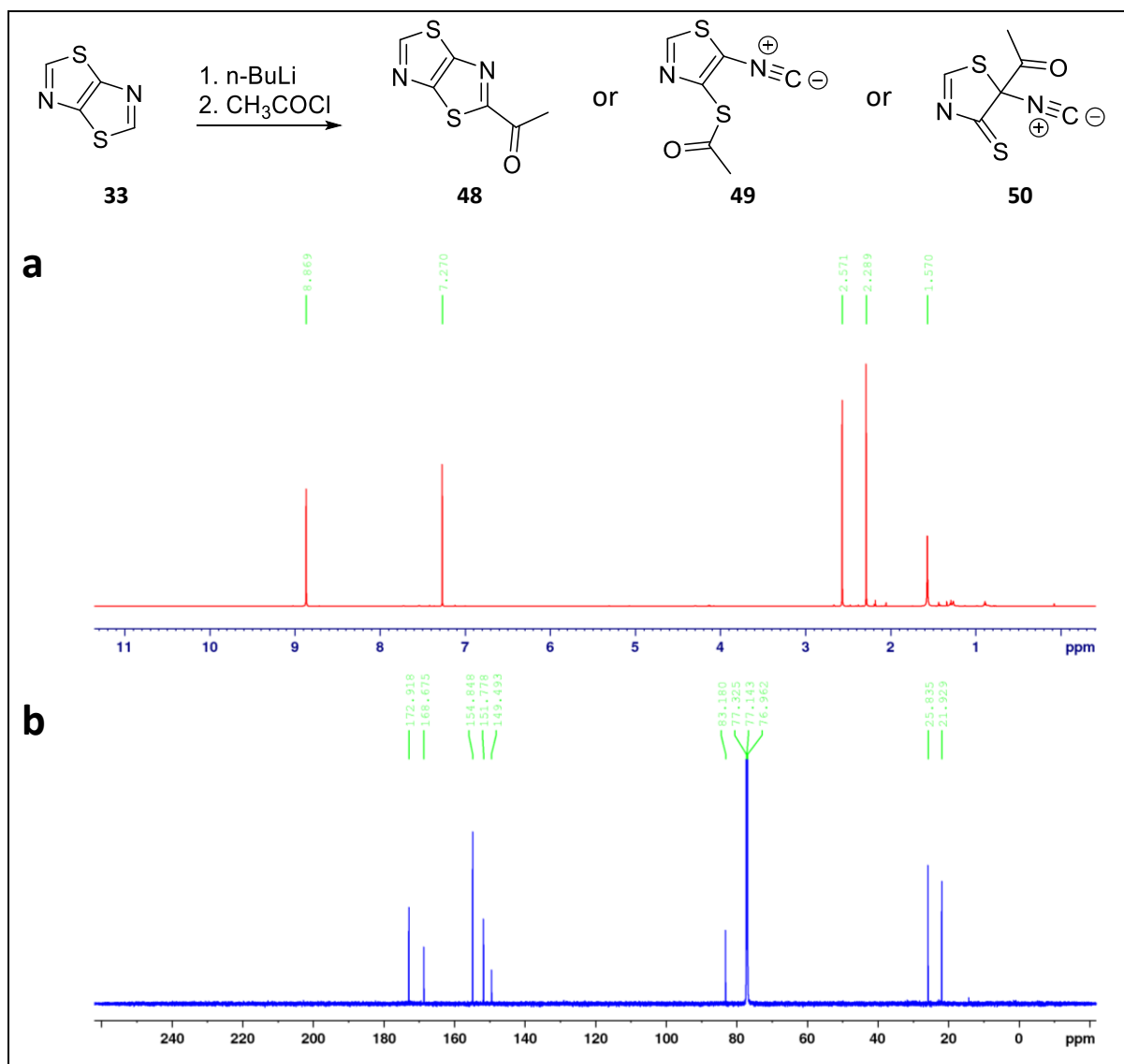
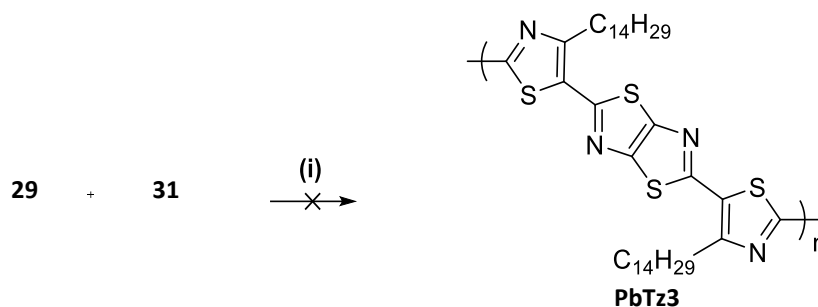


**Figure 4.5.** Reaction of lithiated 33 with acetyl chloride. **a)**  $^1\text{H}$  and **b)**  $^{13}\text{C}$  NMRs of the low  $R_f$  separated product.

Having successfully synthesised the monomers 29 and 31, a Stille cross-coupling polymerisation was attempted and is outlined in Scheme 4.6. After completion of the reaction no significant colour change was observed. In the formation of high molecular weight polymers, or even lower molecular weight oligomers, a redshifted absorption band compared to monomers, indicative of a lowering in the optical bandgap, was expected. The UV-vis absorption spectrum of the Stille polymerised PbTz3 in Figure 4.6 however, shows no shift in the absorption maxima or onset when compared to the monomer 31. Approximately an hour after the completion of the reaction a white crystalline solid began to precipitate out of the reaction mixture which was filtered and dried in vacuo. The filtrate then had all solvent removed in vacuo. The  $^1\text{H}$  NMR spectra of the precipitate, in Figure 4.6, revealed that the

unreacted monomer 31 had precipitated out of the reaction confirming that polymerisation had not occurred under Stille conditions.

A comparison of  $^1\text{H}$  NMR of the dried filtrate and the monomer 29, in Figure 4.6, shows an additional singlet at 8.95 ppm matching that of the C2 hydrogen on 33. This suggests that the trimethylstannyl group of monomer 29 had decoupled from the thiazolo[5,4-*d*]thiazole ring during reaction. In order to investigate the temperature dependant stability of 29 thermogravimetric analysis (TGA) was carried out and is shown in Figure 4.6. A mass loss of approximately 70% with onset at 79 °C was observed which corresponds to a loss in two trimethylstannyl groups. This confirms that the monomer 29 is not stable at the high temperatures required for cross-coupling polymerisations and the two trimethylstannyl groups were thermally cleaved before reaction could occur.



**Scheme 4.6.** The palladium catalyzed Stille cross-coupling reaction of the monomers 29 and 31 to make PbTz3. Reagents and conditions: **(i)** Chlorobenzene,  $\text{Pd}_2(\text{dba})_3$  (0.02 eq.),  $\text{P}(o\text{-tol})_3$  (0.08 eq.), microwave 100 °C 1 minute, 120 °C 3 minutes, 140 °C 5 minutes and 160 °C 5 minutes.

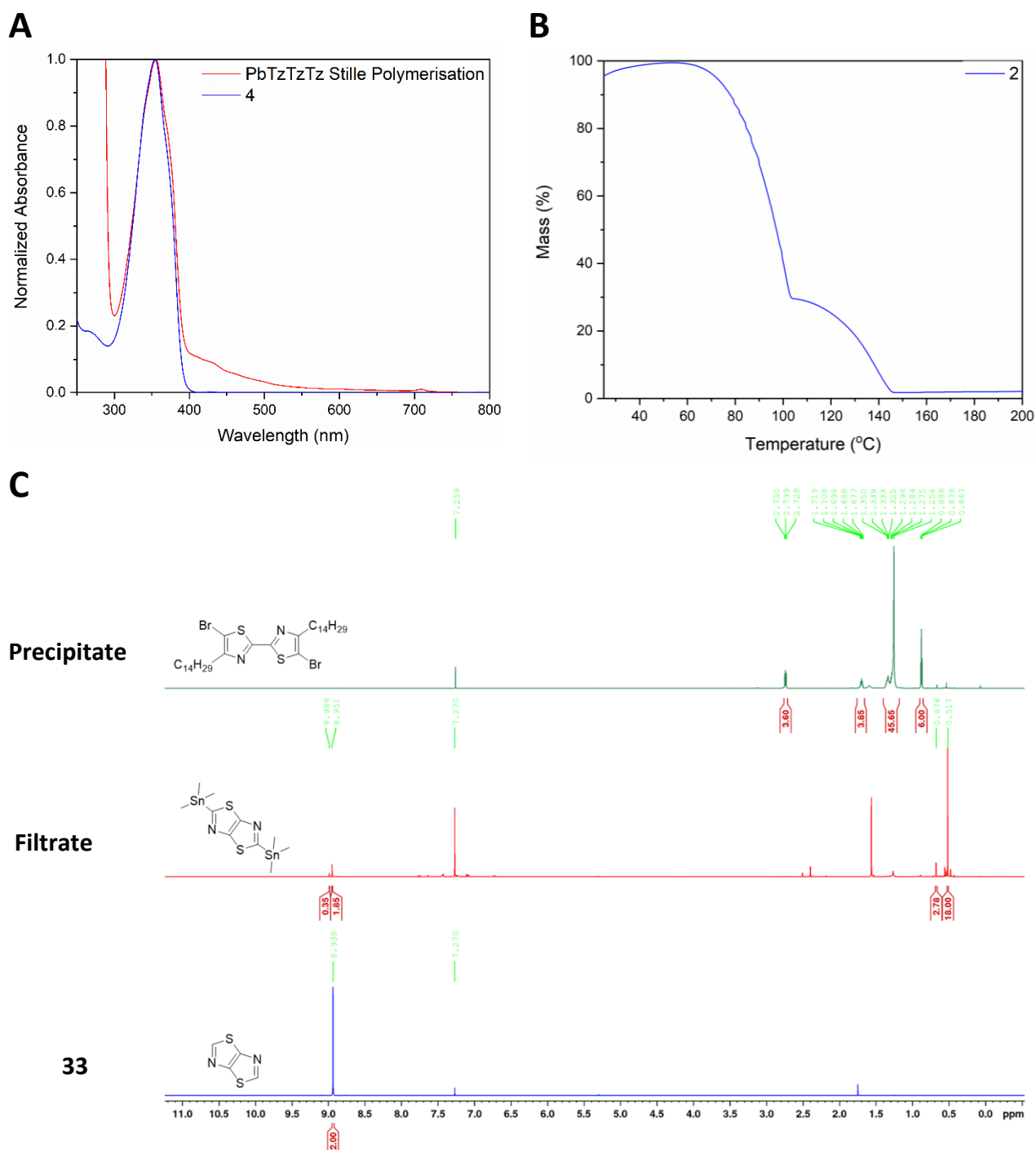
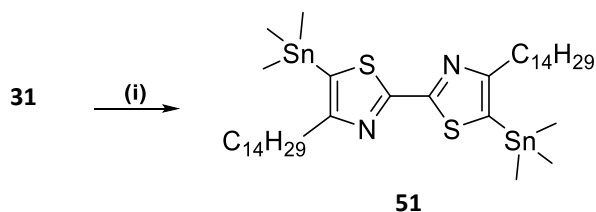


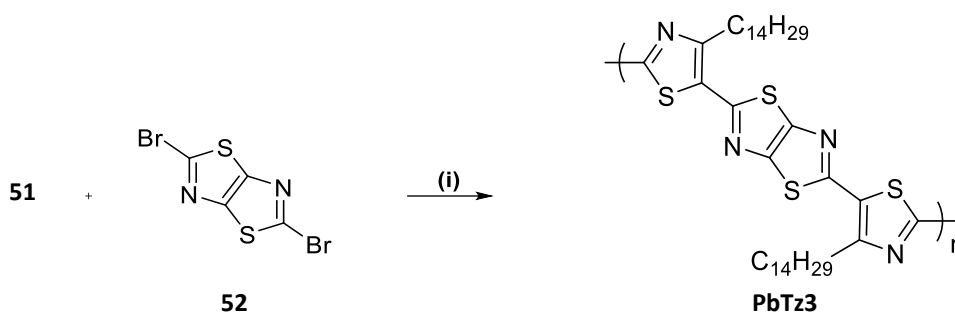
**Figure 4.6.** Analysis of the products from Stille cross-coupling polymerisation of 29 and 31. **a)** UV-vis absorption spectroscopy of the completed reaction mixture compared to the monomer 31. **b)** Thermogravimetric analysis (TGA) of the monomer 29. **c)**  $^1\text{H}$  NMR of separated precipitate and filtrate from the completed reaction mixture compared to unsubstituted thiazolo[5,4-*d*]thiazole.

The instability of monomer 29 meant that an alternative route to PbTz3 was needed. Reversing the functionalities of the monomers for Stille polymerisation was first attempted. This was not ideal since the 5,5'-hydrogens of the alkyl-2,2'-bithiazole, 35, are the least acidic and direct metalation on this position was not possible with *n*-butyllithium or *t*-butyllithium.

In addition to this lithium-halogen exchange on 31 using *n*-butyllithium was unsuccessful. Scheme 4.7 shows the eventual successful lithium-halogen exchange with 4 equivalents *t*-butyllithium (*t*-BuLi). This was followed by electrophilic substitution with trimethyltin chloride to give 51 in a moderate yield of 59%. The monomer 51 could then be used in the Stille polymerisation outlined in Scheme 4.8.



**Scheme 4.7.** Reagents and conditions: (i) THF,  $-94\text{ }^{\circ}\text{C}$ , *t*-BuLi (4.8 eq.), 1 h,  $\text{Me}_3\text{SnCl}$ , r.t. overnight.

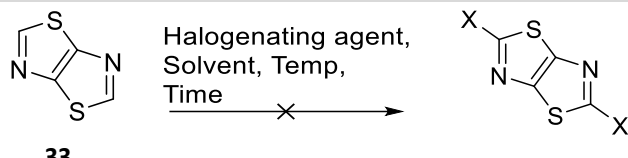


**Scheme 4.8.** Proposed Stille cross-coupling polymerisation between 51 and 2,5-dibromothiazolo[5,4-*d*]thiazole to make PbTz3. Reagents and conditions: (i) Chlorobenzene,  $\text{Pd}_2(\text{dba})_3$  (0.02 eq.),  $\text{P}(o\text{-tol})_3$  (0.08 eq.), microwave  $100\text{ }^{\circ}\text{C}$  1 minute,  $120\text{ }^{\circ}\text{C}$  3 minutes,  $140\text{ }^{\circ}\text{C}$  5 minutes and  $160\text{ }^{\circ}\text{C}$  5 minutes.

The 2,5-dibromothiazolo[5,4-*d*]thiazole (52) monomer in Scheme 4.8 has previously been synthesised from 33.<sup>298</sup> A large excess of bromine was used as brominating agent and 2 equivalents of pyridine as catalyst. The reaction was unselective to mono and di-brominated products and it was claimed that the barrier to the second halogenation was actually lower than the first. Repeating the experiment in refluxing chloroform or tetrahydrofuran (THF) lead to no reaction (entries 1 and 2, Table 4.2). It was previously proposed that the active halogenating agent in these reactions is the N-halogenated pyridinium cation. The use of chloroform as solvent may provide some competition in the formation of the N-halo pyridinium cation due to the acidic nature of chloroform. It is unknown however as to why the reaction could not be carried out in THF.

The same report described unsuccessful attempts at brominating 33 with NBS under normal conditions and in highly acidic environments.<sup>298</sup> Halogenation of aromatics deactivated to electrophilic substitution has previously been achieved by using sulphuric acid, trifluoroacetic

acid and triflic acid as solvent, presumably the strong acid solvent was used to activate the mildly electrophilic halogen.<sup>312, 313</sup> Electrophilic aromatic substitutions ( $S_EAr$ ) using bromine, NBS and N-iodosuccinimide (NIS) were carried out and are outlined in entries 3 to 6 Table 4.2. Each reaction yielded no di-halogenated product, less than 5% mono-halogenated and an almost quantitative recovery of pure starting material. This series of reactions suggests that 33 was too electron deficient to be used as a substrate in direct  $S_EAr$  using halogens as electrophiles. It is possible however that the strong acids could act to protonate 33 and deactivate it to electrophilic attack. Possible alternative conditions are discussed in the outlook.

Table 4.2. Reactions of 33 with Electrophilic bromine under different conditions.						
						
Entry	Halogenating Agent (equivalents)	Solvent	Temperature (°C)	Time (h)	Mono-substituted Yield (%) <sup>[a]</sup>	Di-substituted Yield (%) <sup>[a]</sup>
1 <sup>[b]</sup>	Br <sub>2</sub> (10)	THF	Reflux	4	0	0
2 <sup>[b]</sup>	Br <sub>2</sub> (10)	CHCl <sub>3</sub>	Reflux	4	0	0
3	NBS (3)	CHCl <sub>3</sub> :AcOH 1:1	Ambient	14	<5	0
4	NBS (2.2)	H <sub>2</sub> SO <sub>4</sub> :TFA 1:1	50	24	<5	0
5	NBS (2.2)	TFA	Ambient	24	<5	0
6	NIS (2.2)	TFA	Ambient	24	0	0

[a] Isolated yield after separation on silica column. [b] 2 equivalents of pyridine also used as catalyst.

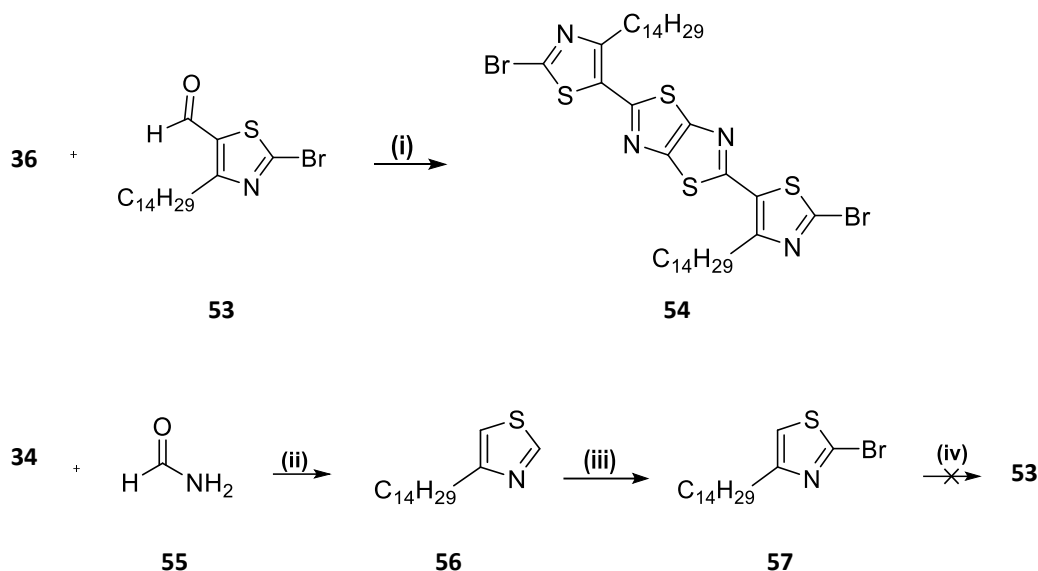
Since the compound 29 was successfully obtained in low yield by lithiation and electrophilic substitution of 33, treatment of 33 with strong base and quenching with bromine electrophiles was attempted. Using the same procedure as in the formation of 29 but using

CBr<sub>4</sub> as electrophile yielded no brominated product. The same large amounts of insoluble black material were found in the completed reaction mixtures as in previous metalations of 33. Mono-lithiation with one equivalent of *n*-butyllithium and one equivalent CBr<sub>4</sub> also yielded no product. The reaction was lower yielding than in any of the previous attempts at lithiation of 33 and none of the substituted ring-closed or isocyanate products, previously seen in oxazoles, were separated from the reaction mixtures. At this point attempts to synthesize PbTz3 through cross-coupling polymerisations of the monomers 51 and 52 were abandoned.

In order to avoid the functionalisation of 33 it was envisaged that the macromonomer 54 could be made using the reaction outlined in Scheme 4.9. Testing of different polymerisation conditions would then be required, and possibilities are discussed later in the outlook section of this chapter. First it was necessary to obtain the thiazole-5-carbaldehyde, 53, which could be used in ring-closing condensation with dithioamide, described by Ketcham,<sup>297</sup> to give the thiazole-flanked thiazolo[5,4-*d*]thiazole (54). The proposed route to 54 is shown in Scheme 4.9. Hantzsch thiazole synthesis using the thioamide of formamide (55) and  $\alpha$ -bromoketone (34) gave 4-tetradecyl-thiazole (56) in 87% yield. The 2-position of thiazoles are inert to direct electrophilic attack so electrophilic bromine could not be used to functionalise.<sup>301</sup> Instead the most acidic 2-position was metalated with *n*-butyllithium and trapped with CBr<sub>4</sub> to give 57 in a yield of 22%.

Finally, deprotonation of the 5-position of 57 was attempted. LDA was used as the strong-base, to avoid lithium-halogen exchange, and the deprotonated intermediate was quenched with DMF to give the 5-carbaldehyde 53. It became apparent in the <sup>1</sup>H NMR of the crude reaction mixture (Figure 4.7) that the majority product contained no aldehyde and no substitution on the 2-position. The signal at 8.91 ppm was assigned as a hydrogen on the 2-carbon of thiazole. This was likely a result of an intramolecular lithium-halogen exchange through a process known as halogen-dance. Most reported examples of thiazole halogen-dance reactions involve a migration of halogen from either the 2 or 5 position to the 4-position.<sup>295, 314-317</sup> The driving force for migration is quoted as being the added stabilisation of the anion when on the 5-position by a flanked bromine. The halogen-dance process is outlined in Figure 4.7 and it is the first example we know of in which the halogen migrates from the 2-position to the 5-position. We believe this is for two reasons. The 4-position is blocked by the electron donating alkyl group which destabilises the anion on the 5-position.

It has also previously been seen that deprotonated aromatics will undergo halogen-dance rearrangement so that the carbanion is on the more acidic position.<sup>316, 318</sup> With the 5-position of thiazole being the least acidic and the 2-position being the most acidic it is therefore not surprising that the 5-lithiated thiazole 58 rearranges to 59 as outlined in Figure 4.7.



**Scheme 4.9.** Reagents and conditions: **(i)** Nitrobenzene, dithiooxamide (0.5 eq.), 200 °C, 1 h, then r.t., THF, chloranil (0.2 eq.), 70 °C, 20 min. **(ii)** 55, P<sub>2</sub>S<sub>5</sub> (0.1 eq.), 1,4-dioxane, 0 °C, then 34 (0.7 eq), reflux, 1 h. **(iii)** THF, -78 °C, *n*-BuLi (1.2 eq.), 1 h to r.t., -78 °C, CBr<sub>4</sub> (1.2 eq.), 2 h to r.t. **(iv)** THF, -78 °C, LDA (1.2 eq.), 1 h to r.t., -78 °C, DMF (1.2 eq.), 2 h to r.t. **(v)** THF, -78 °C, *n*-BuLi (1.2 eq.), 1 h to r.t., -78 °C, DMF (1.2 eq.), overnight to r.t.



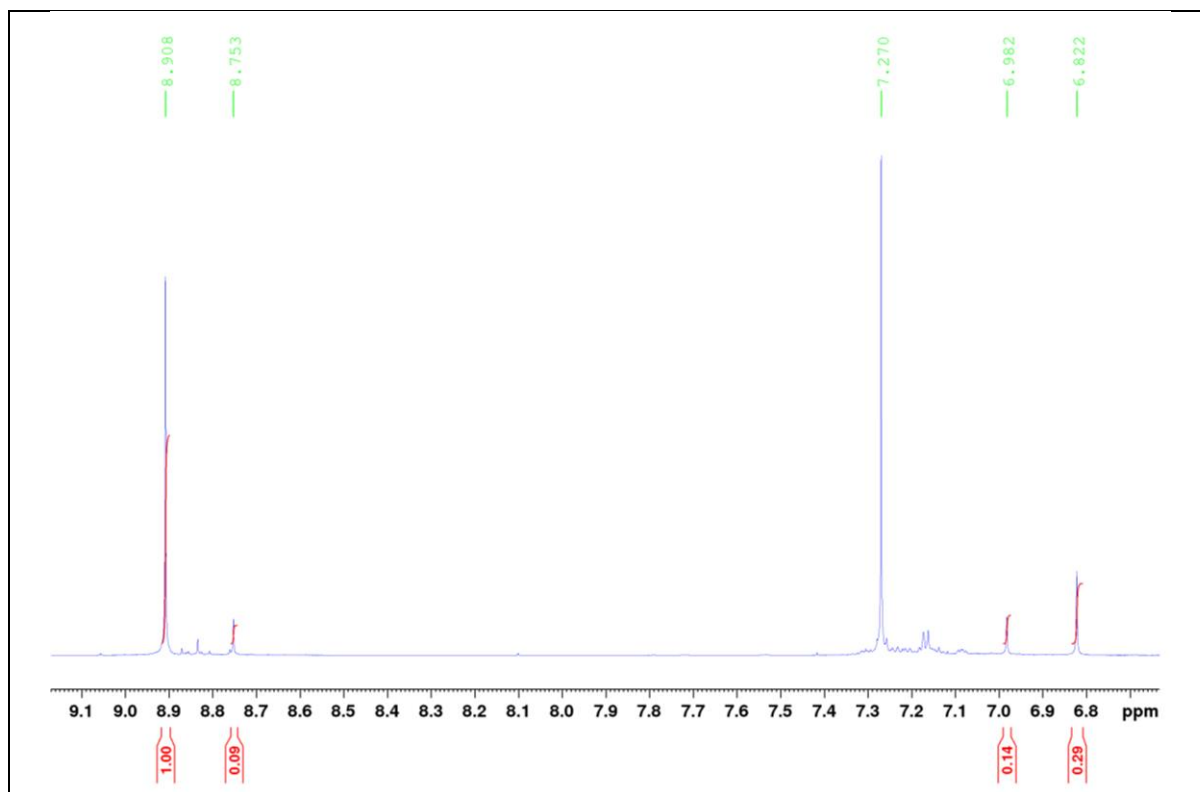
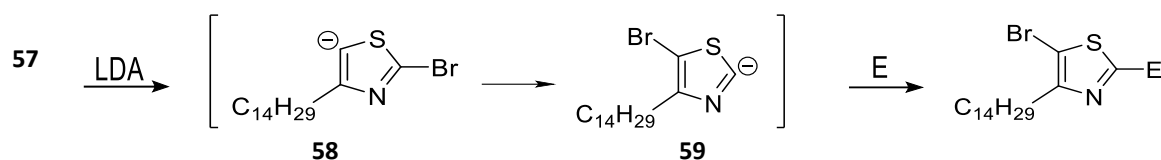
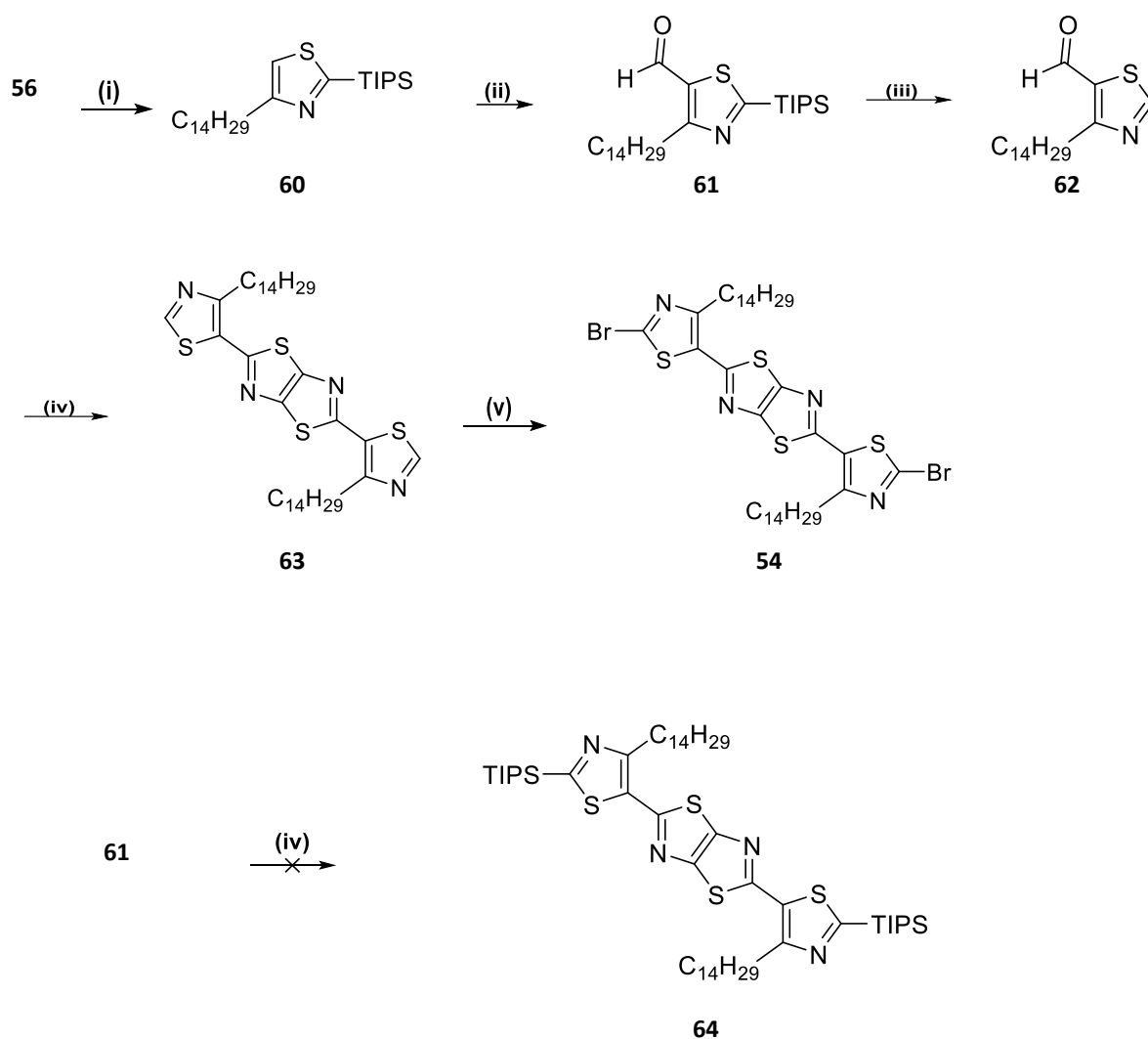


**Figure 4.7.** Top: Schematic representation of the halogen-dance reaction on deprotonated 57 with bromine migrating from 2 to 5 position. Bottom:  $^1\text{H}$  NMR of the metalated reaction mixture after quenching.

Since it was not possible to deprotonate the 5-position of 57 without rearrangement, it was decided that the macromonomer would be functionalised with bromine at the final opportunity. The 5-position of thiazole can undergo electrophilic substitution with activating groups on the 2 or 4-positions and direct electrophilic bromination on the 5-position was considered.<sup>301</sup> A subsequent lithium-halogen exchange could then be performed allowing for quenching with DMF to give 62. In order to avoid any further rearrangements through halogen-dance however it was decided that it was best to protect the 2-position with an alkylsilane. There is a previous example of trimethylsilyl (TMS) protecting groups migrating from the 2-position to the 5-position upon lithiation,<sup>316</sup> likely for the same reasons that a halogen-dance was observed in the lithiation of 57. It was therefore decided that 56 should be 2-protected with a triisopropylsilyl group (TIPS). 4-tetradecyl-2-triisopropylsilylthiazole-5-carbaldehyde (60) was therefore synthesised via lithiation and quenching with triisopropylsilyl chloride in 73% yield, as outlined in Scheme 4.10.

60 was successfully deprotected on the 5-position and quenched with DMF to give TIPS protected thiazolyl-5-carbaldehyde 61 in 81% yield. Double condensation ring-closure reactions to give 64 lead to complicated mixtures. The isolation of unreacted starting material and TIPS cleaved starting material suggested that the protecting group of the 2-silylthiazole was not stable to the high temperatures of reaction. It was therefore decided to deprotect 61 with TBAF to give the thiazolyl-5-carbaldehyde (62) in 44% yield, which was used for further testing of condensation ring-closure reactions.

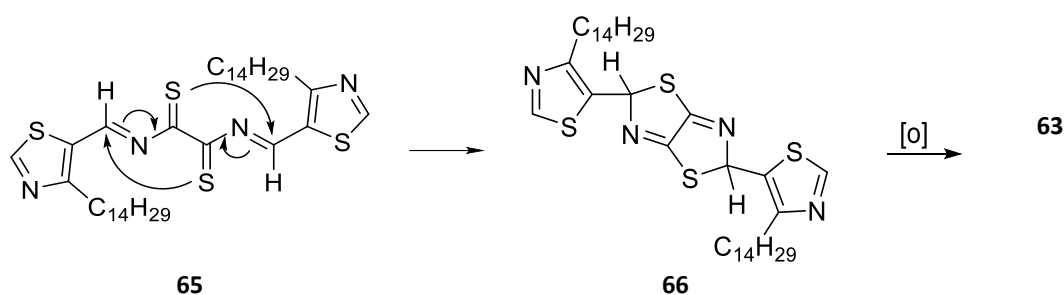


**Scheme 4.10.** Reagents and conditions: **(i)** THF,  $-78\text{ }^{\circ}\text{C}$ , *n*-BuLi (1.2 eq.), 1 h to r.t.,  $-78\text{ }^{\circ}\text{C}$ , TIPS-Cl (1.2 eq.), overnight to r.t. **(ii)** THF,  $-78\text{ }^{\circ}\text{C}$ , *n*-BuLi (1.2 eq.), 1 h to r.t.,  $-78\text{ }^{\circ}\text{C}$ , DMF (1.2 eq.), overnight to r.t. **(iii)** THF,  $0\text{ }^{\circ}\text{C}$ , TBAF (1.3 eq.), overnight to r.t. **(iv)** Nitrobenzene, dithiooxamide (36) (0.5 eq.),  $200\text{ }^{\circ}\text{C}$ , 1 h, then r.t., THF, chloranil (0.2 eq.),  $70\text{ }^{\circ}\text{C}$ , 20 min. **(v)** THF,  $-78\text{ }^{\circ}\text{C}$ , LDA (2.4 eq.), 1.5 h to r.t.,  $-78\text{ }^{\circ}\text{C}$ ,  $\text{CBr}_4$  (2.4 eq.), overnight to r.t.

The earliest examples of thiazolo[5,4-*d*]thiazole formation through ring-closing condensation involve large excesses of liquid aldehydes and no solvent.<sup>297, 306, 319, 320</sup> With only small

amounts of the aldehyde 62 available it was impossible however to perform test reactions while using it in such excesses as to act as both reagent and solvent. The use of solvent would be advantageous if it allowed for successful reactions using stoichiometric amounts of starting materials. Examples exist in the literature of reactions of aromatic aldehydes and dithiooxamide using DMF,<sup>321-326</sup> chlorinated aromatics<sup>327</sup> or nitrobenzene<sup>328, 329</sup> as solvent. Reviewing the literature revealed that reactions employing refluxing DMF as solvent were generally lower yielding, and used considerably longer reaction times, than when nitrobenzene was used.

The use of unsubstituted thiazolyl-5-carbaldehydes as reagents has also been reported in DMF,<sup>322</sup> however higher yields were reported when nitrobenzene was used with microwave heating at 150°C.<sup>328</sup> The method also involved the addition of an oxidant, chloranil, towards the end of reaction. The known intermediates of reaction 65 and 66 are shown in Scheme 4.11. It has been proposed that for the reaction to go to completion dehydrogenation of the intermediate 66 by a mild oxidant is required.<sup>306, 328</sup>



**Scheme 4.11.** Known intermediates in the reaction of aromatic aldehydes with dithiooxamide and their cyclisation and oxidation to form thiazolo[5,4-*d*]thiazoles.

Based on the previously discussed literature and proposed mechanism it was therefore decided to carry out our initial reactions on 62 at high temperature (>150 °C) using nitrobenzene as solvent and chloranil as oxidant. Chlorobenzene was also tested as an alternative solvent. The three reaction conditions outlined in Table 4.3 were attempted in the synthesis of 63 and the product separated from reaction mixture in each case by column chromatography on silica gel. The product 63 was identified in each case by <sup>1</sup>H and <sup>13</sup>C NMR as well as the [M+H]<sup>+</sup> molecular ion peak from ESI mass spectral analysis. A previously reported upfield shift in the aromatic proton, compared to starting material 62, was observed in <sup>1</sup>H NMR spectra.<sup>329</sup> This was due to the loss of the deshielding aldehyde group, the proton of which was also not observed.

Entry 2 gave the highest yields of 30%. Using lower temperatures gave moderately lower yields of 21%. Analysis of the crude reaction mixture and separated side products from both entry 1 and 2 showed no signs of the intermediates 65 and 66. Previously these intermediates have been visible in unseparated reaction mixtures which did not use an oxidant.<sup>306, 328</sup> This suggests that each reaction in nitrobenzene went to completion with the addition of 0.5 equivalents of chloranil. The reaction in chlorobenzene, heated under microwave irradiation, (entry 3) gave only recovery of starting material. The slightly oxidative nature of nitrobenzene may mean it is a better choice of solvent for this reaction.

A possible explanation for the low yields may be that the initial step of the reaction involves nucleophilic attack of the thioamide on the carbonyl carbon of the aldehyde. Electron deficient aromatic groups may withdraw electron density from the carbonyl carbon making it more susceptible to nucleophilic attack. The electron donating alkyl group on 62 could lead to a slight deactivation of this carbon to nucleophilic attack. Another possibility is that the long alkyl chain simply blocks the aldehyde from nucleophilic attack. Further study into conditions and substituent effects are needed, however.

Table 4.3. Reactions of 62 with dithioamide.				
<b>62</b>	<b>36</b>		<b>63</b>	
Entry <sup>[a]</sup>	Solvent	Temperature (°C)	Time (h) <sup>[b]</sup>	Yield (%) <sup>[c]</sup>
1	Nitrobenzene	150	1	21
2	Nitrobenzene	200	1	30
3	Chlorobenzene	180 <sup>[d]</sup>	1	0
<p>[a] All reactions used 2 equivalents 62 with respect to 36 [b] After the completion of each reaction THF and chloranil (0.5 eq.) were added and the reaction heated to 70 °C for 20 min. [c] Isolated yield after separation on silica column. [d] Heating carried out under microwave irradiation.</p>				

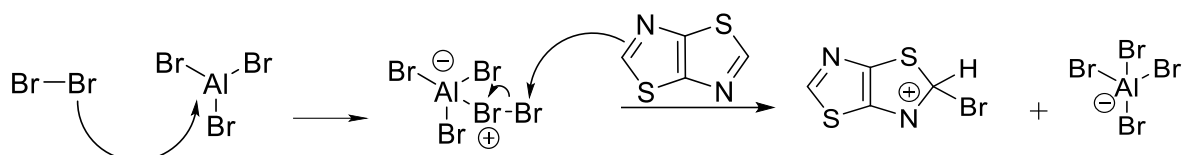
The brominated monomer unit 54 was finally synthesised as described in Scheme 4.10. The 2-positions of the flanked thiazole units are inactive to electrophilic substitution and, like in the synthesis of 57, bromination was achieved through deprotonation with strong base and electrophilic substitution with  $\text{CBr}_4$ . As previously described in Scheme 4.4, Scheme 4.5, Figure 4.5 and in previous literature concerning the metalation of thiazoles with electron-withdrawing groups on the 5-position,<sup>295, 296, 298</sup> it was assumed the low yield of 37% was due to a ring-opening to the isocyanate and subsequent decomposition. Similar large amounts of insoluble black material were observed as when 33 was treated with strong base.

### 4.3 Conclusions and Outlook

In conclusion the novel polymer PbTzTT was synthesised and comparisons of some optoelectronic properties were made with PbTTT. An expected stabilisation of both the HOMO and LUMO were observed in PbTzTT leading to a slightly higher solid-state EA. A considerable increase in the IP of 0.46 eV was also observed, further experimentation is needed to fully understand the large extent of this increase.

Significant problems in synthesising the polymer PbTz3 were encountered. The low yielding and labour intensive classical route to thiazolo[5,4-*d*]thiazole, coupled with its inactivity to electrophilic attack and instability upon metalation, caused significant problems in finding a route to a monomer for palladium catalysed cross-couplings. A brief investigation into selectivity of the metalated thiazolo[5,4-*d*]thiazole towards different electrophiles was performed. It was seen that stannyl electrophiles can be used to isolate the monomer 29 in low yields, it was deemed unsuitable for polymerisation however due to its instability at elevated temperatures.

Electrophilic halogenation of the thiazolo[5,4-*d*]thiazole was unsuccessful using strong Bronsted acids as solvents and it was suggested that this was due to the protonation of aromatic leading to deactivation. A reaction could be attempted however using bromine as brominating agent and a Lewis acid, such as  $\text{AlBr}_3$ , to activate the bromine to electrophilic attack as outlined in Scheme 4.12, avoiding any possibility of protonation.



**Scheme 4.12.** Possible use of Lewis acid catalyst for the electrophilic halogenation of thiazolo[5,4-*d*]thiazole.

An alternate route to the monomer 54 was designed. In reaching 54 some light was shed on the stability of 2-bromothiazoles to metalation. Halogen dance type rearrangements were observed in thiazoles with blocked 4-positions, the bromine migrating from the 2-position of thiazole to the 5-position. This allowed for metalation on the thermodynamically more stable 2-position. In order to avoid rearrangements such as this the route to 54 was redesigned as to involve silyl protection on the 2-position and 54 was synthesised in low yields.

After the successful synthesis of monomer 54 the immediate outlook involves its polymerisation to give PbTz3. Previously polymerisations of thiazole monomers halogenated on the 2-position have been achieved through Stille type polymerisations. Functionalising half of the monomers with trialkyltin functional groups<sup>316</sup> or reaction of 54 with hexamethylditin could be carried out. It would be preferential to avoid the use of highly toxic alkyl-tin reagents and some alternative reactions are outlined below.

Other metal catalysed cross-couplings could be used. Suzuki coupling could also be attempted although this will require one further transformation of the monomer to the boronate ester or acid.<sup>330</sup> Homo-polymerisations of di-brominated monomers have also previously been achieved using Yamamoto coupling.<sup>331-333</sup> An advantage to using this reductive cross-coupling is that no further functionalisation to create a nucleophilic aryl component is necessary, i.e. organo-tin and organo-boronate functionalities are avoided. A stoichiometric amount of Ni(0) catalyst is required and an excess of zinc or manganese to reduce the catalyst back to Ni(0).<sup>334</sup>

There are numerous high-yielding examples of the homo-coupling of 2-bromothiazoles using palladium acetate as catalyst.<sup>299, 335, 336</sup> Mildly basic conditions were used to reduce the catalyst to a usable Pd(0) state. The reaction is reportedly effective with both electron-withdrawing and electron-donating substituents, however the thiazolo[5,4-*d*]thiazole substituent of 54 is likely more electron-withdrawing than most substituents so far reported. A stepwise cross-coupling polymerisation with palladium acetate under basic conditions seems like a reasonable starting point for polymerisation of 54.

Grignard metathesis (GRIM) and Kumada type polymerisations have previously been successful on thiazole containing polymers.<sup>186, 337</sup> In the metalation and bromination of 63 however, it became apparent that the 2-position of the thiazole was susceptible to the ring-opening outlined in Scheme 4.5. Metalation by insertion of magnesium in the GRIM process may also lead to the same ring-opening which would likely translate to intolerably low molecular weights and yields in polymerisation to give PbTz3.

## Chapter 5. Conclusions

With the rapid rate of growth of the wider field of organic electronics it is becoming increasingly necessary for an increased understanding of the processes underpinning n-type charge generation. Chapter 2 and Chapter 3 of this work explore the nature by which n-type doping occurs, principally by investigating two mechanisms of electron transfer. The true nature of n-type charge transfer involving organic semiconductors is complex and has been discussed for a number of years. The work carried out in Chapter 3 adds to that discussion and ultimately lends weight to the idea that the transfer of one electron from fluoride to electron deficient aromatic is unfavourable.<sup>168-170</sup> Intramolecular charge transfer has shown promise in recent years as an alternative to introducing external doping species. The work in Chapter 2 however reveals that the structures and underlying mechanisms of a promising self-doping semiconductor are more complicated than assumed. The nature of intramolecular charge transfer, the decomposition pathways of quaternary ammonium hydroxides and the products of rylene diimides treated with aqueous bases all play a part in the generation of an n-doped semiconductor. Controlling each of these factors, during synthesis and processing, will be important in the near future as these materials begin to be applied in devices.<sup>338, 339</sup>

Chapter 2 dealt with the mechanism of quaternary ammonium dopants covalently bound to electron deficient conjugated units. The long-lived air stability of quaternary ammonium doped rylene diimides made them promising candidates for wider device fabrication without encapsulation. In this work structural characterisation through combined spectroscopic techniques highlighted that the imide groups, often used as the point of functionalisation for NDI and PDI conductors and semiconductors, are susceptible to hydrolysis during ion exchange of the precursor. The resulting ring-opened products can undergo the reverse condensation reactions to reform the cyclic imide. This ring-closing reaction is at play during the removal of solvent and complicates the already unknown mechanism of doping. This has implications on how we view previous literature concerning quaternary ammonium dopants. Previous studies on the mechanism of doping have not provided structural characterisations<sup>172</sup> and in one case the amine and imide nitrogen has been used in XPS studies to determine the quaternary ammonium moieties role in doping.<sup>174</sup> The ring-opened structure identified in this work, and the dynamic nature of the hydrolysis reaction, means



that amide nitrogen is also present in varying concentrations depending on film forming conditions and complicates previous spectroscopic studies. It is now apparent that future studies in to doping mechanisms must take in to account the hydrolysis of the rylene imide.

It was previously suggested that covalently binding dopants to semiconductors was an effective way of avoiding morphological incompatibility between the two.<sup>171,172</sup> In the case of NDI-OH, this work suggests however that there are still structure-morphology relationships which have an impact on the electrical performance of processed thin-films. AFM images of the films reveal large crystalline domains with increased grain boundaries in films drop-cast at low temperatures. These same films exhibit low conductivities and it was shown that at lower temperatures less ring-closing condensation of the hydrolysed product occurs. It is now possible to consider that films formed at high temperatures contain more naphthalene diimide units than those formed at lower temperature which likely contain ring-opened amides. The effect the chemical composition of the films has on the FMOs and morphology of films needs to be investigated further, however initial electrical conductivity measurements suggest more reformation of NDI is preferable.

As discussed in previous literature concerning PDIs doped by quaternary ammonium salts, the pathway by which the quaternary ammonium moiety decomposes at high temperature is unknown. How the products of this decomposition contribute to n-type doping is also still under investigation and should be the primary focus of future work on these compounds. Previous studies, both theoretical<sup>234, 235</sup> and experimental<sup>233</sup>, have concluded that the primary products of quaternary ammonium decomposition are those of an E2 Hoffmann type elimination. Similar experiments, using a combination of thermogravimetric and mass spectral analysis, could be used to confirm the presence of the Hoffmann product, trimethylamine, upon thermal decomposition of NDI-OH. The subsequent interactions between the products of decomposition and the NDI core could then be investigated in a similar way to the work carried out in Chapter 3 however the presence of ring-opened NDI products may complicate this analysis. An initial computational study, in which  $\Delta G$  of possible doping species complexing with ring-opened or closed NDIs is calculated,<sup>169, 340</sup> should help to direct further experimental work on this topic.

The second n-doping system investigated, in Chapter 3, was BDOPV and 2F-BDOPV doped with fluoride salts. The role which fluoride anions play in the introduction of n-type charge

carriers to organic semiconductors has been much studied in recent years with many mechanisms being proposed.<sup>165, 166, 168-170</sup> A large part of the debate surrounding fluoride dopants has concerned the efficacy of a direct electron transfer with fluoride anions as donors. The results outlined in Chapter 3 are in agreement with the most current literature and suggest that the role of fluoride anions is more complicated than simply acting as an electron donor.<sup>168-170</sup>

We initially observed a contrast in absorption spectra of BDOPV derivatives doped by fluoride in solutions of DMF and CHCl<sub>3</sub>. Differences in the interactions between fluoride and the two different solvents were immediately observed by NMR and suggested that fluoride preferentially acted as a base rather than electron donor. In deuterated chloroform the observation of CHCl<sub>3</sub> showed fluoride was acting to deprotonate the solvent and the subsequent trichloromethanide anions then went on to deprotonate water. A slow deuterium hydrogen exchange with water and solvent d<sub>7</sub>-DMF was also observed. This exchange has previously been observed in solutions of d<sub>6</sub>-DMSO.<sup>284</sup> In addition to this the inactivity of fluoride salts as dopants in certain chlorinated solvents has also been reported.<sup>170</sup> The characterisation of reactions between TBAF·3H<sub>2</sub>O and the solvents DMF and CHCl<sub>3</sub> outlined in Chapter 3 therefore compliment previous literature.

The consequences of the reactions of fluoride with solvents on the mechanisms of doping were then investigated. Structural characterisation of the doped species suggested that the active dopant was hydroxyl anions rather than fluoride. The observation of no EPR signal and high wavelength absorption features at zero equivalents of dopant raised the possibility that no electron transfer had taken place at all. The possibility that the absorbance features observed initially were due to aggregation effects still remain. A lack of EPR signal however may be due to BDOPVs ability to stabilise spin neutral bipolarons and is not necessarily an indication that charge carriers are not present. Further studies involving the doping of BDOPV derivatives must first confirm the presence of charge carriers before direct comparisons can be drawn between the interactions of fluoride with previously studied NDI derivatives and BDOPV. The UV-vis-NIR absorption data in DMF solutions, presented in Chapter 3, does indicate the presence of radical type BDOPV species, this needs to be confirmed with a more in depth EPR study however.

As well as exploring the fundamentals of n-type doping the work presented in this thesis attempts to address the lack of viable n-type semiconducting polymers. The possibility of synthesising n-type polymers exhibiting similar long-range order to PbTTT was explored in Chapter 4. Two polymers, PbTzTT and PbTz3, were designed which incorporated electron withdrawing imine bonds into the PbTTT architecture through the replacement of thiophene and thieno[3,2-*b*]thiophene rings with thiazole and thiazolo[5,4-*d*]thiazoles. This design rationale has previously been applied to the polymer P3HT where introduction of thiazole rings successfully stabilised both the HOMO and LUMO levels.<sup>186</sup> In addition to this thiazole rings have also been used as acceptor units in donor-acceptor and all-acceptor polymers for over a decade.<sup>341</sup>

Successful synthesis of the polymer PbTzTT was achieved through Stille cross-coupling polymerisation of the monomers 5,5'-dibromo-4,4'-ditetradecyl-2,2'-bithiazole and bis(trimethylstannyl)thieno[3,2-*b*]thiophene. The electron affinity and ionisation potential of PbTzTT were estimated by electrochemical and optical absorption techniques and were compared to the polymer PbTTT. An expected stabilisation of both the HOMO and LUMO energy levels was observed in PbTzTT when compared to PbTTT. The large increase in ionisation potential (5.50 eV for PbTzTT compared to 5.04 eV for PbTTT) measured by cyclic voltammetry on the thin film was unexpected, however. This led to a large increase in the observed electrochemical band gap and is surprising given the introduction of thiazole units would be expected to lead to more donor-acceptor character in PbTzTT compared to PbTTT.

The use of thiazolo[5,4-*d*]thiazole units in semiconductors has been limited to a few examples.<sup>342-345</sup> This is largely due to inefficient published synthetic procedures to reach unsubstituted thiazolo[5,4-*d*]thiazole and the subsequent chemical inertness of the heterocyclic ring.<sup>297, 298, 306</sup> The functionalisation of thiazolo[5,4-*d*]thiazole heterocycles for use as monomers in Stille coupling polymerisations to give PbTz3 was explored. As previously reported,<sup>298</sup> the electron withdrawing effect of two imine bonds made thiazolo[5,4-*d*]thiazole inert to electrophilic substitution reactions. Metalation also led to decomposition of the heterocycle before an electrophile could be introduced. There were indications however that ring-opened isocyanate intermediates can be preferentially trapped by particular electrophiles. In addition to this low yields of the substituted 2,5-bis(trimethylstannyl)thiazolo[5,4-*d*]thiazole product, made by metalation and quenching with

trimethyltin chloride, further indicated that metalation does not necessarily lead to full decomposition and ring-closed products can also be trapped. The possibility that a choice of electrophiles may be capable of trapping ring-closed thiazoles or ring-opened isocyanates means that further comparisons can be drawn with the reactions of lithiated 1,3-oxazoles.<sup>292, 293, 309-311</sup> Future studies, employing a variety of electrophiles, could be used to identify suitable reaction conditions for capture of isocyanate and thiazole type products and widen the synthetic scope of thiazolo[5,4-*d*]thiazoles and other 5-substituted thiazoles.

The complications in the functionalisation of thiazolo[5,4-*d*]thiazole lead to the design of an alternate route to PbTz3. Successful synthesis of the monomer 2,5-bis-5(4-tetradecyl-2-bromothiazole)thiazolo[5,4-*d*]thiazole was achieved through the use of a double ring-closing condensation reaction. Some optimisation of the reaction conditions was required, and it was found that a mild oxidant improved the yield of this reaction. Although the overall yield of this multi-step procedure to reach 2,5-bis-5(4-tetradecyl-2-bromothiazole)thiazolo[5,4-*d*]thiazole was low, 2%, it was preferable to avoid the harsh conditions of the oxidation step involved in thiazolo[5,4-*d*]thiazole synthesis and the difficulties in its functionalisation.

The work presented in this thesis has attempted to broaden the horizons of research into n-type organic semiconductors. In recent years interest surrounding n-type materials has led to a surge in publications concerning the topic. A drive to replace fullerenes as acceptor components in photovoltaic devices has seen a rise in the number of molecular n-type semiconductors.<sup>7, 346</sup> The production of new dopants has still been slightly slower, however. A notable exception to this is the 2020 reports of molecular hydride dopants based on triaminomethanes (TAM),<sup>347, 348</sup> which have been used to dope BDOPV polymers and achieve conductivities of over 20 S cm<sup>-1</sup>. These strikingly high conductivity values mean that we are beginning to see comparable electrical performance between n-type and p-type materials. Even with these improvements, an understanding of the mechanisms underpinning n-type doping is imperative. This makes the work in Chapter 2 and Chapter 3 important. Although the maximum conductivity values of NDI-OH may not reach the heights of TAM doped BDOPV, a clear relationship between structure and electrical properties was observed. Even simply identifying the structure of the dopant precursor revealed things were not as they seemed. Fundamental studies like these are important not only in elucidating the mechanisms surrounding quaternary ammonium and fluoride dopants but will be important for all new

materials in the future. In addition the work presented in Chapter 4 has not only added to the library of available n-type materials; it also allows chemists to see the possibility of expanding the synthetic scope of thiazolo[5,4-*d*]thiazole. The reactions described in Chapter 4 go some way to bringing about routes to the incorporation of this rarely used but theoretically advantageous ring-system.

# Chapter 6. Experimental Section

## 6.1 Experimental Chapter 2 - Structure and Mechanisms of Quaternary Amine Self-Dopants.

**General:** Commercially available compounds and solvents were used as received. Solution NMR spectra were recorded using a Bruker Avance III 400 and Neo 700 spectrometer, operating at 400 and 700 MHz, respectively. Chemical shifts are reported in ppm with the residual solvent peak of  $\text{CHCl}_3$  ( $\delta = 7.27$  ppm, s) DMSO ( $\delta = 2.50$  ppm, s) or  $\text{H}_2\text{O}$  ( $\delta = 4.79$  ppm, s) as the internal standard for  $^1\text{H}$  NMR. UV-Vis spectra were recorded in DMSO or aqueous solutions or thin-films on glass substrates on a Shimadzu UV-2600 or Shimadzu UV-3600i Plus UV-VIS-NIR spectrophotometer. Thin-films were drop-cast onto glass substrates from 5 mg/mL, 2.5 mg/mL or 0.5 mg/mL solutions from aqueous solutions. Fourier Transform Infrared (FTIR) spectroscopy was recorded on a Shimadzu IRTracer-100 with an attenuated total reflectance (ATR) setup. High resolution mass spectrometry (HRMS) with electrospray ionisation (ESI) was performed via direct injection on a Thermo Orbitrap Exactive Plus Mass Spectrometer. Atomic force microscopy was carried out in tapping mode on a Bruker Dimension<sup>®</sup> Icon<sup>™</sup> Scanning Probe Microscope. X-ray fluorescence was carried out under an inert Helium atmosphere with a Malvern Panalytical Epsilon 4 spectrometer equipped with a silver (Ag) anode X-ray tube.

**Electrochemical Measurements:** Cyclic voltammetry (CV) was performed on an Autolab/PGSTAT101 potentiostat in 0.1 M solutions of tetrabutylammonium hexafluorophosphate as electrolyte. Glassy carbon was used as working electrode, a platinum wire as counter electrode and silver/silver nitrate ( $\text{Ag}/\text{Ag}^+$ ) as reference electrode. The FMO energy levels were then estimated according to the equations  $\text{FMO (eV)} = -4.71 - E_{\text{onset}}$  where  $E_{\text{onset}}$  is the onset of reduction (LUMO) or oxidation (HOMO).

**Conductivity Measurements:** Glass slides were cleaned with soap and deionised water, acetone and then IPA by sonication for 15 minutes in each solvent. This was followed by  $\text{O}_2$

plasma cleaning for 30 minutes. Films of NDI-OH were then drop-cast from 5 mg/mL aqueous solutions. Thickness of films was measured with a Dektak 3ST surface profiler. Conductivity was then measured in air using a Keithley 4200 semiconductor characterisation system. Using four probes a Van der Pauw geometry was used in which horizontal and vertical resistances,  $R_h$  and  $R_v$ , were measured and related to the sheet resistance,  $R_s$ , of the sample according to equation 6.1.

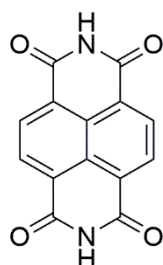
$$e^{\frac{-\pi R_h}{R_s}} + e^{\frac{-\pi R_v}{R_s}} = 1 \quad 6.1$$

With a known thickness of thin-film,  $t$ , the resistivity,  $\rho$ , could then be calculated according to equation 6.2 and the electrical conductivity,  $\sigma$ , calculated according to equation 6.3.

$$\rho = R_s \times t \quad 6.2$$

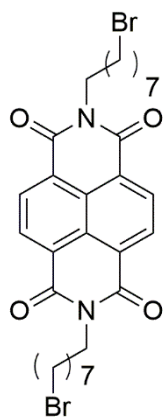
$$\sigma = \frac{1}{\rho} \quad 6.3$$

**Synthetic Procedures:** All compounds were synthesised according to procedures below:



### 1,4,5,8-Naphthalenetetracarboxylic diimide (6)

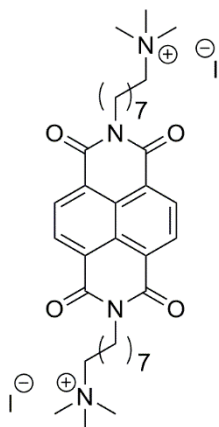
Naphthalenetetracarboxylate dianhydride (5) (8.00 g, 0.0300 mol) and ammonium acetate (46.3 g, 0.600 mol) were suspended in acetic acid (200 mL). The orange reaction mixture was stirred under reflux for 1 hour then cooled to room temperature and filtered. Washed thoroughly with acetic acid, methanol and diethyl ether to give the product as an orange solid (5.76 g, 72%). FTIR  $\nu_{\max}/\text{cm}^{-1}$ : 3062 (N-H), 1734 (C=O, asym. str), 1674 (C=O, sym. str).



### **N,N'-Bis(8-bromooctyl)-1,4,5,8-naphthalenetetracarboxylic diimide (7)**

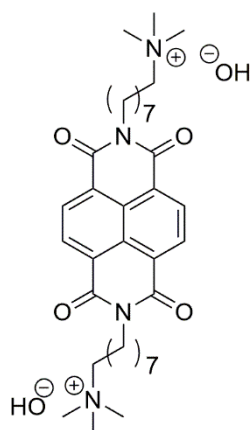
6 (1.70 g, 6.38 mmol) and 1-bromooctanol (3.28 mL, 19.1 mmol) were stirred in anhydrous THF (30 mL) and cooled to 0 °C. A solution of diethyl azodicarboxylate (3.77 mL, 19.1 mmol) and triphenylphosphine (5.02 g, 19.1 mmol) in anhydrous THF (20 mL) was then added to this dropwise under a nitrogen atmosphere and the reaction was stirred at room temperature overnight. Solvent was evaporated and the crude oil was run through a short silica plug with DCM as eluent. Further purification by column chromatography (3:7 hexane:DCM) and recrystallisation from ethyl acetate/hexane gave the pure product as yellow crystals (0.801 g, 21%). <sup>1</sup>H NMR (700 MHz, CDCl<sub>3</sub>) δ 8.75 (4H, s, ArH), 4.19 (4H, t, *J* = 7.7 Hz, NCH<sub>2</sub>), 3.40 (4H, t, *J* = 6.9 Hz, CH<sub>2</sub>Br), 1.85 (4H, quin, *J* = 7.2 Hz, NCH<sub>2</sub>CH<sub>2</sub>), 1.74 (4H, quin, *J* = 7.6 Hz, CH<sub>2</sub>CH<sub>2</sub>Br), 1.32-1.45 (16H, m, (CH<sub>2</sub>)<sub>4</sub>); <sup>13</sup>C NMR (176 MHz, CDCl<sub>3</sub>) δ 163.0 (NCO), 131.1 (ArC), 126.8 (ArC), 126.8 (ArC), 41.0 (CH<sub>2</sub>N(CH<sub>3</sub>)<sub>3</sub>), 34.1 CH<sub>3</sub>Br), 32.1 (CH<sub>2</sub>), 29.2 (CH<sub>2</sub>), 28.7 (CH<sub>2</sub>), 28.2 (CH<sub>2</sub>), 28.1 (CH<sub>2</sub>), 27.0 (CH<sub>2</sub>); HRMS (ESI) *m/z*: 647.1105; calculated for [C<sub>30</sub>H<sub>36</sub>Br<sub>2</sub> N<sub>2</sub>O<sub>4</sub>+H]<sup>+</sup> = 647.1120





**N,N'-Bis(8-(trimethylammoniumiodide)octylene)-1,4,5,8-naphthalenetetracarboxylic diimide (NDI-NMe<sub>3</sub>I)**

7 (0.500 g, 0.770 mmol) and dimethylamine (2.00 M in THF, 38.6 mL, 77.1 mmol) were dissolved in anhydrous THF (25 mL) and stirred under reflux overnight in a nitrogen atmosphere. Reaction mixture was cooled to room temperature and excess dimethylamine was removed by bubbling with a stream of nitrogen for 2 hours. Solvent THF was removed in vacuo. The resultant oil was then dissolved in chloroform (27 mL) and iodomethane (0.290 mL, 3.86 mmol) was added before being refluxed for 2 hours. The reaction mixture was cooled to room temperature and a brown precipitate was filtered and washed with chloroform, hexane, ethanol and diethyl ether before being recrystallised from acetone/water to give the product as an orange solid (0.296 g, 44%). <sup>1</sup>H NMR (700 MHz, DMSO) δ 8.64 (4H, s, ArH), 4.04 (4H, t, *J* = 7.7 Hz, NCH<sub>2</sub>), 3.27 (4H, m, CH<sub>2</sub>N(CH<sub>3</sub>)<sub>3</sub>I), 3.04 (18H, s, N(CH<sub>3</sub>)<sub>3</sub>I), 1.63-1.68 (8H, m, NCH<sub>2</sub>(CH<sub>2</sub>)<sub>2</sub>), 1.31-1.39 (12H, m, (CH<sub>2</sub>)<sub>3</sub>), 1.28 (4H, m, CH<sub>2</sub>); <sup>13</sup>C NMR (176 MHz, DMSO) δ 162.6 (NCO), 130.5 (ArC), 126.3 (ArC), 126.2 (ArC), 65.3 (CH<sub>2</sub>N(CH<sub>3</sub>)<sub>3</sub>), 52.2 (N(CH<sub>3</sub>)<sub>3</sub>), 40.1 (NCH<sub>2</sub>), 28.5 (CH<sub>2</sub>), 28.4 (CH<sub>2</sub>), 27.4 (CH<sub>2</sub>), 26.5 (CH<sub>2</sub>), 25.7 (CH<sub>2</sub>), 22.0 (CH<sub>2</sub>); HRMS (ESI) *m/z*: 303.2068; calculated for [C<sub>36</sub>H<sub>52</sub>N<sub>4</sub>O<sub>4</sub>+H]<sup>+</sup> = 303.2067



**N,N'-Bis(8-(trimethylammoniumhydroxide)octylene)-1,4,5,8-naphthalenetetracarboxylic diimide (NDI-OH)**

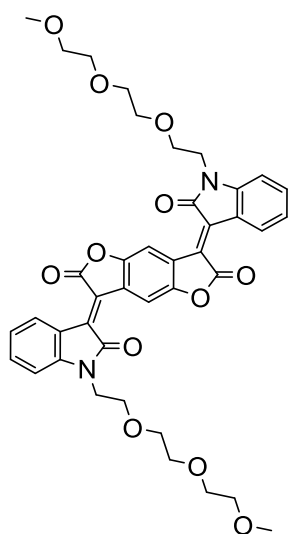
NDI-NMe<sub>3</sub><sup>+</sup> (50.0 mg, 0.0572 mmol) was dissolved in 5 mL of de-ionised water and washed through ion-exchange resin (DOWEX 550A, Sigma) with 2 mL THF and 5 mL more water. THF was evaporated in vacuo to leave a colourless aqueous solution of 5 mg/mL. An NMR sample was prepared in the same way using deuterium oxide rather than water. <sup>1</sup>H NMR (700 MHz, D<sub>2</sub>O) δ 8.59 (1H, d, *J* = 7.5 Hz, ArH), 8.57 (1H, d, *J* = 7.5 Hz, ArH), 7.95 (1H, d, *J* = 7.5 Hz, ArH), 7.91 (1H, d, *J* = 7.5 Hz, ArH), 4.10 (2H, t, *J* = 7.4 Hz, NCH<sub>2</sub>), 3.40 (2H, t, *J* = 7.1, NCH<sub>2</sub>), 3.31 -3.26 (4H, m, CH<sub>2</sub>N(CH<sub>3</sub>)<sub>3</sub>OH), 3.09 (9H, s, N(CH<sub>3</sub>)<sub>3</sub>OH), 3.08 (9H, s, N(CH<sub>3</sub>)<sub>3</sub>OH), 1.80-1.74 (4H, m, NCH<sub>2</sub>CH<sub>2</sub>), 1.71-1.66 (4H, m, CH<sub>2</sub>), 1.44-1.35 (16H, m, (CH<sub>2</sub>)<sub>4</sub>); <sup>13</sup>C NMR (176 MHz, D<sub>2</sub>O) δ 175.2 (COO<sup>-</sup>), 171.3 (NCO, amide), 166.3 (NCO, imide), 166.3 (NCO, imide), 144.7 (ArC), 140.7 (ArC), 132.4 (ArC), 131.3 (ArC), 129.5 (ArC), 128.3 (ArC), 128.1 (ArC), 125.2 (ArC), 124.3 (ArC), 122.9 (ArC), 67.3 (CH<sub>2</sub>N(CH<sub>3</sub>)<sub>3</sub>), 67.3 (CH<sub>2</sub>N(CH<sub>3</sub>)<sub>3</sub>), 53.3 (N(CH<sub>3</sub>)<sub>3</sub>), 41.2 (NCH<sub>2</sub>, imide), 40.6 (NCH<sub>2</sub>, amide) 28.6 (CH<sub>2</sub>), 28.6 (CH<sub>2</sub>), 28.5 (CH<sub>2</sub>), 28.5 (CH<sub>2</sub>), 28.5 (CH<sub>2</sub>), 27.4 (CH<sub>2</sub>), 26.6 (CH<sub>2</sub>), 26.5 (CH<sub>2</sub>), 25.9 (CH<sub>2</sub>), 25.8 (CH<sub>2</sub>), 22.7 (CH<sub>2</sub>), 22.7 (CH<sub>2</sub>); *m/z* (ESI) 623.39 (4%, M<sup>+</sup>-OH), 312.39 (100%, M<sup>2+</sup>-OH). A more detailed spectroscopic assignment is discussed in the main text.

## 6.2 Experimental Chapter 3 - Exploring the Chemical Mechanism Behind n-type Fluoride Doping of BDOPV Semiconductors

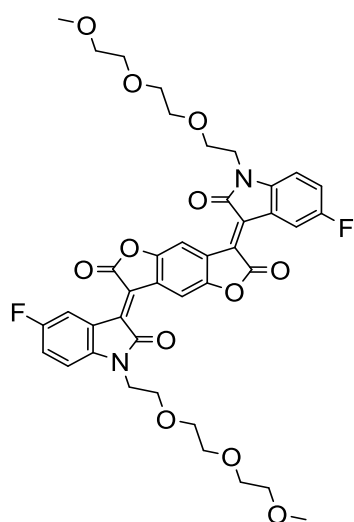
**General:** Commercially available compounds and solvents were used as received. Solution NMR spectra were recorded using a Bruker Avance III 400 and Neo 700 spectrometer, operating at 400 and 700 MHz, respectively. Chemical shifts are reported in ppm with the residual solvent peak of  $\text{CHCl}_3$  ( $\delta = 7.27$  ppm, s) or DMF ( $\delta = 8.04$  ppm, s) as the internal standard for  $^1\text{H}$  NMR. UV-Vis-NIR spectra were recorded in chloroform or DMF on a Shimadzu UV-3600i Plus UV-VIS-NIR spectrophotometer. Electron paramagnetic resonance (EPR) spectra were recorded on a Bruker e-scan spectrometer with a microwave frequency of 9.77 GHz and microwave power of 1.5 mW.

**Electrochemical Measurements:** Cyclic voltammetry (CV) was performed on an Autolab/PGSTAT101 potentiostat in 0.1 M solutions of tetrabutylammonium hexafluorophosphate as electrolyte. Glassy carbon was used as working electrode, a platinum wire as counter electrode and silver/silver nitrate ( $\text{Ag}/\text{Ag}^+$ ) as reference electrode. The FMO energy levels were then estimated according to the equations  $\text{FMO (eV)} = -4.71 - E_{\text{onset}}$  where  $E_{\text{onset}}$  is the onset of reduction (LUMO) or oxidation (HOMO).

**Synthetic Procedures:** BDOPV and 2F-BDOPV compounds were synthesised by Zhijie Guo (Nielsen group, Queen Mary University of London) by a modified procedure of that reported by Lei et al.<sup>261</sup> Characterisation data for both BDOPV and 2F-BDOPV is shown below. NDI-TEG, used as reference material for EPR measurements, was synthesised by Zhijie Guo according to a previously reported procedure.<sup>349</sup>

**BDOPV:**

$^1\text{H}$  NMR (400 MHz,  $\text{CDCl}_3$ )  $\delta$  9.07 (2H, s, ArH), 9.00 (2H, d,  $J = 7.8$  Hz, ArH), 7.36 (2H, t,  $J = 7.8$  Hz, ArH), 7.03 (2H, t,  $J = 7.8$  Hz, ArH), 6.94 (2H, d,  $J = 7.8$  Hz, ArH), 3.98 (4H, t,  $J = 5.6$  Hz,  $\text{NCH}_2\text{CH}_2\text{O}$ ), 3.78 (4H, t,  $J = 5.6$  Hz,  $\text{NCH}_2$ ), 3.65 (4H, m,  $\text{OCH}_2$ ), 3.58 (8H, m,  $\text{O}(\text{CH}_2)_2$ ), 3.48 (2H, m,  $\text{OCH}_2$ ), 3.35 (6H, s,  $\text{OCH}_3$ )

**2F-BDOPV:**

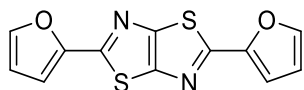
$^1\text{H}$  NMR (400 MHz,  $\text{CDCl}_3$ , 323 K)  $\delta$  9.11 (2H, s, ArH), 8.81 (2H, m,  $J = 8.7$  Hz, ArH), 7.09 (2H, m, ArH), 6.93 (2H, m, ArH), 3.98 (4H, t,  $J = 4.8$  Hz,  $\text{NCH}_2\text{CH}_2\text{O}$ ), 3.78 (4H, t,  $J = 4.8$  Hz,  $\text{NCH}_2$ ), 3.64 (4H, m,  $\text{OCH}_2$ ), 3.58 (8H, m,  $\text{O}(\text{CH}_2)_2$ ), 3.50 (4H, m,  $\text{OCH}_2$ ), 3.36 (6H, s,  $\text{OCH}_3$ )

## 6.3 Experimental Chapter 4 - Synthesis of Thiazole Containing Highly Ordered Polymers

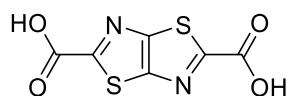
**General:** Commercial nitrobenzene was extracted with aqueous 2 M NaOH (3 × 20 mL), water (3 × 20 mL), aqueous 1 M HCl (3 × 20 mL), and water (3 × 20 mL) followed by drying over MgSO<sub>4</sub>, filtering and storing under 4 Å molecular sieves. Other commercially available compounds and solvents were used as received. Solution NMR spectra were recorded using a Bruker Avance III 400 and Neo 700 spectrometer, operating at 400 and 700 MHz, respectively. Chemical shifts are reported in ppm with the residual solvent peak of CHCl<sub>3</sub> ( $\delta$  = 7.27 ppm, s) or tetrachloroethane ( $\delta$  = 6.00 ppm, s) as the internal standard. UV-Vis spectra were recorded in chlorobenzene solutions or thin-films on glass substrates on a Shimadzu UV-2600 spectrophotometer. Thin-films were spin-coated onto glass substrates from a 2 mg/mL solution in chlorobenzene. Fourier Transform Infrared (FTIR) spectroscopy was recorded on a Shimadzu IRTracer-100 with an attenuated total reflectance (ATR) setup. High resolution mass spectrometry (HRMS) with electrospray ionisation (ESI) was performed via direct injection on a Thermo Orbitrap Exactive Plus Mass Spectrometer. Thermogravimetric analysis (TGA) was performed on a Netzsch STA 449 C in an ambient atmosphere.

**Electrochemical Measurements:** Cyclic voltammetry (CV) was performed on a Autolab/PGSTAT101 potentiostat in 0.1 M solutions of tetrabutylammonium hexafluorophosphate as electrolyte. Glassy carbon was used as working electrode, a platinum wire as counter electrode and silver/silver nitrate (Ag/Ag<sup>+</sup>) as pseudo-reference electrode. The half-potential of a 0.01 M solution of ferrocene in electrolyte solution was used as an external standard for calibration. The FMO energy levels were then estimated according to the equations  $FMO (eV) = -4.8 - E_{onset}$  where  $E_{onset}$  is the onset of reduction (LUMO) or oxidation (HOMO).

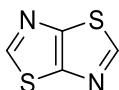
**Synthetic Procedures:** The monomer bis(trimethylstannyl)thieno[3,2-*b*]thiophene (28) and the polymer PbTTT were synthesized by Bob Schroeder according to the procedure reported by McCulloch et al.<sup>220</sup> All other compounds were synthesised according to procedures below.



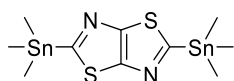
**2,5-Bis(2-furyl)thiazolo[5,4-*d*]thiazole (38):** Dithiooxamide (20.0 g, 0.166 mol), furfural (172 mL, 2.08 mol) and phenol (62.6 g, 0.665 mol) were combined in a round-bottom flask and heated to 190 °C. The reaction mixture was held at this temperature for 1.5 hours and then allowed to cool to room temperature overnight. A brown solid was then filtered and washed with ethanol, hexane and diethyl ether. The crude solid was then recrystallised from chloroform twice and dried to give the pure product as green crystals (10.1 g, 22%). <sup>1</sup>H NMR (700 MHz, CDCl<sub>3</sub>) δ 7.57 (2H, m, ArH), 7.09 (2H, d, *J* = 3.4 Hz, ArH), 6.60 (2H, q, *J* = 1.7 Hz, ArH); <sup>13</sup>C NMR (176 MHz, CDCl<sub>3</sub>) δ 158.7 (N=CS), 150.7 (NCS), 148.8 (OC), 144.3 (OC), 112.8 (ArC), 110.3 (ArC); HRMS (ESI) *m/z*: 274.9943; calculated for [C<sub>12</sub>H<sub>6</sub>N<sub>2</sub>O<sub>2</sub>S<sub>2</sub>+H]<sup>+</sup> = 274.9943



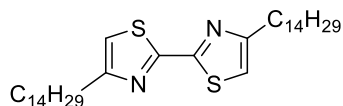
**2,5-Thiazolo[5,4-*d*]thiazole-2,5-dicarboxylic acid (39):** 2,5-di-2-Furylthiazolo[5,4-*d*]thiazole (9.00 g, 0.033 mol) was suspended in *t*-butanol and stirred at 90 °C for 2 hours. The fine suspension was then cooled to 60 °C and water (80 mL) and aliquat 336 (2.5 mL) was added. The reaction mixture was cooled to approximately 10 °C by a water/ice bath. Potassium permanganate (55.2 g, 0.349 mol) was added in portions with the reaction temperature monitored and maintained at 20 – 40 °C. The dark purple reaction mixture was then stirred overnight at room temperature, quenched with 1.5 M aqueous sodium bisulfite (100 mL) and stirred for 1 hour more. The precipitate was filtered, washed sparingly with water and allowed to air dry. The brown filter cake was stirred at 100 °C in water and hot filtered. The solid was boiled and filtered twice more and the pale brown filtrates were combined and acidified with concentrated HCl to a pH of 1. After standing overnight a white precipitate formed which was filtered and washed with water, cooled in an ice bath and dried under vacuum overnight (2.95 g, 39%). Final product was too insoluble for NMR and mass spectrometry. FTIR  $\nu_{\text{max}}$ /cm<sup>-1</sup>: 3359 (O-H), 1931 (C=O).



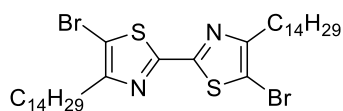
**Thiazolo[5,4-*d*]thiazole (33):** 2,5-Thiazolo[5,4-*d*]thiazolecarboxylic acid (2.75 g, 2.00 mmol) was suspended in ethanol (250 mL) and refluxed overnight. The colourless solution was cooled to room temperature and the solvent evaporated to leave an off-white crude which was purified by column chromatography (100% DCM). The pure product was a white crystalline solid (1.38 g, 81%).  $^1\text{H}$  NMR (700 MHz,  $\text{CDCl}_3$ )  $\delta$  8.94 (2H, s, ArH);  $^{13}\text{C}$  NMR (176 MHz,  $\text{CDCl}_3$ )  $\delta$  155.4 (N=CS), 151.0 (NCS); HRMS (ESI)  $m/z$ : 142.9733; calculated for  $[\text{C}_{12}\text{H}_6\text{N}_2\text{O}_2\text{S}_2+\text{H}]^+ = 142.9732$



**2,5-Bis(trimethylstannyl)thiazolo[5,4-*d*]thiazole (29):** Thiazolo[5,4-*d*]thiazole (400 mg, 2.81 mmol) was dissolved in anhydrous THF (10 mL) and cooled to  $-78$  °C. Lithium diisopropylamide (2.00 M in THF, 1.69 mL, 3.38 mmol) was added dropwise and stirred at  $-78$  °C for 1 hour. Trimethyltin chloride (1 M in THF, 3.38 mL, 3.38 mmol) was added dropwise and the solution was allowed to warm to room temperature over the course of 1 hour. The reaction mixture was again cooled to  $-78$  °C and lithium diisopropylamide (2.00 M in THF, 1.69 mL, 3.38 mmol) was added dropwise and stirred at  $-78$  °C for 1 hour. Trimethyltin chloride (1.00 M in THF, 3.38 mL, 3.38 mmol) was added dropwise and the solution was allowed to warm to room temperature overnight. The reaction was quenched with saturated ammonium chloride and organics were extracted with DCM (3  $\times$  50 mL). Combined organic layers were washed with water (3  $\times$  50 mL) and brine (3  $\times$  50 mL) before drying over magnesium sulphate, filtering and evaporating solvent. The brown solid crude was recrystallised from acetonitrile to give the pure product as white crystals (223 mg, 17%).  $^1\text{H}$  NMR (700 MHz,  $\text{CDCl}_3$ )  $\delta$  0.52 (18H, s,  $\text{SnCH}_3$ );  $^{13}\text{C}$  NMR (176 MHz,  $\text{CDCl}_3$ )  $\delta$  179.8 (N=CSnMe $_3$ ), 157.5 (NCS), -7.8 ( $\text{SnCH}_3$ ); HRMS (ESI)  $m/z$ : 468.8960 calculated for  $[\text{C}_{10}\text{H}_{18}\text{N}_2\text{S}_2\text{Sn}_2+\text{H}]^+ = 468.9030$



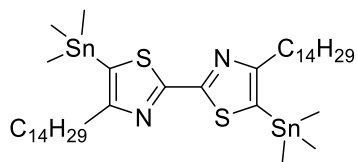
**4,4'-Ditetradecyl-2,2'-bithiazole (35):** Dithiooxamide (2.69 g, 22.4 mmol) and 1-bromo-2-hexadecanone (15.0 g, 47.0 mmol) were suspended in anhydrous 1,4-dioxane (200 mL) and stirred overnight at room temperature. The reaction mixture was quenched with water (200 mL) and extracted with DCM (3 × 150 mL). Combined organic layers were then washed with water (3 × 150 mL) and brine (3 × 150 mL) before being dried over magnesium sulphate, filtered and evaporated. The crude product was purified by column chromatography (3:7 DCM:hexane) and further by recrystallisation from chloroform/methanol. The pure product was pale orange needles (5.07 g, 40%). <sup>1</sup>H NMR (700 MHz, CDCl<sub>3</sub>) δ 6.95 (2H, s, ArH), 2.81 (4H, t, *J* = 7.7 Hz, ArCH<sub>2</sub>), 1.74 (4H, quin, *J* = 7.6 Hz, ArCH<sub>2</sub>CH<sub>2</sub>), 1.38 – 1.26 (44H, m, (CH<sub>2</sub>)<sub>11</sub>), 0.89 (6H, t, *J* = 7.1 Hz, (CH<sub>2</sub>)<sub>11</sub>CH<sub>3</sub>); <sup>13</sup>C NMR (176 MHz, CDCl<sub>3</sub>) δ 160.9 (N=CS), 159.3 (NCC<sub>14</sub>H<sub>29</sub>), 114.6 (SCH), 32.0 (NCCH<sub>2</sub>), 31.6 (CH<sub>2</sub>), 29.8 (CH<sub>2</sub>), 29.8 (CH<sub>2</sub>), 29.7 (CH<sub>2</sub>), 29.7 (CH<sub>2</sub>), 29.7 (CH<sub>2</sub>), 29.5 (CH<sub>2</sub>), 29.4 (CH<sub>2</sub>), 29.3 (CH<sub>2</sub>), 29.3 (CH<sub>2</sub>), 22.8 (CH<sub>2</sub>), 14.2 (CH<sub>3</sub>); HRMS (ESI) *m/z*: 561.4278; calculated for [C<sub>34</sub>H<sub>60</sub>N<sub>2</sub>S<sub>2</sub>+H]<sup>+</sup> = 561.4276



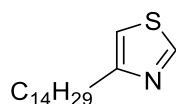
**5,5'-Dibromo-4,4'-ditetradecyl-2,2'-bithiazole (31):** 4,4'-Ditetradecyl-2,2'-bithiazole (5.00 g, 8.91 mmol) was dissolved in chloroform (200 mL) and acetic acid (100 mL). NBS (5.55 g, 31.2 mmol) was added in four portions and the reaction mixture heated to 50 °C and stirred overnight. The reaction mixture was cooled to room temperature and quenched with water (100 mL). Organics were extracted with DCM (3 × 250 mL) and combined organic layers were washed with water (3 × 250 mL) and brine (3 × 250 mL) before being dried over magnesium sulphate, filtered and evaporated. The crude solid was then recrystallised from hexane to give the pure product as white needles (2.32 g, 36%). <sup>1</sup>H NMR (700 MHz, CDCl<sub>3</sub>) δ 2.75 (4H, t, *J* = 7.6 Hz, ArCH<sub>2</sub>), 1.71 (4H, quin, *J* = 7.3 Hz, ArCH<sub>2</sub>CH<sub>2</sub>), 1.34 – 1.26 (44H, m, (CH<sub>2</sub>)<sub>11</sub>), 0.89 (6H, t, *J* = 6.9 Hz, (CH<sub>2</sub>)<sub>11</sub>CH<sub>3</sub>); <sup>13</sup>C NMR (176 MHz, CDCl<sub>3</sub>) δ 160.1 (N=CS), 157.5 (NCC<sub>14</sub>H<sub>29</sub>), 106.9 (SCBr), 32.1 (NCCH<sub>2</sub>), 29.8 (CH<sub>2</sub>), 29.8 (CH<sub>2</sub>), 29.8 (CH<sub>2</sub>), 29.8 (CH<sub>2</sub>), 29.8 (CH<sub>2</sub>), 29.7 (CH<sub>2</sub>), 29.6



(CH<sub>2</sub>), 29.5 (CH<sub>2</sub>), 29.5 (CH<sub>2</sub>), 29.3 (CH<sub>2</sub>), 28.8 (CH<sub>2</sub>), 22.8 (CH<sub>2</sub>), 14.3 (CH<sub>3</sub>); HRMS (ESI) m/z: 719.2380; calculated for [C<sub>34</sub>H<sub>58</sub>Br<sub>2</sub>N<sub>2</sub>S<sub>2</sub>+H]<sup>+</sup> = 719.2458

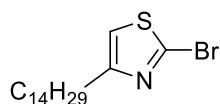


**4,4'-Ditetradecyl-5,5'-ditrimethylstannyl-2,2'-bithiazole (51):** 5,5'-Dibromo-4,4'-ditetradecyl-2,2'-bithiazole (100 mg, 0.139 mmol) was suspended in anhydrous THF (6 mL). The solution was cooled to -94 °C in a liquid nitrogen/acetone bath and *tert*-butyllithium (1.70 M in pentane, 0.392 mL, 0.667 mmol) was added dropwise. The reaction mixture was held in a dry-ice/acetone bath for 1 hour and cooled back down to -94 °C. Trimethyltin chloride (1 M in THF, 0.334 mL, 0.334 mmol) was added dropwise and the solution was allowed to warm to room temperature overnight. The reaction was quenched with saturated ammonium chloride (10 mL) and organics extracted with DCM (3 × 10 mL). The combined organic layers were washed with water (3 × 10 mL) and brine (3 × 10 mL) before being dried over magnesium sulphate, filtered and solvent evaporated. The crude orange oil was cooled in an ice-bath and the resultant crystals were recrystallised from a 1:1 mixture of acetonitrile and isopropanol to give the pure product as off-white needles (72.8 mg, 59%). <sup>1</sup>H NMR (700 MHz, CDCl<sub>3</sub>) δ 2.76 (4H, t, *J* = 7.9 Hz, ArCH<sub>2</sub>), 1.71 (4H, quin, *J* = 7.7 Hz, ArCH<sub>2</sub>CH<sub>2</sub>), 1.36 – 1.26 (44H, m, (CH<sub>2</sub>)<sub>11</sub>), 0.89 (6H, t, *J* = 7.1 Hz, (CH<sub>2</sub>)<sub>11</sub>CH<sub>3</sub>), 0.43 (16H, s, SnCH<sub>3</sub>); <sup>13</sup>C NMR (176 MHz, CDCl<sub>3</sub>) δ 165.3 (N=CS), 165.3 (NCC<sub>14</sub>H<sub>29</sub>), 125.6 (SCSnMe<sub>3</sub>), 33.6 (NCCH<sub>2</sub>), 32.1 (CH<sub>2</sub>), 31.3 (CH<sub>2</sub>), 29.8 (CH<sub>2</sub>), 29.8 (CH<sub>2</sub>), 29.8 (CH<sub>2</sub>), 29.7 (CH<sub>2</sub>), 29.6 (CH<sub>2</sub>), 29.6 (CH<sub>2</sub>), 29.5 (CH<sub>2</sub>), 22.8 (CH<sub>2</sub>), 14.3 (CH<sub>2</sub>), -7.6 (CH<sub>2</sub>); HRMS (ESI) m/z: 887.3559 calculated for [C<sub>40</sub>H<sub>76</sub>N<sub>2</sub>S<sub>2</sub>Sn<sub>2</sub>+H]<sup>+</sup> = 887.3561

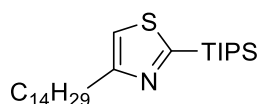


**4-Tetradecylthiazole (56):** Formamide (1.87 mL, 47.0 mmol) and diphosphorous pentasulfide (2.09 g, 4.70 mmol) were stirred in anhydrous 1,4-dioxane (500 mL) and cooled to 0 °C. 1-bromohexadecan-2-one (10.0 g, 31.3 mmol) was added in portions over 20 minutes and then

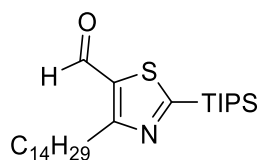
refluxed for 1 hour. The reaction mixture was then cooled to room temperature and aqueous HCl (1 M, 62 mL) was added and refluxed for 1 hour. Saturated NaHCO<sub>3</sub> was then added dropwise at room temperature until a white precipitate formed. Organics were extracted with DCM (3 × 200 mL) and combined organic layers were then washed with water (3 × 200 mL) before being dried over MgSO<sub>4</sub>, filtered and solvent evaporated. The crude solid was then purified by column chromatography (1:20, EtOAc:hexane) to give a white crystalline solid (7.66 g, 87%). <sup>1</sup>H NMR (700 MHz, CDCl<sub>3</sub>) δ 8.73 (1H, d, *J* = 2.0 Hz, ArH), 6.91 (1H, s, ArH), 2.82 (2H, t, *J* = 15.5 Hz, ArCH<sub>2</sub>), 1.72 (2H, quin, *J* = 7.5 Hz, ArCH<sub>2</sub>CH<sub>2</sub>) 1.35 – 1.25 (22H, m, (CH<sub>2</sub>)<sub>11</sub>), 0.87 (3H, t, *J* = 7.1 Hz, (CH<sub>2</sub>)<sub>11</sub>CH<sub>3</sub>); <sup>13</sup>C NMR (176 MHz, CDCl<sub>3</sub>) δ 158.7 (N=CS), 152.3 (NCC<sub>14</sub>H<sub>29</sub>), 112.5 (SCH), 32.1 (NCCH<sub>2</sub>), 31.5 (CH<sub>2</sub>), 29.8 (CH<sub>2</sub>), 29.8 (CH<sub>2</sub>), 29.8 (CH<sub>2</sub>), 29.8 (CH<sub>2</sub>), 29.8 (CH<sub>2</sub>), 29.7 (CH<sub>2</sub>), 29.6 (CH<sub>2</sub>), 29.5 (CH<sub>2</sub>), 29.4 (CH<sub>2</sub>), 22.8 (CH<sub>2</sub>), 14.3 (CH<sub>3</sub>); HRMS (ESI) *m/z*: 282.2255; calculated for [C<sub>17</sub>H<sub>31</sub>NS+H]<sup>+</sup> = 282.2256.



**4-Tetradecyl-2-bromothiazole (57):** 4-Tetradecylthiazole (4.00 g, 14.2 mmol) was dissolved in anhydrous THF (20 mL) and cooled to –78 °C. *N*-butyllithium (1.60 M in hexanes, 10.7 mL, 17.1 mmol) was added dropwise and the reaction stirred at –78 °C for 30 minutes before being allowed to warm to room temperature over 30 minutes. The reaction was cooled back down to –78 °C and carbon tetrabromide (5.66 g, 17.1 mmol) was added at once and allowed to reach room temperature over 2 hours. The reaction was quenched with saturated ammonium chloride and extracted with DCM (3 × 100 mL). Combined organic layers were washed with water (3 × 100 mL), dried over magnesium sulphate, filtered and solvent evaporated. The crude oil was purified by column chromatography (100 % hexanes) to give the pure product as a white solid (1.11 g, 22%). <sup>1</sup>H NMR (700 MHz, CDCl<sub>3</sub>) δ 6.82 (1H, s, ArH<sub>3</sub>), 2.73 (2H, t, *J* = 7.7 Hz, ArCH<sub>2</sub>), 1.68 (2H, quin, *J* = 7.4 Hz, ArCH<sub>2</sub>CH<sub>2</sub>), 1.35 – 1.26 (22H, m, (CH<sub>2</sub>)<sub>11</sub>), 0.88 (3H, t, *J* = 7.1 Hz, CH<sub>3</sub>); <sup>13</sup>C NMR (176 MHz, CDCl<sub>3</sub>) δ 158.5 (NCC<sub>14</sub>H<sub>29</sub>), 134.9 (N=CBr), 116.6 (SC), 32.1 (NCCH<sub>2</sub>), 31.8 (CH<sub>2</sub>), 29.8 (CH<sub>2</sub>), 29.8 (CH<sub>2</sub>), 29.8 (CH<sub>2</sub>), 29.8 (CH<sub>2</sub>), 29.7 (CH<sub>2</sub>), 29.5 (CH<sub>2</sub>), 29.3 (CH<sub>2</sub>), 29.1 (CH<sub>2</sub>), 22.8 (CH<sub>2</sub>), 14.3 (CH<sub>3</sub>); HRMS (ESI) *m/z*: 360.1357; calculated for [C<sub>17</sub>H<sub>30</sub>NSBr+H]<sup>+</sup> = 360.1355

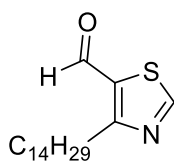


**4-Tetradecyl-2-triisopropylsilylthiazole (60):** 4-Tetradecylthiazole (3.30 g, 11.7 mmol) was dissolved in anhydrous THF (40 mL) and cooled to  $-78\text{ }^{\circ}\text{C}$  in a dry-ice/acetone bath. *N*-Butyllithium (1.60 M in hexanes, 8.78 mL, 14.0 mmol) was added dropwise and stirred for 1 hour before warming to room temperature. The red solution was then cooled back to  $-78\text{ }^{\circ}\text{C}$  and triisopropylsilyl chloride (3.00 mL, 14.0 mmol) was added dropwise and allowed to reach room temperature overnight. The reaction was quenched with saturated ammonium chloride and organics were extracted with DCM ( $3 \times 50\text{ mL}$ ). Combined organic layers were then washed with water ( $3 \times 50\text{ mL}$ ), dried over magnesium sulphate, filtered and solvent evaporated. The crude oil was then purified by column chromatography (1:100, EtOAc:hexane) to give the pure product as a pale orange oil (3.75 g, 73%).  $^1\text{H}$  NMR (700 MHz,  $\text{CDCl}_3$ )  $\delta$  7.03 (1H, s, ArH), 2.88 (2H, t,  $J = 7.6\text{ Hz}$ , ArCH<sub>2</sub>), 1.74 (2H, quin,  $J = 7.4\text{ Hz}$ , ArCH<sub>2</sub>CH<sub>2</sub>), 1.44 (3H, sept,  $J = 7.6\text{ Hz}$ , SiCH(CH<sub>3</sub>)<sub>2</sub>), 1.36 – 1.26 (22H, m, (CH<sub>2</sub>)<sub>11</sub>), 1.14 (18H, d,  $J = 7.5\text{ Hz}$ , SiCH(CH<sub>3</sub>)<sub>2</sub>), 0.89 (3H, t,  $J = 7.1\text{ Hz}$ , (CH<sub>2</sub>)<sub>11</sub>CH<sub>3</sub>);  $^{13}\text{C}$  NMR (176 MHz,  $\text{CDCl}_3$ )  $\delta$  168.8 (N=CS), 160.9 (NCC<sub>14</sub>H<sub>29</sub>), 115.0 (SCH), 32.1 (NCCH<sub>2</sub>), 31.4 (CH<sub>2</sub>), 29.8 (CH<sub>2</sub>), 29.8 (CH<sub>2</sub>), 29.8 (CH<sub>2</sub>), 29.8 (CH<sub>2</sub>), 29.8 (CH<sub>2</sub>), 29.7 (CH<sub>2</sub>), 29.6 (CH<sub>2</sub>), 29.5 (CH<sub>2</sub>), 29.4 (CH<sub>2</sub>), 22.8 (CH<sub>2</sub>), 18.6 (SiCH(CH<sub>3</sub>)<sub>2</sub>), 14.3 (CH<sub>3</sub>), 11.8 (SiCH(CH<sub>3</sub>)<sub>2</sub>); HRMS (ESI)  $m/z$ : 438.3556; calculated for  $[\text{C}_{26}\text{H}_{51}\text{NSSi}+\text{H}]^+ = 438.3590$



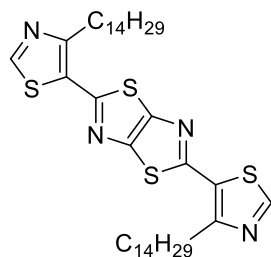
**4-Tetradecyl-2-triisopropylsilylthiazole-5-carbaldehyde (61):** 4-Tetradecyl-2-triisopropylsilylthiazole (3.00 g, 6.85 mmol) was dissolved in anhydrous THF (40 mL) and cooled to  $-78\text{ }^{\circ}\text{C}$  in a dry-ice/acetone bath. *N*-Butyllithium (1.60 M in hexanes, 6.85 mL, 8.22 mmol) was added dropwise and stirred for 1 hour before warming to room temperature. The red solution was then cooled back to  $-78\text{ }^{\circ}\text{C}$  and dimethylformamide (0.636 mL, 8.22 mmol)

was added dropwise and allowed to reach room temperature overnight. The reaction was quenched with saturated ammonium chloride and organics were extracted with DCM (3 × 50 mL). Combined organic layers were then washed with water (3 × 50 mL), dried over magnesium sulphate, filtered and solvent evaporated. The crude oil was then purified by column chromatography (1:100, EtOAc:hexane) to give the pure product as a pale orange oil (2.57 g, 81%). <sup>1</sup>H NMR (700 MHz, CDCl<sub>3</sub>) δ 10.12 (1H, s, CHO), 3.15 (2H, t, *J* = 7.4 Hz, ArCH<sub>2</sub>), 1.81 (2H, quin, *J* = 7.4 Hz, ArCH<sub>2</sub>CH<sub>2</sub>), 1.45 (3H, sept, *J* = 7.4 Hz, SiCH(CH<sub>3</sub>)<sub>2</sub>), 1.36 – 1.25 (22H, m, (CH<sub>2</sub>)<sub>11</sub>), 1.14 (18H, d, *J* = 7.5 Hz, SiCH(CH<sub>3</sub>)<sub>2</sub>), 0.89 (3H, t, *J* = 7.1 Hz, (CH<sub>2</sub>)<sub>11</sub>CH<sub>3</sub>); <sup>13</sup>C NMR (176 MHz, CDCl<sub>3</sub>) δ 182.5 (CHO), 179.2 (N=CS), 168.0 (NCC<sub>14</sub>H<sub>29</sub>), 134.4 (SCH), 32.1 (NCCH<sub>2</sub>), 30.2 (CH<sub>2</sub>), 30.2 (CH<sub>2</sub>), 29.8 (CH<sub>2</sub>), 29.8 (CH<sub>2</sub>), 29.8 (CH<sub>2</sub>), 29.7 (CH<sub>2</sub>), 29.7 (CH<sub>2</sub>), 29.5 (CH<sub>2</sub>), 29.3 (CH<sub>2</sub>), 22.8 (CH<sub>2</sub>), 18.5 (SiCH(CH<sub>3</sub>)<sub>2</sub>), 14.3 (CH<sub>3</sub>), 11.7 (SiCH(CH<sub>3</sub>)<sub>2</sub>); HRMS (ESI) *m/z*: 466.3533; calculated for [C<sub>27</sub>H<sub>51</sub>NOSSi+H]<sup>+</sup> = 466.3533

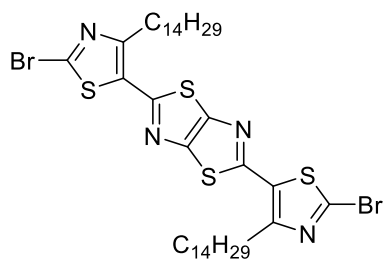


**4-Tetradecylthiazole-5-carbaldehyde (62):** 4-Tetradecyl-2-triisopropylsilylthiazole-5-carbaldehyde (2.50 g, 5.37 mmol) was dissolved in anhydrous THF (100 mL) and cooled to 0 °C in an ice-bath. Tetrabutylammonium fluoride (1.00 M in THF, 7.08 mL, 7.08 mmol) was added dropwise and the reaction mixture was allowed to stir at room temperature overnight. The reaction was quenched with water (100 mL) and organics were extracted with DCM (3 × 100 mL). The combined organic layers were washed with water (3 × 100 mL), dried over magnesium sulphate, filtered and the solvent was evaporated. The crude oil was purified by column chromatography (1:10, EtOAc:hexane) to give the pure product as an orange oil (0.680 g, 41%). <sup>1</sup>H NMR (700 MHz, CDCl<sub>3</sub>) δ 10.15 (1H, s, CHO), 8.99 (1H, s, ArH), 3.13 (2H, t, *J* = 7.6 Hz, ArCH<sub>2</sub>), 1.81 (2H, quin, *J* = 7.5 Hz, ArCH<sub>2</sub>CH<sub>2</sub>), 1.38 – 1.26 (22H, m, (CH<sub>2</sub>)<sub>11</sub>), 1.14 (18H, d, *J* = 7.5 Hz, SiCH(CH<sub>3</sub>)<sub>2</sub>), 0.89 (3H, t, *J* = 6.9 Hz, (CH<sub>2</sub>)<sub>11</sub>CH<sub>3</sub>); <sup>13</sup>C NMR (176 MHz, CDCl<sub>3</sub>) δ 182.4 (CHO), 166.7 (N=CS), 159.0 (NCC<sub>14</sub>H<sub>29</sub>), 133.0 (SCH), 32.0 (NCCH<sub>2</sub>), 30.3 (CH<sub>2</sub>), 30.1 (CH<sub>2</sub>), 30.1 (CH<sub>2</sub>), 29.8 (CH<sub>2</sub>), 29.8 (CH<sub>2</sub>), 29.8 (CH<sub>2</sub>), 29.8 (CH<sub>2</sub>), 29.7 (CH<sub>2</sub>), 29.6 (CH<sub>2</sub>), 29.5 (CH<sub>2</sub>), 29.5

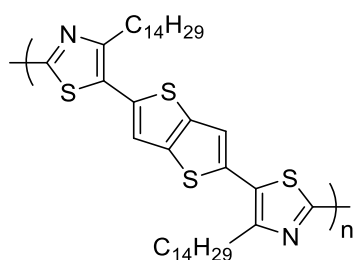
(CH<sub>2</sub>), 29.4 (CH<sub>2</sub>), 22.8 (CH<sub>2</sub>), 14.2 (CH<sub>3</sub>); HRMS (ESI) m/z: 310.2198; calculated for [C<sub>18</sub>H<sub>31</sub>NOS+H]<sup>+</sup> = 310.2199



**2,5-Bis-5(4-tetradecylthiazole)thiazolo[5,4-d]thiazole (63):** Dithiooxamide (107 mg, 0.890 mmol) and 4-tetradecylthiazole-5-carbaldehyde (550 mg, 1.78 mmol) were placed into an oven dried vial. Nitrobenzene (0.89 mL) was added and the mixture degassed by a constant flow of nitrogen for 30 minutes. The vial was then hermetically sealed, and the reaction mixture stirred at 200 °C for 1 hour. After cooling to room temperature anhydrous THF (4.5 mL) and chloranil (109 mg, 0.443 mmol) were added and heated to 70 °C for 20 minutes. The solution was then kept at 4 °C overnight over which time a brown precipitate formed which was filtered. The crude product was then purified by column chromatography (100 % DCM). The pure product was an orange solid (189 mg, 30%). <sup>1</sup>H NMR (700 MHz, CDCl<sub>3</sub>) δ 8.79 (2H, s, ArH), 3.17 (4H, t, J = 7.8 Hz, ArCH<sub>2</sub>), 1.85 (4H, quin, J = 7.7 Hz, ArCH<sub>2</sub>CH<sub>2</sub>), 1.47 (4H, quin, J = 7.5 Hz, CH<sub>2</sub>), 1.37 (4H, quin, J = 7.2 Hz, CH<sub>2</sub>) 1.31 – 1.26 (36H, m, (CH<sub>2</sub>)<sub>9</sub>), 0.88 (6H, t, J = 7.1 Hz, (CH<sub>2</sub>)<sub>11</sub>CH<sub>3</sub>); <sup>13</sup>C NMR (176 MHz, CDCl<sub>3</sub>) δ 159.9 (N=CS, thiazolothiazole), 157.3 (NCC<sub>14</sub>H<sub>29</sub>), 153.4 (N=CS, thiazole), 150.9 (SCN, thiazolothiazole), 127.2 (SC, thiazole), 32.1 (NCCH<sub>2</sub>), 31.5 (CH<sub>2</sub>), 31.1 (CH<sub>2</sub>), 29.8 (CH<sub>2</sub>), 29.8 (CH<sub>2</sub>), 29.8 (CH<sub>2</sub>), 29.8 (CH<sub>2</sub>), 29.8 (CH<sub>2</sub>), 29.7 (CH<sub>2</sub>), 29.7 (CH<sub>2</sub>), 29.6 (CH<sub>2</sub>), 29.5 (CH<sub>2</sub>), 29.1 (CH<sub>2</sub>), 22.8 (CH<sub>2</sub>), 14.3 (CH<sub>3</sub>); HRMS (ESI) m/z: 701.3766; calculated for [C<sub>38</sub>H<sub>60</sub>N<sub>4</sub>S<sub>4</sub>+H]<sup>+</sup> = 701.3774.



**2,5-Bis-5(4-tetradecyl-2-bromothiazole)thiazolo[5,4-*d*]thiazole (54)** 2,5-Bis-5(4-tetradecylthiazole)thiazolo[5,4-*d*]thiazole (160 mg, 0.228 mmol) was dissolved in anhydrous THF (10 mL) and cooled to  $-78\text{ }^{\circ}\text{C}$  in a dry-ice/acetone bath. Lithium diisopropylamide (2.00 M in alkanes, 0.274 mL, 0.547 mmol) was added dropwise and was stirred at  $-78\text{ }^{\circ}\text{C}$  for 1.5 h before allowing too warm to room temperature. After cooling back to  $-78\text{ }^{\circ}\text{C}$  carbon tetrabromide (182 mg, 0.547 mmol) was added at once and the reaction allowed to reach room temperature overnight. The reaction was quenched with saturated ammonium chloride and extracted with DCM ( $3 \times 10\text{ mL}$ ). Combined organic layers were washed with water ( $3 \times 10\text{ mL}$ ) and brine ( $3 \times 10\text{ mL}$ ), dried over magnesium sulphate, filtered and solvent was evaporated. The crude solid was purified by column chromatography (1:1 DCM:hexane) to give the pure product as an orange solid (72.5 mg, 37%).  $^1\text{H}$  NMR (700 MHz,  $\text{CDCl}_3$ )  $\delta$  3.08 (4H, t,  $J = 7.9\text{ Hz}$ ,  $\text{ArCH}_2$ ), 1.81 (4H, quin,  $J = 7.7\text{ Hz}$ ,  $\text{ArCH}_2\text{CH}_2$ ), 1.45 (4H, quin,  $J = 7.5\text{ Hz}$ ,  $\text{CH}_2$ ), 1.36 (4H, quin,  $J = 7.0\text{ Hz}$ ,  $\text{CH}_2$ ) 1.31 – 1.26 (36H, m,  $(\text{CH}_2)_9$ ), 0.89 (6H, t,  $J = 7.1\text{ Hz}$ ,  $(\text{CH}_2)_{11}\text{CH}_3$ );  $^{13}\text{C}$  NMR (176 MHz,  $\text{CDCl}_3$ )  $\delta$  158.7 (N=CS, thiazolothiazole), 156.7 (NCC $_{14}\text{H}_{29}$ ), 150.9 (SCN, thiazolothiazole), 137.3 (CBr), 130.8 (SC, thiazole), 32.1 (NCCH $_2$ ), 31.7 (CH $_2$ ), 31.1 (CH $_2$ ), 29.8 (CH $_2$ ), 29.8 (CH $_2$ ), 29.8 (CH $_2$ ), 29.8 (CH $_2$ ), 29.7 (CH $_2$ ), 29.5 (CH $_2$ ), 29.5 (CH $_2$ ), 29.6 (CH $_2$ ), 28.9 (CH $_2$ ), 22.8 (CH $_2$ ), 14.3 (CH $_3$ ); HRMS (ESI)  $m/z$ : 859.2005; calculated for  $[\text{C}_{38}\text{H}_{58}\text{Br}_2\text{N}_4\text{S}_4+\text{H}]^+ = 859.1963$



**Poly(2,5-bis-5(4-tetradecylthiazole)thieno[3,2-*b*]thiophene) (PbTzTT):** 5,5'-Dibromo-4,4'-tetradecyl-2,2'-bithiazole (617 mg, 0.858 mmol), 2,5-bis(trimethylstannyl)thieno[3,2-

*b*]thiophene (400 mg, 0.858 mmol) and tri(*o*-tolyl)phosphine (20.9 mg, 0.0687 mmol) were placed in an oven dried microwave vial and dissolved in anhydrous chlorobenzene (3.43 mL). The reaction mixture was heated to 40 °C and degassed by a constant flow of nitrogen for 30 minutes. Tris(dibenzylideneacetone)dipalladium (15.7 mg, 0.0171 mmol) was added at once and the vial hermetically sealed. The reaction mixture was heated in a microwave reactor at 100 °C for 2 minutes, 120 °C for 3 minutes, 140 °C for 5 minutes, 160 °C for 5 minutes and 180 °C for 40 minutes. After cooling to room temperature trimethyl(phenyl)tin (15.6 μL, 0.0858 mmol) was added. The reaction mixture was heated in a microwave reactor at 100 °C for 1 minute, 120 °C for 3 minutes, 140 °C for 5 minutes and 160 °C for 5 minutes. After cooling to room temperature bromobenzene (18.1 μL, 0.171 mmol) was added. The reaction mixture was heated in a microwave reactor at 100 °C for 1 minute, 120 °C for 3 minutes, 140 °C for 5 minutes and 160 °C for 5 minutes. The resultant gel was scraped into tetrachloroethane (10 mL) and heated to 80 °C. The polymer was then precipitated out of methanol, stirred for 2 hours and filtered into a Soxhlet thimble. A Soxhlet extraction was then performed with methanol, acetone and hexane, each for 24 hours. Finally, the polymer was extracted with chlorobenzene for 48 hours and precipitated from methanol to give the polymer as a green solid (291 mg, 48%).  $\lambda_{\text{max}} = 547 \text{ nm}$  (chlorobenzene solution);  $^1\text{H NMR}$  (400 MHz,  $d_2$ -TCE, 60 °C, residual solvent peak calibrated to 6.00 ppm)  $\delta$  7.39 (2H, s, *ArH*), 1.53 (12H, broad m, *CH*<sub>2</sub>), 1.31 (36H, broad m, *CH*<sub>2</sub>), 0.91 (6H, broad m, *CH*<sub>3</sub>).

# References

1. Chiang, C. K.; Fincher, C. R.; Park, Y. W.; Heeger, A. J.; Shirakawa, H.; Louis, E. J.; Gau, S. C.; MacDiarmid, A. G., Electrical Conductivity in Doped Polyacetylene. *Physical Review Letters* **1977**, *39* (17), 1098-1101.
2. Meng, L.; Zhang, Y.; Wan, X.; Li, C.; Zhang, X.; Wang, Y.; Ke, X.; Xiao, Z.; Ding, L.; Xia, R.; Yip, H.-L.; Cao, Y.; Chen, Y., Organic and solution-processed tandem solar cells with 17.3% efficiency. *Science* **2018**, *361* (6407), 1094-1098.
3. Günes, S.; Neugebauer, H.; Sariciftci, N. S., Conjugated Polymer-Based Organic Solar Cells. *Chemical Reviews* **2007**, *107* (4), 1324-1338.
4. Kim, H.; Nam, S.; Jeong, J.; Lee, S.; Seo, J.; Han, H.; Kim, Y., Organic solar cells based on conjugated polymers : History and recent advances. *Korean Journal of Chemical Engineering* **2014**, *31* (7), 1095-1104.
5. Inganäs, O., Organic Photovoltaics over Three Decades. *Advanced Materials* **2018**, *30* (35), 1800388.
6. Wang, G.; Melkonyan, F. S.; Facchetti, A.; Marks, T. J., All-Polymer Solar Cells: Recent Progress, Challenges, and Prospects. *Angewandte Chemie International Edition* **2019**, *58* (13), 4129-4142.
7. Wadsworth, A.; Moser, M.; Marks, A.; Little, M. S.; Gasparini, N.; Brabec, C. J.; Baran, D.; McCulloch, I., Critical review of the molecular design progress in non-fullerene electron acceptors towards commercially viable organic solar cells. *Chemical Society Reviews* **2019**, *48* (6), 1596-1625.
8. Salehi, A.; Fu, X.; Shin, D.-H.; So, F., Recent Advances in OLED Optical Design. *Advanced Functional Materials* **2019**, *29* (15), 1808803.
9. Wong, M. Y.; Zysman-Colman, E., Purely Organic Thermally Activated Delayed Fluorescence Materials for Organic Light-Emitting Diodes. *Advanced Materials* **2017**, *29* (22), 1605444.
10. Jeong, H.; Shin, H.; Lee, J.; Kim, B.; Park, Y.-I.; Yook, K. S.; An, B.-K.; Park, J., Recent progress in the use of fluorescent and phosphorescent organic compounds for organic light-emitting diode lighting. *Journal of Photonics for Energy* **2015**, *5* (1), 057608.
11. Bell, L. E., Cooling, Heating, Generating Power, and Recovering Waste Heat with Thermoelectric Systems. *Science* **2008**, *321* (5895), 1457-1461.
12. Snyder, G. J.; Toberer, E. S., Complex thermoelectric materials. *Nat Mater* **2008**, *7* (2), 105-114.
13. Zhang, Q.; Sun, Y.; Xu, W.; Zhu, D., Organic Thermoelectric Materials: Emerging Green Energy Materials Converting Heat to Electricity Directly and Efficiently. *Advanced Materials* **2014**, *26* (40), 6829-6851.
14. Russ, B.; Glaudell, A.; Urban, J. J.; Chabinyk, M. L.; Segalman, R. A., Organic thermoelectric materials for energy harvesting and temperature control. *Nature Reviews Materials* **2016**, *1*, 16050.
15. Cowen, L. M.; Atoyo, J.; Carnie, M. J.; Baran, D.; Schroeder, B. C., Review—Organic Materials for Thermoelectric Energy Generation. *ECS Journal of Solid State Science and Technology* **2017**, *6* (3), N3080-N3088.
16. Wang, H.; Yu, C., Organic Thermoelectrics: Materials Preparation, Performance Optimization, and Device Integration. *Joule* **2019**, *3* (1), 53-80.
17. Campoy-Quiles, M., Will organic thermoelectrics get hot? *Philosophical Transactions of the Royal Society A: Mathematical, Physical and Engineering Sciences* **2019**, *377* (2152), 20180352.
18. Sirringhaus, H., 25th Anniversary Article: Organic Field-Effect Transistors: The Path Beyond Amorphous Silicon. *Advanced Materials* **2014**, *26* (9), 1319-1335.
19. Paterson, A. F.; Singh, S.; Fallon, K. J.; Hodsden, T.; Han, Y.; Schroeder, B. C.; Bronstein, H.; Heeney, M.; McCulloch, I.; Anthopoulos, T. D., Recent Progress in High-Mobility Organic Transistors: A Reality Check. *Advanced Materials* **2018**, *30* (36), 1801079.
20. Kim, M.; Ryu, S. U.; Park, S. A.; Choi, K.; Kim, T.; Chung, D.; Park, T., Donor–Acceptor-Conjugated Polymer for High-Performance Organic Field-Effect Transistors: A Progress Report. *Advanced Functional Materials* **2019**, *n/a* (n/a), 1904545.
21. Inal, S.; Rivnay, J.; Suiu, A.-O.; Malliaras, G. G.; McCulloch, I., Conjugated Polymers in Bioelectronics. *Accounts of Chemical Research* **2018**, *51* (6), 1368-1376.
22. Borges-González, J.; Kousseff, C. J.; Nielsen, C. B., Organic semiconductors for biological sensing. *Journal of Materials Chemistry C* **2019**, *7* (5), 1111-1130.
23. Wang, X.; Geng, Z.; Cong, H.; Shen, Y.; Yu, B., Organic Semiconductors for Photothermal Therapy and Photoacoustic Imaging. *ChemBioChem* **2019**, *20* (13), 1628-1636.
24. Huo, Y.; Xing, X.; Zhang, C.; Wang, X.; Li, Y., An all organic redox flow battery with high cell voltage. *RSC Advances* **2019**, *9* (23), 13128-13132.
25. Chen, H.; Cong, G.; Lu, Y.-C., Recent progress in organic redox flow batteries: Active materials, electrolytes and membranes. *Journal of Energy Chemistry* **2018**, *27* (5), 1304-1325.
26. Singh, V.; Kim, S.; Kang, J.; Byon, H. R., Aqueous organic redox flow batteries. *Nano Research* **2019**, *12* (9), 1988-2001.
27. Lin, Y.; Li, Y.; Zhan, X., Small molecule semiconductors for high-efficiency organic photovoltaics. *Chemical Society Reviews* **2012**, *41* (11), 4245-4272.
28. Geoghegan, M.; Hadziioannou, G., *Polymer Electronics*. OUP Oxford: 2013.



29. Colson, J. W.; Dichtel, W. R., Rationally synthesized two-dimensional polymers. *Nature Chemistry* **2013**, *5* (6), 453-465.
30. Ebrahimi, M.; Rosei, F., Organic analogues of graphene. *Nature* **2017**, *542* (7642), 423-424.
31. Bi, S.; Yang, C.; Zhang, W.; Xu, J.; Liu, L.; Wu, D.; Wang, X.; Han, Y.; Liang, Q.; Zhang, F., Two-dimensional semiconducting covalent organic frameworks via condensation at arylmethyl carbon atoms. *Nature Communications* **2019**, *10* (1), 2467.
32. Köhler, A.; Bäessler, H., Electronic and Optical Processes of Organic Semiconductors. In *Electronic Processes in Organic Semiconductors*, Köhler, A.; Bäessler, H., Eds. Wiley: Weinheim, 2015; pp 193-305.
33. Misra, P. K., Chapter 18 - Novel Materials. In *Physics of Condensed Matter*, Misra, P. K., Ed. Academic Press: Boston, 2012; pp 599-631.
34. Narayan, M. R.; Singh, J., Excitonic Processes in Organic Semiconductors and Their Applications in Organic Photovoltaic and Light Emitting Devices. In *Excitonic and Photonic Processes in Materials*, Singh, J.; Williams, R. T., Eds. Springer Singapore: Singapore, 2015; pp 229-251.
35. Bredas, J.-L., Mind the gap! *Materials Horizons* **2014**, *1* (1), 17-19.
36. Coropceanu, V.; Cornil, J.; da Silva Filho, D. A.; Olivier, Y.; Silbey, R.; Brédas, J.-L., Charge Transport in Organic Semiconductors. *Chemical Reviews* **2007**, *107* (4), 926-952.
37. Yavuz, I., Dichotomy between the band and hopping transport in organic crystals: insights from experiments. *Physical Chemistry Chemical Physics* **2017**, *19* (38), 25819-25828.
38. Marcus, R. A.; Sutin, N., Electron transfers in chemistry and biology. *Biochimica et Biophysica Acta (BBA) - Reviews on Bioenergetics* **1985**, *811* (3), 265-322.
39. Monroe, D., Hopping in Exponential Band Tails. *Physical Review Letters* **1985**, *54* (2), 146-149.
40. Schmechel, R.; von Seggern, H., Electronic Traps in Organic Transport Layers. In *Physics of Organic Semiconductors*, Brütting, D., Ed. 2006; pp 271-303.
41. Sze, S.; Ng, K. K., Physics and Properties of Semiconductors—A Review. In *Physics of Semiconductor Devices*, Sze, S.; Ng, K. K., Eds. John Wiley and Sons: Hoboken, 2006; pp 5-75.
42. Thurmond, C. D., The Standard Thermodynamic Functions for the Formation of Electrons and Holes in Ge, Si, GaAs, and GaP. *Journal of The Electrochemical Society* **1975**, *122* (8), 1133.
43. Madelung, O., Physical data. In *Semiconductors — Basic Data*, Madelung, O., Ed. Springer Berlin Heidelberg: Berlin, Heidelberg, 1996; pp 5-298.
44. Eranna, G., *Crystal growth and evaluation of Silicon for VLSI and ULSI*. CRC Press: 2014; p 1-395.
45. Hase, H.; Salzmann, I., 11 - Doping in organic semiconductors. In *Handbook of Organic Materials for Electronic and Photonic Devices (Second Edition)*, Ostroverkhova, O., Ed. Woodhead Publishing: 2019; pp 349-383.
46. Lögdlund, M.; Lazzaroni, R.; Stafström, S.; Salaneck, W. R.; Brédas, J. L., Direct observation of charge-induced  $\pi$ -electronic structural changes in a conjugated polymer. *Physical Review Letters* **1989**, *63* (17), 1841-1844.
47. Parthasarathy, G.; Shen, C.; Kahn, A.; Forrest, S. R., Lithium doping of semiconducting organic charge transport materials. *Journal of Applied Physics* **2001**, *89* (9), 4986-4992.
48. Méndez, H.; Heimel, G.; Opitz, A.; Sauer, K.; Barkowski, P.; Oehzelt, M.; Soeda, J.; Okamoto, T.; Takeya, J.; Arlin, J.-B.; Balandier, J.-Y.; Geerts, Y.; Koch, N.; Salzmann, I., Doping of Organic Semiconductors: Impact of Dopant Strength and Electronic Coupling. *Angewandte Chemie International Edition* **2013**, *52* (30), 7751-7755.
49. Zhao, X.; Madan, D.; Cheng, Y.; Zhou, J.; Li, H.; Thon, S. M.; Bragg, A. E.; DeCoster, M. E.; Hopkins, P. E.; Katz, H. E., High Conductivity and Electron-Transfer Validation in an n-Type Fluoride-Anion-Doped Polymer for Thermoelectrics in Air. *Advanced Materials* **2017**, *29* (34), 1606928.
50. Liu, J.; Qiu, L.; Portale, G.; Koopmans, M.; ten Brink, G.; Hummelen, J. C.; Koster, L. J. A., N-Type Organic Thermoelectrics: Improved Power Factor by Tailoring Host-Dopant Miscibility. *Advanced Materials* **2017**, *29* (36), 1701641.
51. Méndez, H.; Heimel, G.; Winkler, S.; Frisch, J.; Opitz, A.; Sauer, K.; Wegner, B.; Oehzelt, M.; Röthel, C.; Duhm, S.; Többsens, D.; Koch, N.; Salzmann, I., Charge-transfer crystallites as molecular electrical dopants. *Nature Communications* **2015**, *6* (1), 8560.
52. Pingel, P.; Zhu, L.; Park, K. S.; Vogel, J.-O.; Janietz, S.; Kim, E.-G.; Rabe, J. P.; Brédas, J.-L.; Koch, N., Charge-Transfer Localization in Molecularly Doped Thiophene-Based Donor Polymers. *The Journal of Physical Chemistry Letters* **2010**, *1* (13), 2037-2041.
53. Li, H.; DeCoster, M. E.; Ireland, R. M.; Song, J.; Hopkins, P. E.; Katz, H. E., Modification of the Poly(bisdodecylquaterthiophene) Structure for High and Predominantly Nonionic Conductivity with Matched Dopants. *Journal of the American Chemical Society* **2017**, *139* (32), 11149-11157.
54. Torrance, J. B., The difference between metallic and insulating salts of tetracyanoquinodimethone (TCNQ): how to design an organic metal. *Accounts of Chemical Research* **1979**, *12* (3), 79-86.
55. Pingel, P.; Neher, D., Comprehensive picture of p-type doping of P3HT with the molecular acceptor F4-TCNQ. *Physical Review B* **2013**, *87* (11), 115209.
56. Arkhipov, V. I.; Heremans, P.; Emelianova, E. V.; Bäessler, H., Effect of doping on the density-of-states distribution and carrier hopping in disordered organic semiconductors. *Physical Review B* **2005**, *71* (4), 045214.
57. Pingel, P.; Schwarzl, R.; Neher, D., Effect of molecular p-doping on hole density and mobility in poly(3-hexylthiophene). *Applied Physics Letters* **2012**, *100* (14), 143303.
58. Jacobs, I. E.; Moulé, A. J., Controlling Molecular Doping in Organic Semiconductors. *Advanced Materials* **2017**, *29* (42), 1703063.

59. Gao, W.; Kahn, A., Controlled p-doping of zinc phthalocyanine by coevaporation with tetrafluorotetracyanoquinodimethane: A direct and inverse photoemission study. *Applied Physics Letters* **2001**, *79* (24), 4040-4042.
60. Kanai, K.; Akaike, K.; Koyasu, K.; Sakai, K.; Nishi, T.; Kamizuru, Y.; Nishi, T.; Ouchi, Y.; Seki, K., Determination of electron affinity of electron accepting molecules. *Applied Physics A* **2009**, *95* (1), 309-313.
61. Salzmann, I.; Heimel, G.; Oehzelt, M.; Winkler, S.; Koch, N., Molecular Electrical Doping of Organic Semiconductors: Fundamental Mechanisms and Emerging Dopant Design Rules. *Accounts of Chemical Research* **2016**, *49* (3), 370-378.
62. Cochran, J. E.; Junk, M. J. N.; Glauddell, A. M.; Miller, P. L.; Cowart, J. S.; Toney, M. F.; Hawker, C. J.; Chmelka, B. F.; Chabinyk, M. L., Molecular Interactions and Ordering in Electrically Doped Polymers: Blends of PBTTT and F4TCNQ. *Macromolecules* **2014**, *47* (19), 6836-6846.
63. Kang, K.; Watanabe, S.; Broch, K.; Sepe, A.; Brown, A.; Nasrallah, I.; Nikolka, M.; Fei, Z.; Heeney, M.; Matsumoto, D.; Marumoto, K.; Tanaka, H.; Kuroda, S.-i.; Sirringhaus, H., 2D coherent charge transport in highly ordered conducting polymers doped by solid state diffusion. *Nature Materials* **2016**, *15* (8), 896-902.
64. Shirakawa, H.; Louis, E. J.; MacDiarmid, A. G.; Chiang, C. K.; Heeger, A. J., Synthesis of electrically conducting organic polymers: halogen derivatives of polyacetylene, (CH). *Journal of the Chemical Society, Chemical Communications* **1977**, (16), 578-580.
65. Chiang, C. K.; Park, Y. W.; Heeger, A. J.; Shirakawa, H.; Louis, E. J.; MacDiarmid, A. G., Conducting polymers: Halogen doped polyacetylene. *The Journal of Chemical Physics* **1978**, *69* (11), 5098-5104.
66. Minakata, T.; Nagoya, I.; Ozaki, M., Highly ordered and conducting thin film of pentacene doped with iodine vapor. *Journal of Applied Physics* **1991**, *69* (10), 7354-7356.
67. Matsuo, Y.; Sasaki, A.; Yoshida, Y.; Ikehata, S., New stage structure of iodine doped pentacene film. *Materials Science and Engineering: B* **1999**, *60* (2), 133-136.
68. Brinkmann, M.; Videva, V. S.; Bieber, A.; André, J. J.; Turek, P.; Zuppiroli, L.; Bugnon, P.; Schaer, M.; Nuesch, F.; Humphry-Baker, R., Electronic and Structural Evidences for Charge Transfer and Localization in Iodine-Doped Pentacene. *The Journal of Physical Chemistry A* **2004**, *108* (40), 8170-8179.
69. Cazayous, M.; Sacuto, A.; Horowitz, G.; Lang, P.; Zimmers, A.; Lobo, R. P. S. M., Iodine insertion in pentacene thin films investigated by infrared and Raman spectroscopy. *Physical Review B* **2004**, *70* (8), 081309.
70. Jakabovič, J.; Vincze, A.; Kováč, J.; Srnánek, R.; Kováč Jr, J.; Dobročka, E.; Donoval, D.; Heinemeyer, U.; Schreiber, F.; Machovič, V.; Uherek, F., Surface and interface analysis of iodine-doped pentacene structures for OTFTs. *Surface and Interface Analysis* **2011**, *43* (1-2), 518-521.
71. McCullough, R. D.; Tristram-Nagle, S.; Williams, S. P.; Lowe, R. D.; Jayaraman, M., Self-orienting head-to-tail poly(3-alkylthiophenes): new insights on structure-property relationships in conducting polymers. *Journal of the American Chemical Society* **1993**, *115* (11), 4910-4911.
72. McCullough, R. D.; Lowe, R. D., Enhanced electrical conductivity in regioselectively synthesized poly(3-alkylthiophenes). *Journal of the Chemical Society, Chemical Communications* **1992**, (1), 70-72.
73. Jen, K.-Y.; Miller, G. G.; Elsenbaumer, R. L., Highly conducting, soluble, and environmentally-stable poly(3-alkylthiophenes). *Journal of the Chemical Society, Chemical Communications* **1986**, (17), 1346-1347.
74. Salmón, M.; Kanazawa, K. K.; Diaz, A. F.; Krounbi, M., A chemical route to pyrrole polymer films. *Journal of Polymer Science: Polymer Letters Edition* **1982**, *20* (3), 187-193.
75. Proń, A.; Kucharski, Z.; Budrowski, C.; Zagórska, M.; Krichene, S.; Suwalski, J.; Dehe, G.; Lefrant, S., Mössbauer spectroscopy studies of selected conducting polypyrroles. *The Journal of Chemical Physics* **1985**, *83* (11), 5923-5927.
76. Myers, R. E., Chemical oxidative polymerization as a synthetic route to electrically conducting polypyrroles. *Journal of Electronic Materials* **1986**, *15* (2), 61-69.
77. Armes, S. P., Optimum reaction conditions for the polymerization of pyrrole by iron(III) chloride in aqueous solution. *Synthetic Metals* **1987**, *20* (3), 365-371.
78. Korobov, M. M.; Pervova, Y. V.; Sidorov, L. N., Electron Affinity of Iron(III) Chloride. *Mendeleev Communications* **1992**, *2* (2), 41-42.
79. Liang, Z.; Zhang, Y.; Souri, M.; Luo, X.; Boehm, Alex M.; Li, R.; Zhang, Y.; Wang, T.; Kim, D.-Y.; Mei, J.; Marder, S. R.; Graham, K. R., Influence of dopant size and electron affinity on the electrical conductivity and thermoelectric properties of a series of conjugated polymers. *Journal of Materials Chemistry A* **2018**, *6* (34), 16495-16505.
80. Schmid, G.; Wemken, J. H.; Maltenerberger, A.; Diez, C.; Jaeger, A.; Dobbertin, T.; Hietsoi, O.; Dubceac, C.; Petrukhina, M. A., Fluorinated Copper(I) Carboxylates as Advanced Tunable p-Dopants for Organic Light-Emitting Diodes. *Advanced Materials* **2014**, *26* (6), 878-885.
81. Pecqueur, S.; Maltenerberger, A.; Petrukhina, M. A.; Halik, M.; Jaeger, A.; Pentlehn, D.; Schmid, G., Wide Band-Gap Bismuth-based p-Dopants for Opto-Electronic Applications. *Angewandte Chemie International Edition* **2016**, *55* (35), 10493-10497.
82. King, R. B., Organosulfur Derivatives of the Metal Carbonyls. III. The Reaction between Molybdenum Hexacarbonyl and Bis-(trifluoromethyl)-dithietene. *Inorganic Chemistry* **1963**, *2* (3), 641-642.
83. Qi, Y.; Sajoto, T.; Barlow, S.; Kim, E.-G.; Brédas, J.-L.; Marder, S. R.; Kahn, A., Use of a High Electron-Affinity Molybdenum Dithiolene Complex to p-Dope Hole-Transport Layers. *Journal of the American Chemical Society* **2009**, *131* (35), 12530-12531.

84. Qi, Y.; Sajoto, T.; Kröger, M.; Kandabarow, A. M.; Park, W.; Barlow, S.; Kim, E.-G.; Wielunski, L.; Feldman, L. C.; Bartynski, R. A.; Brédas, J.-L.; Marder, S. R.; Kahn, A., A Molybdenum Dithiolene Complex as p-Dopant for Hole-Transport Materials: A Multitechnique Experimental and Theoretical Investigation. *Chemistry of Materials* **2010**, *22* (2), 524-531.
85. Jozefowicz, M.; Yu, L. T.; Perichon, J.; Buvet, R., Propriétés Nouvelles des Polymères Semiconducteurs. *Journal of Polymer Science Part C: Polymer Symposia* **1969**, *22* (2), 1187-1195.
86. Doriomedoff, M.; Hautière-Cristofini, F.; de Surville, R.; Jozefowicz, M.; Yu, L.-T.; Buvet, R., Conductivité en courant continu des sulfates de polyanilines. *J. Chim. Phys.* **1971**, *68*, 1055-1069.
87. Macdiarmid, A. G.; Chiang, J.-C.; Halpern, M.; Huang, W.-S.; Mu, S.-L.; Nanaxakkara, L. D.; Wu, S. W.; Yaniger, S. I., "Polyaniline": Interconversion of Metallic and Insulating Forms. *Molecular Crystals and Liquid Crystals* **1985**, *121* (1-4), 173-180.
88. Travers, J. P.; Chroboczek, J.; Devreux, F.; Genoud, F.; Nechtschein, M.; Syed, A.; Genies, E. M.; Tsintavis, C., Transport and Magnetic Resonance Studies of Polyaniline. *Molecular Crystals and Liquid Crystals* **1985**, *121* (1-4), 195-199.
89. Chiang, J.-C.; MacDiarmid, A. G., 'Polyaniline': Protonic acid doping of the emeraldine form to the metallic regime. *Synthetic Metals* **1986**, *13* (1), 193-205.
90. Ćirić-Marjanović, G., Recent advances in polyaniline research: Polymerization mechanisms, structural aspects, properties and applications. *Synthetic Metals* **2013**, *177*, 1-47.
91. Epstein, A. J.; Ginder, J. M.; Zuo, F.; Woo, H. S.; Tanner, D. B.; Richter, A. F.; Angelopoulos, M.; Huang, W. S.; MacDiarmid, A. G., Insulator-to-metal transition in polyaniline: Effect of protonation in emeraldine. *Synthetic Metals* **1987**, *21* (1), 63-70.
92. Wudl, F.; Angus, R. O.; Lu, F. L.; Allemand, P. M.; Vachon, D.; Nowak, M.; Liu, Z. X.; Schaffer, H.; Heeger, A. J., Poly-p-phenyleneamineimine: synthesis and comparison to polyaniline. *Journal of the American Chemical Society* **1987**, *109* (12), 3677-3684.
93. Vachon, D.; Angus, R. O.; Lu, F. L.; Nowak, M.; Liu, Z. X.; Schaffer, H.; Wudl, F.; Heeger, A. J., Polyaniline is poly-para-phenyleneamineimine: proof of structure by synthesis. *Synthetic Metals* **1987**, *18* (1), 297-302.
94. Macdiarmid, A. G.; Chiang, J. C.; Richter, A. F.; Epstein, A. J., Polyaniline: a new concept in conducting polymers. *Synthetic Metals* **1987**, *18* (1), 285-290.
95. Ausserlechner, S. J.; Gruber, M.; Hetzel, R.; Flesch, H.-G.; Lading, L.; Hauser, L.; Haase, A.; Buchner, M.; Resel, R.; Schürer, F.; Stadlober, B.; Trimmel, G.; Zojer, K.; Zojer, E., Mechanism of surface proton transfer doping in pentacene based organic thin-film transistors. *physica status solidi (a)* **2012**, *209* (1), 181-192.
96. Yurash, B.; Cao, D. X.; Brus, V. V.; Leifert, D.; Wang, M.; Dixon, A.; Seifrid, M.; Mansour, A. E.; Lungwitz, D.; Liu, T.; Santiago, P. J.; Graham, K. R.; Koch, N.; Bazan, G. C.; Nguyen, T.-Q., Towards understanding the doping mechanism of organic semiconductors by Lewis acids. *Nature Materials* **2019**, *18* (12), 1327-1334.
97. Fan, X.; Nie, W.; Tsai, H.; Wang, N.; Huang, H.; Cheng, Y.; Wen, R.; Ma, L.; Yan, F.; Xia, Y., PEDOT:PSS for Flexible and Stretchable Electronics: Modifications, Strategies, and Applications. *Advanced Science* **2019**, *6* (19), 1900813.
98. Fan, Z.; Ouyang, J., Thermoelectric Properties of PEDOT:PSS. *Advanced Electronic Materials* **2019**, *5* (11), 1800769.
99. Zhu, Z.; Liu, C.; Jiang, F.; Xu, J.; Liu, E., Effective treatment methods on PEDOT:PSS to enhance its thermoelectric performance. *Synthetic Metals* **2017**, *225*, 31-40.
100. Sun, K.; Zhang, S.; Li, P.; Xia, Y.; Zhang, X.; Du, D.; Isikgor, F. H.; Ouyang, J., Review on application of PEDOTs and PEDOT:PSS in energy conversion and storage devices. *Journal of Materials Science: Materials in Electronics* **2015**, *26* (7), 4438-4462.
101. Shi, H.; Liu, C.; Jiang, Q.; Xu, J., Effective Approaches to Improve the Electrical Conductivity of PEDOT:PSS: A Review. *Advanced Electronic Materials* **2015**, *1* (4), 1500017.
102. Groenendaal, L.; Jonas, F.; Freitag, D.; Pielartzik, H.; Reynolds, J. R., Poly(3,4-ethylenedioxythiophene) and Its Derivatives: Past, Present, and Future. *Advanced Materials* **2000**, *12* (7), 481-494.
103. Lang, U.; Müller, E.; Naujoks, N.; Dual, J., Microscopical Investigations of PEDOT:PSS Thin Films. *Advanced Functional Materials* **2009**, *19* (8), 1215-1220.
104. Gangopadhyay, R.; Das, B.; Molla, M. R., How does PEDOT combine with PSS? Insights from structural studies. *RSC Advances* **2014**, *4* (83), 43912-43920.
105. Yi, C.; Wilhite, A.; Zhang, L.; Hu, R.; Chuang, S. S. C.; Zheng, J.; Gong, X., Enhanced Thermoelectric Properties of Poly(3,4-ethylenedioxythiophene):poly(styrenesulfonate) by Binary Secondary Dopants. *ACS Applied Materials & Interfaces* **2015**, *7* (17), 8984-8989.
106. Fan, Z.; Du, D.; Yu, Z.; Li, P.; Xia, Y.; Ouyang, J., Significant Enhancement in the Thermoelectric Properties of PEDOT:PSS Films through a Treatment with Organic Solutions of Inorganic Salts. *ACS Applied Materials & Interfaces* **2016**, *8* (35), 23204-23211.
107. Luo, J.; Billep, D.; Blaudeck, T.; Sheremet, E.; Rodriguez, R. D.; Zahn, D. R. T.; Toader, M.; Hietschold, M.; Otto, T.; Gessner, T., Chemical post-treatment and thermoelectric properties of poly(3,4-ethylenedioxythiophene):poly(styrenesulfonate) thin films. *Journal of Applied Physics* **2014**, *115* (5), 054908.
108. Kim, J. Y.; Jung, J. H.; Lee, D. E.; Joo, J., Enhancement of electrical conductivity of poly(3,4-ethylenedioxythiophene)/poly(4-styrenesulfonate) by a change of solvents. *Synthetic Metals* **2002**, *126* (2-3), 311-316.
109. Kumar, S. R. S.; Kurra, N.; Alshareef, H. N., Enhanced high temperature thermoelectric response of sulphuric acid treated conducting polymer thin films. *Journal of Materials Chemistry C* **2016**, *4* (1), 215-221.
110. Kiefer, D.; Kroon, R.; Hofmann, A. I.; Sun, H.; Liu, X.; Giovannitti, A.; Stegerer, D.; Cano, A.; Hynynen, J.; Yu, L.; Zhang, Y.; Nai, D.; Harrelson, T. F.; Sommer, M.; Moulé, A. J.; Kemerink, M.; Marder, S. R.; McCulloch, I.; Fahlman, M.;

- Fabiano, S.; Müller, C., Double doping of conjugated polymers with monomer molecular dopants. *Nature Materials* **2019**, *18* (2), 149-155.
111. Rainbolt, J. E.; Koech, P. K.; Polikarpov, E.; Swensen, J. S.; Cosimbescu, L.; Von Ruden, A.; Wang, L.; Sapochak, L. S.; Padmaperuma, A. B.; Gaspar, D. J., Synthesis and characterization of p-type conductivity dopant 2-(3-(adamantan-1-yl)propyl)-3,5,6-trifluoro-7,7,8-tetracyanoquinodimethane. *Journal of Materials Chemistry C* **2013**, *1* (9), 1876-1884.
112. Gao, Z. Q.; Mi, B. X.; Xu, G. Z.; Wan, Y. Q.; Gong, M. L.; Cheah, K. W.; Chen, C. H., An organic p-type dopant with high thermal stability for an organic semiconductor. *Chemical Communications* **2008**, (1), 117-119.
113. Koech, P. K.; Padmaperuma, A. B.; Wang, L.; Swensen, J. S.; Polikarpov, E.; Darsell, J. T.; Rainbolt, J. E.; Gaspar, D. J., Synthesis and Application of 1,3,4,5,7,8-Hexafluorotetracyanonaphthoquinodimethane (F6-TNAP): A Conductivity Dopant for Organic Light-Emitting Devices. *Chemistry of Materials* **2010**, *22* (13), 3926-3932.
114. Zhang, F.; Kahn, A., Investigation of the High Electron Affinity Molecular Dopant F6-TCNNQ for Hole-Transport Materials. *Advanced Functional Materials* **2018**, *28* (1), 1703780.
115. Fukunaga, T., Negatively substituted trimethylenecyclopropane dianions. *Journal of the American Chemical Society* **1976**, *98* (2), 610-611.
116. Fukunaga, T.; Gordon, M. D.; Krusic, P. J., Negatively substituted trimethylenecyclopropanes and their radical anions. *Journal of the American Chemical Society* **1976**, *98* (2), 611-613.
117. Karpov, Y.; Erdmann, T.; Raguzin, I.; Al-Hussein, M.; Binner, M.; Lappan, U.; Stamm, M.; Gerasimov, K. L.; Beryozkina, T.; Bakulev, V.; Anokhin, D. V.; Ivanov, D. A.; Günther, F.; Gemming, S.; Seifert, G.; Voit, B.; Di Pietro, R.; Kiriya, A., High Conductivity in Molecularly p-Doped Diketopyrrolopyrrole-Based Polymer: The Impact of a High Dopant Strength and Good Structural Order. *Advanced Materials* **2016**, *28* (28), 6003-6010.
118. Karpov, Y.; Erdmann, T.; Stamm, M.; Lappan, U.; Guskova, O.; Malanin, M.; Raguzin, I.; Beryozkina, T.; Bakulev, V.; Günther, F.; Gemming, S.; Seifert, G.; Hamsch, M.; Mannsfeld, S.; Voit, B.; Kiriya, A., Molecular Doping of a High Mobility Diketopyrrolopyrrole-Dithienylthieno[3,2-b]thiophene Donor-Acceptor Copolymer with F6TCNNQ. *Macromolecules* **2017**, *50* (3), 914-926.
119. Liu, Y.; Nell, B.; Ortstein, K.; Wu, Z.; Karpov, Y.; Beryozkina, T.; Lenk, S.; Kiriya, A.; Leo, K.; Reineke, S., High Electron Affinity Molecular Dopant CN6-CP for Efficient Organic Light-Emitting Diodes. *ACS Applied Materials & Interfaces* **2019**, *11* (12), 11660-11666.
120. Saska, J.; Gonel, G.; Bedolla-Valdez, Z. I.; Aronow, S. D.; Shevchenko, N. E.; Dudnik, A. S.; Moulé, A. J.; Mascal, M., A Freely Soluble, High Electron Affinity Molecular Dopant for Solution Processing of Organic Semiconductors. *Chemistry of Materials* **2019**, *31* (5), 1500-1506.
121. Solomeshch, O.; Yu, Y. J.; Goryunkov, A. A.; Sidorov, L. N.; Tuktarov, R. F.; Choi, D. H.; Jin, J.-I.; Tessler, N., Ground-State Interaction and Electrical Doping of Fluorinated C60 in Conjugated Polymers. *Advanced Materials* **2009**, *21* (44), 4456-4460.
122. Meerheim, R.; Olthof, S.; Hermenau, M.; Scholz, S.; Petrich, A.; Tessler, N.; Solomeshch, O.; Lüsse, B.; Riede, M.; Leo, K., Investigation of C60F36 as low-volatility p-dopant in organic optoelectronic devices. *Journal of Applied Physics* **2011**, *109* (10), 103102.
123. Tadich, A.; Edmonds, M. T.; Ley, L.; Fromm, F.; Smets, Y.; Mazej, Z.; Riley, J.; Pakes, C. I.; Seyller, T.; Wanke, M., Tuning the charge carriers in epitaxial graphene on SiC(0001) from electron to hole via molecular doping with C60F48. *Applied Physics Letters* **2013**, *102* (24), 241601.
124. Schlitz, R. A.; Brunetti, F. G.; Gludell, A. M.; Miller, P. L.; Brady, M. A.; Takacs, C. J.; Hawker, C. J.; Chabinyc, M. L., Solubility-Limited Extrinsic n-Type Doping of a High Electron Mobility Polymer for Thermoelectric Applications. *Advanced Materials* **2014**, *26* (18), 2825-2830.
125. Liu, J.; Qiu, L.; Alessandri, R.; Qiu, X.; Portale, G.; Dong, J.; Talsma, W.; Ye, G.; Sengrhan, A. A.; Souza, P. C. T.; Loi, M. A.; Chiechi, R. C.; Marrink, S. J.; Hummelen, J. C.; Koster, L. J. A., Enhancing Molecular n-Type Doping of Donor-Acceptor Copolymers by Tailoring Side Chains. *Advanced Materials* **2018**, *30* (7), 1704630.
126. Saldi, F.; Ghanbaja, J.; Marêché, J. F.; Billaud, D., Compared temperature dependence of the electrical conductivity of unoriented and stretched polycetylenes doped with heavy alkali metals. *Solid State Communications* **1991**, *78* (11), 941-945.
127. Ali Benamara, A.; Galtier, M.; Montaner, A., N doping of polyacetylene. *Synthetic Metals* **1991**, *41* (1), 45-48.
128. Kim, C. S.; Lee, S.; Tinker, L. L.; Bernhard, S.; Loo, Y.-L., Cobaltocene-Doped Viologen as Functional Components in Organic Electronics. *Chemistry of Materials* **2009**, *21* (19), 4583-4588.
129. Chan, C. K.; Amy, F.; Zhang, Q.; Barlow, S.; Marder, S.; Kahn, A., N-type doping of an electron-transport material by controlled gas-phase incorporation of cobaltocene. *Chemical Physics Letters* **2006**, *431* (1), 67-71.
130. Chan, C. K.; Kahn, A.; Zhang, Q.; Barlow, S.; Marder, S. R., Incorporation of cobaltocene as an n-dopant in organic molecular films. *Journal of Applied Physics* **2007**, *102* (1), 014906.
131. Chan, C. K.; Zhao, W.; Barlow, S.; Marder, S.; Kahn, A., Decamethylcobaltocene as an efficient n-dopant in organic electronic materials and devices. *Organic Electronics* **2008**, *9* (5), 575-581.
132. Liang, Z.; Gregg, B. A., Compensating Poly(3-hexylthiophene) Reveals Its Doping Density and Its Strong Exciton Quenching by Free Carriers. *Advanced Materials* **2012**, *24* (24), 3258-3262.
133. Cho, N.; Yip, H.-L.; Hau, S. K.; Chen, K.-S.; Kim, T.-W.; Davies, J. A.; Zeigler, D. F.; Jen, A. K. Y., n-Doping of thermally polymerizable fullerenes as an electron transporting layer for inverted polymer solar cells. *Journal of Materials Chemistry* **2011**, *21* (19), 6956-6961.

134. Avila, J.; La-Placa, M.-G.; Longhi, E.; Sessolo, M.; Barlow, S.; Marder, S. R.; Bolink, H. J., Ruthenium pentamethylcyclopentadienyl mesitylene dimer: a sublimable n-dopant and electron buffer layer for efficient n-i-p perovskite solar cells. *Journal of Materials Chemistry A* **2019**, *7* (45), 25796-25801.
135. Guo, S.; Kim, S. B.; Mohapatra, S. K.; Qi, Y.; Sajoto, T.; Kahn, A.; Marder, S. R.; Barlow, S., n-Doping of Organic Electronic Materials using Air-Stable Organometallics. *Advanced Materials* **2012**, *24* (5), 699-703.
136. Olthof, S.; Mehraeen, S.; Mohapatra, S. K.; Barlow, S.; Coropceanu, V.; Brédas, J.-L.; Marder, S. R.; Kahn, A., Ultralow Doping in Organic Semiconductors: Evidence of Trap Filling. *Physical Review Letters* **2012**, *109* (17), 176601.
137. Pulvirenti, F.; Wegner, B.; Noel, N. K.; Mazzotta, G.; Hill, R.; Patel, J. B.; Herz, L. M.; Johnston, M. B.; Riede, M. K.; Snaith, H. J.; Koch, N.; Barlow, S.; Marder, S. R., Modification of the fluorinated tin oxide/electron-transporting material interface by a strong reductant and its effect on perovskite solar cell efficiency. *Molecular Systems Design & Engineering* **2018**, *3* (5), 741-747.
138. Harada, K.; Werner, A. G.; Pfeiffer, M.; Bloom, C. J.; Elliott, C. M.; Leo, K., Organic Homo Junction Diodes with a High Built-in Potential: Interpretation of the Current-Voltage Characteristics by a Generalized Einstein Relation. *Physical Review Letters* **2005**, *94* (3), 036601.
139. Bloom, C. J.; Elliott, C. M.; Schroeder, P. G.; France, C. B.; Parkinson, B. A., Low Work Function Reduced Metal Complexes as Cathodes in Organic Electroluminescent Devices. *The Journal of Physical Chemistry B* **2003**, *107* (13), 2933-2938.
140. Harada, K.; Riede, M.; Leo, K.; Hild, O. R.; Elliott, C. M., Pentacene homo junctions: Electron and hole transport properties and related photovoltaic responses. *Physical Review B* **2008**, *77* (19), 195212.
141. Menke, T.; Ray, D.; Meiss, J.; Leo, K.; Riede, M., In-situ conductivity and Seebeck measurements of highly efficient n-dopants in fullerene C60. *Applied Physics Letters* **2012**, *100* (9), 093304.
142. Al-shadeedi, A.; Liu, S.; Keum, C.-M.; Kasemann, D.; Hoßbach, C.; Bartha, J.; Bunge, S. D.; Lüssem, B., Minority Currents in n-Doped Organic Transistors. *ACS Applied Materials & Interfaces* **2016**, *8* (47), 32432-32439.
143. Ferraris, J.; Cowan, D. O.; Walatka, V.; Perlstein, J. H., Electron transfer in a new highly conducting donor-acceptor complex. *Journal of the American Chemical Society* **1973**, *95* (3), 948-949.
144. Nollau, A.; Pfeiffer, M.; Fritz, T.; Leo, K., Controlled n-type doping of a molecular organic semiconductor: Naphthalenetetracarboxylic dianhydride (NTCDA) doped with bis(ethylenedithio)-tetrathiafulvalene (BEDT-TTF). *Journal of Applied Physics* **2000**, *87* (9), 4340-4343.
145. Ishii, H.; Sugiyama, K.; Yoshimura, D.; Ito, E.; Ouchi, Y.; Seki, K., Energy-level alignment at model interfaces of organic electroluminescent devices studied by UV photoemission: trend in the deviation from the traditional way of estimating the interfacial electronic structures. *IEEE Journal of Selected Topics in Quantum Electronics* **1998**, *4* (1), 24-33.
146. Senku, T.; Kaname, K.; Eiji, K.; Takashi, I.; Toshio, N.; Yukio, O.; Kazuhiko, S., Doping Effect of Tetrathianaphthacene Molecule in Organic Semiconductors on Their Interfacial Electronic Structures Studied by UV Photoemission Spectroscopy. *Japanese Journal of Applied Physics* **2005**, *44* (6R), 3760.
147. Wei, P.; Oh, J. H.; Dong, G.; Bao, Z., Use of a 1H-Benzoimidazole Derivative as an n-Type Dopant and To Enable Air-Stable Solution-Processed n-Channel Organic Thin-Film Transistors. *Journal of the American Chemical Society* **2010**, *132* (26), 8852-8853.
148. Zheng, L.; Zhou, Q.; Deng, X.; Yuan, M.; Yu, G.; Cao, Y., Methanofullerenes Used as Electron Acceptors in Polymer Photovoltaic Devices. *The Journal of Physical Chemistry B* **2004**, *108* (32), 11921-11926.
149. Zhu, X.-Q.; Zhang, M.-T.; Yu, A.; Wang, C.-H.; Cheng, J.-P., Hydride, Hydrogen Atom, Proton, and Electron Transfer Driving Forces of Various Five-Membered Heterocyclic Organic Hydrides and Their Reaction Intermediates in Acetonitrile. *Journal of the American Chemical Society* **2008**, *130* (8), 2501-2516.
150. Lu, M.; Nicolai, H. T.; Wetzelaer, G.-J. A. H.; Blom, P. W. M., N-type doping of poly(p-phenylene vinylene) with air-stable dopants. *Applied Physics Letters* **2011**, *99* (17), 173302.
151. Zeng, Y.; Zheng, W.; Guo, Y.; Han, G.; Yi, Y., Doping mechanisms of N-DMBI-H for organic thermoelectrics: hydrogen removal vs. hydride transfer. *Journal of Materials Chemistry A* **2020**.
152. Naab, B. D.; Guo, S.; Olthof, S.; Evans, E. G. B.; Wei, P.; Millhauser, G. L.; Kahn, A.; Barlow, S.; Marder, S. R.; Bao, Z., Mechanistic Study on the Solution-Phase n-Doping of 1,3-Dimethyl-2-aryl-2,3-dihydro-1H-benzimidazole Derivatives. *Journal of the American Chemical Society* **2013**, *135* (40), 15018-15025.
153. Naab, B. D.; Zhang, S.; Vandewal, K.; Salleo, A.; Barlow, S.; Marder, S. R.; Bao, Z., Effective Solution- and Vacuum-Processed n-Doping by Dimers of Benzimidazoline Radicals. *Advanced Materials* **2014**, *26* (25), 4268-4272.
154. Griffith, O. L.; Anthony, J. E.; Jones, A. G.; Lichtenberger, D. L., Electronic Properties of Pentacene versus Triisopropylsilylethynyl-Substituted Pentacene: Environment-Dependent Effects of the Silyl Substituent. *Journal of the American Chemical Society* **2010**, *132* (2), 580-586.
155. Zhang, S.; Naab, B. D.; Jucov, E. V.; Parkin, S.; Evans, E. G. B.; Millhauser, G. L.; Timofeeva, T. V.; Risko, C.; Brédas, J.-L.; Bao, Z.; Barlow, S.; Marder, S. R., n-Dopants Based on Dimers of Benzimidazoline Radicals: Structures and Mechanism of Redox Reactions. *Chemistry – A European Journal* **2015**, *21* (30), 10878-10885.
156. Naab, B. D.; Gu, X.; Kurosawa, T.; To, J. W. F.; Salleo, A.; Bao, Z., Role of Polymer Structure on the Conductivity of N-Doped Polymers. *Advanced Electronic Materials* **2016**, *2* (5), 1600004.
157. Yuan, D.; Huang, D.; Zhang, C.; Zou, Y.; Di, C.-a.; Zhu, X.; Zhu, D., Efficient Solution-Processed n-Type Small-Molecule Thermoelectric Materials Achieved by Precisely Regulating Energy Level of Organic Dopants. *ACS Applied Materials & Interfaces* **2017**, *9* (34), 28795-28801.

158. Han, Y.; Fei, Z.; Lin, Y.-H.; Martin, J.; Tuna, F.; Anthopoulos, T. D.; Heeney, M., Anion-induced N-doping of naphthalenediimide polymer semiconductor in organic thin-film transistors. *npj Flexible Electronics* **2018**, *2* (1), 11.
159. Alkorta, I.; Rozas, I.; Elguero, J., Interaction of Anions with Perfluoro Aromatic Compounds. *Journal of the American Chemical Society* **2002**, *124* (29), 8593-8598.
160. Mascal, M.; Armstrong, A.; Bartberger, M. D., Anion-Aromatic Bonding: A Case for Anion Recognition by  $\pi$ -Acidic Rings. *Journal of the American Chemical Society* **2002**, *124* (22), 6274-6276.
161. Mascal, M.; Yakovlev, I.; Nikitin, E. B.; Fetting, J. C., Fluoride-Selective Host Based on Anion- $\pi$  Interactions, Ion Pairing, and Hydrogen Bonding: Synthesis and Fluoride-Ion Sandwich Complex. *Angewandte Chemie International Edition* **2007**, *46* (46), 8782-8784.
162. Dawson, R. E.; Hennig, A.; Weimann, D. P.; Emery, D.; Ravikumar, V.; Montenegro, J.; Takeuchi, T.; Gabutti, S.; Mayor, M.; Mareda, J.; Schalley, C. A.; Matile, S., Experimental evidence for the functional relevance of anion- $\pi$  interactions. *Nature Chemistry* **2010**, *2*, 533.
163. Quiñero, D.; Garau, C.; Rotger, C.; Frontera, A.; Ballester, P.; Costa, A.; Deyà, P. M., Anion- $\pi$  Interactions: Do They Exist? **2002**, *114* (18), 3539-3542.
164. Quiñero, D.; Garau, C.; Frontera, A.; Ballester, P.; Costa, A.; Deyà, P. M., Counterintuitive interaction of anions with benzene derivatives. *Chemical Physics Letters* **2002**, *359* (5), 486-492.
165. Guha, S.; Saha, S., Fluoride Ion Sensing by an Anion- $\pi$  Interaction. *Journal of the American Chemical Society* **2010**, *132* (50), 17674-17677.
166. Guha, S.; Goodson, F. S.; Roy, S.; Corson, L. J.; Gravenmier, C. A.; Saha, S., Electronically Regulated Thermally and Light-Gated Electron Transfer from Anions to Naphthalenediimides. *Journal of the American Chemical Society* **2011**, *133* (39), 15256-15259.
167. Rananaware, A.; Samanta, M.; Bhosale, R. S.; Kobaisi, M. A.; Roy, B.; Bheemireddy, V.; Bhosale, S. V.; Bandyopadhyay, S.; Bhosale, S. V., Photomodulation of fluoride ion binding through anion- $\pi$  interactions using a photoswitchable azobenzene system. *Scientific Reports* **2016**, *6*, 22928.
168. Bélanger-Chabot, G.; Ali, A.; Gabbai, F. P., On the Reaction of Naphthalene Diimides with Fluoride Ions: Acid/Base versus Redox Reactions. **2017**, *56* (33), 9958-9961.
169. Tam, T. L. D.; Xu, J. W., The role of fluoride in anion- $\pi$  interaction with naphthalene diimide. *Chemical Communications* **2019**, *55* (44), 6225-6228.
170. Li, J.; Pang, X.; Wang, Y.; Che, Y.; Zhao, J., A new insight into fluoride anion in electron transfer reactions. *Catalysis Today* **2014**, *224*, 258-262.
171. Gregg, B. A.; Cormier, R. A., Doping Molecular Semiconductors: n-Type Doping of a Liquid Crystal Perylene Diimide. *Journal of the American Chemical Society* **2001**, *123* (32), 7959-7960.
172. Reilly, T. H.; Hains, A. W.; Chen, H.-Y.; Gregg, B. A., A Self-Doping, O<sub>2</sub>-Stable, n-Type Interfacial Layer for Organic Electronics. *Advanced Energy Materials* **2012**, *2* (4), 455-460.
173. Russ, B.; Robb, M. J.; Brunetti, F. G.; Miller, P. L.; Perry, E. E.; Patel, S. N.; Ho, V.; Chang, W. B.; Urban, J. J.; Chabiny, M. L.; Hawker, C. J.; Segalman, R. A., Power Factor Enhancement in Solution-Processed Organic n-Type Thermoelectrics Through Molecular Design. *Advanced Materials* **2014**, *26* (21), 3473-3477.
174. Russ, B.; Robb, M. J.; Popere, B. C.; Perry, E. E.; Mai, C.-K.; Fronk, S. L.; Patel, S. N.; Mates, T. E.; Bazan, G. C.; Urban, J. J.; Chabiny, M. L.; Hawker, C. J.; Segalman, R. A., Tethered tertiary amines as solid-state n-type dopants for solution-processable organic semiconductors. *Chemical Science* **2016**, *7* (3), 1914-1919.
175. Bronstein, H.; Nielsen, C. B.; Schroeder, B. C.; McCulloch, I., The role of chemical design in the performance of organic semiconductors. *Nature Reviews Chemistry* **2020**, *4* (2), 66-77.
176. Wang, K.-L.; Leung, M.-k.; Hsieh, L.-G.; Chang, C.-C.; Lee, K.-R.; Wu, C.-L.; Jiang, J.-C.; Tseng, C.-Y.; Wang, H.-T., Conjugated polymers containing electron-deficient main chains and electron-rich pendant groups: Synthesis and application to electroluminescence. *Organic Electronics* **2011**, *12* (6), 1048-1062.
177. Fu, B.; Wang, C.-Y.; Rose, B. D.; Jiang, Y.; Chang, M.; Chu, P.-H.; Yuan, Z.; Fuentes-Hernandez, C.; Kippelen, B.; Brédas, J.-L.; Collard, D. M.; Reichmanis, E., Molecular Engineering of Nonhalogenated Solution-Processable Bithiazole-Based Electron-Transport Polymeric Semiconductors. *Chemistry of Materials* **2015**, *27* (8), 2928-2937.
178. Carsten, B.; Szarko, J. M.; Lu, L.; Son, H. J.; He, F.; Botros, Y. Y.; Chen, L. X.; Yu, L., Mediating Solar Cell Performance by Controlling the Internal Dipole Change in Organic Photovoltaic Polymers. *Macromolecules* **2012**, *45* (16), 6390-6395.
179. Wang, S.; Sun, H.; Erdmann, T.; Wang, G.; Fazzi, D.; Lappan, U.; Puttison, Y.; Chen, Z.; Berggren, M.; Crispin, X.; Kiriya, A.; Voit, B.; Marks, T. J.; Fabiano, S.; Facchetti, A., A Chemically Doped Naphthalenediimide-Bithiazole Polymer for n-Type Organic Thermoelectrics. *Advanced Materials* **2018**, *30* (31), 1801898.
180. Holliday, S.; Ashraf, R. S.; Nielsen, C. B.; Kirkus, M.; Röhr, J. A.; Tan, C.-H.; Collado-Fregoso, E.; Knall, A.-C.; Durrant, J. R.; Nelson, J.; McCulloch, I., A Rhodanine Flanked Nonfullerene Acceptor for Solution-Processed Organic Photovoltaics. *Journal of the American Chemical Society* **2015**, *137* (2), 898-904.
181. Bürgi, L.; Turbiez, M.; Pfeiffer, R.; Bienewald, F.; Kirner, H.-J.; Winnewisser, C., High-Mobility Ambipolar Near-Infrared Light-Emitting Polymer Field-Effect Transistors. *Advanced Materials* **2008**, *20* (11), 2217-2224.
182. Shen, L.; Tang, Z.; Wang, X.; Liu, H.; Chen, Y.; Li, X., Effects of aromatic substituents on the electronic structure and excited state energy levels of diketopyrrolopyrrole derivatives for singlet fission. *Physical Chemistry Chemical Physics* **2018**, *20* (35), 22997-23006.
183. Glenis, S.; Benz, M.; LeGoff, E.; Schindler, J. L.; Kannewurf, C. R.; Kanatzidis, M. G., Polyfuran: a new synthetic approach and electronic properties. *Journal of the American Chemical Society* **1993**, *115* (26), 12519-12525.

184. Joule, J. A.; Mills, K., *Heterocyclic Chemistry*. John Wiley & Sons: Oxford, 2010.
185. Marino, G., The direction of the dipole moments of furan, thiophen, and pyrrole: A controversial question. *Journal of Heterocyclic Chemistry* **1972**, *9* (4), 817-819.
186. Bronstein, H.; Hurhangee, M.; Fregoso, E. C.; Beatrup, D.; Soon, Y. W.; Huang, Z.; Hadipour, A.; Tuladhar, P. S.; Rossbauer, S.; Sohn, E.-H.; Shoaee, S.; Dimitrov, S. D.; Frost, J. M.; Ashraf, R. S.; Kirchartz, T.; Watkins, S. E.; Song, K.; Anthopoulos, T.; Nelson, J.; Rand, B. P.; Durrant, J. R.; McCulloch, I., Isostructural, Deeper Highest Occupied Molecular Orbital Analogues of Poly(3-hexylthiophene) for High-Open Circuit Voltage Organic Solar Cells. *Chemistry of Materials* **2013**, *25* (21), 4239-4249.
187. van Mullekom, H. A. M.; Vekemans, J. A. J. M.; Havinga, E. E.; Meijer, E. W., Developments in the chemistry and band gap engineering of donor-acceptor substituted conjugated polymers. *Materials Science and Engineering: R: Reports* **2001**, *32* (1), 1-40.
188. Marszalek, T.; Li, M.; Pisula, W., Design directed self-assembly of donor-acceptor polymers. *Chemical Communications* **2016**, *52* (73), 10938-10947.
189. Holliday, S.; Li, Y.; Luscombe, C. K., Recent advances in high performance donor-acceptor polymers for organic photovoltaics. *Progress in Polymer Science* **2017**, *70*, 34-51.
190. Brocks, G.; Tol, A., Small Band Gap Semiconducting Polymers Made from Dye Molecules: Polysquaraines. *The Journal of Physical Chemistry* **1996**, *100* (5), 1838-1846.
191. Brocks, G.; Tol, A., A theoretical study of polysquaraines. *Synthetic Metals* **1996**, *76* (1), 213-216.
192. Mullekom, v. H. A. M. The chemistry of high and low band gap  $\pi$ -conjugated polymers. Phd Thesis 1 (Research TU/e / Graduation TU/e), Technische Universiteit Eindhoven, Eindhoven, 2000.
193. Ajayaghosh, A., Donor-acceptor type low band gap polymers: polysquaraines and related systems. *Chemical Society Reviews* **2003**, *32* (4), 181-191.
194. Havinga, E. E.; ten Hoeve, W.; Wynberg, H., Alternate donor-acceptor small-band-gap semiconducting polymers; Polysquaraines and polycroconaines. *Synthetic Metals* **1993**, *55* (1), 299-306.
195. Havinga, E. E.; ten Hoeve, W.; Wynberg, H., A new class of small band gap organic polymer conductors. *Polymer Bulletin* **1992**, *29* (1), 119-126.
196. Pu, K.; Mei, J.; Jokerst, J. V.; Hong, G.; Antaris, A. L.; Chattopadhyay, N.; Shuhendler, A. J.; Kurosawa, T.; Zhou, Y.; Gambhir, S. S.; Bao, Z.; Rao, J., Diketopyrrolopyrrole-Based Semiconducting Polymer Nanoparticles for In Vivo Photoacoustic Imaging. *Advanced Materials* **2015**, *27* (35), 5184-5190.
197. Huang, S.; Upputuri, P. K.; Liu, H.; Pramanik, M.; Wang, M., A dual-functional benzobisthiadiazole derivative as an effective theranostic agent for near-infrared photoacoustic imaging and photothermal therapy. *Journal of Materials Chemistry B* **2016**, *4* (9), 1696-1703.
198. Venkateshvaran, D.; Nikolka, M.; Sadhanala, A.; Lemaur, V.; Zelazny, M.; Kepa, M.; Hurhangee, M.; Kronemeijer, A. J.; Pecunia, V.; Nasrallah, I.; Romanov, I.; Broch, K.; McCulloch, I.; Emin, D.; Olivier, Y.; Cornil, J.; Beljonne, D.; Sirringhaus, H., Approaching disorder-free transport in high-mobility conjugated polymers. *Nature* **2014**, *515* (7527), 384-388.
199. Takeda, T.; Suzuki, Y.; Kawamata, J.; Noro, S.-i.; Nakamura, T.; Akutagawa, T., The emergent intramolecular hydrogen bonding effect on the electronic structures of organic electron acceptors. *Physical Chemistry Chemical Physics* **2017**, *19* (35), 23905-23909.
200. Nielsen, C. B.; Turbiez, M.; McCulloch, I., Recent Advances in the Development of Semiconducting DPP-Containing Polymers for Transistor Applications. *Advanced Materials* **2013**, *25* (13), 1859-1880.
201. Xiaowei, Z.; Antonio, F.; Stephen, B.; J., M. T.; A., R. M.; R., W. M.; R., M. S., Rylene and Related Diimides for Organic Electronics. *Advanced Materials* **2011**, *23* (2), 268-284.
202. Liu, Q.; Bottle, S. E.; Sonar, P., Developments of Diketopyrrolopyrrole-Dye-Based Organic Semiconductors for a Wide Range of Applications in Electronics. *Advanced Materials* **2020**, *32* (4), 1903882.
203. Von Eller-Pandraud, H., Structure cristalline de l'isoindigo. *Acta Crystallographica* **1960**, *13* (11), 936-938.
204. Estrada, L. A.; Stalder, R.; Abboud, K. A.; Risko, C.; Brédas, J.-L.; Reynolds, J. R., Understanding the Electronic Structure of Isoindigo in Conjugated Systems: A Combined Theoretical and Experimental Approach. *Macromolecules* **2013**, *46* (22), 8832-8844.
205. Stalder, R.; Mei, J.; Graham, K. R.; Estrada, L. A.; Reynolds, J. R., Isoindigo, a Versatile Electron-Deficient Unit For High-Performance Organic Electronics. *Chemistry of Materials* **2014**, *26* (1), 664-678.
206. Jackson, N. E.; Savoie, B. M.; Kohlstedt, K. L.; Olvera de la Cruz, M.; Schatz, G. C.; Chen, L. X.; Ratner, M. A., Controlling Conformations of Conjugated Polymers and Small Molecules: The Role of Nonbonding Interactions. *Journal of the American Chemical Society* **2013**, *135* (28), 10475-10483.
207. Conboy, G.; Spencer, H. J.; Angioni, E.; Kanibolotsky, A. L.; Findlay, N. J.; Coles, S. J.; Wilson, C.; Pitak, M. B.; Risko, C.; Coropceanu, V.; Brédas, J.-L.; Skabara, P. J., To bend or not to bend – are heteroatom interactions within conjugated molecules effective in dictating conformation and planarity? *Materials Horizons* **2016**, *3* (4), 333-339.
208. Turbiez, M.; Frère, P.; Leriche, P.; Mercier, N.; Roncali, J., Poly(3,6-dimethoxy-thieno[3,2-b]thiophene): a possible alternative to poly(3,4-ethylenedioxythiophene) (PEDOT). *Chemical Communications* **2005**, (9), 1161-1163.
209. Daoust, G.; Leclerc, M., Structure-property relationships in alkoxy-substituted polythiophenes. *Macromolecules* **1991**, *24* (2), 455-459.
210. Thorley, K. J.; McCulloch, I., Why are S-F and S-O non-covalent interactions stabilising? *Journal of Materials Chemistry C* **2018**, *6* (45), 12413-12421.

211. Hwang, J.; Park, J.; Kim, Y. J.; Ha, Y. H.; Park, C. E.; Chung, D. S.; Kwon, S.-K.; Kim, Y.-H., Indolo[3,2-b]indole-Containing Donor–Acceptor Copolymers for High-Efficiency Organic Solar Cells. *Chemistry of Materials* **2017**, *29* (5), 2135-2140.
212. Nielsen, C. B.; White, A. J. P.; McCulloch, I., Effect of Fluorination of 2,1,3-Benzothiadiazole. *The Journal of Organic Chemistry* **2015**, *80* (10), 5045-5048.
213. Boufflet, P.; Han, Y.; Fei, Z.; Treat, N. D.; Li, R.; Smilgies, D.-M.; Stingelin, N.; Anthopoulos, T. D.; Heeney, M., Using Molecular Design to Increase Hole Transport: Backbone Fluorination in the Benchmark Material Poly(2,5-bis(3-alkylthiophen-2-yl)thieno[3,2-b]-thiophene (pBTTT). *Advanced Functional Materials* **2015**, *25* (45), 7038-7048.
214. Yao, Z.-F.; Wang, J.-Y.; Pei, J., Control of  $\pi$ - $\pi$  Stacking via Crystal Engineering in Organic Conjugated Small Molecule Crystals. *Crystal Growth & Design* **2018**, *18* (1), 7-15.
215. Dou, J.-H.; Zheng, Y.-Q.; Yao, Z.-F.; Lei, T.; Shen, X.; Luo, X.-Y.; Yu, Z.-A.; Zhang, S.-D.; Han, G.; Wang, Z.; Yi, Y.; Wang, J.-Y.; Pei, J., A Cofacially Stacked Electron-Deficient Small Molecule with a High Electron Mobility of over 10 cm<sup>2</sup> V<sup>-1</sup> s<sup>-1</sup> in Air. *Advanced Materials* **2015**, *27* (48), 8051-8055.
216. Głowacki, E. D.; Coskun, H.; Blood-Forsythe, M. A.; Monkowius, U.; Leonat, L.; Grzybowski, M.; Gryko, D.; White, M. S.; Aspuru-Guzik, A.; Sariciftci, N. S., Hydrogen-bonded diketopyrrolopyrrole (DPP) pigments as organic semiconductors. *Organic Electronics* **2014**, *15* (12), 3521-3528.
217. Dhar, J.; Karothu, D. P.; Patil, S., Herringbone to cofacial solid state packing via H-bonding in diketopyrrolopyrrole (DPP) based molecular crystals: influence on charge transport. *Chemical Communications* **2015**, *51* (1), 97-100.
218. Fu, C.; Beldon, P. J.; Peregichka, D. F., H-Bonding Control of Supramolecular Ordering of Diketopyrrolopyrroles. *Chemistry of Materials* **2017**, *29* (7), 2979-2987.
219. Dou, J.-H.; Zheng, Y.-Q.; Yao, Z.-F.; Yu, Z.-A.; Lei, T.; Shen, X.; Luo, X.-Y.; Sun, J.; Zhang, S.-D.; Ding, Y.-F.; Han, G.; Yi, Y.; Wang, J.-Y.; Pei, J., Fine-Tuning of Crystal Packing and Charge Transport Properties of BDOPV Derivatives through Fluorine Substitution. *Journal of the American Chemical Society* **2015**, *137* (50), 15947-15956.
220. McCulloch, I.; Heeney, M.; Bailey, C.; Genevicius, K.; MacDonald, I.; Shkunov, M.; Sparrowe, D.; Tierney, S.; Wagner, R.; Zhang, W.; Chabiny, M. L.; Kline, R. J.; McGehee, M. D.; Toney, M. F., Liquid-crystalline semiconducting polymers with high charge-carrier mobility. *Nature Materials* **2006**, *5*, 328.
221. Cho, E.; Risko, C.; Kim, D.; Gysel, R.; Cates Miller, N.; Breiby, D. W.; McGehee, M. D.; Toney, M. F.; Kline, R. J.; Bredas, J.-L., Three-Dimensional Packing Structure and Electronic Properties of Biaxially Oriented Poly(2,5-bis(3-alkylthiophene-2-yl)thieno[3,2-b]thiophene) Films. *Journal of the American Chemical Society* **2012**, *134* (14), 6177-6190.
222. Biniek, L.; Leclerc, N.; Heiser, T.; Bechara, R.; Brinkmann, M., Large Scale Alignment and Charge Transport Anisotropy of pBTTT Films Oriented by High Temperature Rubbing. *Macromolecules* **2013**, *46* (10), 4014-4023.
223. DeLongchamp, D. M.; Kline, R. J.; Lin, E. K.; Fischer, D. A.; Richter, L. J.; Lucas, L. A.; Heeney, M.; McCulloch, I.; Northrup, J. E., High Carrier Mobility Polythiophene Thin Films: Structure Determination by Experiment and Theory. *Advanced Materials* **2007**, *19* (6), 833-837.
224. Brocorens, P.; Van Vooren, A.; Chabiny, M. L.; Toney, M. F.; Shkunov, M.; Heeney, M.; McCulloch, I.; Cornil, J.; Lazzaroni, R., Solid-State Supramolecular Organization of Polythiophene Chains Containing Thienothiophene Units. *Advanced Materials* **2009**, *21* (10-11), 1193-1198.
225. Zhang, Q.; Sun, Y.; Jiao, F.; Zhang, J.; Xu, W.; Zhu, D., Effects of structural order in the pristine state on the thermoelectric power-factor of doped PBTTT films. *Synthetic Metals* **2012**, *162* (9), 788-793.
226. Chabiny, M. L.; Toney, M. F.; Kline, R. J.; McCulloch, I.; Heeney, M., X-ray Scattering Study of Thin Films of Poly(2,5-bis(3-alkylthiophen-2-yl)thieno[3,2-b]thiophene). *Journal of the American Chemical Society* **2007**, *129* (11), 3226-3237.
227. Lei, T.; Cao, Y.; Zhou, X.; Peng, Y.; Bian, J.; Pei, J., Systematic Investigation of Isoindigo-Based Polymeric Field-Effect Transistors: Design Strategy and Impact of Polymer Symmetry and Backbone Curvature. *Chemistry of Materials* **2012**, *24* (10), 1762-1770.
228. de Leeuw, D. M.; Simenon, M. M. J.; Brown, A. R.; Einerhand, R. E. F., Stability of n-type doped conducting polymers and consequences for polymeric microelectronic devices. *Synthetic Metals* **1997**, *87* (1), 53-59.
229. Gregg, B. A.; Chen, S.-G.; Branz, H. M., On the superlinear increase in conductivity with dopant concentration in excitonic semiconductors. *Applied Physics Letters* **2004**, *84* (10), 1707-1709.
230. Matsunaga, Y.; Goto, K.; Kubono, K.; Sako, K.; Shinmyozu, T., Photoinduced Color Change and Photomechanical Effect of Naphthalene Diimides Bearing Alkylamine Moieties in the Solid State. *Chemistry – A European Journal* **2014**, *20* (24), 7309-7316.
231. Schmidt, S. B.; Biskup, T.; Jiao, X.; McNeill, C. R.; Sommer, M., Controlling intermolecular redox-doping of naphthalene diimides. *Journal of Materials Chemistry C* **2019**, *7* (15), 4466-4474.
232. Schmidt, S. B.; Hönig, M.; Shin, Y.; Cassinelli, M.; Perinot, A.; Caironi, M.; Jiao, X.; McNeill, C. R.; Fazzi, D.; Biskup, T.; Sommer, M., Radical Anion Yield, Stability, and Electrical Conductivity of Naphthalene Diimide Copolymers n-Doped with Tertiary Amines. *ACS Applied Polymer Materials* **2020**, *2* (5), 1954-1963.
233. Edson, J. B.; Macomber, C. S.; Pivovar, B. S.; Boncella, J. M., Hydroxide based decomposition pathways of alkyltrimethylammonium cations. *Journal of Membrane Science* **2012**, *399-400*, 49-59.
234. Chempath, S.; Boncella, J. M.; Pratt, L. R.; Henson, N.; Pivovar, B. S., Density Functional Theory Study of Degradation of Tetraalkylammonium Hydroxides. *The Journal of Physical Chemistry C* **2010**, *114* (27), 11977-11983.



235. Chempath, S.; Einsla, B. R.; Pratt, L. R.; Macomber, C. S.; Boncella, J. M.; Rau, J. A.; Pivovar, B. S., Mechanism of Tetraalkylammonium Headgroup Degradation in Alkaline Fuel Cell Membranes. *The Journal of Physical Chemistry C* **2008**, *112* (9), 3179-3182.
236. Nakano, M.; Sawamoto, M.; Yuki, M.; Takimiya, K., N,N'-Unsubstituted Naphthodithiophene Diimide: Synthesis and Derivatization via N-Alkylation and -Arylation. *Organic Letters* **2016**, *18* (15), 3770-3773.
237. Hansen, J. G.; Feeder, N.; Hamilton, D. G.; Gunter, M. J.; Becher, J.; Sanders, J. K. M., Macrocyclization and Molecular Interlocking via Mitsunobu Alkylation: Highlighting the Role of C-H...O Interactions in Templating. *Organic Letters* **2000**, *2* (4), 449-452.
238. Fletcher, S., The Mitsunobu reaction in the 21st century. *Organic Chemistry Frontiers* **2015**, *2* (6), 739-752.
239. Fernando, R.; Etheridge, F.; Muller, E.; Sauvé, G., Tuning the optical and electrochemical properties of core-substituted naphthalenediimides with styryl imide substituent. *New Journal of Chemistry* **2015**, *39* (4), 2506-2514.
240. Guo, Z.; Panda, D. K.; Maity, K.; Lindsey, D.; Parker, T. G.; Albrecht-Schmitt, T. E.; Barrera-Esparza, J. L.; Xiong, P.; Zhou, W.; Saha, S., Modulating the electrical conductivity of metal-organic framework films with intercalated guest  $\pi$ -systems. *Journal of Materials Chemistry C* **2016**, *4* (5), 894-899.
241. Kim, M. B.; Dixon, D. W., Hydrolysis of aliphatic naphthalene diimides: effect of charge placement in the side chains. *Journal of Physical Organic Chemistry* **2008**, *21* (9), 731-737.
242. Barros, T. C.; Cuccovia, I. M.; Farah, J. P. S.; Masini, J. C.; Chaimovich, H.; Politi, M. J., Mechanism of 1,4,5,8-naphthalene tetracarboxylic acid dianhydride hydrolysis and formation in aqueous solution. *Organic & Biomolecular Chemistry* **2006**, *4* (1), 71-82.
243. Barros, T. C.; Brochsztain, S.; Toscano, V. G.; Filho, P. B.; Politi, M. J., Photophysical characterization of a 1,4,5,8-naphthalenediimide derivative. *Journal of Photochemistry and Photobiology A: Chemistry* **1997**, *111* (1), 97-104.
244. Wintgens, V.; Valat, P.; Kossanyi, J.; Biczok, L.; Demeter, A.; Bérces, T., Spectroscopic properties of aromatic dicarboximides. Part 1.—N—H and N-methyl-substituted naphthalimides. *Journal of the Chemical Society, Faraday Transactions* **1994**, *90* (3), 411-421.
245. Deegan, R. D.; Bakajin, O.; Dupont, T. F.; Huber, G.; Nagel, S. R.; Witten, T. A., Capillary flow as the cause of ring stains from dried liquid drops. *Nature* **1997**, *389* (6653), 827-829.
246. Usta, H.; Risko, C.; Wang, Z.; Huang, H.; Delimeroglu, M. K.; Zhukhovitskiy, A.; Facchetti, A.; Marks, T. J., Design, Synthesis, and Characterization of Ladder-Type Molecules and Polymers. Air-Stable, Solution-Processable n-Channel and Ambipolar Semiconductors for Thin-Film Transistors via Experiment and Theory. *Journal of the American Chemical Society* **2009**, *131* (15), 5586-5608.
247. Jones, B. A.; Facchetti, A.; Wasielewski, M. R.; Marks, T. J., Tuning Orbital Energetics in Arylene Diimide Semiconductors. Materials Design for Ambient Stability of n-Type Charge Transport. *Journal of the American Chemical Society* **2007**, *129* (49), 15259-15278.
248. Kumar, S.; Ajayakumar, M. R.; Hundal, G.; Mukhopadhyay, P., Extraordinary Stability of Naphthalenediimide Radical Ion and Its Ultra-Electron-Deficient Precursor: Strategic Role of the Phosphonium Group. *Journal of the American Chemical Society* **2014**, *136* (34), 12004-12010.
249. Kumar, S.; Mukhopadhyay, P., Ambient stable naphthalenediimide radical ions: synthesis by solvent-free, sonication, mechanical grinding or milling protocols. *Green Chemistry* **2018**, *20* (20), 4620-4628.
250. Fulmer, G. R.; Miller, A. J. M.; Sherden, N. H.; Gottlieb, H. E.; Nudelman, A.; Stoltz, B. M.; Bercaw, J. E.; Goldberg, K. I., NMR Chemical Shifts of Trace Impurities: Common Laboratory Solvents, Organics, and Gases in Deuterated Solvents Relevant to the Organometallic Chemist. *Organometallics* **2010**, *29* (9), 2176-2179.
251. Satterlee, J. D., Fundamental Concepts of NMR in Paramagnetic Systems. Part II: Relaxation Effects. *Concepts in Magnetic Resonance* **1990**, *2* (3), 119-129.
252. Pohl, R.; Dračinský, M.; Slavětinská, L.; Buděšínský, M., The observed and calculated <sup>1</sup>H and <sup>13</sup>C chemical shifts of tertiary amines and their N-oxides. *Magnetic Resonance in Chemistry* **2011**, *49* (6), 320-327.
253. Kaake, L. G.; Barbara, P. F.; Zhu, X. Y., Intrinsic Charge Trapping in Organic and Polymeric Semiconductors: A Physical Chemistry Perspective. *The Journal of Physical Chemistry Letters* **2010**, *1* (3), 628-635.
254. Milita, S.; Liscio, F.; Cowen, L.; Cavallini, M.; Drain, B. A.; Degouée, T.; Luong, S.; Fenwick, O.; Guagliardi, A.; Schroeder, B. C.; Masciocchi, N., Polymorphism in N,N'-dialkyl-naphthalene diimides. *Journal of Materials Chemistry C* **2020**, *8* (9), 3097-3112.
255. Xu, J.; Chen, B.; Lv, J.; Chang, D.; Niu, D.; Hu, S.; Zhang, X.; Xin, Z.; Wang, L., Aryl modification of diketopyrrolopyrrole-based quaternary ammonium salts and their applications in copper electrodeposition. *Dyes and Pigments* **2019**, *170*, 107559.
256. Young, N. A.; Drew, S. C.; Maniam, S.; Langford, S. J., Systematically Studying the Effect of Fluoride on the Properties of Cyclophanes Bearing Naphthalene Diimide and Dialkoxyaryl Groups. **2017**, *12* (13), 1668-1675.
257. Dawson, R. E.; Hennig, A.; Weimann, D. P.; Emery, D.; Ravikumar, V.; Montenegro, J.; Takeuchi, T.; Gabutti, S.; Mayor, M.; Mareda, J.; Schalley, C. A.; Matile, S., Experimental evidence for the functional relevance of anion- $\pi$  interactions. *Nat Chem* **2010**, *2* (7), 533-538.
258. Stephenson, M. T.; Shine, H. J., Cation radicals. 47. Reaction of perylene cation radical with fluoride ion and of perylene with xenon difluoride. Formation of 1-fluoro-, 3-fluoro-, and a difluoroperylene. Complications with chloride ion impurity. *The Journal of Organic Chemistry* **1981**, *46* (15), 3139-3141.
259. Bélanger-Chabot, G.; Ali, A.; Gabbai, F. P., On the Reaction of Naphthalene Diimides with Fluoride Ions: Acid/Base versus Redox Reactions. *Angewandte Chemie International Edition* **2017**, *56* (33), 9958-9961.

260. Weber, C. D.; Bradley, C.; Lonergan, M. C., Solution phase n-doping of C60 and PCBM using tetrabutylammonium fluoride. *Journal of Materials Chemistry A* **2014**, *2* (2), 303-307.
261. Lei, T.; Dou, J.-H.; Cao, X.-Y.; Wang, J.-Y.; Pei, J., Electron-Deficient Poly(p-phenylene vinylene) Provides Electron Mobility over 1 cm<sup>2</sup> V<sup>-1</sup> s<sup>-1</sup> under Ambient Conditions. *Journal of the American Chemical Society* **2013**, *135* (33), 12168-12171.
262. Ting, L.; Jin-Hu, D.; Xiao-Yu, C.; Jie-Yu, W.; Jian, P., A BDOPV-Based Donor–Acceptor Polymer for High-Performance n-Type and Oxygen-Doped Ambipolar Field-Effect Transistors. *Advanced Materials* **2013**, *25* (45), 6589-6593.
263. Shi, K.; Zhang, F.; Di, C.-A.; Yan, T.-W.; Zou, Y.; Zhou, X.; Zhu, D.; Wang, J.-Y.; Pei, J., Toward High Performance n-Type Thermoelectric Materials by Rational Modification of BDPPV Backbones. *Journal of the American Chemical Society* **2015**, *137* (22), 6979-6982.
264. Li, J.; Rochester, C. W.; Jacobs, I. E.; Aasen, E. W.; Friedrich, S.; Stroeve, P.; Moulé, A. J., The effect of thermal annealing on dopant site choice in conjugated polymers. *Organic Electronics* **2016**, *33*, 23-31.
265. Nielsen, C. B.; Giovannitti, A.; Sbircea, D.-T.; Bandiello, E.; Niazi, M. R.; Hanifi, D. A.; Sessolo, M.; Amassian, A.; Malliaras, G. G.; Rivnay, J.; McCulloch, I., Molecular Design of Semiconducting Polymers for High-Performance Organic Electrochemical Transistors. *Journal of the American Chemical Society* **2016**, *138* (32), 10252-10259.
266. Giovannitti, A.; Nielsen, C. B.; Sbircea, D.-T.; Inal, S.; Donahue, M.; Niazi, M. R.; Hanifi, D. A.; Amassian, A.; Malliaras, G. G.; Rivnay, J.; McCulloch, I., N-type organic electrochemical transistors with stability in water. *Nature Communications* **2016**, *7*, 13066.
267. Kiefer, D.; Giovannitti, A.; Sun, H.; Biskup, T.; Hofmann, A.; Koopmans, M.; Cendra, C.; Weber, S.; Anton Koster, L. J.; Olsson, E.; Rivnay, J.; Fabiano, S.; McCulloch, I.; Müller, C., Enhanced n-Doping Efficiency of a Naphthalenediimide-Based Copolymer through Polar Side Chains for Organic Thermoelectrics. *ACS Energy Letters* **2018**, *3* (2), 278-285.
268. Liu, J.; Garman, M. P.; Dong, J.; van der Zee, B.; Qiu, L.; Portale, G.; Hummelen, J. C.; Koster, L. J. A., Doping Engineering Enables Highly Conductive and Thermally Stable n-Type Organic Thermoelectrics with High Power Factor. *ACS Applied Energy Materials* **2019**, *2* (9), 6664-6671.
269. Comins, D. L.; Joseph, S. P., N,N-Dimethylformamide. In *Encyclopedia of Reagents for Organic Synthesis*, 2001.
270. Würthner, F.; Kaiser, T. E.; Saha-Möller, C. R., J-Aggregates: From Serendipitous Discovery to Supramolecular Engineering of Functional Dye Materials. *Angewandte Chemie International Edition* **2011**, *50* (15), 3376-3410.
271. Spano, F. C., The Spectral Signatures of Frenkel Polarons in H- and J-Aggregates. *Accounts of Chemical Research* **2010**, *43* (3), 429-439.
272. Ko, E.-Y.; Lim, C.-H.; Kyoo-Hyun, C., Additions of Acetonitrile and Chloroform to Aromatic Aldehydes in the Presence of Tetrabutylammonium Fluoride. *Bulletin of the Korean Chemical Society* **2006**, *27*.
273. Hudlicky, M., Chemical shifts of fluorine in hydrogen fluoride and fluoride ion. *Journal of Fluorine Chemistry* **1985**, *28* (4), 461-472.
274. Sun, H.; DiMaggio, S. G., Anhydrous Tetrabutylammonium Fluoride. *Journal of the American Chemical Society* **2005**, *127* (7), 2050-2051.
275. Sharma, R. K.; Fry, J. L., Instability of anhydrous tetra-n-alkylammonium fluorides. *The Journal of Organic Chemistry* **1983**, *48* (12), 2112-2114.
276. Evoniuk, C. J.; Gomes, G. d. P.; Hill, S. P.; Fujita, S.; Hanson, K.; Alabugin, I. V., Coupling N–H Deprotonation, C–H Activation, and Oxidation: Metal-Free C(sp<sup>3</sup>)–H Aminations with Unprotected Anilines. *Journal of the American Chemical Society* **2017**, *139* (45), 16210-16221.
277. Pichette Drapeau, M.; Fabre, I.; Grimaud, L.; Ciofini, I.; Ollevier, T.; Taillefer, M., Transition-Metal-Free  $\alpha$ -Arylation of Enolizable Aryl Ketones and Mechanistic Evidence for a Radical Process. *Angewandte Chemie International Edition* **2015**, *54* (36), 10587-10591.
278. Budavari, S.; O'Neil, M. J.; Smith, A.; Heckelman, P. E., *The Merck Index, an Encyclopedia of Chemicals, Drugs, and Biologicals - Eleventh Edition*. Merck Co.: Inc. Rahway, NJ, 1989.
279. Babij, N. R.; McCusker, E. O.; Whiteker, G. T.; Canturk, B.; Choy, N.; Creemer, L. C.; Amicis, C. V. D.; Hewlett, N. M.; Johnson, P. L.; Knobelsdorf, J. A.; Li, F.; Lorsbach, B. A.; Nugent, B. M.; Ryan, S. J.; Smith, M. R.; Yang, Q., NMR Chemical Shifts of Trace Impurities: Industrially Preferred Solvents Used in Process and Green Chemistry. *Organic Process Research & Development* **2016**, *20* (3), 661-667.
280. Sarneski, J. E.; Surprenant, H. L.; Molen, F. K.; Reilley, C. N., Chemical shifts and protonation shifts in carbon-13 nuclear magnetic resonance studies of aqueous amines. *Analytical Chemistry* **1975**, *47* (13), 2116-2124.
281. Ng, C. K.; Tam, T. L. D.; Wei, F.; Lu, X.; Wu, J., Anion– $\pi$  and anion– $\pi$ -radical interactions in bis(triphenylphosphonium)-naphthalene diimide salts. *Organic Chemistry Frontiers* **2019**, *6* (1), 110-115.
282. Sun, H.; DiMaggio, S. G., Room-Temperature Nucleophilic Aromatic Fluorination: Experimental and Theoretical Studies. *Angewandte Chemie International Edition* **2006**, *45* (17), 2720-2725.
283. Allen, L. J.; Muhuhi, J. M.; Bland, D. C.; Merzel, R.; Sanford, M. S., Mild Fluorination of Chloropyridines with in Situ Generated Anhydrous Tetrabutylammonium Fluoride. *The Journal of Organic Chemistry* **2014**, *79* (12), 5827-5833.
284. Schimler, S. D.; Ryan, S. J.; Bland, D. C.; Anderson, J. E.; Sanford, M. S., Anhydrous Tetramethylammonium Fluoride for Room-Temperature S<sub>N</sub>Ar Fluorination. *The Journal of Organic Chemistry* **2015**, *80* (24), 12137-12145.
285. Shapet'ko, N. N.; Shigorin, D. N., NMR study of intramolecular hydrogen bond protons in quinoid structures. *Journal of Structural Chemistry* **1968**, *8* (3), 474-476.
286. Bhosale, S. V.; Jani, C. H.; Langford, S. J., Chemistry of naphthalene diimides. *Chemical Society Reviews* **2008**, *37* (2), 331-342.

287. Scott, J. C.; Pfluger, P.; Krounbi, M. T.; Street, G. B., Electron-spin-resonance studies of pyrrole polymers: Evidence for bipolarons. *Physical Review B* **1983**, *28* (4), 2140-2145.
288. Klymchenko, A. S., Solvatochromic and Fluorogenic Dyes as Environment-Sensitive Probes: Design and Biological Applications. *Accounts of Chemical Research* **2017**, *50* (2), 366-375.
289. Yuan, Z.; Buckley, C.; Thomas, S.; Zhang, G.; Bargigia, I.; Wang, G.; Fu, B.; Silva, C.; Brédas, J.-L.; Reichmanis, E., A Thiazole–Naphthalene Diimide Based n-Channel Donor–Acceptor Conjugated Polymer. *Macromolecules* **2018**, *51* (18), 7320-7328.
290. Liu, J.; Ye, G.; Zee, B. v. d.; Dong, J.; Qiu, X.; Liu, Y.; Portale, G.; Chiechi, R. C.; Koster, L. J. A., N-Type Organic Thermoelectrics of Donor–Acceptor Copolymers: Improved Power Factor by Molecular Tailoring of the Density of States. *Advanced Materials* **2018**, *30* (44), 1804290.
291. Heeney, M.; Bailey, C.; Genevicius, K.; Shkunov, M.; Sparrowe, D.; Tierney, S.; McCulloch, I., Stable Polythiophene Semiconductors Incorporating Thieno[2,3-b]thiophene. *Journal of the American Chemical Society* **2005**, *127* (4), 1078-1079.
292. Dondoni, A.; Fantin, G.; Fogagnolo, M.; Medici, A.; Pedrini, P., Synthesis and carbodemetalation reactions of 4-methyl- and 5-aryl-2-(trimethylsilyl)oxazoles. Carbon-carbon bond formation at C-2 of the oxazole ring. *The Journal of Organic Chemistry* **1987**, *52* (15), 3413-3420.
293. Pirrung, M. C.; Ghorai, S., Versatile, Fragrant, Convertible Isonitriles. *Journal of the American Chemical Society* **2006**, *128* (36), 11772-11773.
294. Bayh, O.; Awad, H.; Mongin, F.; Hoarau, C.; Bischoff, L.; Trécourt, F.; Quéguiner, G.; Marsais, F.; Blanco, F.; Abarca, B.; Ballesteros, R., Deprotonation of Benzoxazole and Oxazole Using Lithium Magnesates. *The Journal of Organic Chemistry* **2005**, *70* (13), 5190-5196.
295. Stangeland, E. L.; Sammakia, T., Use of Thiazoles in the Halogen Dance Reaction: Application to the Total Synthesis of WS75624 B. *The Journal of Organic Chemistry* **2004**, *69* (7), 2381-2385.
296. Usta, H.; Sheets, W. C.; Denti, M.; Generali, G.; Capelli, R.; Lu, S.; Yu, X.; Muccini, M.; Facchetti, A., Perfluoroalkyl-Functionalized Thiazole–Thiophene Oligomers as N-Channel Semiconductors in Organic Field-Effect and Light-Emitting Transistors. *Chemistry of Materials* **2014**, *26* (22), 6542-6556.
297. Johnson, J. R.; Rotenberg, D. H.; Ketcham, R., Thiazolothiazoles. II. Parent heterocycle and its carboxylic and amino derivatives. *Journal of the American Chemical Society* **1970**, *92* (13), 4046-4050.
298. Benin, V.; Yeates, A. T.; Dudis, D., Preparation of halogenated derivatives of thiazolo[5,4-d]thiazole via direct electrophilic aromatic substitution. *Journal of Heterocyclic Chemistry* **2008**, *45* (3), 811-819.
299. Hassan, J.; Lavenot, L.; Gozzi, C.; Lemaire, M., A convenient catalytic route to symmetrical functionalized bithiophenes. *Tetrahedron Letters* **1999**, *40* (5), 857-858.
300. Dondoni, A.; Fogagnolo, M.; Medici, A.; Negri, E., Palladium-Mediated Cross-Coupling Reactions Between Stannyl- and Bromothiazoles. Preparation of Thiazole Oligomers. *Synthesis* **1987**, *1987* (02), 185-186.
301. Dondoni, A.; Merino, P., 3.06 - Thiazoles. In *Comprehensive Heterocyclic Chemistry II*, Katritzky, A. R.; Rees, C. W.; Scriven, E. F. V., Eds. Pergamon: Oxford, 1996; pp 373-474.
302. Hestand, N. J.; Spano, F. C., Expanded Theory of H- and J-Molecular Aggregates: The Effects of Vibronic Coupling and Intermolecular Charge Transfer. *Chemical Reviews* **2018**, *118* (15), 7069-7163.
303. Kim, Y.; Cook, S.; Tuladhar, S. M.; Choulis, S. A.; Nelson, J.; Durrant, J. R.; Bradley, D. D. C.; Giles, M.; McCulloch, I.; Ha, C.-S.; Ree, M., A strong regioregularity effect in self-organizing conjugated polymer films and high-efficiency polythiophene:fullerene solar cells. *Nature Materials* **2006**, *5* (3), 197-203.
304. Yamamoto, T.; Arai, M.; Kokubo, H.; Sasaki, S., Copolymers of Thiophene and Thiazole. Regiocontrol in Synthesis, Stacking Structure, and Optical Properties. *Macromolecules* **2003**, *36* (21), 7986-7993.
305. Osaka, I.; Sauvé, G.; Zhang, R.; Kowalewski, T.; McCullough, R. D., Novel Thiophene-Thiazolothiazole Copolymers for Organic Field-Effect Transistors. *Advanced Materials* **2007**, *19* (23), 4160-4165.
306. Johnson, J. R.; Ketcham, R., Thiazolothiazoles. I. The Reaction of Aromatic Aldehydes with Dithioamide. *Journal of the American Chemical Society* **1960**, *82* (11), 2719-2724.
307. Bevk, D.; Marin, L.; Lutsen, L.; Vanderzande, D.; Maes, W., Thiazolo[5,4-d]thiazoles – promising building blocks in the synthesis of semiconductors for plastic electronics. *RSC Advances* **2013**, *3* (29), 11418-11431.
308. Li, Z.; Carmichael, I.; Ptasińska, S., Dissociative electron attachment induced ring opening in five-membered heterocyclic compounds. *Physical Chemistry Chemical Physics* **2018**, *20* (27), 18271-18278.
309. Dondoni, A.; Dall'Occo, T.; Fantin, G.; Fogagnolo, M.; Medici, A.; Pedrini, P., Intramolecular insertion of the isonitrile group into an oxygen–silicon bond. Synthesis of a 2-trimethylsilyloxazole via the  $\alpha$ -isocyano silyl enol ether. *Journal of the Chemical Society, Chemical Communications* **1984**, (4), 258-260.
310. Hodges, J. C.; Patt, W. C.; Connolly, C. J., Reactions of lithiooxazole. *The Journal of Organic Chemistry* **1991**, *56* (1), 449-452.
311. Vedejs, E.; Luchetta, L. M., A Method for Iodination of Oxazoles at C-4 via 2-Lithiooxazoles. *The Journal of Organic Chemistry* **1999**, *64* (3), 1011-1014.
312. Brown, W. D.; Gouliaev, A. H., Bromination of Isoquinoline, Quinoline, Quinazoline and Quinoxaline in Strong Acid. *Synthesis* **2002**, *2002* (01), 0083-0086.
313. Bergström, M.; Suresh, G.; Naidu, V. R.; Unelius, C. R., N-Iodosuccinimide (NIS) in Direct Aromatic Iodination. *European Journal of Organic Chemistry* **2017**, *2017* (22), 3234-3239.
314. Stanetty, P.; Schnürch, M.; Mereiter, K.; Mihovilovic, M. D., Investigations of the Halogen Dance Reaction on N-Substituted 2-Thiazolamines. *The Journal of Organic Chemistry* **2005**, *70* (2), 567-574.

315. Schnürch, M.; Spina, M.; Khan, A. F.; Mihovilovic, M. D.; Stanetty, P., Halogen dance reactions—A review. *Chemical Society Reviews* **2007**, *36* (7), 1046-1057.
316. Al-Hashimi, M.; Labram, J. G.; Watkins, S.; Motevalli, M.; Anthopoulos, T. D.; Heeney, M., Synthesis and Characterization of Fused Pyrrolo[3,2-d:4,5-d']bisthiazole-Containing Polymers. *Organic Letters* **2010**, *12* (23), 5478-5481.
317. Getmanenko, Y. A.; Tongwa, P.; Timofeeva, T. V.; Marder, S. R., Base-Catalyzed Halogen Dance Reaction and Oxidative Coupling Sequence as a Convenient Method for the Preparation of Dihalo-bisheteroarenes. *Organic Letters* **2010**, *12* (9), 2136-2139.
318. Sauter, F.; Fröhlich, H.; Kalt, W., Synthesis of 2-Substituted 3,5-Dibromothiophenes via a Rearrangement Reaction: A New Example of a Base-Catalyzed Halogen Dance Reaction. *Synthesis* **1989**, *1989* (10), 771-773.
319. Li, D.; Yuan, Y.; Bi, H.; Yao, X.; Zhao, X.; Tian, W.; Wang, Y.; Zhang, H., Boron-Bridged  $\pi$ -Conjugated Ladders as Efficient Electron-Transporting Emitters. *Inorganic Chemistry* **2011**, *50* (11), 4825-4831.
320. Yang, M.; Peng, B.; Liu, B.; Zou, Y.; Zhou, K.; He, Y.; Pan, C.; Li, Y., Synthesis and Photovoltaic Properties of Copolymers from Benzodithiophene and Thiazole. *The Journal of Physical Chemistry C* **2010**, *114* (41), 17989-17994.
321. Jung, I. H.; Jung, Y. K.; Lee, J.; Park, J.-H.; Woo, H. Y.; Lee, J.-I.; Chu, H. Y.; Shim, H.-K., Synthesis and electroluminescent properties of fluorene-based copolymers containing electron-withdrawing thiazole derivatives. *Journal of Polymer Science Part A: Polymer Chemistry* **2008**, *46* (21), 7148-7161.
322. Mamada, M.; Nishida, J.-i.; Kumaki, D.; Tokito, S.; Yamashita, Y., n-Type Organic Field-Effect Transistors with High Electron Mobilities Based on Thiazole-Thiazolothiazole Conjugated Molecules. *Chemistry of Materials* **2007**, *19* (22), 5404-5409.
323. Jung, J. Y.; Han, S. J.; Chun, J.; Lee, C.; Yoon, J., New thiazolothiazole derivatives as fluorescent chemosensors for Cr<sup>3+</sup> and Al<sup>3+</sup>. *Dyes and Pigments* **2012**, *94* (3), 423-426.
324. Ziessel, R.; Nano, A.; Heyer, E.; Bura, T.; Retailleau, P., Rational Design of New Thiazolo-Thiazole Dyes as Input Energy Units in Molecular Dyads. *Chemistry – A European Journal* **2013**, *19* (8), 2582-2588.
325. Jung, I. H.; Yu, J.; Jeong, E.; Kim, J.; Kwon, S.; Kong, H.; Lee, K.; Woo, H. Y.; Shim, H.-K., Synthesis and Photovoltaic Properties of Cyclopentadithiophene-Based Low-Bandgap Copolymers That Contain Electron-Withdrawing Thiazole Derivatives. *Chemistry – A European Journal* **2010**, *16* (12), 3743-3752.
326. Lee, S. K.; Cho, J. M.; Goo, Y.; Shin, W. S.; Lee, J.-C.; Lee, W.-H.; Kang, I.-N.; Shim, H.-K.; Moon, S.-J., Synthesis and characterization of a thiazolo[5,4-d]thiazole-based copolymer for high performance polymer solar cells. *Chemical Communications* **2011**, *47* (6), 1791-1793.
327. Ando, S.; Nishida, J.-i.; Tada, H.; Inoue, Y.; Tokito, S.; Yamashita, Y., High Performance n-Type Organic Field-Effect Transistors Based on  $\pi$ -Electronic Systems with Trifluoromethylphenyl Groups. *Journal of the American Chemical Society* **2005**, *127* (15), 5336-5337.
328. Dessi, A.; Calamante, M.; Mordini, A.; Zani, L.; Taddei, M.; Reginato, G., Microwave-activated synthesis of thiazolo[5,4-d]thiazoles by a condensation/oxidation sequence. *RSC Advances* **2014**, *4* (3), 1322-1328.
329. Knighton, R. C.; Hallett, A. J.; Kariuki, B. M.; Pope, S. J. A., A one-step synthesis towards new ligands based on aryl-functionalised thiazolo[5,4-d]thiazole chromophores. *Tetrahedron Letters* **2010**, *51* (41), 5419-5422.
330. Martin, R.; Buchwald, S. L., Palladium-Catalyzed Suzuki-Miyaura Cross-Coupling Reactions Employing Dialkylbiaryl Phosphine Ligands. *Accounts of Chemical Research* **2008**, *41* (11), 1461-1473.
331. Pei, Q.; Yang, Efficient Photoluminescence and Electroluminescence from a Soluble Polyfluorene. *Journal of the American Chemical Society* **1996**, *118* (31), 7416-7417.
332. Sainova, D.; Miteva, T.; Nothofer, H. G.; Scherf, U.; Glowacki, I.; Ulanski, J.; Fujikawa, H.; Neher, D., Control of color and efficiency of light-emitting diodes based on polyfluorenes blended with hole-transporting molecules. *Applied Physics Letters* **2000**, *76* (14), 1810-1812.
333. Izuhara, D.; Swager, T. M., Poly(Pyridinium Phenylene)s: Water-Soluble N-Type Polymers. *Journal of the American Chemical Society* **2009**, *131* (49), 17724-17725.
334. Poremba, K. E.; Dibrell, S. E.; Reisman, S. E., Nickel-Catalyzed Enantioselective Reductive Cross-Coupling Reactions. *ACS Catalysis* **2020**, *10* (15), 8237-8246.
335. Hassan, J.; Gozzi, C.; Lemaire, M., Palladium-catalysed symmetrical and unsymmetrical coupling of aryl halides. *Comptes Rendus de l'Académie des Sciences - Series IIC - Chemistry* **2000**, *3* (6), 517-521.
336. Oniwa, K.; Kikuchi, H.; Kanagasekaran, T.; Shimotani, H.; Ikeda, S.; Asao, N.; Yamamoto, Y.; Tanigaki, K.; Jin, T., Biphenyl end-capped bithiazole co-oligomers for high performance organic thin film field effect transistors. *Chemical Communications* **2016**, *52* (27), 4926-4929.
337. Pammer, F.; Passlack, U., Head-to-Tail Regioregular Polythiazole Prepared via Kumada-Coupling Polycondensation. *ACS Macro Letters* **2014**, *3* (2), 170-174.
338. Tian, Y.; Xu, X.; Wang, J.; Yao, C.; Li, L., Solution-Processed White Organic Light-Emitting Diodes with Enhanced Efficiency by Using Quaternary Ammonium Salt Doped Conjugated Polyelectrolyte. *ACS Applied Materials & Interfaces* **2014**, *6* (11), 8631-8638.
339. Wang, Z.; Zheng, N.; Zhang, W.; Yan, H.; Xie, Z.; Ma, Y.; Huang, F.; Cao, Y., Self-Doped, n-Type Perylene Diimide Derivatives as Electron Transporting Layers for High-Efficiency Polymer Solar Cells. *Advanced Energy Materials* **2017**, *7* (15), 1700232.
340. Giese, M.; Albrecht, M.; Rissanen, K., Anion- $\pi$  Interactions with Fluoroarenes. *Chemical Reviews* **2015**, *115* (16), 8867-8895.

341. Shi, Y.; Guo, H.; Qin, M.; Wang, Y.; Zhao, J.; Sun, H.; Wang, H.; Wang, Y.; Zhou, X.; Facchetti, A.; Lu, X.; Zhou, M.; Guo, X., Imide-Functionalized Thiazole-Based Polymer Semiconductors: Synthesis, Structure–Property Correlations, Charge Carrier Polarity, and Thin-Film Transistor Performance. *Chemistry of Materials* **2018**, *30* (21), 7988-8001.
342. Wakioka, M.; Ishiki, S.; Ozawa, F., Synthesis of Donor–Acceptor Polymers Containing Thiazolo[5,4-d]thiazole Units via Palladium-Catalyzed Direct Arylation Polymerization. *Macromolecules* **2015**, *48* (22), 8382-8388.
343. Wang, Y.; Wang, Y.; Zhu, L.; Liu, H.; Fang, J.; Guo, X.; Liu, F.; Tang, Z.; Zhang, M.; Li, Y., A novel wide-bandgap small molecule donor for high efficiency all-small-molecule organic solar cells with small non-radiative energy losses. *Energy & Environmental Science* **2020**, *13* (5), 1309-1317.
344. Samal, M.; Valligatla, S.; Saad, N. A.; Rao, M. V.; Rao, D. N.; Sahu, R.; Biswal, B. P., A thiazolo[5,4-d]thiazole-bridged porphyrin organic framework as a promising nonlinear optical material. *Chemical Communications* **2019**, *55* (74), 11025-11028.
345. Qi, F.; Song, J.; Xiong, W.; Huo, L.; Sun, X.; Sun, Y., Two wide-bandgap fluorine-substituted benzotriazole based terpolymers for efficient polymer solar cells. *Dyes and Pigments* **2018**, *155*, 126-134.
346. Yan, C.; Barlow, S.; Wang, Z.; Yan, H.; Jen, A. K. Y.; Marder, S. R.; Zhan, X., Non-fullerene acceptors for organic solar cells. *Nature Reviews Materials* **2018**, *3* (3), 18003.
347. Yang, C.-Y.; Ding, Y.-F.; Huang, D.; Wang, J.; Yao, Z.-F.; Huang, C.-X.; Lu, Y.; Un, H.-I.; Zhuang, F.-D.; Dou, J.-H.; Di, C.-a.; Zhu, D.; Wang, J.-Y.; Lei, T.; Pei, J., A thermally activated and highly miscible dopant for n-type organic thermoelectrics. *Nature Communications* **2020**, *11* (1), 3292.
348. Lu, Y.; Yu, Z.-D.; Liu, Y.; Ding, Y.-F.; Yang, C.-Y.; Yao, Z.-F.; Wang, Z.-Y.; You, H.-Y.; Cheng, X.-F.; Tang, B.; Wang, J.-Y.; Pei, J., The Critical Role of Dopant Cations in Electrical Conductivity and Thermoelectric Performance of n-Doped Polymers. *Journal of the American Chemical Society* **2020**, *142* (36), 15340-15348.
349. De, S.; Ramakrishnan, S., Folding of a Donor-Containing Ionene by Intercalation with an Acceptor. *Chemistry – An Asian Journal* **2011**, *6* (1), 149-156.